CHALMERS
UNIVERSITY OF TECHNOLOGY

Chalmers University of Technology Master's thesis

Binder jetting of aluminum alloys: Design for Additive Manufacturing and Material Characterization

Master's thesis in Product Development and Material Engineering

Didarul Alam
Omkar Rajan Dessai

Department of Industrial and Material Science
CHALMERS UNIVERSITY OF TECHNOLOGY
Gothenburg, Sweden 2024
www.chalmers.se

Master's thesis 2024

Binder jetting of Aluminum Alloys: Design for Additive Manufacturing and Material Characterization

Didarul Alam
Omkar Dessai

CHALMERS
UNIVERSITY OF TECHNOLOGY

Department of Industrial and Material Sciences
Center for additive manufacture (Metal)
Chalmers University of Technology
Gothenburg, Sweden 2024

Binder jetting of aluminum alloys: Design for Additive Manufacturing and Material characterization

Supervisor at Volvo Car Corporation: Torbjörn Larsson
Supervisor at Chalmers: Anok Babu Nagaram and Eduard Hryha
Examiner at Chalmers: Eduard Hryha

Master's Thesis 2024
Department of Industrial and Material Science
Center for Additive Manufacturing (Metal) - CAM^2
Chalmers University of Technology
SE-412 96 Gothenburg
Telephone +46 31 772 1000

The thesis work was performed in the framework of the Centre for Additive Manufacturing-Metal (CAM^2) in collaboration with Volvo Car Corporation, Gothenburg, Sweden and RICOH Company LTD.

Printed by Chalmers Digital Printing
Gothenburg, Sweden 2024

Abstract

Binder jetting technology (BJT) is an additive manufacturing (AM) process wherein a liquid binder is deposited on the power bed to join the particles together layer by layer, thus creating the desired geometry. This process can print various metals and polymers with higher productivity. Even so, among other metals, aluminum alloys are not commercially available to be produced by BJT. However, due to aluminum's intrinsic characteristics and properties, the passenger and commercial vehicle industries extensively utilize this metal. For this reason, it is a highly desired material for BJT/M in the automotive industry due to the possibility of printing complex shapes and having higher productivity than other metal additive manufacturing technologies. A Japanese company, RICOH Company Ltd, is currently working on developing technology for printing aluminum alloys in BJT. In this master thesis, design for AM and material characterization studies were conducted in collaboration with Volvo Car Corporation (VCC) and RICOH to study a heat sink for the headlamp for the XC90 production series car against two different aluminum alloys. As-produced aluminum alloy was 4000 series aluminum alloy, which had a Si content of less than 10 wt.%, and high pressure die casted aluminum alloy had a Si content of 12 wt.%. A study of design guidelines was carried out by printing design artefacts, and the geometry evaluation was done using scanning and superimposing CAD data. This provided knowledge about critical design features that can be produced using the technology and the limit. $10mm^3$ produced cubes were analyzed for porosity using Light Optical Microscopy (LOM). Density verification on the cubes using LOM, Geometrical, and Archimedes showed a relatively high density of 98% with a standard deviation of 0.91. The primary function of the heatsink studied here is dissipating heat away from other components. Thus, thermal conductivity and convection performance were measured. Thermal conductivity for as-sintered material was found to be 154.41 W/mK at room temperature (20 °C), and it was increased to 166.68 W/mK after Hot Isostatic pressing (HIP), compared to 97.94 W/mK for as-casted aluminum alloy which is currently being used. To improve the thermal convection, the new design features, namely Gyroid with varying wall thicknesses, were produced as test pieces and tested in the experimental setup to determine the design with the best performance. Heat dissipation increased by 99% in free convection and 82% in forced convection compared to the as-casted heatsink; this was demonstrated during the experiment. A new heatsink design produced using BJT Al alloys also resulted in a weight reduction of 42% to the existing design. Regarding the mechanical properties, HV5 was found to be 51.91% less for as-sintered aluminum alloy compared to as-casted aluminum alloy and 48.98% less for as-sintered aluminum alloy when HK1 was considered. The microstructure analysis showed that the reason for the thermal conductivity increase and hardness decrease in the aluminum alloy produced by BJT/M is connected to the lower Si content. Hence, the lower fraction of AlSi-precipitates was produced.

Keywords: Additive manufacturing, Binder Jetting for Metals, Gyroid Structures, Material Characterisation, Hardness, Thermal conductivity, Thermal convection, Hot Isostatic Pressing

Acknowledgements

We would like to extend our heartfelt gratitude to all the individuals who have supported and guided us throughout our journey to completing this master's thesis. The master's thesis was carried out at the pilot plant & concept center at Volvo Car Corporation, Gothenburg, Sweden, and the Center for additive manufacturing (CAM^2) at Chalmers. This was done as part of a Final degree project for the Master of Science in Product Development and Material Engineering at Chalmers University of Technology, Sweden in collaboration with Volvo Car Corporation.
First and foremost, we would like to express our sincere appreciation to our industrial supervisor, Torbjörn Larsson, for allowing us to work on this research project in a real-world setting. His valuable insights, constant encouragement, and constructive feedback were instrumental in shaping the direction of this thesis.
We are extremely grateful to our examiner and academic supervisor Eduard Hryha for providing us with all the shared expertise and mentorship in the field of additive manufacturing and Binder jetting technology for metals in particular. His academic expertise has been pivotal in strengthening the theoretical foundation of this research. We are also deeply indebted to our academic co-supervisor, Anok Babu Nagaram, for his scholarly guidance, expert advice, and unwavering support. His academic expertise has been pivotal in strengthening the theoretical foundation of this research.
We would like to take this opportunity to thank Markus Enmark and Alberto Cabo Rio for sharing their experience and practical knowledge that was helpful during the laboratory work and also helped us structure the thesis. We are also deeply indebted to Erika Steyn, Daniel Gren, and Dr. Antonio Mulone for supporting us with the needed training.
We would like to express our gratitude to Miyazaki Yoshiyuki and his team at RICOH as the technology provider company in this project for allowing us to work with their technology in printing various parts.
We would also like to extend our appreciation to the faculty members, research peers, and staff who have contributed in various ways to this thesis, including their thoughtful discussions and technical assistance. We acknowledge that this thesis would not have been possible without the collective efforts and support of all these individuals, and we are truly grateful for their contributions.

January 29, 2024
Gothenburg, Sweden.

Didarul Alam & Omkar Dessai

List of Acronyms

Below is the list of acronyms that have been used throughout this thesis listed below:

AM	Additive Manufacturing
PBF/LB	Powder Bed Fusion - Laser Beam
PBF/EB	Powder Bed Fusion - Electron Beam
BJT	Binder Jetting Technology
HPDC	High Pressure Die Casting
AlSi	Aluminum Silicate
SS	Solid State Sintering
LPS	Liquid Phase Sintering
SLPS	Supersolidus Liquid Phase Sintering
MG	Microgrid
PV	Photovoltaic
RES	Renewable-based Energy Sources
LOM	Light Optical Microscopy
HIP	Hot Isostatic Pressing

Contents

List of Figures

List of Tables

1
Introduction

1.1 Background

Heat removal from mechanical and electrical devices is becoming increasingly important as society's reliance on electronics and computational power grows. Thermal management equipment, such as heat sinks, heat exchangers, and heat spreaders, is frequently used to remove heat. Like electronics, automobiles also use efficient heat dissipation from their working parts to function correctly. It is known that to reduce weight and price, automotives are mainly made out of aluminum alloy. Hence it is crucial that the aluminum alloy can perform as per requirements. Currently, to increase the longevity and efficiency of the car's headlamp, high-pressure die-casted aluminum alloy is used. This is mainly due to its high production rate and lower manufacturing cost than other methods. However, there is still room to improve, possibly by introducing additive manufacturing (AM), which can enable the design of more complex shapes and improve performance & properties while getting close to similar productivity.

Through a layer-by-layer process, additive manufacturing (AM) generates accurate models or things directly from computer-aided design (CAD) models with minimal geometric limitations. Using several processes, AM may be applied to practically any material [4]. Each approach has specific applications and constraints [5].

In powder bed fusion, a heat source is used as a Laser beam (PBF/LB) or electron beam (PBF/EB) to fuse raw materials together and print the parts. On the other hand, Binder jetting technology is a multistep AM process "in which a liquid bonding agent is selectively deposited to join powder materials," according to ISO/ASTM 52900 [6]. Due to the higher production rate compared to PBF/LB, one of the most sought-after AM technologies for the automotive industry is Binder jetting technology (BJT). It glues the particles together to produce the shape layer by layer, eliminating the need for heat during fabrication. Furthermore, unbound powder temporarily supports unconnected regions of the component, allowing interior volumes to develop and reducing material waste [7]. This procedure is usually referred to as the printing stage in BJT and must be followed by de-powdering, curing, sintering, and further post-processing to achieve the final material properties[8]. The quality of these final products determines the process's application space. These final qualities depend on various process parameters, including the raw material, powder bed formation, construction parameters, sintering, as mentioned before, and post-processing techniques such as surface smoothening and heat treatment.

Binder jetting technology for metals (BJT/M) has numerous potential advantages

as an AM process. It may, for example, deal with almost any powdered feedstock and integrate functionally-graded components. Because it only has to print the binder—a portion of the overall part volume—BJT systems have a comparatively high build rate when compared to other printing methods like Powder Bed Fusion – Laser Beam [9]. A 100-nozzle print head, for example, can produce parts at speeds of up to 200 cm^3 per minute [4].
Numerous studies have been conducted and continue to be driven to grasp the full potential of this method [10]. The flexibility of conceptualizing and creating intricate patterns with BJT/M comes with its own difficulties. Discussions are currently taking place in process parameter optimization, surface-roughness management, support structure removal, post-processing needs, compatible raw materials, and cost-competitiveness compared to traditional methods for bulk production.
In this master thesis, design for additive manufacturing is explored for this particular BJT/M technology provided by RICOH Company Ltd. by printing various artefacts related to the heat sink for the Volvo XC90 model production car. Hardness, thermal conductivity, and thermal convection tests are measured to understand performance compared to the as-casted heat sink currently used in the XC90 production series car model.

1.2 Aim and research questions

Additive Manufacturing components including Binder jetting technology for Metals (BJT/M) do not always fulfill the product requirements. In the case of BJT/M, it is mostly due to the presence of distortions, porosity, and shrinkage that influence the final component tolerances and properties.
Hence, in this project, it was decided to evaluate these aspects with respect to the existing component. For this purpose, one of the heat sinks in the headlamp of the Volvo XC90 production series car was taken for re-design and printing using BJT/M for aluminum alloys. Based on the issue under investigation following research questions were formulated to be answered in this project.

- How to design for selected application using the BJT/M technology for aluminum alloys?
- What are the thermal and mechanical properties of Al-alloys produced by the BJT/M process?
- What does the design methodology look like in the different process steps compared to the existing technology in BJT/M?
- Does the produced application add any new features, improvements, performance, or other values to consider?

These questions were answered at the end of the Thesis based on the knowledge gained from the project.

2

Literature Study

2.1 Binder jetting for metal

Binder jetting technology is an AM method defined as a "process in which a liquid bonding agent is selectively deposited to join powder particles" [6]. During the process, the spreading of a powder layer in a build-box is followed by the deposition of a binder, which selectively glues the particles together. This procedure is repeated layer-by-layer to join the powder within the designed three-dimensional geometry in the resulting powder bed [8]. The typical BJT printer system can be divided into several main parts: a binder deposition system, powder dispensing, and recoating system build platform, and excess powder collecting chamber, as illustrated in 2.1.

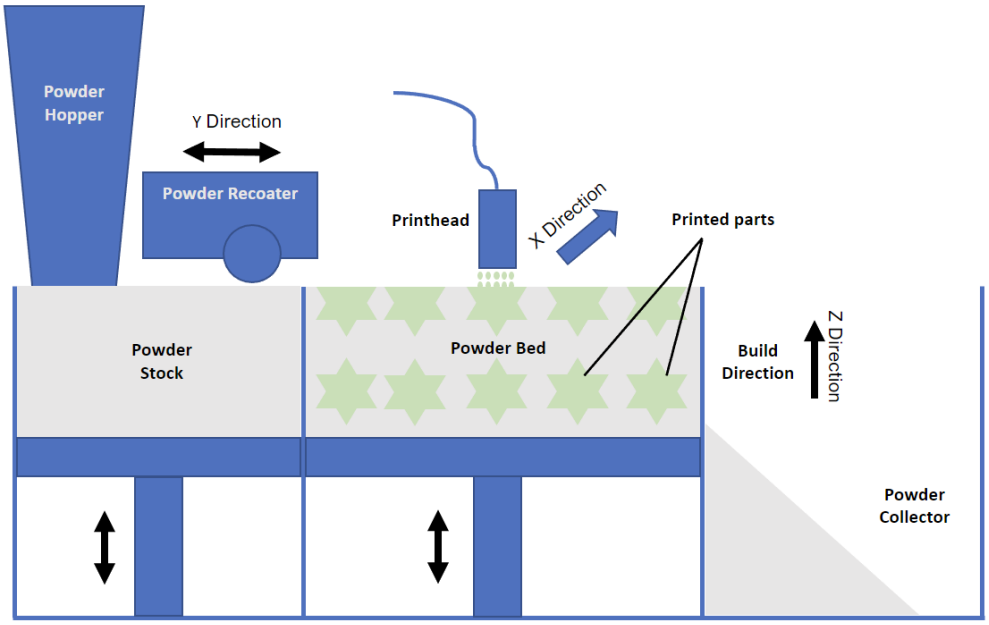

Figure 2.1: Typical schematic process diagram of BJT/M [1]

BJT printer systems come in a variety of configurations, with the primary differences being the size of the powder bed, the features of the printhead, and the operation of the powder dispensing and recoating mechanism [1]. These systems' performance can be adjusted by altering several factors that have an impact on the printing process, green components, and eventually the finished sintered components. Three categories can be used to classify these variables:

- **Features of Powder Feedstock**
- **Spreading and Deposition of Powder**
- **Binder Placement**

The influence of each of these parameters throughout the BJT printing process determines the printing quality and characteristics of the green component, which represents the initial condition for the subsequent de-binding and sintering processes. The binder deposition system and the powder spreading and re-coating system can be separated into two major systems that must cooperate to print the desired part. The arrangement of the particles within the produced part will be significantly influenced by the operating principles of these mechanisms and the settings chosen for their operation. These fundamental elements, which define the characteristics of the BJT green components, are shown in 2.2.

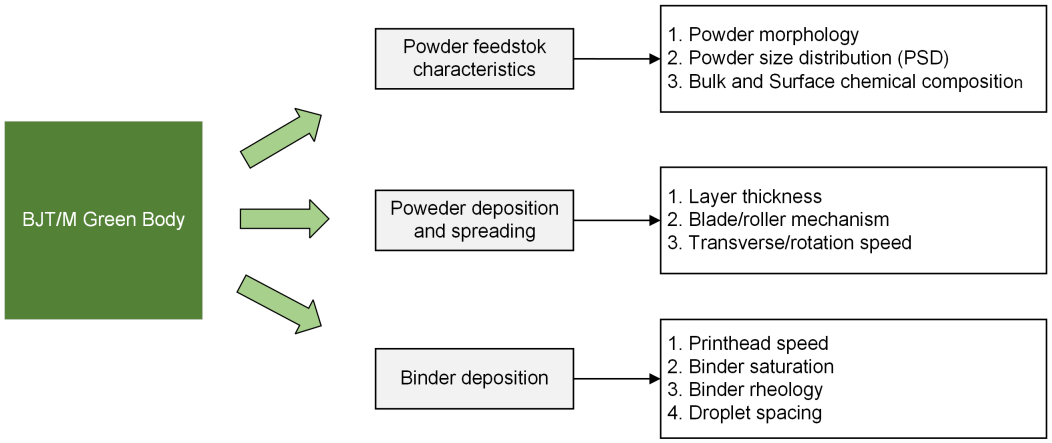

Figure 2.2: Major factors that determine the characteristics of BJT Green Body [1]

For powder-bed-based AM techniques, spherical-shaped particles are typically preferred due to the excellent flowability [8, 11, 12], but the recent studies [8, 13] employed using irregular shaped particles produced by water atomization. The atomization process naturally results in a normal (Gaussian) PSD distribution, which is known as the particle size distribution, or PSD. PSD is commonly represented by the cumulative percentile values D10, D50, and D90 and can be measured using various methods (such as XRD method, Malvern Particle Size Analyzer) [1].
Generally, the mean size of BJT powders can range from sub-micron sizes to over $100\mu m$. Although agglomeration problems could arise during the printing process, smaller powder (5 μm) has better sintering activity, which leads to faster densification [1]. Smaller particles are favored during sintering for faster densification and better final characteristics, but larger particles are favored during printing due to greater flowability and higher packing density. Hence, a compromise solution must be found for each unique situation. One of the properties of the powder is the packing density. Whereas tap density is the density of powder that has been tapped to settle its contents in a container under specific conditions, apparent density is measured on loosely packed particles [1].
The powder bed packing density often resides between the apparent and tap densities

of the powder being used because there is no external pressure applied during powder deposition or printing [1]. Each powder layer is applied to the previous print layer using the powder spreading mechanism. As it affects how the particles are arranged while printing, it also has a significant influence on the quality of the powder bed that is created. The design of the mechanism (such as the type of blade or roller) and the characteristics of the particles will have the most effects on how the powder material interacts with the printing parameters. All of these characteristics, along with the printing parameters, will affect how the particles are arranged within the layer after spreading.
To bind the chosen volume of particles together, the liquid binder is deposited on each layer. The printhead, the system that moves it, and the binding solution are the three essential parts. The distribution of binder droplets would depend on the cartridge movement path and binder deposition parameters since the impact of binder droplets on the powder bed may perturb it [14].
For the sintering process, where the evolution of the green components will be greatly influenced by the initial porous green structure, the control of these possible flaws is essential [1]. The geometrical precision and ultimate surface roughness of the parts are also impacted by the interaction between the powder and the binder. The BJT process, which must adhere to certain requirements, also relies heavily on the binder solution utilized. A few specifications to give the green components the required strength without impairing the sintering procedure and final properties.
It is necessary to cure the binder in order to improve the mechanical strength of the bound metal part for handling. Next, during depowerding, green components are removed. The green components are then sintered to achieve consolidation.

2.2 Debinding process

The binder within the green bodies must burn off before going forward with the sintering process [1]. The debinding process creates the pyrolysis of the binder component at a relatively low temperature, breaking down and evaporating the binder out of the green component [15]. Generally, the debinding process can be done in the same sintering cycle in the same furnace or prior to the sintering stage in a separate oven.
A component's microstructure and phase transitions during the sintering process may be impacted by the presence of carbon residues from the binder in the component [16, 17].
The impact of carbon residues during the sintering of stainless steel 316L has been demonstrated in earlier research [18]. However, the impact of binders during the sintering of AlSi-alloys hasn't been published yet. Yet, when proper debinding is done, the amount of these residues is minimal, thus not adversely affecting the sintering process and providing desirable properties of the component.
Generally, thermal analysis methods are used to determine the debinding process [1]. For example, thermogravimetry analysis (TGA) enables high-precision assessment of the binder removal, by mass loss during debinding when in contact with the process atmosphere, and illustrates the kinetics of the binder decomposition. RICOH's propitiatory binder is used in the current thesis study, and the suggested debinding

procedures from the technology provided were utilized.

2.3 Sintering process

Sintering is a thermal process that uses mass transport mechanism to bind particles into solid structures [1]. This bonding contributes to the densification and strengthening of the components during sintering. The relative density is a popular way to express the degree of sintering at the macroscale and is a measure of the ratio between measured density to the theoretical density (in g/cm^3). The internal microstructure evolves as a result of pore volume reduction and temperature distribution, whereas the geometry experiences volumetric/dimension changes as a result of the sintering process.
Sintering is categorized in different classes such as solid-state sintering and liquid state sintering. When particles are heated during sintering, solid linkages between them are created. By eliminating free surfaces, the linkages lower surface energy, and grain boundary area is subsequently eliminated by grain growth [19]. This sintering process is known as solid-state sintering. Although dimensional change is undesirable in many sintering systems, it is possible to reduce the pore volume with prolonged heating, which results in compact shrinkage. Hence, there are two types of industrial sintering: types that concentrate on densification and types that concentrate on strengthening without necessarily causing dimensional change. Through sintering at relatively high temperatures, structural materials such as silicon nitride, alumina, cemented carbides, steels, and silicon carbide are treated to full density. Contrarily, densification is decreased when structures like capacitors, cores, and mechanical spacers are sintered [19]. The adhesion of solid particles created by liquid formation, on the other hand, is what propels LPS [19]. Several powder materials are used in this procedure, one of which has a significantly lower melting point than the others, such as W-Ni or Fe-Cu alloys. AlSi alloy used in this study is typically sintered by Liquid Phase Sintering (LPS) due to its ability of pore fillings [20]. Since aluminum alloy has a lower melting point, it is also possible to achieve a higher density in a shorter time [21] . On the other hand, stable oxide film acts as an effective diffusion barrier for the sintering to continue during SS [22], which resulted in the selecting of LPS for densification.

2.3.1 Liquid phase sintering

The reduction in total interfacial energy is what propels sintering. By (a) replacing high surface energy interfaces with lower surface energy interfaces, such as replacing solid-vapour interfaces with grain boundaries, or (b) decreasing the total surface area per unit volume, the total interfacial energy can be reduced [21]. According to Kingery's classical theory [21], liquid phase sintering happens as a result of three concurrent mechanisms, as depicted in figure 2.3. These mechanisms are (1) particle rearrangement, which results in rapid densification; (2) contact flattening by solution re-precipitation, which reduces the distance between the particles' centers; and (3) the coalescence of solid particles, where solid-state sintering mechanisms constrain densification. As the sintering process continues, the dominating mechanism evolves.

Although it has been criticized, Kingslay's theory is still considered the foundation for understanding LPS.

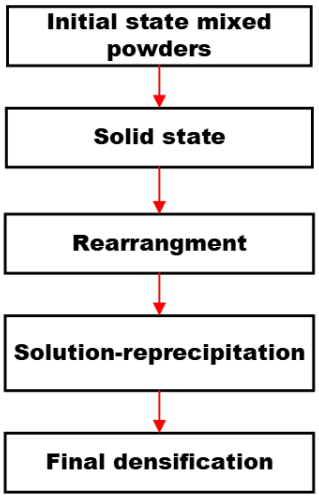

Figure 2.3: Simple schematic diagram of LPS [2]

The typical temperature range for sintering aluminum alloy is 570°C to 620°C. The low-melting additive powders can then melt and interfuse to form liquid phases. High liquid fraction typically accelerates densification [19] but also makes dimensional control more challenging [22]. Densification happens during sintering via various overlapping but balanced mechanisms [21], all of which are influenced by temperature, time, and ambient conditions.
In a typical circumstance, solid particles are soluble in liquid [2]. Its solubility makes the liquid penetrate the solid, creating a capillary force that draws the grains together. In addition, the high temperature softens the solid, which aids the densification process. Liquids are related to high diffusion rates, resulting in rapid sintering or lower sintering temperatures [2].
Based on Kingery's classical theory on LPS, [2] also explains the LPS phenomena which are easy to visualize. Based on this literature , During heating, the solid grains undergo solid-state sintering. Microstructure evolution processes are conceivable depending on the solid–liquid solubility interactions. The surface energy associated with pores causes their annihilation, whereas microstructure coarsening increases the material's tensile strength in the as-sintered state compared to the as-printed state. [19]. Hence, the liquid phase's surface tension is a crucial influence in determining the sintering rate of LPS.
The key factors to control the LPS consist of, interfacial energies, wetting, spreading, penetration, segregation, contact angle, capillarity, contact force, and solubility [19]. In the case of contact angle, the lower the contact angle, the better the densification, meaning better wettability of liquid in the solid-liquid interface. In the case of wetting, a high liquid content guarantees quick densification [19]. However, if there is an excessive amount of liquid, distortion will develop. The wetting of the liquid in the solid-liquid interface can also be aided by chemical reactions. A large contact angle implies insufficient wetting, therefore, the liquid withdraws from the solid [2].

This causes compact swelling and liquid exudation from pores. Hence, depending on the contact angle, liquid transformation results in either densification or expansion. The extent of the capillary effect is determined by liquid volume, particle size, and contact angle [2]. When the dihedral angle is considered, lower is better [19].

2.4 Sintering of aluminum alloys

Aluminum is always protected by an oxide due to its extremely high affinity for oxygen [22]. Aluminum powders are made mainly using the air atomization technique and, hence, typically have an oxygen content of around 0.3-0.6 wt.%. resulting in the formation of a thermodynamically stable oxide film (Al_2O_3 film) of a few nm (around 2 nm according to [23]) forms on the surface. The oxide coating effectively prevents the inter-particle diffusion of aluminum atoms and the diffusion of solute atoms into the aluminum powder particles [22]. To facilitate successful sintering, the oxide film must be chemically reduced or physically disrupted. In the case of physically disrupting the oxide layer, high pulverization of powder is needed during solid-state sintering. However, there will still be the presence of oxide particles which will continuously hinder the sintering process [22]. As a result, mechanical disruption frequently falls short of allowing for substantial sintering.
As the oxide layer (Al_2O_3 film) in the aluminum alloy has a higher melting point, it is not anticipated that liquid aluminum will wet alumina near the melting point of the metal. However, the solid-liquid interface must have a smaller contact angle to be wettable [2]. Magnesium is therefore added as a minor alloying element to break the oxide layer as a workaround. Magnesium can decrease aluminum oxide via reaction, therefore rupturing the oxide coating sufficiently to enable diffusion, wetting, and sintering via the production of spinel ($MgAl_2O_4$) [24]. Depending on the particle size of the aluminum, the highest effect occurs at 0.1 wt% Mg.
The powder being aluminum 4000 series, it can be said that the trace amount of Mg is essential for this sintering to occur effectively.
For the sintering of aluminum alloy, the sintering atmosphere also plays a significant role. Nitrogen is more effective than Argon for sintering aluminum, while magnesium is an active component. Based on [25], The self-gettering theory is formed to explain this phenomenon. Deep inside the pore network of P / M aluminum alloy, the gas flow rate (either Ar or N_2) is substantially lower than at the surface, resulting in the consumption of O_2 by the aluminum quicker than it can be replaced by incoming gas. The local oxygen partial pressure will then decrease. Aluminum essentially functions as a self-getter. Thermal expansion occurs during the sintering process, but because the pore network lacks a large concentration of O_2, the oxide layer is not regenerated. As a result, fresh metal is exposed to the sintering atmosphere. In the presence of N_2, exposed metal will rapidly undergo the reaction described by the equation.

$$2Al + N_2 = 2AlN$$

which is exothermic. This will result in a local rise in temperature, which may promote local melting and facilitate sintering.

2.5 Effects of silicon on thermal conductivity of Al-Si alloys

The rate at which heat moves through a material is measured by its thermal conductivity. It is primarily controlled by thermal consumption processes (Specific heat), elastic vibrations of the lattice (phonons), and electrical conductivity. If the influence of phonons is minimal (as it is for pure metals), the mobility of electrons, or electric conductivity, σ_e is what primarily affects thermal conductivity [26]. Electrons are scattered when they come into contact with moving, vibrating atoms, as depicted in the figure 2.4 [27]. Electrical resistance and thermal resistance are produced by flaws and phonon scattering acting on free electrons. The mean free range of the free electrons thus serves as the primary determinant of their electrical and thermal conductivity. Furthermore, according to [28], the ability of an alloy to transfer heat increases with the length of the average free route of phonons. Nevertheless, crystal defects such as stacking faults and twins, as well as precipitates formed because of secondary alloying elements, would scatter phonons, reducing the average free path and ultimately having a negative impact on thermal conduction.

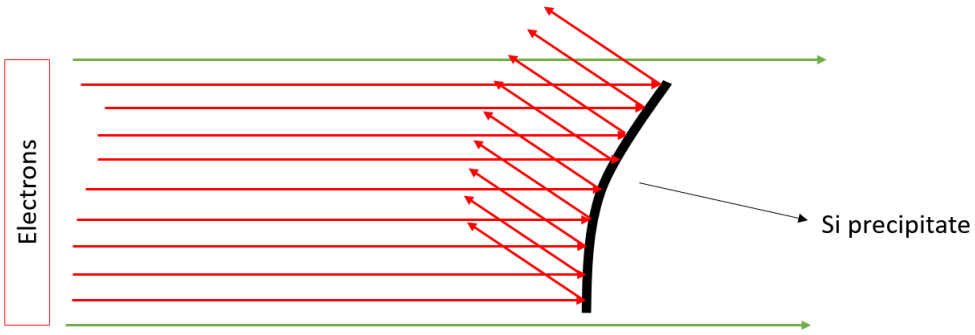

Figure 2.4: Schematic diagram of collision of free electrons with eutectic Si containing particles

While the heat conductivity of pure aluminum (237 Wm/K) is high, it is typically poor in alloys made of aluminum and silicon. For instance, the A380 alloy has a heat conductivity of just 96 Wm/K. Thermal conductivity is impacted by alloying elements in various ways [3]. They disintegrate in the matrix phase and impact the phonon and electron pathways, as mentioned before. The solubility limit is reached when the concentration levels of alloying elements are above it, resulting in variable morphologies and amounts of precipitates, which alter the thermal conductivity. It is also mentioned in this paper, [3] that, through altering the routes for electron migration and phonon contributions, microstructures linked to a variety of thermo-mechanical properties also have an impact on thermal conductivity. The strength of aluminum alloys can be significantly increased by adding Si [29]. The thermal conductivity in Al alloys is primarily controlled by electronic thermal conductivity and secondarily by lattice thermal conductivity [30]. As mentioned previously, adding alloying elements significantly reduce electrical conductivity and thermal conductivity, with elements in the solid solution having lower values than the same number of

elements that form intermetallic phases. These latter often exhibit a proportionate decrease in thermal conductivity with increasing volume fraction [31]. According to [27], the primary intermetallic phase of Al-Si binary alloys, eutectic Si, serves as the thermal energy carrier's scattering center. For low Si element contents, the α Al grain size in binary Al-Si alloys decreases as the Si percentage rises. The number of grain boundaries grows, which slows down the flow of free electrons and lowers thermal conductivity. figure 2.5 shows a summary of the thermal conductivity of different alloying elements in the aluminum matrix.

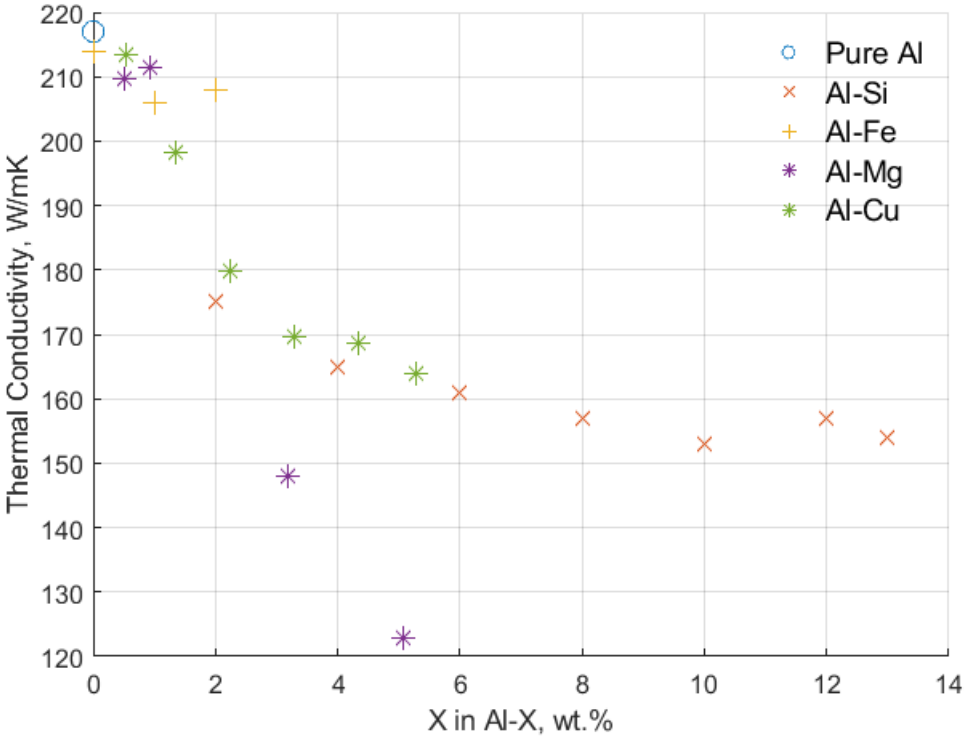

Figure 2.5: Thermal conductivity of binary Al-Si, Al-Cu, Al-Fe, and Al-Mg alloys [3]

According to [3], the thermal conductivity of Al-Si alloys reduces as the Si concentration rises up to 6 wt%. The thermal conductivity essentially stays constant at 157 W/mK when the Si concentration surpasses 6 wt% [3]. This is because, according to [3], the eutectic components and Si proeutectics did not significantly alter the free routes for electron migration when Si was present as an equiaxed phase in the hypereutectic alloys, raising the Si concentration had no impact on the thermal conductivity of the composites. Up until the larger volume percentage of proeutectic Si became the dominant phase in the hypereutectic alloys, the almost flat thermal conductivity could be maintained. For foundry alloys, the electrical conductivity in the Al-Si binary alloy falls from 29.26 to 25.33 mS/m and the thermal conductivity from 182.38 to 164.16 Wm-1 K with increasing Si concentration [27]. The addition of Si, Fe, Mg, Mn, and Cu also reduces thermal conductivity. Moreover, it was discovered that the Mn element significantly reduced thermal conductivity

[32]. The morphology (shape and size) of eutectic Si, in addition to the impacts of the alloying elements, has a significant impact on the thermal conductivity of Al-Si alloys [33, 27, 34]. It is discussed that the size of the α-Al grain varies with the change in Si content [27]. Moreover, as the Si content rises up to 9 wt%, nucleation undercooling, and recalescence increase. The constitutional undercooling of different kinds of solutes in the Al solution can be layered on one another, according to [35], The presence of trace amounts of Fe (6 ppm), Cu (8 ppm), Mg (4 ppm), and Ti (1 ppm) makes it difficult to obtain a high-purity Al-Si binary alloy. As a result, the Si does not combine with these impurity elements to produce intermetallic compounds when the Si level is low. The compositional supercooling of the melt, on the other hand, increases with increasing Si concentration and encourages grain refinement. Moreover, as Si concentration rises, the growth restriction factor rises as well, which prevents the formation of a-Al grains. In contrast, if the Si concentration is increased further, the size of the a-Al grains grows. This is because as Si is reacted with other impurity elements in the melt to produce intermetallic compounds, the effect of composition supercooling is diminished. Although the thermal conductivity of single-phase materials is well understood, heterogeneous alloys such as Al-Si comprise the majority of those utilized in industry. [26].

2.6 Heat exchange performance

Heat sinks are the devices or objects which are generally used to take away heat from the electronic and other devices producing heat. They act as heat reservoirs absorbing excess amounts of heat away from the heat generating device [36]. Normally heat is carried away from the heat source to the heat sink via conduction and dissipation of the heat from the heat sink to the environment takes place by convection [37]. Conduction is directly proportional to the heat transfer area and the difference of temperature across the layers. Conductive heat transfer across the plane wall of thickness ΔX and area A, having temperature difference across the layers ΔT is given by:

$$Q_{cond} = kA\frac{\Delta T}{\Delta X}$$

where k is the thermal conductivity of the material[38]. Hence, Heat carried away by conduction also depends upon the material property. In this study, the focus was not on change of parameters ΔT or ΔX , since the input heat from the headlamp is predefined while the length of the heat sink cannot be increased due to space constants inside the car. Thus, the thermal conductivity of the produced AlSi is of great significance.

While the convective heat transfer can be given by Newtons law of cooling $Q_{conv} = hA(T_s - T_\infty)$, where h is the convective heat transfer coefficient, while the A is the surface area. It is not practical in many cases to increase the heat transfer coefficient. Hence increase in the surface area is the known method for increasing the convective heat transfer, as can be seen in the case of heatsinks with fins. While increasing the surface area alone does not guarantee an increase in performance

since packing the fins too closely reduces the heat transfer coefficient due to extra resistance in the added fins [39]. It also increases the mass of the heatsink which is undesired property in this application. By disturbing the flow channel in the fluid, the heat and mass transfer by the fluid also increases, thus resulting in higher heat transfer performance. This disturbance to the flow is better achieved in triply periodic minimum surface(TPMS) lattice structures like gyroid compared to the conventional fin-based heat sink fluid gets flown into non-flow channels due to the complex shape of the gyroids and thus more secondary flow in the fluid causing increased convection [40].

2.7 Design guidelines for Binder jetting for metal

DfAM is a methodology of creating, optimizing, and adapting the components, assemblies or products in order to utilize the benefit offered by AM [41]. DfAM in general offers a great deal of freedom to design the parts without the limitations put on by conventional manufacturing processes. DfAM designers have fewer limitations when it comes to the geometry of the part. Thus resulting in the creation of complex parts by combining one or more components into one component [42].

While there is a lot of freedom while designing the parts for AM, there are certain limitations as well. These need to be taken care of to ensure that parts are manufactured successfully. This includes both pre and post-processing along with the printing of the parts [43]. These limitations are taken care of for all the AM processes by the defined set of rules called as design guidelines. They can be defined as the information that helps in understanding the particular AM process, the procedures involved, and the best practices for designing the part [44], due to the differences in AM processes, their procedures and geometrical properties. Each of the AM processes has its own set of design guidelines that must be followed to achieve the best end results.

To fabricate components using BJT/M, the following design guidelines have to be followed:

- **Maximum Component Size**: Although theoretically, the maximum size that can be produced is approximately equivalent to the size of the build volume after compensating for clearances on all the sides. But as the size of the component increases it becomes unstable due to increased anisotropic shrinkage. This means that many iterations and design changes with each iteration are required to successfully obtain the part. Basic knowledge in BJT/M is an optimum set for printing is considered to 50mm in any direction[45], but depending on geometry it could sometimes become larger. Larger parts need to be handled with more care since the brittleness in the green component increases with size.

- **Wall Thickness**: Standing walls which are non-supported should at least have a minimum thickness of 2mm. While walls with a thickness of 1mm have support on one side or both sides. While the height-to-thickness ratio should be 8:1 or less at all times.

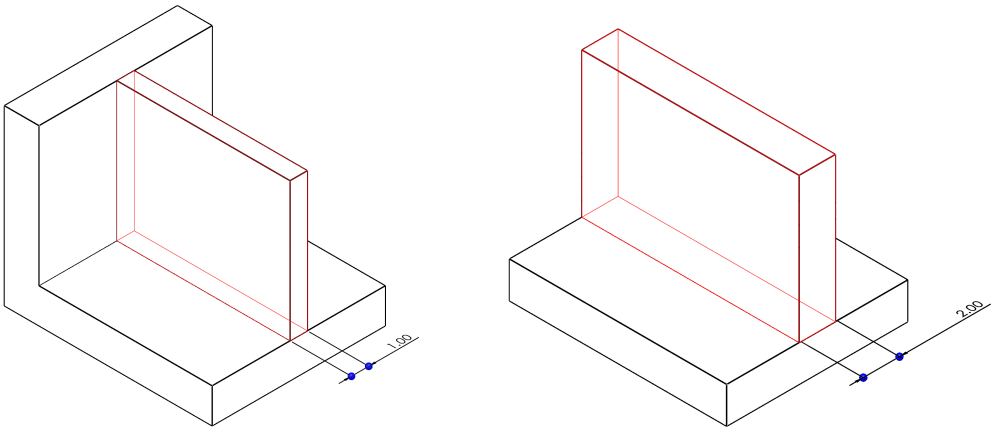

(a) (b)

Figure 2.6: Recommended Wall Thickness Printable by MBJ

- **Overhang Angles**: The angle between the vertical surface/face of the component and the surface of the build plate should be 60 degrees or more.
- **Overhangs**: These features can be subdivided into two types based on the thickness and length of the overhang. The maximum length which can be produced accurately is 10mm. While the minimum thickness of 2mm should be maintained for the overhang feature. Refer to the figure 2.7.

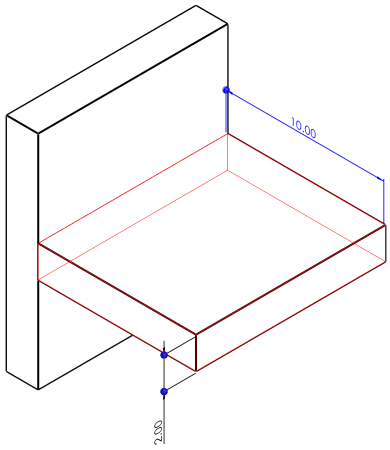

Figure 2.7: Overhang length and thickness for BJT/M

- **Powder removal holes**: It depends significantly on the design. For parts designed with shells, this feature is critical. While solid parts may also require escape holes to remove the powder from critical areas. It is recommended to have a minimum of two escape holes of 5mm in diameter[43]. Refer to the figure 2.8.

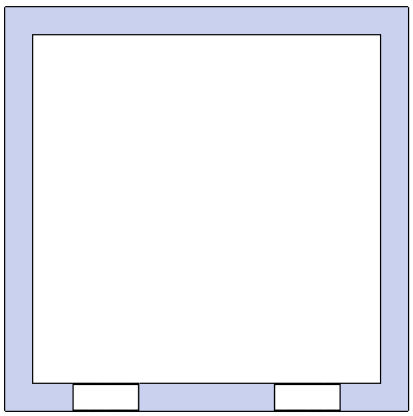

Figure 2.8: Powder Removal holes for Shell parts in BJT/M

- **Radius**: It is recommended to provide a fillet of 1mm minimum at corners, knife Edges formed between two surfaces. These sharp features can result in a stress concentration, especially during the sintering [43]. They can also help with the removal of the powder without damaging the geometry during de-powdering. Refer to the figure 2.9.

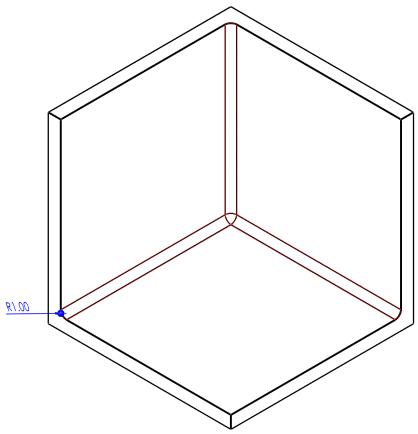

Figure 2.9: Radius at corners and sharp edges for BJT/M

- **Base Thickness**: The surface of the component parallel and in contact with the build surface can be produced with as little thickness as 1mm[46].
- **Font Size depth and Width**: Samples engraved with features such as by providing identification numbers or fonts need to have the minimum depth and the width of 1 mm to be achievable [47].
- **Minimum Feature Size**: Although BJT/M has the highest resolution when it comes to metal powder AM. The main concern is damaging the components during the handling. Therefore it is recommended to have the feature size no less than 2mm [48]. Refer to figure 2.11.

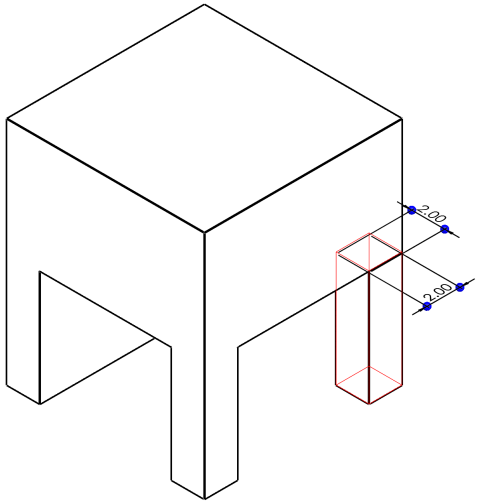

Figure 2.10: Minimum recommended printable feature by BJT/M

- **Tolerances**: Tolerance in the close-fitting parts are not often discussed when it comes to guidelines but it can be considered as a good practice, to keep tolerances of 1mm between close-fit components.

- **Lattice**: One of the major advantages of AM is the ability to print lattice structures. Lattice can be formed using the network of struts or by using the walls. They provide lightweight high specific strength, and higher stiffness[49]. In the case of MBJ it is recommended to print the lattice with a minimum 1 mm thickness of the walls or the diameters of the struts.

- **Horizontal Holes**: Since BJT/M has a very high resolution, very small hole diameters can be produced. However, due to restrictions on powder removals larger diameters are recommended for higher depths. Diameters of 0.5 mm can be successfully produced up to the depth of 1mm. This number increases exponentially to 5mm for a depth of 30mm and above [46].

- **Vertical Pins**: vertical non-supported pins should have a minimum diameter of 1mm. For the length of the pins 5mm or higher the diameter must be 2mm minimum for successful printing.

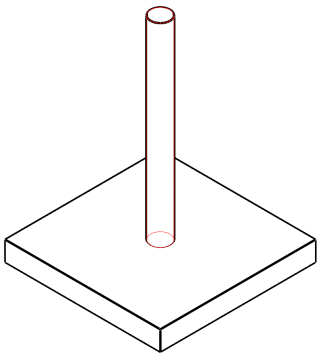

Figure 2.11: Vertical Pins printable by BJT/M

Most of the design guidelines studied and summarised are from previous studies. Also, some public once's by machine providers on their website, but most of them where derived from previous work with stainless steel 316L. Since aluminum alloys are new in the BJ Technique for metals there are no existing design guideline studies to be best of the author's knowledge. The above guidelines only act as the first steps in understanding where the criticality lies in the BJT for Metals. Guidelines specific to the application have been produced and evaluated before being incorporated into the final design. This is further explained in section 4.1.

3

Methods

3.1 Design for Binder jetting technology for metal

In order to print the final part it needs to be designed in a way that complies with the rules of AM and more specifically particular technology. These are the design guidelines for the Binder jetting technique for metals discussed in session 2.7. This is done using a combination of design software. It generally involves using 3D parametric CAD software for an initial form of the design, followed by software for topology optimization. or software that can design complex features like lattice structures i.e. gyroids. Then the design files are sent to build preparation software where things like part print orientation are set, necessary support structures are given, and optimized staking of the part is worked out based on the build box volume. There are few build preparation software available on the market currently. Among them, Materialise Magics by Hexagon is one of the most commonly used software in the industry [50].

In this project, the existing design for the heatsink of Volvo XC90 was used as the reference. The file was in the parent CAD format of software Catia V5 [51]. Modification to the design was done in this software and then the file was taken into N-topology software [52]. It helps to design complex gyroid shapes and other intricate features of the components. It was used to design gyroid for heat dissipation on the heat sink. The final component design was exported as mesh and the build preparation was done using Materialise Magics [50]. Finally, printing was done in RICOH's in-house prototype printer for Binder jetting machine for aluminum alloys [53].

3.2 Material

To understand the sintering anisotropy and microstructural evolution during sintering, sintered cubes were used. As-sintered cubes have a volume of 10x10x10 mm^3, and the theoretical full density of aluminum 4000 series alloy is approximately 2.69 g/cm^3.

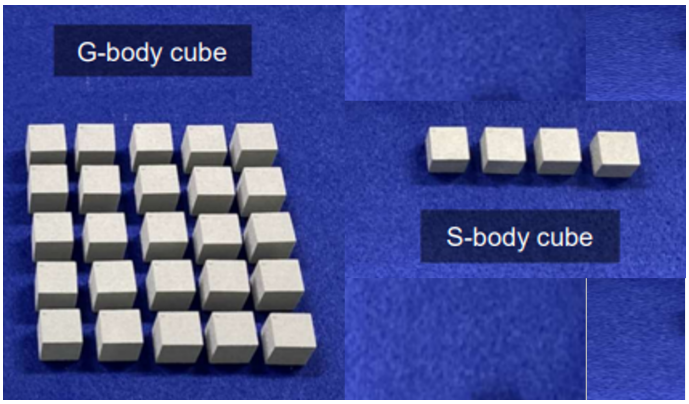

Figure 3.1: Cubes (green body cube and sintered cube)

Cubic samples were oriented in the build space with cubes planes orthogonal to the printing directions: building direction (Z axis), powder spreading - recoater direction (Y axis), and binder deposition direction (X Axis). Each sample was designed with an identification spot produced on the top surface which was used for axis identification.

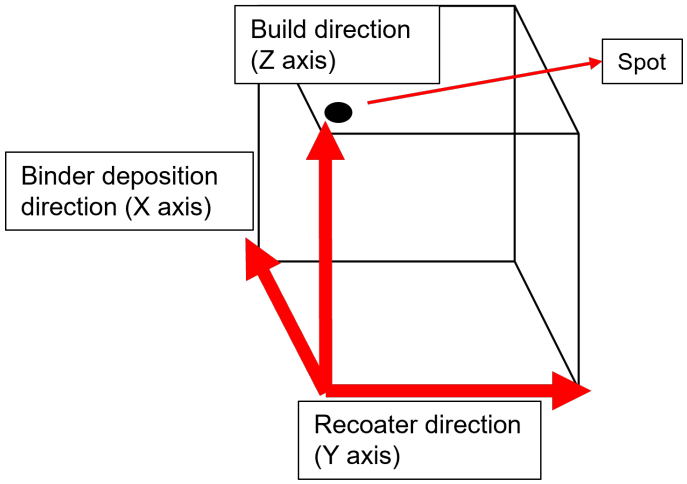

Figure 3.2: Build orientation of cubes

After the printing is done, the samples are extracted through a powder removal process. In this process, at first, the area where the binder is jetted is cured in a drying oven, which is followed by powder removal, namely taking it to a powder station to collect the excess powder. After the powder removal step, the debinding and sintering process was carried out in the same furnace. Debinding and sintering of the green bodies were conducted by continuous heating in a vacuum. Sintering was performed by heating at approximately 600°C for several hours.

3.3 Density measurements

Three approaches were utilized to quantify the relative density of these sintered samples. Geometry-based density was measured using calipers and weight-measuring de-

vices. Archimedes' density follows ASTM standard B328 and uses a high-precision weight-measuring machine. LOM-based density is measured using ImageJ.
The geometry-based density of cubical samples is calculated from weight (m) and volume (V) from dimensional measurements where ρ =2.69 g/cm^3 was used. Using the following equation 3.5.2 relative density was calculated. The measurements were taken with a single-point automatic caliper with a resolution of 0.0001 mm and high-precision balance with a resolution of 0.0001 g as well as with high precision 3D scanning instrument at the Geometry and verification center in Volvo Car Corporation. GOM Inspect was used to measure the x, y & z dimensions of the cubes. The working methodology of GOM inspect is further explained in section 3.4.

$$\rho(\%) = \frac{m}{V \times \rho_f ull} \times 100$$

ASTM B328 standard was used to measure Archimedes' density. The following equation was used to calculate the relative density when Archimedes' density is considered.

$$\rho(\%) = \frac{\frac{W_1}{W_2 - W_3}}{\rho_f ull} \times 100$$

Where,

- W_1 refers to the weight of the dry sample
- W_2 refers to the weight of the sample submerged in water
- W_3 refers to the weight of the sample when pores are filled by water

The LOM-based density was calculated by splitting the cross-section into 30x30 areas of interest (ROI) and measuring area fractional density using image analysis. FIJI ImageJ particle analysis plug-in was used to analyze porosity morphology [1].

3.4 Dimensional and geometrical inspections

As discussed previously in BJT/M, there is a large deviation from the nominal geometry due to deformation and distortion caused during the sintering. This is further increased with an increase in the size of the part. The component targeted in this project is relatively large from a BJT/M perspective. Hence dimensions and geometrical features of the design needed to be evaluated for deviation and distortion from the nominal CAD geometry. Knowledge gained from the evaluation could be then incorporated into the new heat sink design. GOM Inspect by Zeiss[54] is a software that was used for this purpose. It has features that allow for CAD data (nominal geometry) to be compared with the printed components. To get the comparison printed components are required to be converted to Standard Triangle language(STL) files. This was done by 3D scanning the parts using a guided laser beam from Model Maker H120 by Nikon [55]. This system was available at Volvo

Cars Corporation. 3D scanned parts are then saved as STL CAD files which were used for comparison with the nominal CAD. The inspection methodology and the results are summarized in the section 4.1.

3.4.1 Metallography

For metallographic preparation, sintered cubic samples were sectioned along three possible cross-section planes specified by the samples' axes (i.e. XZ, YZ, or XY), whereas, casted samples were sectioned into one orientation. The Metallography of the alloy was divided into several sections. During sectioning for optical microscopy, a nonferrous cutting blade is used whereas, to section for thermal conductivity using laser flash analysis, a diamond wafering blade is used. Sectioning was carried out using a Buehler IsoMet High-Speed Pro machine.

(a) Buehler IsoMet High Speed Pro

(b) Struers Citopress-20 for mounting

Figure 3.3: Metallography-Sectioning and Mounting

During the mounting, x, y, and z directions were marked, in order to keep track of the recoater, binder deposition, and building height direction. Polyfast polymer was used for the mounting procedure. Hot pressing was done and it took approximately 6 minutes to complete both the heating and cooling cycle. Mounting is done using the Struers-Citopress-20 machine.

Table 3.1: The Grinding and Polishing methodology followed for sample preparation

Speed (rpm)	Time (min)	Force (N)	Rotation	Lubricant	Grit/Polishing Cloth
150/150	3:30	15	↻ ↺	Water	220 SiC Foil
150/150	2	15	↻ ↺	Water	320 SiC Foil
150/150	∼3	25	↻ ↺	Water	500 SiC Foil
150/150	3	25	↻ ↺	Water	800 SiC Foil
150/150	∼3	25	↻ ↺	Water	1000 SiC Foil
150/150	3:30	25	↻ ↺	Water	1200 SiC Foil
150/150	∼3	25	↻ ↺	Water	2000 SiC Foil
150/150	∼3	25	↻ ↺	Water	4000 SiC Foil
150/150	6	25	↻ ↺	DiaPro Dac 3 micron	3 micron Cloth
150/150	6	25	↻ ↺	DiaPro Nap 1 micron	1 micron Cloth
150/150	1:30	15	↻ ↺	OP-S	OP-S Cloth

(a) Struers labopol-21 for chamfering the edge

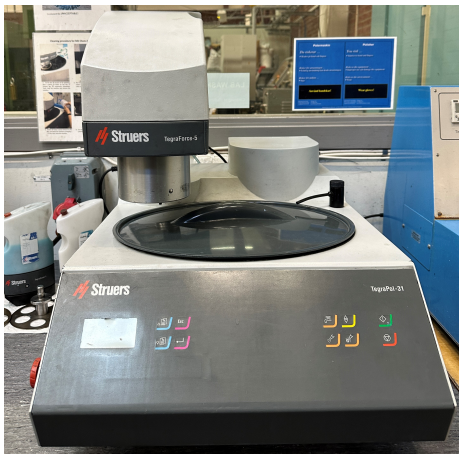

(b) Struers Tegrapol-31 for grinding and polishing

Figure 3.4: Metallography-Polishing and Grinding

Grinding and polishing were done in 2 phases. During the 1st phase, a manual grinding machine, Struers laboplo -21 was used. It was used mainly to chamfer the edge of the polymer mount to prevent it from tearing the grit papers. After the initial manual grinding, during the 2nd phase, Struer Tegrapol-31 was used and several grinding and polishing parameters were followed, mentioned in table 3.1.

3.5 Mechanical properties testing

This section outlines the procedures and principles utilized for the mechanical properties testing of the produced aluminum alloy in the research study whose results are summarized in this report.

3.5.1 Hardness test

Rockwell, Vickers, Brinell, and Knoop are the most common hardness tests. Hardness testing values are arbitrary, meaning that there is no linear relationship between hardness testing values from one load/force to another. Depending on the material, hardness test methods can vary. One more thing that should be kept in mind when it comes to using higher loads, is that higher loads result in lower hardness. Hardness test measurement was done using Struers DuraScan as depicted in figure 3.5, which supports Vickers hardness and Knoop hardness. Generally, Vickers hardness is preferred for ductile materials such as aluminum alloy. In contrast, Knoop hardness is used to determine cracking in brittle materials and to facilitate the hardness testing of thin coatings such as surface coating. The time for indentation has been set to 15 seconds. The ASTM standard E384 for hardness was adopted. The macro hardness test was chosen to measure the material's hardness. The surface was smoothed and ground. The time for indentation has been specified as 10 seconds. 5 measurements were done for each sample and for each orientation. Since as-sintered material is used, HV3, HV 5, or HV 10 is recommended [56]. High loading is advantageous when as-sintered material is used as 'bulk' information is required. In addition, by employing high loads, values can be more consistent because they are less susceptible to micron/pixel variations.

Figure 3.5: Struers DuraScan for Hardness Test Measrurement

3.5.2 Thermal conductivity test

Thermal conductivity (TC) measurements were carried out on a Netzsch LFA 457 MicroFlash® table-top instrument (Netzsch Gmbh, Germany), which employs the Laser Flash Method (LFM) to calculate thermal diffusivity and specific heat values.

The measurement was done by following the ASTM E1461 standard, shown in figure 3.6. The LFA 447 HyperFlash is a vertical system, with the flash source at the base, the sample in the middle, and the detector at the top.

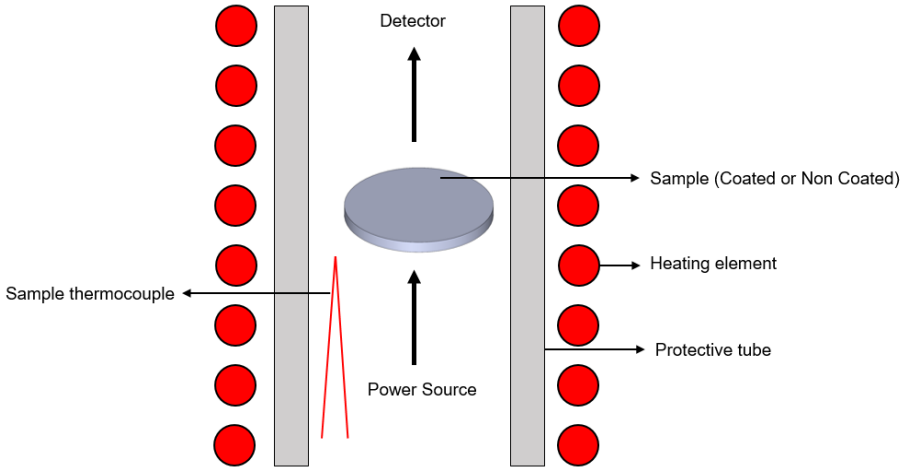

Figure 3.6: Laser Flash Technique

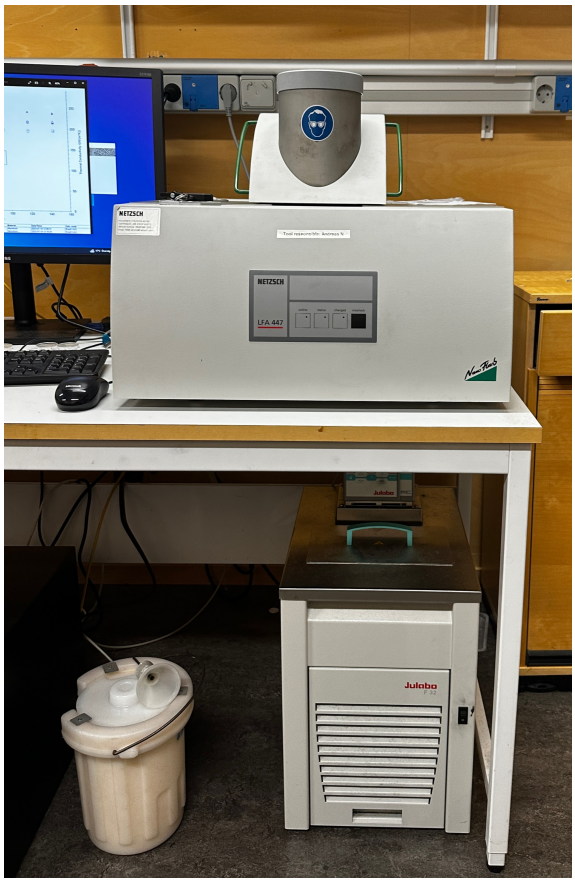

Figure 3.7: LFA 447 Instrument

12.7 mm in diameter and 1 mm thick samples were used for this experiment. The samples were machined using a diamond wafering blade to have better precision and less material removal from a produced or cast bulk sample given by RICOH or from the heat sink of the production series car, model XC90. Due to the machining, the outer surface was smooth.
In order to obtain a good detector signal and to increase the emission ratio, the sample must not reflect light and must feature good emission and absorption [57]. Due to this, samples that have higher reflectivity such as aluminum should be coated. As coating improves the sample's emission/absorption properties, optimizing the signal-to-noise ratio. Graphite coating is done in this experiment as depicted in figure 3.8.

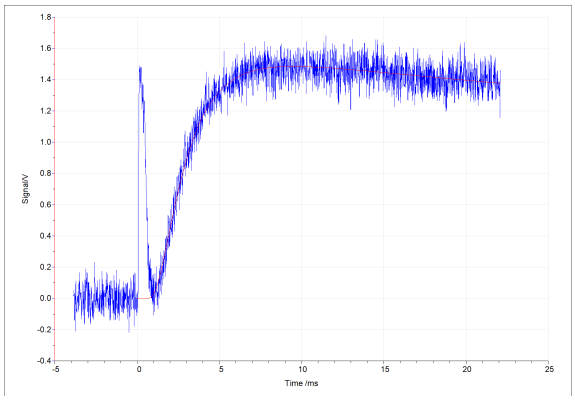

(a) Shot detection without graphite coating

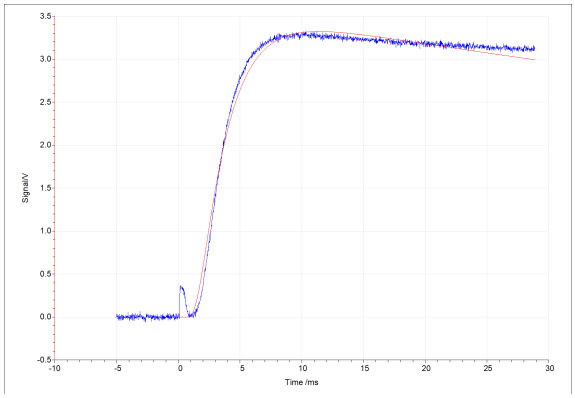

(b) Shot detection with graphite coating

Figure 3.8: Signal to noise performance between graphite coated and without graphite-coated as-sintered aluminum 4000 series alloy sample

Graphite can have higher thermal conductivity than both copper and aluminum. However, when measuring high thermal conductivity materials with short half time the graphite coating will have a larger influence on the half time compared to coating low thermal conductivity samples like polymers. For this reason, dusting is done instead of coating the surface of aluminum samples with graphite in order to have a better signal-to-noise ratio while maintaining high thermal conductivity as depicted in figure 3.9.

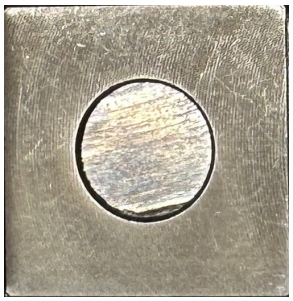

(a) Sample with no graphite coating

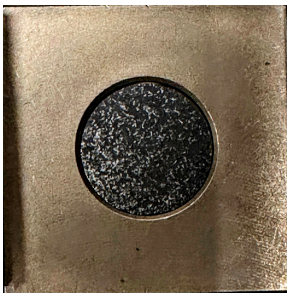

(b) Sample dusted with graphite

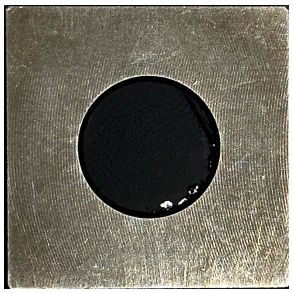

(c) Sample coated with graphite

Figure 3.9: Visual comparison between different coating techniques

Dusting of graphite on the surface was followed by, placing the samples on the sample holder as depicted in figure 3.10. A disk-shaped mask with a big orifice is placed on the top of the sample to control the flash path.

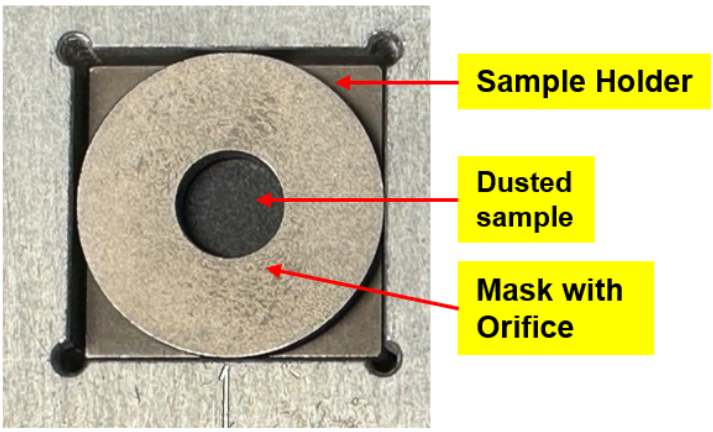

(a) Sample holder

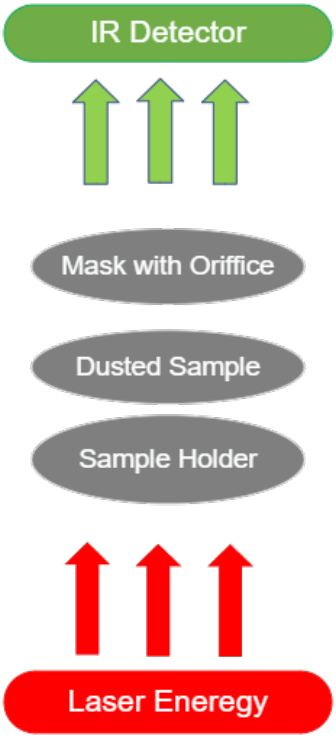

(b) Schematic of radial or in-plane diffusivity measurement.

Figure 3.10: Placement and schematic of in-plane diffusivity measurement

For the specific heat capacity measurement, C_p the samples were not "dusted" but coated with more graphite. The reference POCO graphite was measured "as is." We followed the coating procedure recommended in Netzsch documentation

Using the laser flash technique, thermal diffusivity, and specific heat capacity are measured. Combining these thermophysical properties with the density value permits the following thermal conductivity calculation:

$$\lambda(T) = a(T) \times C_p(T) \times \rho(T)$$

Where,

- λ refers to thermal conductivity $[W/(mK)]$
- c_p refers to specific heat $[J/(gK)]$
- a refers to thermal diffusivity $[mm^2/s]$
- ρ refers to bulk density $[g/cm^3]$.

A total of 6 temperature points was used to calculate the thermal conductivity. The initial temperature was set to 20 °C, and the final temperature was set to 145 °C. Details for the experiment parameters can be found in Table 3.2. LFA analyzer software was used to put the values during the experiment. Co coefficient of linear thermal expansion was assumed to be 0.

Table 3.2: Experiment setting for LFA analyzer

Parameters	Values
Starting Temperature °C	20
Shots	3
Increments °C	25
temperature data points	6
Delay (ms)	0
Main Amp	Changes with temperature

It should be noted that, although the specific heat capacity C_p of as-sintered aluminum 4000 series alloy was measured, it was 0.82 $J/(gK)$. It was characterized by the temperature span used for the measurements. However, in the case of the cast aluminum alloy sample, the same specific heat capacity was used, as mentioned before, due to time restriction as an approximation. In the case of pure aluminum 1050, the specific heat capacity was 0.89 $J/(gK)$ in all temperatures.

3.5.3 Thermal convection test

To understand the heat exchange performance of the 3D-printed heatsink. It was decided to perform the experimental study.
For this reason, a literature study was carried out. It was learned that to perform the test main elements apart from the test piece are the heating element, insulation for the heating element, thermocouples for recording the temperature, DC power regulator, and the data acquisition system. As well to get good-quality results it is essential to conduct the test in a stable ambient temperature.

One of the critical aspects was the loss of heat and thus, good insulation to the back side of the heating element is essential. In the study conducted by Haghighi et.[37] they used additional heater on the back side of the primary heater to control the heat loss. A lot of inspiration was taken from the study carried out by Feng et. [58] called *natural convection on metal foams heat sinks with open slots.*
Based on the studies and research done, test rig design was worked out which can be seen in figure 3.11. The heating element of 2"X2" was used and purchased online from the website Omega [59]. Kypton heater with a maximum power of 40 watts was chosen. Since the test pieces had the substrate area of $40mmX40mm$ heater bigger than this was chosen so as to get the uniform initial distribution of heat throughout the test piece substrate. The heater was operated by connecting it to a power supply through a DC power regulator. This allowed the user to control the input power at any given amount of time.

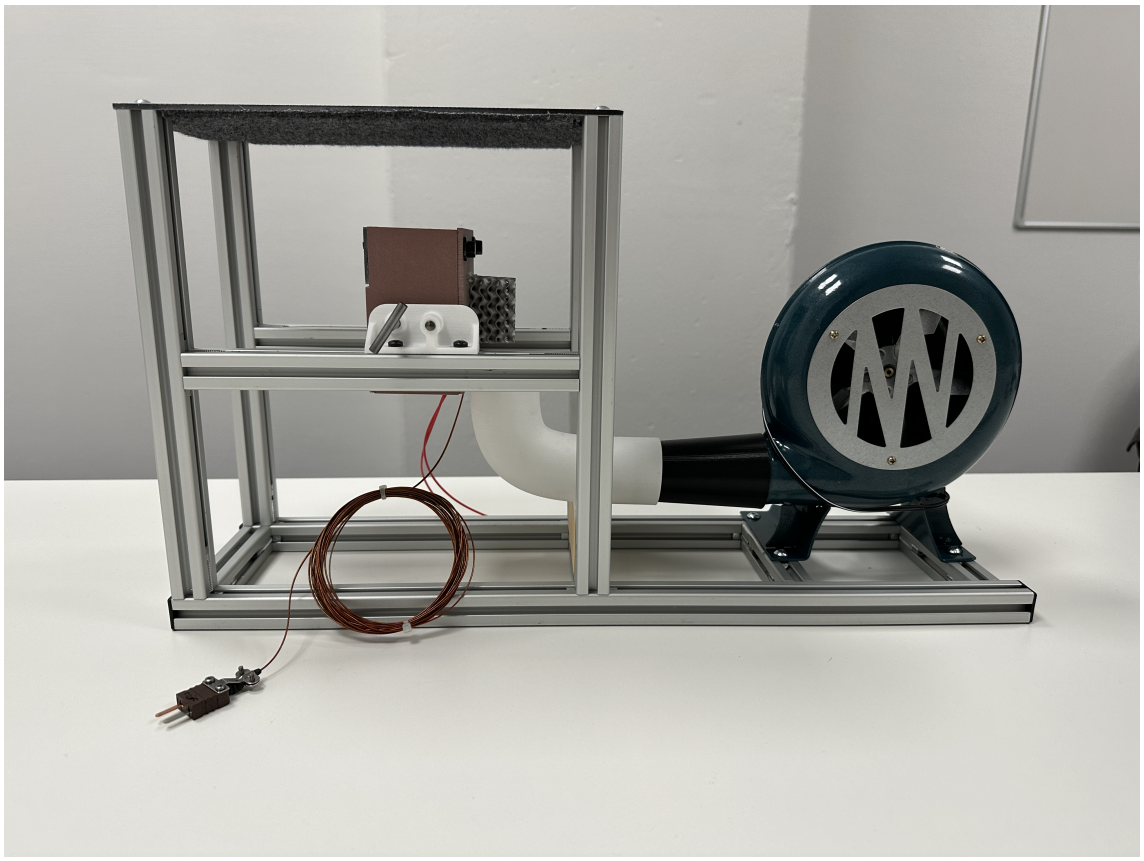

Figure 3.11: Test Rig developed to measure the heat exchange performance of the artefact designs

For the purpose of insulation polyurethane foam having a very low thermal conductivity of $0.0036Wm/k$ was chosen [60]. For the back lid. PU foam of 91mm x 91mm having a thickness of 50mm was taken. The slot was cut out into this to house the heater and the electrical connection to the heater. Whereas front lids had the dimension of 91mm x 91mm x 3mm, with the cutout in the center matching the shape of the testing devices. The front lid was used to prevent the loss of heat from the sides of the substrate. While the back lid was to prevent the loss of heat from the

back as well as the sides of the heating element. A thermocouple was connected at the interface of the heating element and the testing devices to get the temperature at the heater. Data from the thermocouple and the power supply unit was gathered using the data acquisition system called the IPTRONIK's M-Thermo2 u which was loaned from the measuring department at Volvo Car Corporation. To replicate the conditions of the force convection a blower was placed below the testing device, thus allowing the air to blow through the test pieces. The setup was mounted on the frame which is made using the aluminum pipes which are procured from the company called AluFlex AB [61]. These are aluminium pipes that are designed such that they allow for easy and modular fabrication. The top of the frame was made up of horizontal slab aluminium covered with foam used inside the hood of the car to get closer to the air circulation conditions in the Car where the hood of the car blocks the free passage of the hot air upwards. The test rig was placed inside the environmental Chamber to maintain the constant ambient temperature throughout the test which was maintained at $25°C$ throughout. This can be seen in the figure 3.12.

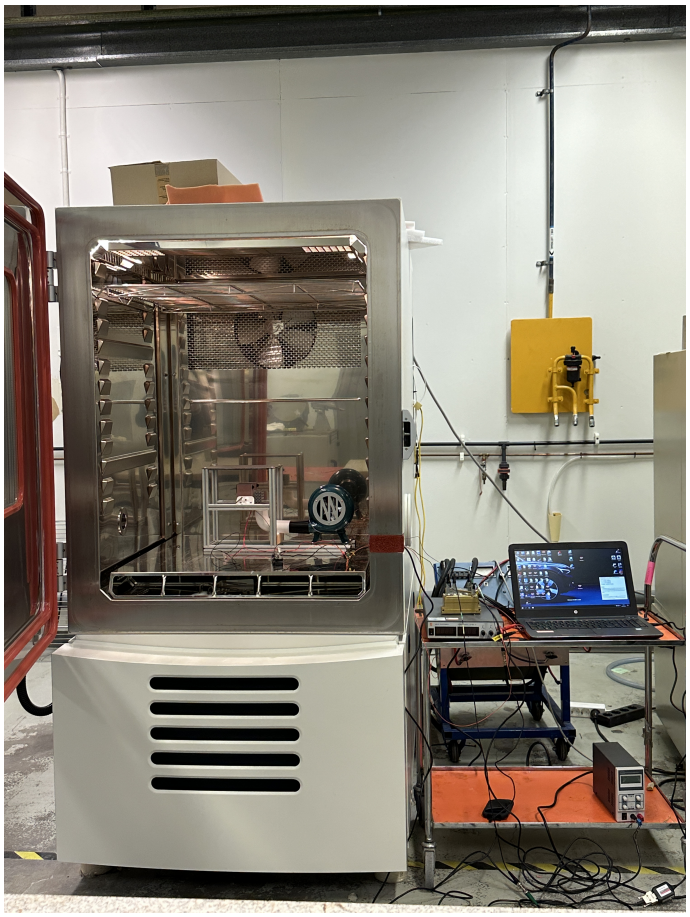

Figure 3.12: Environmental test chamber housing the assembled test rig with the data acquisition system

A simple experimental procedure was worked out to calculate the heat loss as well as the performance of the testing devices, as can be seen in Fig3.13. For the first case,

power was increased gradually such that the temperature at the heater was raised to $35°C$ which resulted in a $\Delta T = 10$. Power reading(P1) was recorded at a constant temperature. The temperature at the heater was considered constant if the change in temperature was less than $0.3°C$ in 5 minutes. Since the boundary for insulation was symmetrical. Loss of power through insulation for specific temperature differences was considered as half of P1. The front insulation lid was replaced with a lid housing a specific design of the heatsink. Then the same procedure was repeated until similar $\Delta T = 10$ was achieved. The power (P2) required to achieve this same temperature difference was measured and logged. Based on this performance of the heating device(P3) was calculated at specific boundary conditions, which is nothing but the power lost through the heating device that is given by:-

$$P3 = P2 - 0.5P1$$

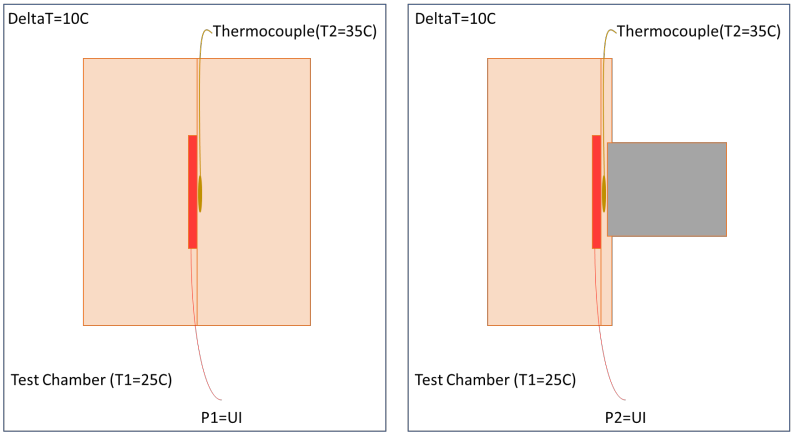

Figure 3.13: Schemetic representation of calculation for power lost through the device

This was repeated for ΔT of 15, 20, 25, 30, and 40 for each of the test devices whose performance was to be tested. All the readings were taken for three different test setups

- Self Convection with vertical test setup was carried at $\Delta T 10, 20, 30\&40$.
- Self Convection with the horizontal test setup was carried at $\Delta T 10, 20, 30\&40$.
- Forced Convection with the vertical test setup was carried at $\Delta T 10, 15, 20\&25$.

All three setups can be seen in Fig 3.14.

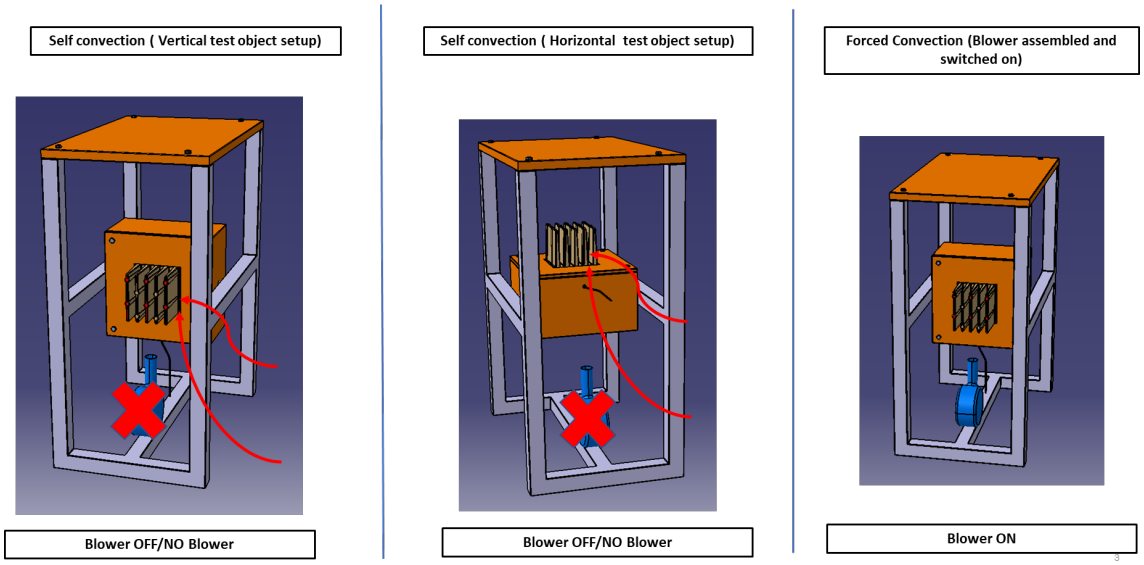

Figure 3.14: Schematic illustration of all three convection setups

This resulted in a total of 63 data points of power lost through various test pieces in 3 different setups. This data was then analyzed by calculating the performance factor as well as computing the increase in performance from free to forced convection. Results were plotted on the bar graph for evaluation. Results can be seen in 4.7.3
To understand which gyroid design performs the best before they could be incorporated in the new heat sink design, artefact gyroid designs mimicking certain features of the heat sink were produced. These shapes had the same overall dimension of 40X40X33 mm including a 3mm thick base plate. Their shapes had thicknesses of 1mm, 1.5mm, and 2mm respectively. While the fourth shape had a varying thickness from the base to the top between 2 to 1 mm respectively.
Furthermore, the fin design very similar in box volume to the gyroid lattice was produced to be tested in the experimental test setup. This was done to evaluate the gyroid designs on more level ground that has similar material properties. Furthermore, the existing heatsink was machined to match the box volume of all the produced shapes approximately. This allowed us to understand the combined effect of the material and the shape produced on thermal conductivity. Details for the test samples can be found in Table 3.3.

3.6 Materials characterisation

This section outlines the procedures and principles utilized for characterization in the research study, whose results are summarized in this report.

3.6.1 Light optical microscopy

A Zeiss Axioscope 7 light optical microscope (LOM) fitted with a Zeiss Axiocam 105 color camera was used to capture images of the polished samples. It is possible to obtain photographs of the whole cross-section by piecing together high-magnification

Table 3.3: Details of the Test Prints

Si no	Geometric Parameters	Gyroid 1mm	Gyroid 1.5 mm	Gyroid 2mm
1	Box Volume=LXBXH(mm^3)	40X40X33	40X40X33	40X40X33
2	Surface Area (mm^3)	34272	34221	33678
3	Material	AlSi	AlSi	AlSi
4	Material Density(kg/m^3)	2800	2800	2800
5	Actual Volume(mm^3)	9296	13961	18679
6	Mass (g)	26.3	39.5	52.86
7	Ratio=SA/VA	3.69	2.45	1.80
Si no	Geometric Parameters	Gyroid 2to1 mm	As-sintered Fins	As-Cast Fins
1	Box Volume=LXBXH(mm^3)	40X40X33	40X40X34	40X40X34.5
2	Surface Area (mm^3)	33907	16526	16803
3	Material	AlSi	AlSi	AlSiCu
4	Material Density(kg/m^3)	2800	2800	2700
5	Actual Volume(mm^3)	13974	24166	25007
6	Mass (g)	39.5	68.4	67.1
7	Ratio=SA/VA	2.43	0.68	0.67

images. Although the wavelength of visible light limits the resolution, it is enough for identifying the particles and pores in the sample produced by BJT/M [1].

Figure 3.15: Zeiss Axioscope 7 light optical microscope

3.7 Post-Processing

3.7.1 Hot Isostatic Pressing - HIP

Hot isostatic pressing (HIP) is a method of fabricating materials in which an initial powder or preformed shape is simultaneously subjected to high temperatures and high isostatic pressures, utilizing a gas transfer medium as depicted in figure 3.16. Principally distinguishing HIP from other processing techniques is using gas as the pressure-transmitting medium to induce equivalent three-dimensional changes in the surrounding materials. Until recently, argon was used almost exclusively; however, presses that can process powders and bulk parts in oxygen-rich or other reactive atmospheres are now available [29].

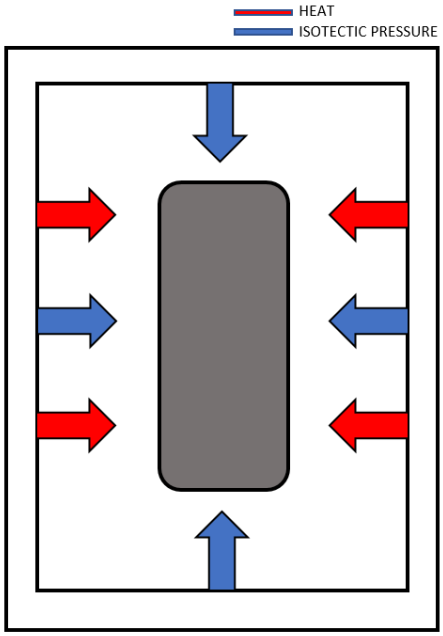

Figure 3.16: Hot Isostatic Pressing schematic

During this thesis, QIH 15L hot Isostatic machine from Quintus Technologies AB was used, depicted in figure 3.17. It has a furnace chamber of 170 mm x 290 mm, at a maximum pressure of 200 MPa and a maximum temperature of 1400 °C. It is possible to utilize either uniform rapid cooling (URC) or Uniform Rapid quenching (URQ) furnace using this machine. However, the selection of either furnace depends on the requirements and productivity. Due to microstructural differences, it appears that the optimal process parameters for hot isostatic pressing additively manufactured materials differ from those established for cast materials [62]. In spite of this, hot isostatic pressing can be used to reduce the porosity of various additively manufactured materials.

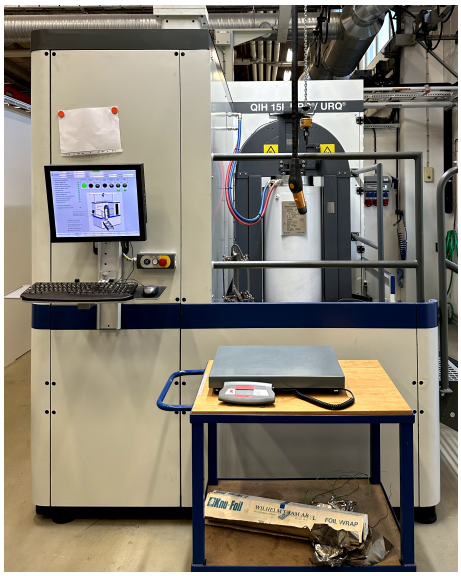

Figure 3.17: QIH 15L from Quintus Technologies AB

HIP was done at the Application Center at RISE in Mölndal. As mentioned before, the machine was a QIH15L, as depicted in figure 3.17. The sample was handled with specialized gloves to avoid any carbon residue. Any pencil marking was also removed using acetone.

Table 3.4: Parameters used during Hot Isostatic Pressing

Parameters	Values
Dwell Pressure (MPa)	150
Heating rate °C /min	7
Dwell Temperature	520
Upper temperature tolerance (°C)	10
Lower Temperature tolerance (°C)	10
Dwell time (min)	120
Cooling rate (°C /s)	15

Hot isostatic pressing was performed at 520 °C for 2 hours at 150 MPa in an Argon atmosphere [63]. Uniform rapid cooling is used instead of uniform rapid quenching, to avoid cracking of the sample. The heating rate was 7°C /s while after the heating, the sample was gas-cooled at a rate of 15 °C /s. The temperature, pressure, and holding time for the sintered sample are given in table 3.4 and figure 3.18.

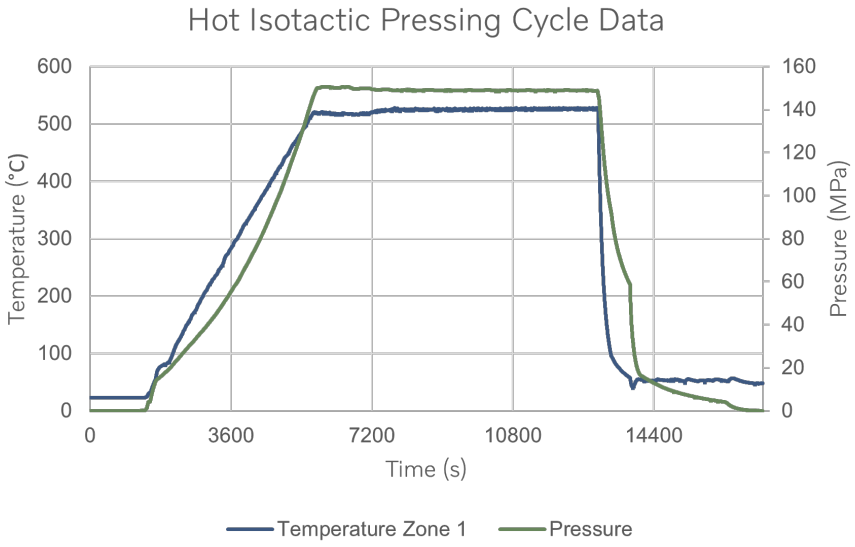

Figure 3.18: HIPing parameters utilized in this work. The Y-axis on the left show the temperature and the Y-axis on the right show the pressure. The X-axis shows time in seconds

4

Results and Discussion

4.1 Verifying the design guidelines

Design guidelines mentioned in the Theory Chapter needed to be optimized before they could be incorporated into the final design. One of the reasons for this was that they were mainly referring to the studies of stainless steel and not aluminium alloys being completely different metals belonging to another family, and behaving differently. This effect is amplified due to changes in the process during the sintering phase with the use of ceramic powder during sintering as support. This meant that parts behaved differently when it came to deformation under gravity as well as shrinkage.

4.1.1 Artefact designs for verifying the guidelines

The first step in verifying the design guidelines involved designing and producing the artefacts that will embody the required guidelines. Since the scope of the project is not just about understanding the design guidelines, but also evaluating the technology from the application point of view. It was decided to print the guidelines which are specific to the application that is heatsink. This was done using two sintering processes which RICOH has under development. In one process they carry the sintering with ceramic powder used as support media this is referred to as ceramic-supported sintering /ceramic support henceforth. The second process is similar to the existing process and hence is called unsupported/convectional sintering henceforth. After careful evaluation of the heatsink, it was decided to print Artefact 1: consisting of threaded screw holes with conventional sintering(1A) and with ceramic-supported sintering(1B), Artefact 2: vertical pins with convectional sintering(2A) and with ceramic-supported sintering(2B), Artefact 3: a bridge of varying spans without baseplate, Artefact 4: a bridge of varying spans with the baseplate. Artefact 5: A tree design consisting of a horizontal overhang, circular holes, and an angular overhang.

For Artefact 1, it was decided to print the threads corresponding to the ISO metric. A thick pitch metric standard was used. All the printed screw-holes had a depth of 10mm. 6 printed threads were M2, M2.5, M3, M3.5, M4, and M4.5. This can be seen in the figure 4.1.

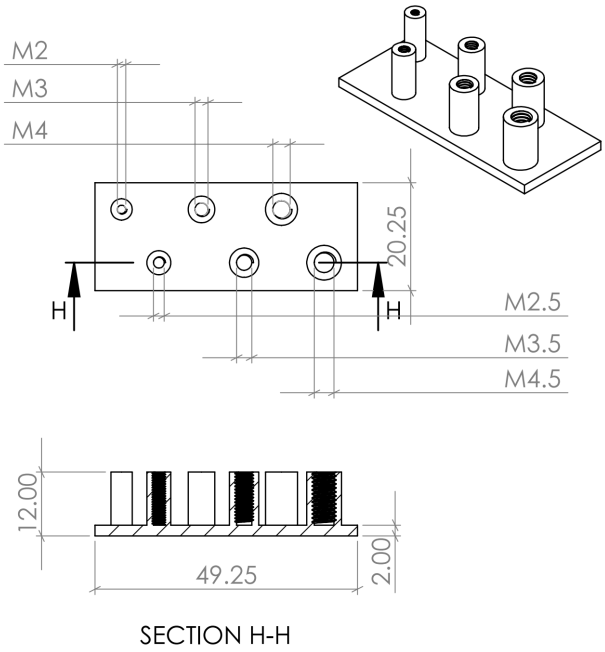

Figure 4.1: Artefact 1 screw Threads in metric standard(all dimensions in mm)

For Artefact 2 a total of 12 vertical pins were printed in four different heights (H1=3mm, H2 =5 mm, H3=8mm, & H4=10mm) on a base plate that was 2mm thick. Each height consisted of 3 pins each having the same height. Pins of H1 had diameters of 1mm, 1.5mm, and 2mm respectively. Pins H2 had diameters of 1mm, 1.5mm, and 2mm respectively. Pins H3 diameters of 1mm, 2mm, and 3mm respectively. Pins H4 had diameters of 1mm, 2mm, and 3mm respectively.

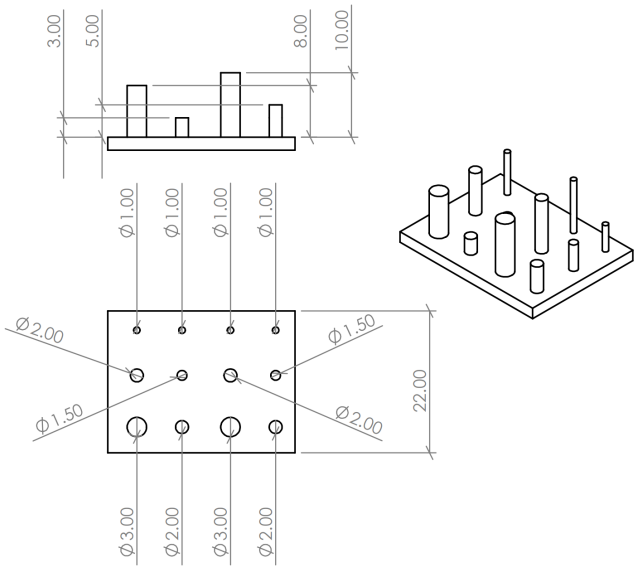

Figure 4.2: Artefact 2 Pins with various heights and diameters (all dimensions in mm)

For the bridges, it was decided to print two artefacts without base-plate (Artefact 3) and with base-plate (Artefact 4) having similar parameters. The thickness of the horizontal wall was kept at 3mm while the bridge legs were kept at 2mm thick constant. It was decided to have the minimum value of 4mm for the bridge span with constant increments of 2mm for every other span. Thus, resulting in a bridge with 10mm as the largest span. Knowledge learned from this was useful from the final design point of view. Details of the bridge artefacts can be seen in figure 4.4.

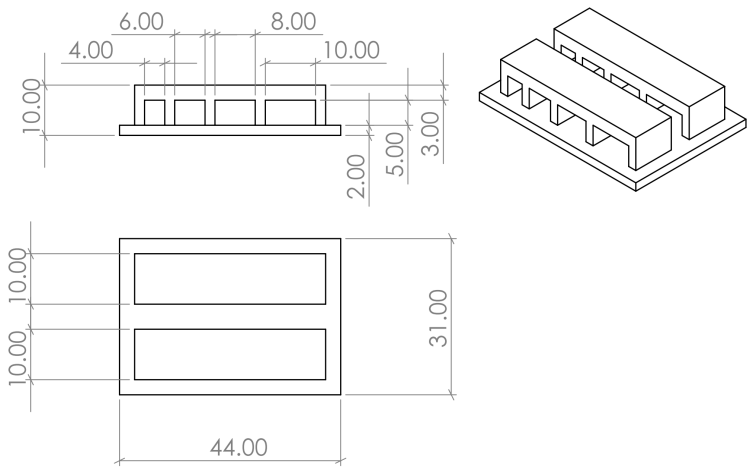

Figure 4.3: CAD-designed artefact for bridges(all dimensions in mm)

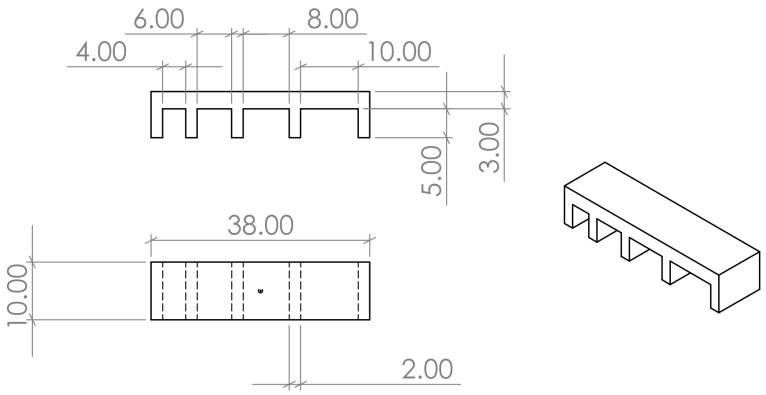

Figure 4.4: CAD-designed artefact for Bridge without base(all dimensions in mm)

A tree design was created to evaluate the overhang thickness, length, and angle in a part. This can be seen in figure 4.5. The feature to evaluate the overhang thickness and length was designed as horizontal branches with various lengths and thicknesses. Horizontal branches were as follows 20mmX4mm, 15X3mm, and 10X2mm. The symmetrical design was placed on the opposite side but a radius of 1mm was provided at the intersection of the branch and the main stem. This was done to understand how deformation varies after providing the radius. While the angles branches were

used to evaluate the overhang angle. It was decided to print 3 branches per side with an overhang angle of 60 degrees. The length and thickness of the branches varied similarly to the horizontal branches, with a radius of 1mm on one side incorporated to non on the other side.

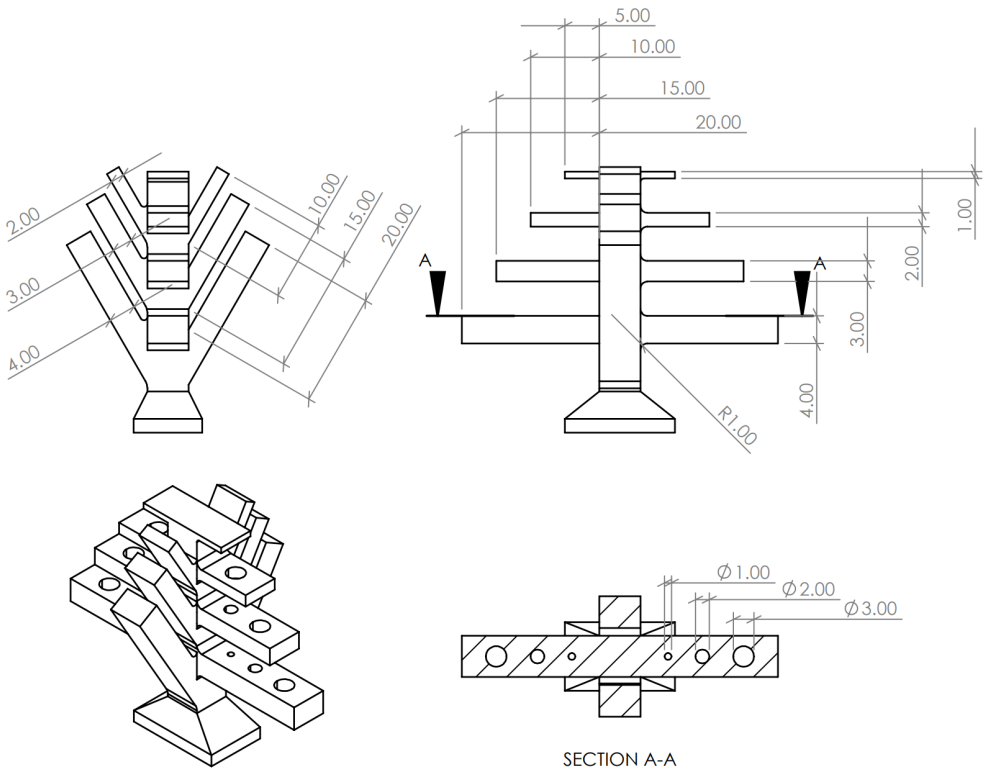

Figure 4.5: CAD design of the artefact for trees(all dimensions in mm)

The below table 4.1 shows the summary of the artefacts with details of evaluation, the scaling factor designed by RICOH for each artefact, and the method that was used for evaluation.

Table 4.1: Table showing the summary of all the artefacts along with the scaling factors designed by RICOH

SI NO	PARTS DESCRIPTION	Artefact Numbering	CAD IMAGE	SCALLING FACTOR			OTHER COMPANSIATION AND USE OF SUPPORTS (ceramic support, friction, gravity compensiation etc.)	EVALUATION	METHOD
				X	Y	Z			
1	THREAD WC	1A	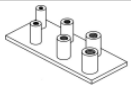	1.15	1.15	1.17	NA	Printability Dimensional Accuracy Screwability	3D scanning and Geometry Inspection Software Screwing
2	THREAD C	1B	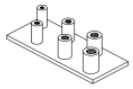	1.15	1.15	1.17	Ceramic support	Printability Form Accuracy Screwability	3D scanning and Geometry Inspection Software Screwing
3	PINS WC	2A		1.15	1.15	1.17	NA	Printability Diameter Perpendicularity	3D scanning and Geometry Inspection Software
4	PINS C	2B		1.15	1.15	1.17	Ceramic support	Printability Diameter Perpendicularity	3D scanning and Geometry Inspection Software
5	BRIDGE WOB 1	3A	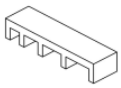	1.1	1.1	1.1	NA	Deflection under gravity Frictional Collapse	3D scanning and Geometry Inspection Software
6	BRIDGE WOB 2	3B		1.1	1.1	1.1	2 largest overhangs compansated for gravity	Deflection under gravity Frictional Collapse	3D scanning and Geometry Inspection Software
	BRIDGE WOB 3	3C	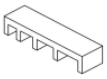	NOT AVALAIBLE			Simufact Compansition for friction and deformation	Deflection under gravity Frictional Collapse	3D scanning and Geometry Inspection Software
7	BRIDGE WB 1	4A	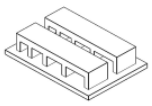	1.1	1.1	1.1	NO	Deflection under gravity Frictional Collapse	3D scanning and Geometry Inspection Software
8	BRIDGE WB 2	4B	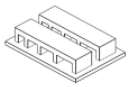	1.1	1.1	1.1	Ceramic support	Deflection under gravity Frictional Collapse	3D scanning and Geometry Inspection Software
9	TREE	5	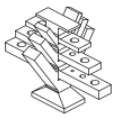	1.1	1.1	1.1	Ceramic support	Not Sure right now after CT scan will take call	CT scanning

various design features in each artefact were decided based on the current design of the heatsink to evaluate how feasible is it to print the critical features of the existing part without compromising the function and also how they can be further optimized.

4.1.2 Results from verifying the guidelines

Printed artefacts were then evaluated to understand the printing feasibility limits of the various design features. To begin with the evaluation it is essential to understand the various directions that are building, re-coating, and binder dispensation. figure 4.6 shows the various directions for all the printed artefacts.

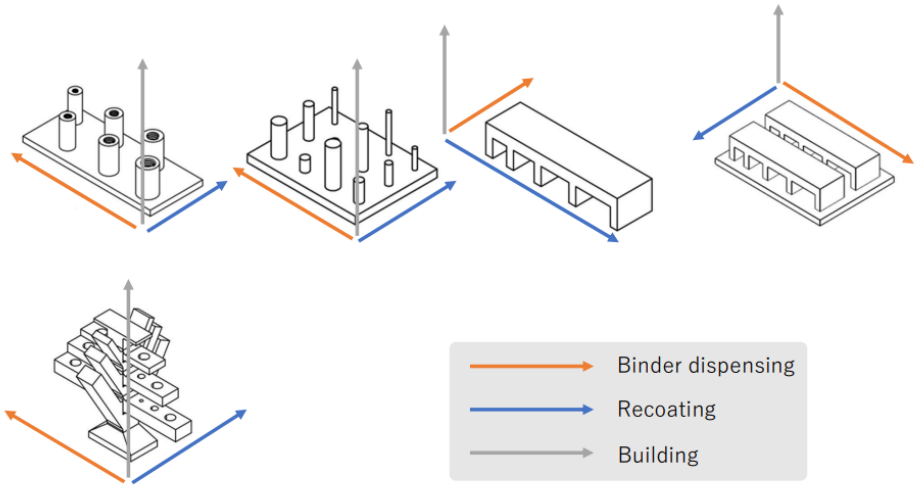

Figure 4.6: Image showing the building, recoating, and binder dispensing direction for all the artefact designs

Artefact 1: Threads were divided into two artefacts 1A: convectionally sintered and 1B: sintered with ceramic support. Both the artefacts were scaled similarly with 15% in X and Y and 17% in Z direction.

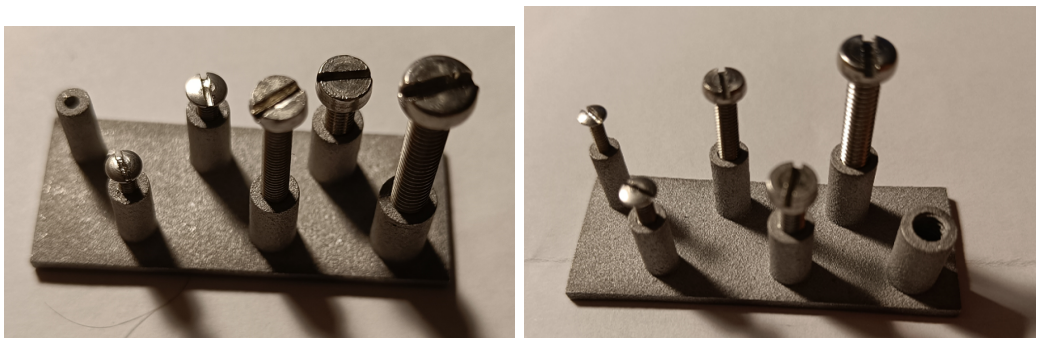

(a) **(b)**

Figure 4.7: Shows the threads after bolting. 4.7a refers to conventionally sintered threads and 4.7b refers to ceramic sintered thread

In the case of threads, it was not possible to evaluate the design using laser scans since internal features on the thread cylinders were hidden from the laser beam.

Thus the best way to evaluate the thread was by screwing them with bolts corresponding to the ISO metric specifications of the thread. Bolts for M4.5 were not available. During the evaluation of 1B, it was found that all the bolts fit perfectly in the threads. In the smallest thread M2 the bolt didn't go all the way to the bottom of the thread. This can be accounted to the trapping of excess powder internally. Whereas in the case of the 1A: bolts fitted in one specification lower than they were designed for. For example, the M4 bolt is fitted in an M4.5 thread hole. While the ease of screwing was the same as 1B.

From this evaluation, it was clear that this technology can print intricate features like thread in both sintering processes. While the shrinkage due to the absence of ceramic support is higher than in the presence of ceramic support and thus needs to be compensated differently. The size difference between the two parts raised concerns about different densification in different parts. To check the densification of both the artefacts, these parts were later CT scanned and compared for porosities. This is found in section 4.5.

Artefact 2: Pins were divided into two artefacts 2A: which was sintered using the convectional sintering and 2B: pins that was sintered in the pool of ceramic powder. Both the artefacts were scaled similarly with 15% in X and Y and 17% in Z direction.

Artefact 2A among the pins with 1mm diameter only one which was processed properly was 3mm in height with a very slight angular deviation of 0.13 degrees in the YZ direction and 1.96-degree deviation in the XZ direction. Both pins with 1.5mm diameter printed with less than 1-degree deflection which was acceptable. All the pins in the last row consisting of D3X10mm, D3X8mm, D2X5mm, and D2X3mm printed successfully with an acceptable deflection as it can be seen in figure 4.8. It was also noticed that the diameters of all the pins were nearly the same as the nominal CAD dimensions with tolerances of positive 0.03mm which is deemed acceptable. The detailed report for this can be found in Appendix A.1.

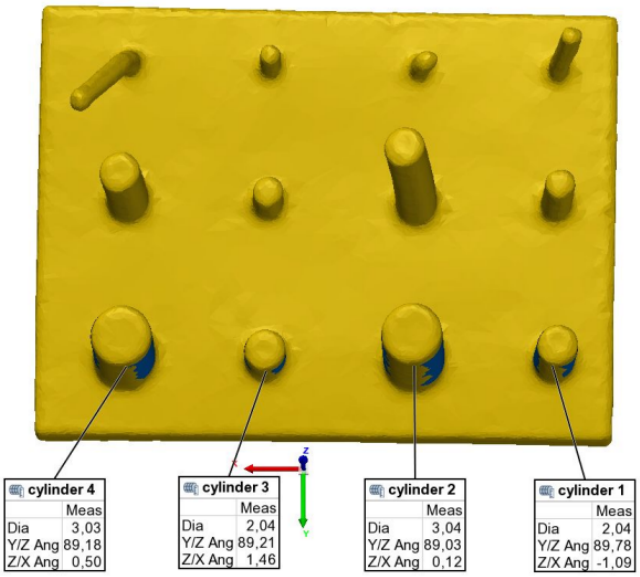

Figure 4.8: Dimension evaluation on the laser-scanned data for pins sintered in unsupported sintering process (Artefact 2A)

Artefact 2B among the pins with ceramic support none of all pins of diameter 1mm produced with a significant deflection in axis and were considered unacceptable. From the ones that were evaluated the best result was a 10X2mm pin which produced nearly perpendicular with a deflection as less as 1.69 degrees in XZ and 0.49 degrees in YZ, while 10X3mm had the second least deflection among all. The diameter of all the pins was larger than the nominal dimension by 0.10 to 0.15. Although all the pins were scaled using the scaling factor mentioned in the table 4.1, higher dimensions than the nominal suggest a lack of densification in part similar to the thread design, a detailed report of the pins Artefact 2B can be found in the appendixA.2.

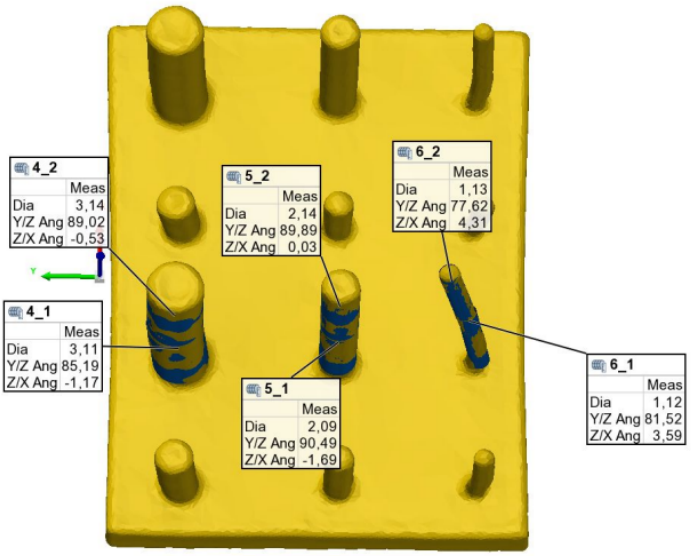

Figure 4.9: Dimension evaluation on the laser scanned data for pins sintered in ceramic media (Artefact 2B)

Artefact 3: Bridge which is varying bridge spans without base was divided into 3A: no compensation apart from the scaling, 3B: two largest spans compensated for gravity, and 3C: geometry was compensated by using Simufact (Hexagon) BJT/M module with optimized parameters for AlSi. In 3A and 3B manual scaling of 10% was applied before printing. All of them were sintered using the non-supported sintering process.

Artefact 3B the bending of the legs internally was observed due to frictional deformation which was highest on the outermost legs with higher tilting on the leg which was in connection with the largest span of 10mm. Although the compensation was done for gravity there was still an overall sagging in the horizontal span of the bridge. Deflection as high as 0.33mm can be seen. This can be accounted to frictional deforamtion which causes the horizontal span to flex due to compressive force exerted on it along with the gravity effect combined causing the bending in the downward direction. The scaling factor used clearly underestimates the shrinkage by certain values. In the case of artefact 3A, no additional compensation was done apart from the normal scaling mentioned above. The results were very similar to artefact 3B apart from the local sagging which was seen in 10 mm and 8mm span. A maximum sagging of 0.51mm was seen in the Artefact. This can be seen in the figure 4.10a. Detailed reports of the comparisons can be seen in Appendices A.3 and A.4.

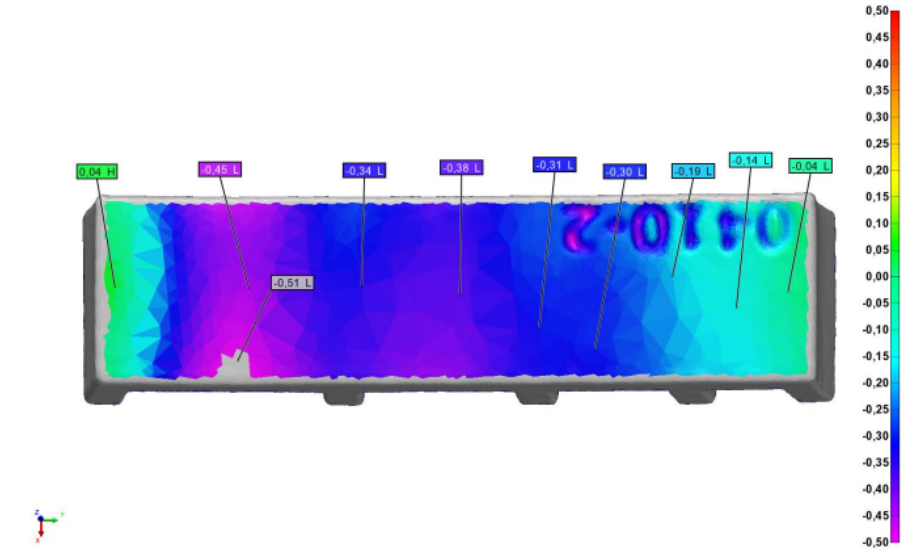

(a)

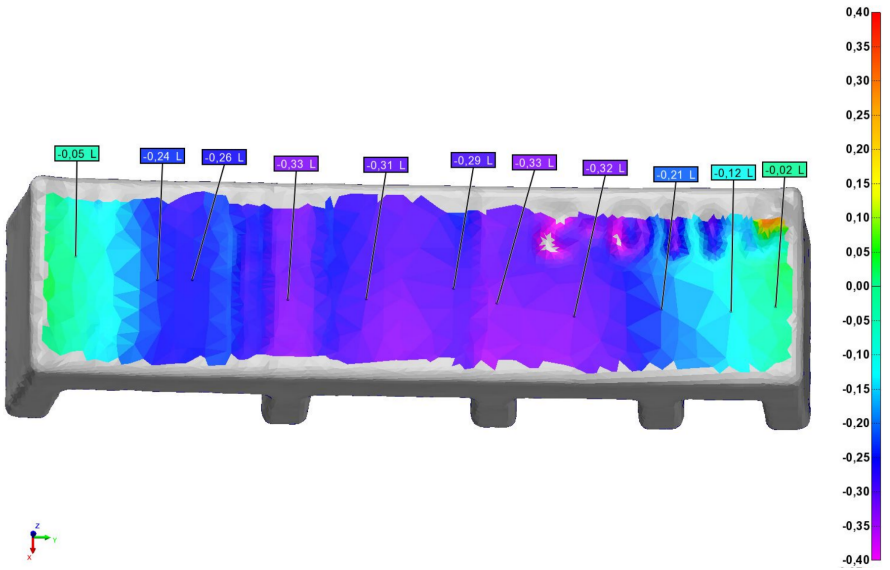

(b)

Figure 4.10: Shows the evaluation of the non-compensated vs compensated bridge geometry for gravity using the scanned data

Artefact 3C was the Simufact compensated bridge geometry by RICOH. The deformation model, compensated model and Final produced & scanned geometry can be seen in figure 4.11.

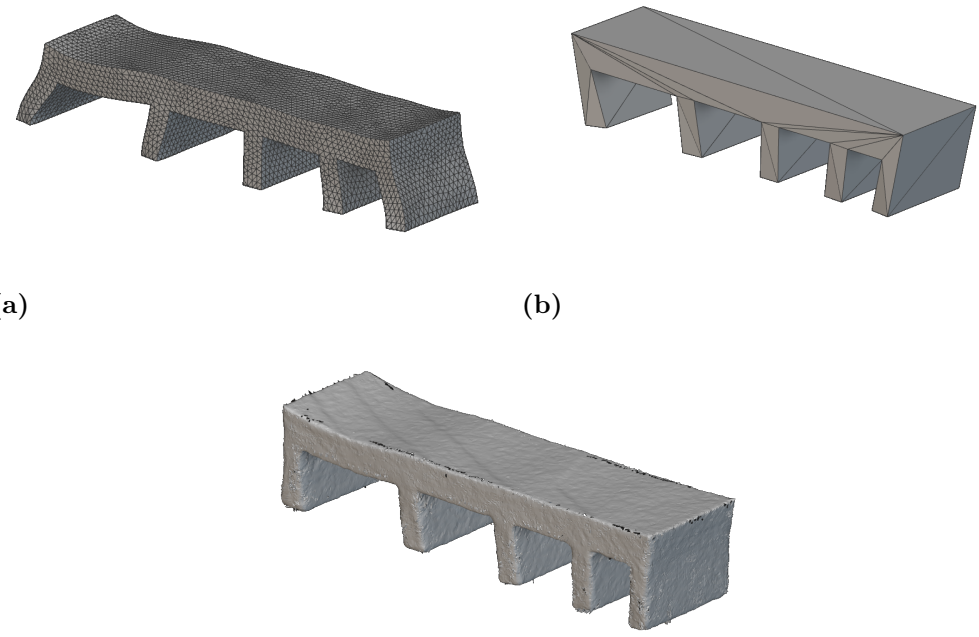

(a) **(b)**

(c)

Figure 4.11: Artefact 3C Bridge using Simufact data: 4.11a Shows the deformation predicted by Simufact, 4.11b Shows the compensation geometry provided by Simufact and 4.11c shows the scanned file for the final print using the compensated CAD data from Simufact

It can be seen that Simufact predicted frictional deformation and deformation due to gravity along with shrinkage. However, the compensation model only accounted for the frictional deformation and shrinkage. This was investigated with RICOH who are in the developing parameters for aluminum in the Binder jetting module of the software and they said that the parameters which produce the compensated geometry are in the early development stage and cannot compensate geometry against the gravitational deformations. The final produced and sintered part was then scanned and evaluated to check the accuracy of the compensations. It showed that there was an improvement in negating the frictional deformation, especially in the outermost legs but the inner legs looked overcompensated this is due to the fact that the effect is not uniform throughout the geometry and very much depends on the design feature and its position in the geometry for example outermost features experience more frictional deformation compared to the inner. This is not accounted for properly by Simufact. The assumption in overall shrinkage was more accurate than both 3A and 3B artefacts which can be seen in AppendixA.5. Due to confidentiality, this scaling factor could not be revealed. Since the horizontal spans were not compensated for gravity in the compensated CAD by software it resulted in very high local sagging of about 0.52mm as maximum. Since the compensation was done for friction there was no overall sagging.

Artefact 4: Bridge with baseplate consisted of two versions 4A: which was sintered

using a conventional sintering process and 4B: wherein ceramic support was used in sintering. Both were scaled by 10% before printing.

Artefact 4A has shrunk and deformed in a similar way to the bridges without base-plate i.e. Artefact 3 in one with conventional process. The only major difference that was observed was the frictional deformation of the legs was negated. This is due to the fact that there was a base-plate in the design which took care of this. This also meant that the deflection of the horizontal span was restricted to two long spans of 8mm and 10mm due to the gravitational effect on the two unsupported spans. This can be seen in figure 4.12a and 4.12b. The detailed report on the bridge with baseplate can be found in Appendix A.6.

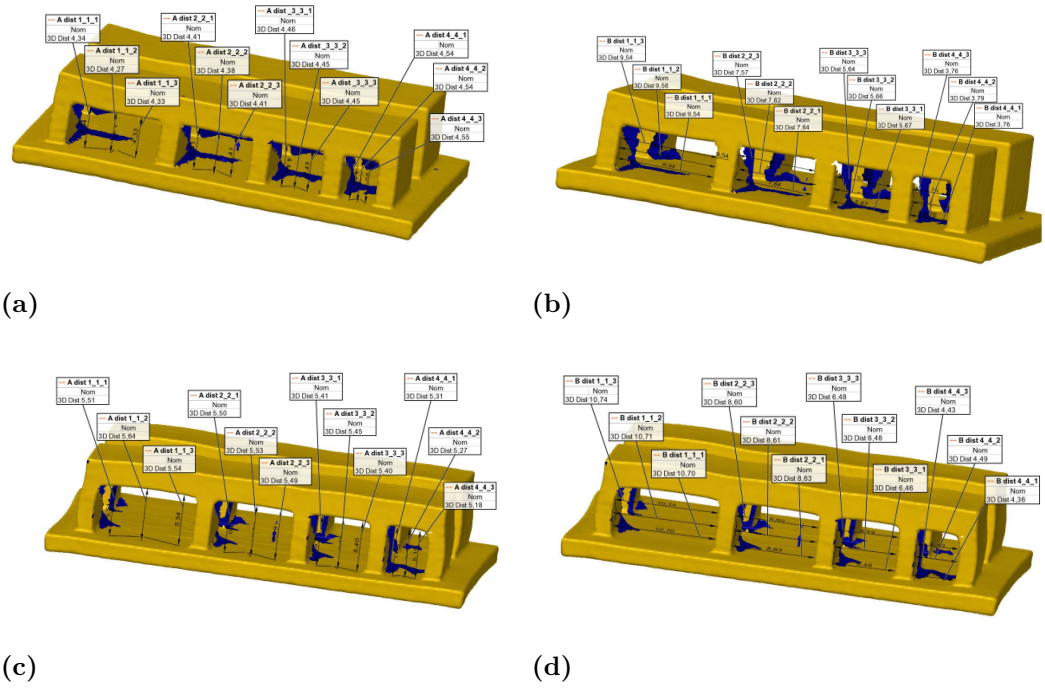

(a) **(b)**

(c) **(d)**

Figure 4.12: Image showing evaluation using scanned data for the bridge with base: without and with ceramic support respectively

Artefact 4B sintered in ceramic powder compared to unsupported one behaved very differently. It can be seen from the figure 4.12c and figure 4.12d, that shrinkage in this component was not uniform. In the continuous columns such as vertical legs and the horizontal span, it shrunk at a higher rate while the hollow spaces between the legs and under the horizontal span were not allowed to reduce in volume by the ceramic powder occupying this space. Hence, the geometrical shape of the component changed to accommodate these changes. Due to lower shrinkage final size of the part is bigger than the nominal CAD, thus densification needs to be cross-verified. Detailed report of evaluation can be found in appendix A.7.

For **Artefact 5:** Tree design first trial was done by sintering the artefact in this conventional sintering process. The result of this was that it failed and broke into pieces during the sintering as seen in figure 4.13a. It was learned that such a complex

geometry with a high aspect ratio was difficult to achieve using the normal process. In the second trial RICOH process for sintering was used, during this the tree was placed in the sintering box and the box was filled with the ceramic powder. The result from the sintering can be seen in figure 4.13b.

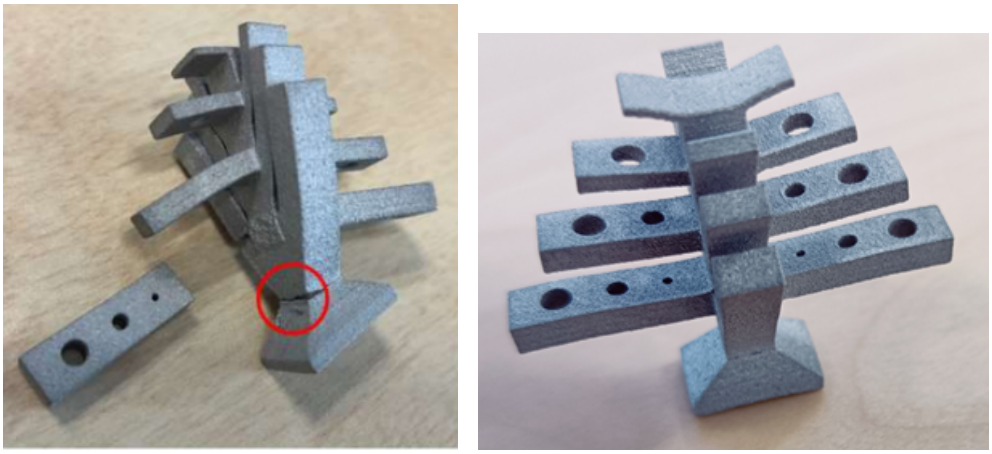

(a) **(b)**

Figure 4.13: The outcome using conventional sintering process 4.13aand The outcome using the ceramic-supported sintering process 4.13b

From the evaluation following things were noted

- The ceramic-supported sintering process allows for the printing of complex geometrics in the first attempt.
- The deformation factor for this process varies significantly from the normal process
- Deformation along the direction of gravity is neglected
- Deformation in the continuous features(tree stem) in the part is different from the protruding features(branches)
- Unlike the normal process where the origin of deformation is the centre of the bottom plan on the tree, in the case of the ceramic process the origin/centre of deformation is concentrated towards the portion in the body that acts as the clamping feature(longest branches)

The tree was also evaluated by laser scanning and superimposing the geometry on the nominal CAD data. This revealed that there were a lot of deviations, especially in the branches. The top branch deviated as much as 2mm upwards from the nominal CAD data as seen in figure 4.14b. While the diameter of the hole features was also larger in thick branches this was assumed due to less densification, which was later confirmed during CT scanning 4.2. Upon careful evaluation, it was understood that the center of densification shifts in the part from the center of the bottom plane, to the feature which acts as the clamping feature in the part. In this case, it was the largest branch in the tree. Thus causing deformation towards the core of the part around the largest branch. This can be seen in figure 4.14d. While the detailed report of geometry verification can be found in the appendixA.8.

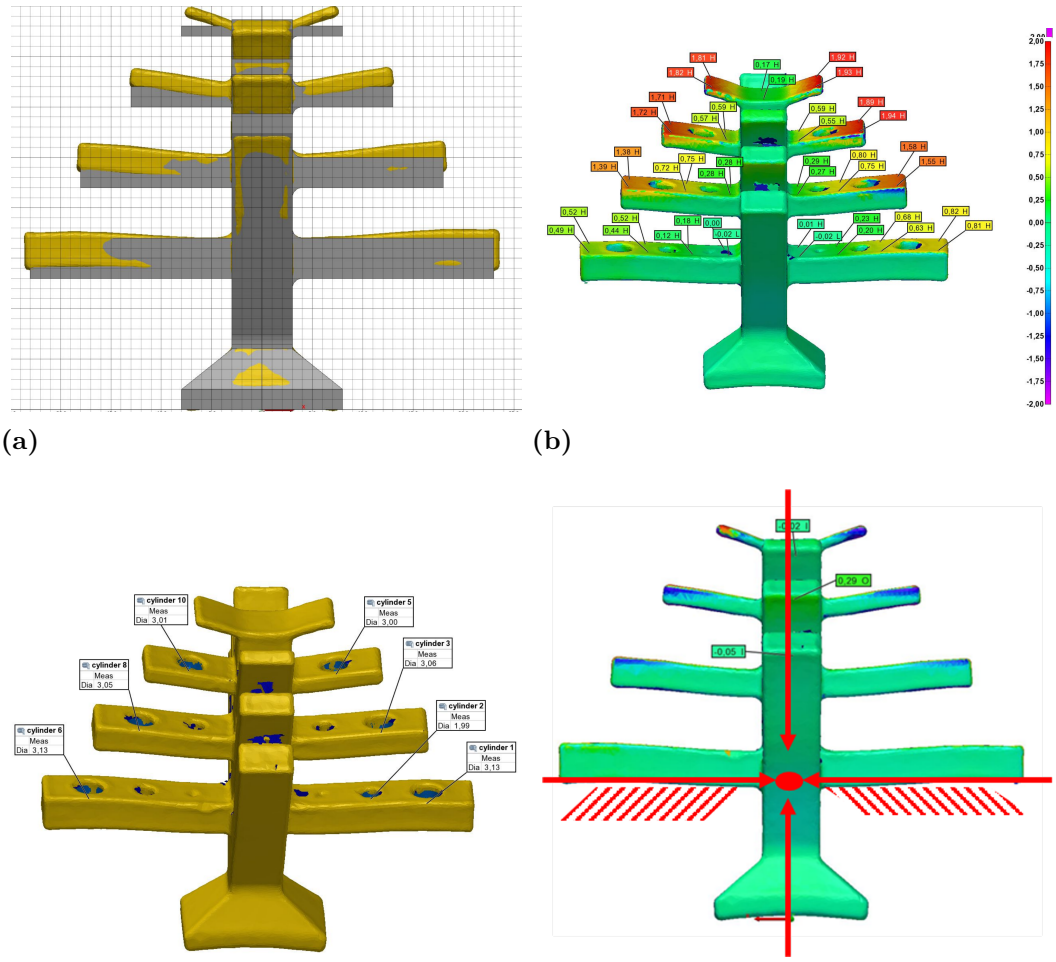

Figure 4.14: Shows the superimposed nominal & scanned geometry 4.14a, shows the measurement of deviation in branches of the tree 4.14b, shows the measurement of the holes on branches 4.14c and shows the centre of densification of the tree 4.14d

4.2 Porosity analysis using CT scanning

Internal defects and porosity analysis were studied for **Artefact 5 Artefact 1A** and **artefact 1B**. Thus, CT scanning of these components was done at the Nikon facility using their CT scanning system XTH225 [64] having an X-ray gun of 225kV.

artefact 5: Tree was scanned and analyzed for porosity in various parts of the tree. The theory employed in this case is to understand how is porosity distributed in various sections of the complex design geometries. Learning from this can be incorporated in the designs of various application parts which have complex geometries most of the time. It was found that there was a high level of porosity in the stem of the tree as well as on the branches which were thicker in dimensions as seen in figure 4.15a. A very high percentage of these pores were mainly high-thickness portions of the tree such as the stem compared to thinner branches such as top branches of 2mm.

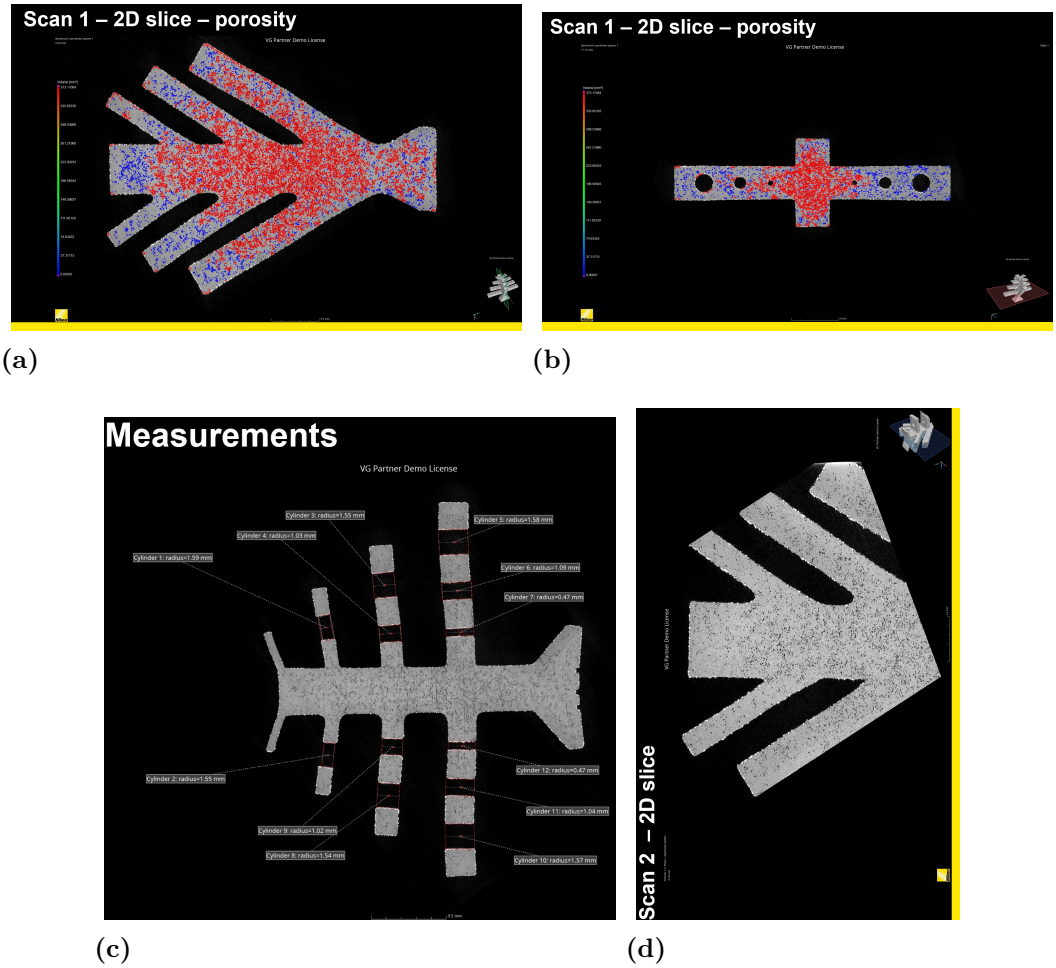

Figure 4.15: Shows the internal porosity in two views i.e. 4.15a & 4.15b. 4.15c shows the result of the measurement of various holes on the tree branch. 4.15d shows the high-resolution scan performed at $10\mu m$ focusing on the specific session of the artefact

Furthermore, upon careful evaluation, it was observed that there was sintering of ceramic powder all along the tree, this is seen as a bright white boundary in the figure 4.15d. The ceramic powder has a higher density compared to aluminum thus the X-ray scans show it's brighter. It could be seen there is more entrapment and sintering of ceramic on smaller holes thus compromising the dimensional accuracy in these holes as seen in the figure 4.15c. Ceramic powder on the surface of the tree can lead to different surface properties like hardness, stiffness etc. compared to aluminium alloys.

4.3 Evaluation of the shrinkage and deflection after sintering

Pre-sintered cubes as well as the four gyroid designs received from RICOH were evaluated for shrinkage along X, Y, and Z directions. Cubes were named S1, S2, S3 and S4. While the gyroids were named G1, G1.5, G2, and G2to1 based on the wall thickness of the gyroids.

4.3.1 Shrinkage in 10mm^3 cubes

Firstly the cubes were scanned to generate the .stl files. These files were then imported in GOM Inspect 1 by 1 and superimposed on the Nominal cube CAD. In the software scanned CAD becomes the mesh while the nominal is called CAD. There are two alignments initial and final. For initial alignment, the *pre-alignment* option was used while for the final *local best-fit* having matching one corner and all the perpendicular faces in that corner was used. After the alignment inspection was carried out for shrinkage along XY, YZ; and XZ planes with a command called *inspection session on CAD* along with *deviation label* command was used along all three planes to study deviation. The data points generated from the images were summarised in the form of a bar graph using Matlab. This can be seen below in figure 4.16.

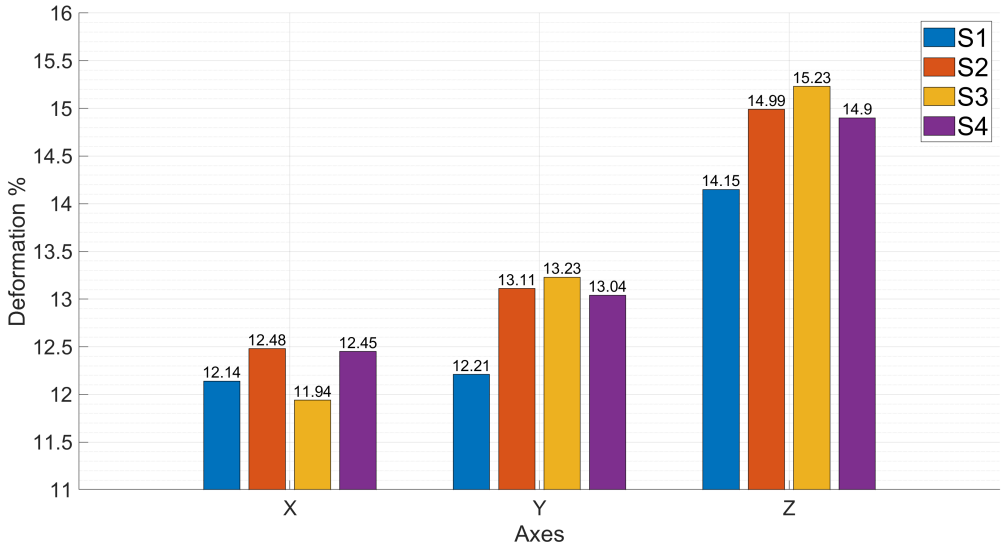

Figure 4.16: Shrinkage percentage of the pre-sintered cubes S1, S2,S3, and S4

From the above image, it can be seen that the average shrinkage along the X-direction is the lowest around 12% to 12.5%. The shrinkage along the re-coater direction that is Y direction in this case is around 13% on average. The highest shrinkage was observed along the building direction that is Z direction at an average of 15%.

4.3.2 Shrinkage and deflection in gyroids shapes

All the gyroids designs were scanned to generate the mesh and then superimposed on the green body CAD data in a similar way to the cubes. This was done with the help of the Geometry Verification Center in Volvo Car Corporation. The software used for this purpose is called *Polyworks* from Innovmetric. Similar principles were used for superimposing the nominal and the actual data. Detailed report generated can be seen in AppendixA.9,A.10,A.11 and A.12. Data points generated from the study were used to understand the average shrinkage in X, Y and Z directions. Additionally, angular deflection due to friction along X and Y was also calculated for all the shapes.
From figure 4.17, it can be seen that shrinkage for all the gyroid designs is highest in the Z direction while it's the lowest in the X direction. Shrinkage in gyroid with 1mm thickness is highest compared to the others in all directions while 2mm has the lowest shrinkage. When we compare the shrinkage in the gyroids with shrinkage in the cubes it can be seen that there is a significant increase in the shrinkage in the z-direction by more than 5%. This is understood that hollow design features tent to shrink more under gravity compared to non-hollow designs like cubes. An interesting finding was the shrinkage in the Z direction for G2to1 was the lowest compared to the rest of the designs at 20.77%. This can be attributed to the design feature that is a strong and dense base compared to the top section where the feature is lightweight gyroid walls. The wall thickness at the top is 1mm compared to 2mm at the base. This means the weight of the feature at the top is the lightest.

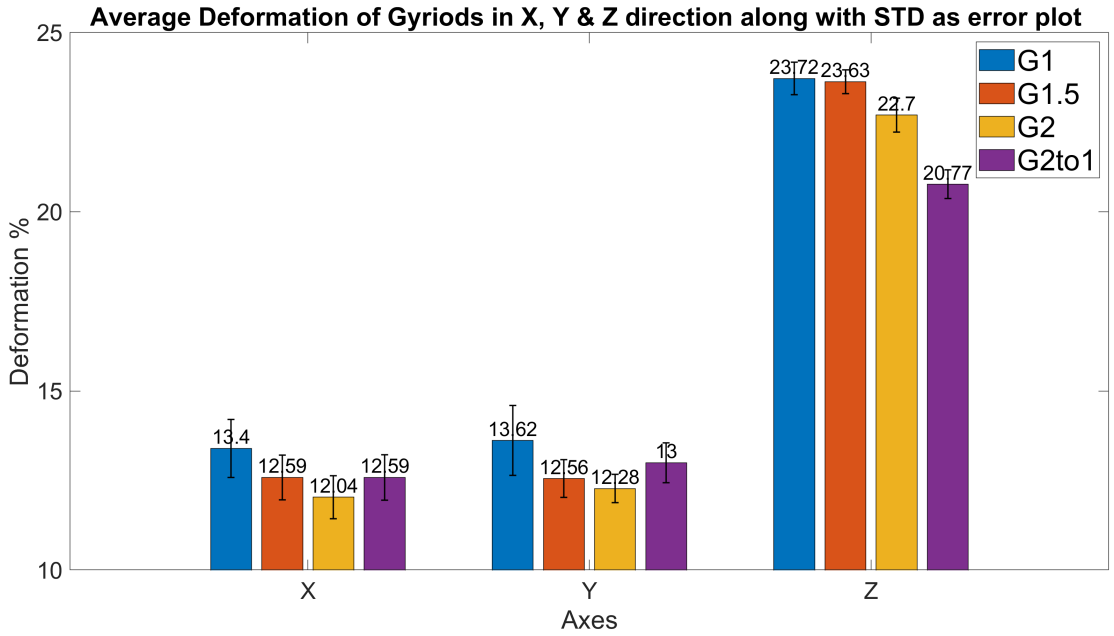

Figure 4.17: X,Y & Z Percentage Deformation for Gyroids G1, G1.5, G2 and G2to1

In the case of angular deflection, it was seen that the deviation in the X direction (binder deposition) was uniformly higher for all the designs compared to the Y direction(material deposition). While the lighter design that is G1 had the highest deflection in both directions compared to the heavier version G2 which showed a deflection of 1.15° in the X direction and $0,63°$ in the Y direction. A summary of the angular deflection can be seen in figure 4.18.

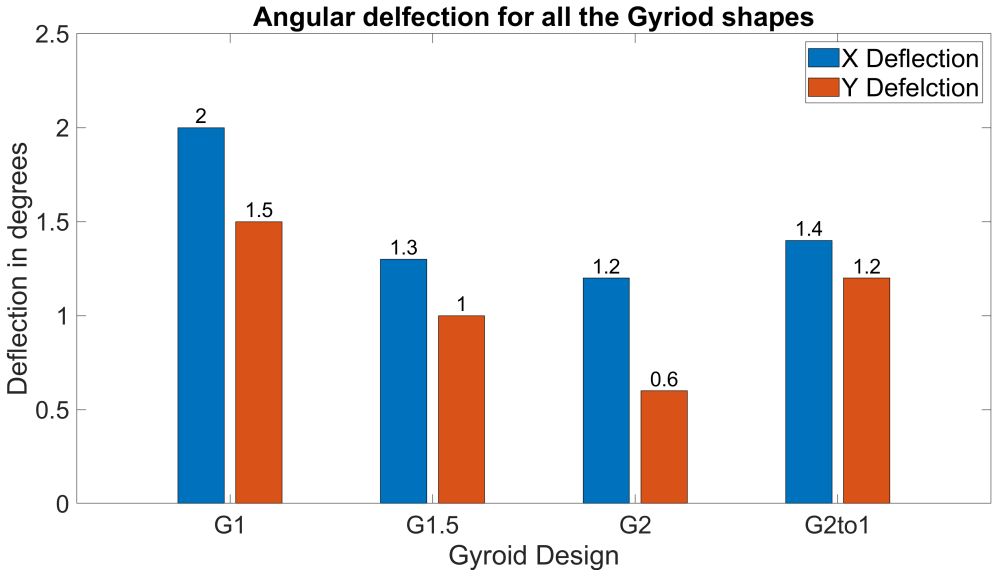

Figure 4.18: Angular deviation in X & Y for Gyroids G1, G1.5, G2 and G2to1

The overall assessment from this study that can be drawn is that lighter gyroid

design tents have a larger deviation in form compared to the heavier alternative both in terms of shrinkage and angular deflection. Unique design features such as that in G2to1 help in reducing the shrinkage, particularly in the Z direction.

4.4 Density measurements

Figure 4.19 display density readings. In the case of cast aluminum alloy given by Volvo Car Corporation from their production series car, model XC90, the relative density was 98.47% when it was measured using a manual calliper. Alternatives upon using ImageJ software (version 1.54d), the relative density obtained was 98.52%. In addition, the relative measured using Archimedes' method gave the lowest value, which was 96.91%.

The relative density of the green body without the binder is 63%. Because of the low green body strength, no LOM-based density measurements were performed on the green body samples. Only geometrical density was measured for the green body that came with the binder. The dimensions were calculated using manual slide calipers and 3D-scanned parts using GOM inspection. After the de-binding process, geometrical measurement was again conducted to calculate the shrinkage of the green body during de-binding. Usually, when the sintering temperature increases, the solid volume percentage rises and the uneven, interconnected porosity transforms into more rounded pores [1, 19].

Density measurements on sintered samples revealed a high degree of densification compared to the green body sample, obtaining relative densities between 97% and 98%. In general, LOM-based density results from various cross-sections are comparable but typically greater than geometry-based and Archimedes density measurement findings. According to figure 4.19, it can be seen that, when the samples are sintered at 600C in a vacuum, according to the geometry-based calculation the relative density is 98.47%, and Archemedis relative density is 96.91%. On the other hand, LOM relative density is 98.52% for XY orientation, 98.28% for XZ orientation, and 98.12% for YZ orientation.

In order to obtain full density, Hot isostatic pressing, commonly known as HIP is used. After HIPing, the relative density obtained was 99.98%. The relative density measured using the geometrical technique, Archimedes technique, and LOM cross-section analysis gave the same result with a standard deviation of 0.03.

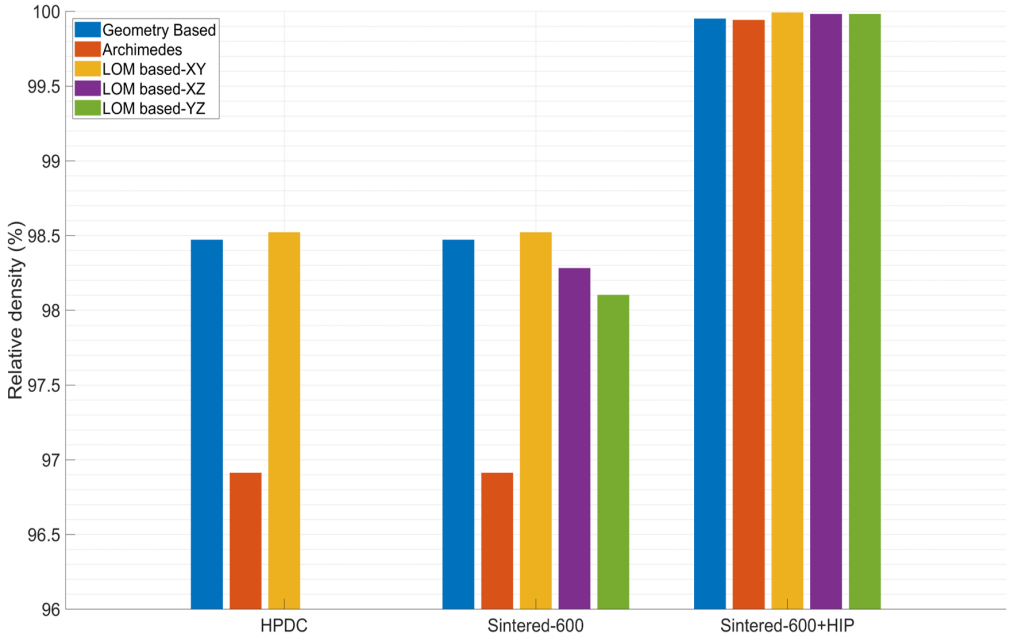

Figure 4.19: Relative densities for studied samples. Here are density values derived using several techniques: Based on geometry, LOM, and Archimedes

4.5 Comparative porosity analysis using CT scanning and light optical microscopy

According to the study of evaluation of design guidelines, it was observed constantly that the same geometrics behaved differently in terms of shrinkage and deviations when they were sintered using ceramic-supported sintering and conventional sintering. Hence, it was decided to do a comparative porosity analysis between two such artefacts. Two methods were used for this study CT scanning and Light Optical microscopy(LOM). CT scanning was used to compare **Artefact 1A & Artefact 1B Threads**, while LOM images were used for **Artefact 4A & Artefact 4B Bridge with base**.

In the case of LOM images, both geometries were cut such that the surface analyzed under an optical microscope for both was an XZ plane. Both had similar resolutions of $2000\mu m$ under a microscope as seen in figure 4.20. Density analysis done by computing the pores in the sample showed similar results of 99.28% and 99.5% densification with and without ceramic supports on these as-sintered parts.

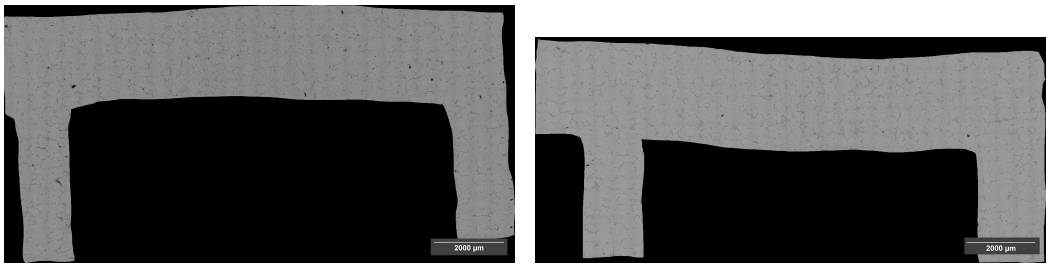

(a) **(b)**

Figure 4.20: shows the Light optical microscopy for bridge with base(artefact 4A and 4B). 4.20a refers to with ceramic and 4.20b refers to without ceramic support

While the result from the CT scanning which was done on threads also showed similar results to that of the LOM. In this case, a 3D view of the porosity in both thread artefacts was studied. From figure 4.21 it was seen that porosity was as minimum as 0.8% overall and was distributed throughout the sample as very small pores. While the ceramic powder was sintered on all the external surfaces of the artefact 4B. This can cause a change in the surface properties of the component. Hence, it is essential to study the surface properties such as fracture toughness, hardness, creep etc. for the parts sintered using ceramic. After a comparative study, it was learned that different shrinkage in the same designs is not due to a lack of densification. Hence, further investigation needs to be done to understand the cause behind the variation in shrinkage with different sintering processes.

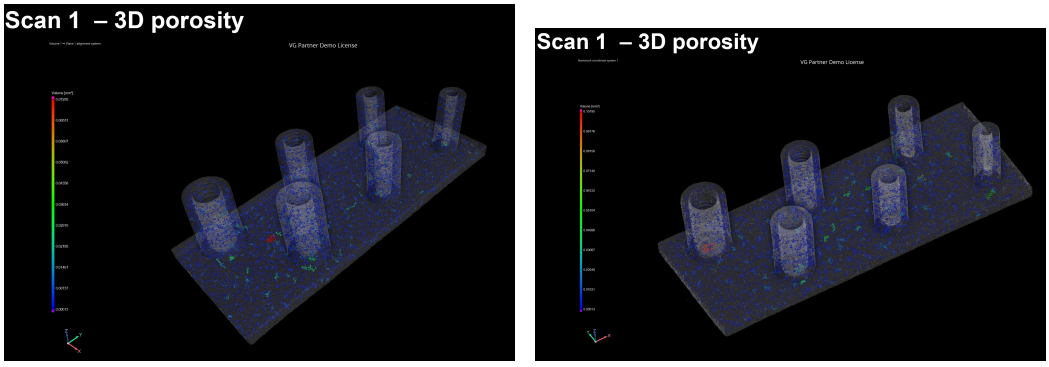

(a) (b)

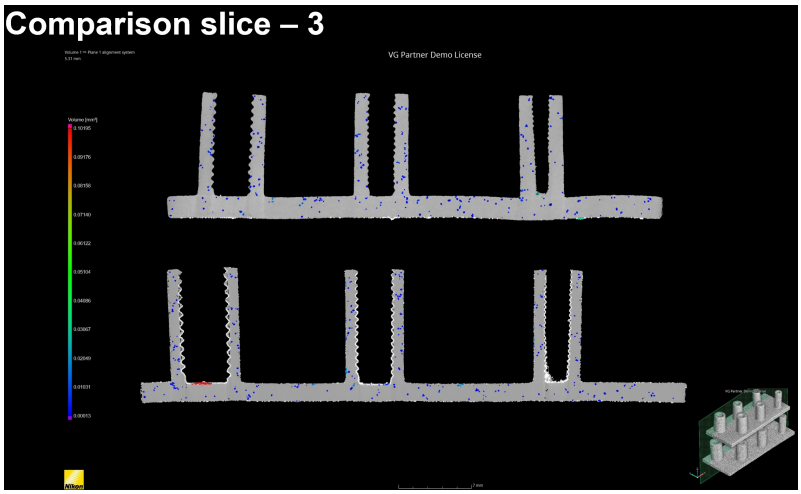

(c)

Figure 4.21: X-ray CT scanning for threads(artefact 1A and 1B). 4.21a refers to without ceramic support and 4.21b refers to with ceramic support

4.6 LOM analysis for as-cast, as-sintered, and HIPed samples

4.6.1 LOM analysis for as-cast Al-12Si-Cu1

The micrograph for the high-pressure die casting Al-Si12-Cu1 is given in 4.22. Silicon has a very low solubility in aluminum; as a result, it precipitates as nearly pure silicon, which is brittle and increases abrasion resistance. The eutectic temperature of aluminum-silicon alloys is 577°C at 11.7 wt% silicon. Due to its lowest potential melting temperature, this is a typical composition for a casting alloy. Consequently, Al-12Si alloys are pretty common. Silicon's low density (2.34 g/cm^3) may be advantageous when attempting to reduce the overall weight of the cast component.

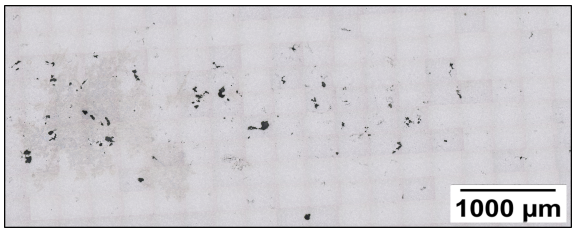

Figure 4.22: As-cast AlSi12CU1 Optical Micrograph

Pores in Al-Si12-Cu1 die-casted series alloy originates from either processing or chemical composition [65]. This was evident in the paper published by [66]. When the Cu content is above 0.2%, the increasing occurrence of the porosity becomes evident and it tends to get larger as the Cu content gets increased, which is in this case 1%. Gas porosity [65] and shrinkage porosity [67] is the two common irregularities that are initiated through a nonoptimized casting route. In the case of high pressure die-casted aluminum alloy sample, it can be seen from figure 4.22 there are larger pores that are surrounded by smaller pores. When the pores have an aspect ratio less than 0.4, it is assumed to be shrinkage porosity. On the other side, when higher than 0.4, it is regarded as gas porosity. Gas porosity, for this reason, is typically circular and bigger than shrinkage porosity, which can be seen in the figure 3.15.

Once the solidification of the alloy progresses, any excess hydrogen, not soluble in the solid and not able to escape the solidified section, will form porosity within the casting, reducing its properties [68]. If the die cavity filling is not in a steady state, additional pores will appear in the casting, an effect that is common in the HPDC process.

4.6.2 LOM analysis for as-sintered aluminum 4000 series alloy

As-produced samples, whether HIPed or not, have three distinct cross-sectional plans (XY, YZ, and YZ). Thus, each sample set's cross-section planes (XY, XZ, YZ) were analyzed. During metallographic preparation (i.e., cutting, grinding, and polishing), it is possible for cross-sections to deviate slightly from an ideal orthogonal plane. figure 4.23 depicts these CAD geometry cross-sections with a small, arbitrary inclination angle for illustrative purposes for as-produced samples with or without HIP. It should be noted that the red stripes are only for illustrative purposes, and not to be confused with building height, as the building height is in the z-direction from the XY plane, as discussed before.

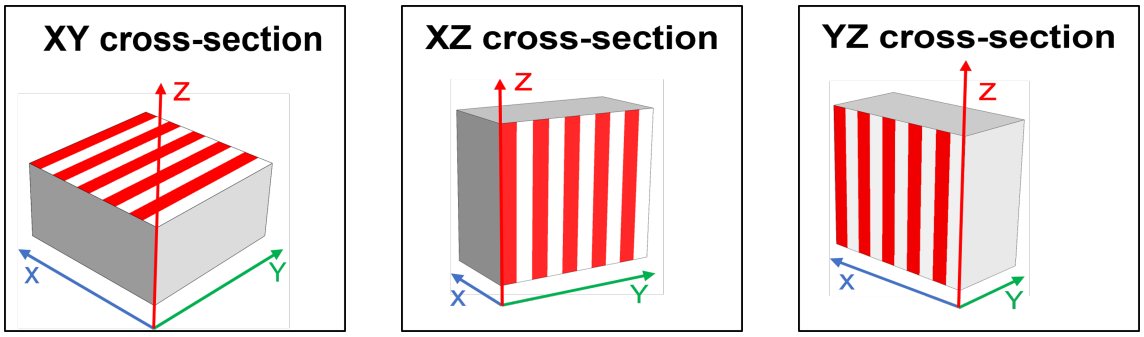

(a) XY cross-section (b) XZ cross-section (c) YZ cross-section

Figure 4.23: CAD cross-section

In the case of as-sintered aluminum 4000 series alloy, Si is mainly precipitated in plate form in the α-Al matrix and the grain boundaries. However, compared to as-cast Al-12Si-Cu1 alloy, the amount of plate-like Si is less, which can be detrimental to defining mechanical and thermal performance. Similarities of plates like Si can be found in different cross-section planes, such as XY, XZ, and YZ, as depicted in figure 4.24.

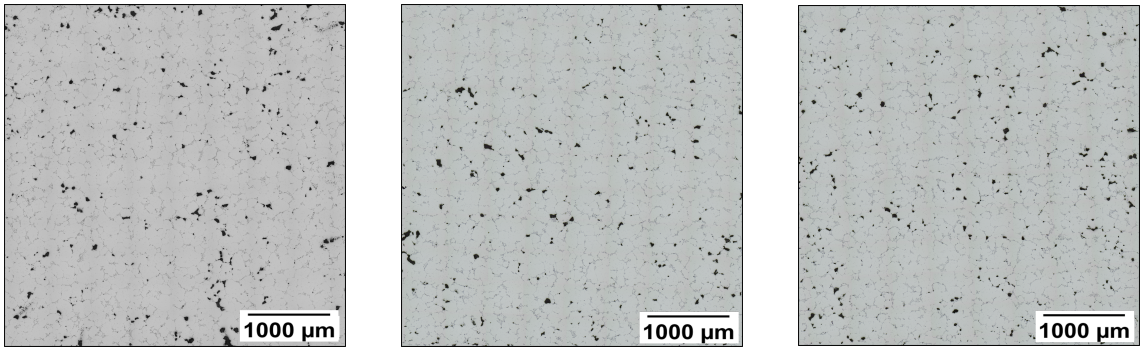

(a) As-sintered aluminum 4000 series alloy for XY orientation (b) As-sintered aluminum 4000 series alloy for XZ orientation (c) As-sintered aluminum 4000 series alloy for YZ orientation

Figure 4.24: Optical micrographs for as-sintered aluminum 4000 series alloy for XY, XZ, and YZ orientation

As-sintered sample at 600 °C exhibited a combination of large, irregularly shaped, and quasi-spherical pores as shown in figure 4.25. Pores are situated mainly in the triple particle boundaries. In the case of the cross-section plane, XY, the pores are homogeneously distributed. However, in the case of the cross-section plan, XZ, and YZ, the pores are not homogeneously distributed. This is most likely attributable to the interlayer porosity formed during printing, where large pores are typically observed between layers [1].
In general, all three cross-sections of sintered samples have larger pores that appear to be aligned in specific areas along an arbitrary direction. Several larger pores were observed in the XZ and YZ cross-sections, aligned preferentially in the horizontal

direction (building plane), whereas there was no preferential orientation in the XY plane [1].

This effect may be related to the previously discussed sample characterization procedure [1]. Therefore, the porosity distribution observed in XY cross-sections would be caused by concentrations of larger pores located within periodic planes along Z (building direction).

4.6.3 LOM analysis for HIPed aluminum 4000 series alloy

In the case of HIPed aluminum 4000 series alloy, it can be seen in figure 4.25, the plate-like structure has been converted in the sphere. However, it's not fully spherodized resulting in some parts of the microstructure still retaining plate-like morphology for Si precipitates.

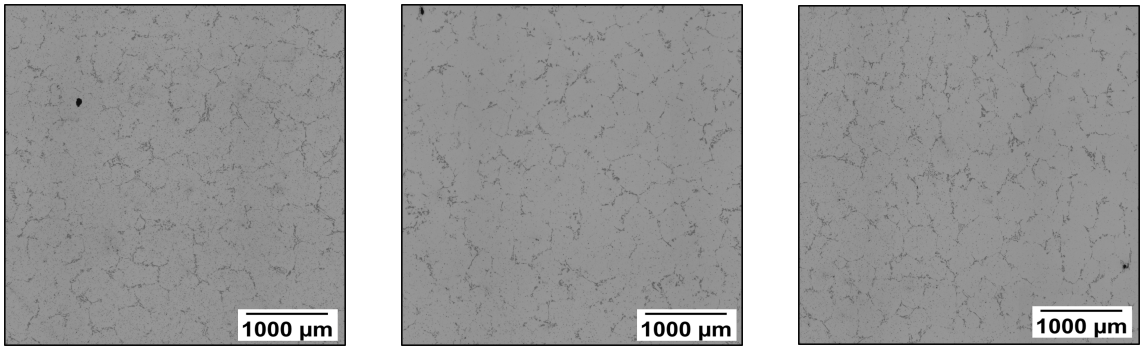

(a) HIPed aluminum 4000 series alloy XY

(b) HIPed aluminum 4000 series alloy XZ

(c) HIPed aluminum 4000 series alloy YZ

Figure 4.25: Optical micrographs for HIPed aluminum 4000 series alloy for XY, XZ, and YZ oritentation

In case of HIPed sample, the porosity has been closed almost completely. Hence, some arbitrary large pores can be found after doing the HIPing.

4.7 Mechanical performance

4.7.1 Hardness test

HV 5 and HK 1 were selected for Vickers hardness and Knoop hardness measurement respectively. Based on the measurement, the hardness is almost the same, with a standard deviation of 0.85 for Vickers hardness and a standard deviation of 2.42 for Knoop hardness in all orientations for sintered material. However, the hardness of cast material shows higher hardness. Regarding the post-processed part using HIP, the hardness remains the same as the as-sintered material.

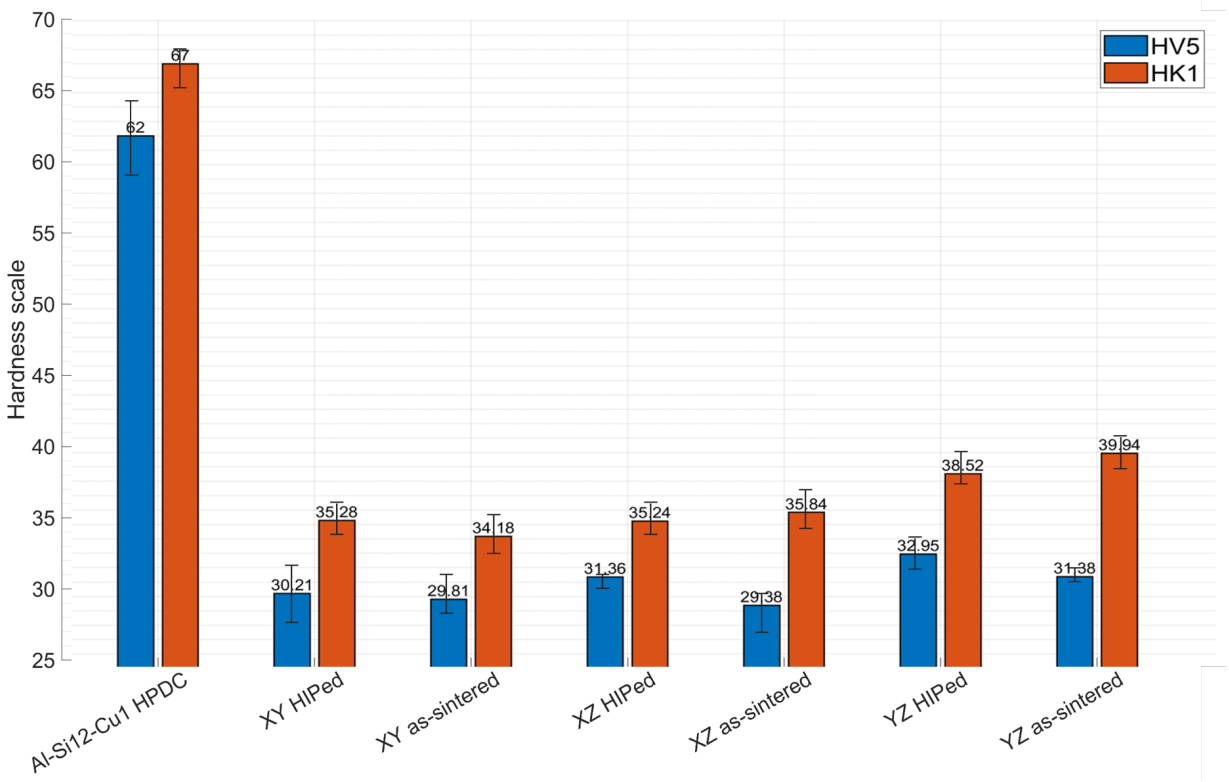

Figure 4.26: Vickers Hardenss and Knoops Hardness of studied materials

A graphical comparison between Vickers hardness with 5Kgf load and Knoop hardness with 1gf load is given in figure 4.26. The hardness of the aluminum 4000 series alloy material was found to be 31 HV5 and 37 HK1 on average, with five indentations for every orientation. As discussed above, the hardness of the HIPed aluminum 4000 series alloy sample remains the same at a standard deviation of 0.25 on average for all planes. On the other hand, in the case of the as-cast Al-Si12-Cu1 part, the hardness is 62 HV5, which is 51.91% higher, and 67 HK1, which is 48.98% higher than the as-sintered part in the case of Vickers hardness and Knoop hardness respectively.

It can be seen from the data that Knoop hardness has a higher value than the Vickers hardness for all the samples. The main reason contributing to the fact is that Knoop hardness is mainly used for determining the hardness of thin surfaces or surface coating. In contrast, Vickers hardness is used for determining the bulk hardness.

Si precipitates are regarded as hard crystal structures. Si precipitates have a needle-like morphology. The hardness of the material increases as the weight fraction of Si precipitates increases [69]. Silicon has a very low solubility in aluminum; therefore, it precipitates as virtually pure silicon, which is hard and improves the abrasion resistance [53].

It can be seen from figure 4.22 that the amount of silicon precipitates increases when the as-cast aluminum alloy is used due to much higher Si-content. The high percentage of needle-like Si precipitates improved the hardness of the as-cast aluminum alloy. However, when as-sintered and HIPed samples were used, it showed a

decrease in hardness compared to as-cast aluminum alloy due to the low amount of existence of the Si precipitates, as shown in figure 4.24 and figure 4.25. The main reason for still having the same hardness after the HIPing compared to as-sintered alloys is that HIPing without heat treatment can close out some pores. However, to have the complete spherodization, additional heat treatment is necessary, followed by HIPing.

4.7.2 Thermal conductivity test

In the case of as-cast and as-sintered aluminum alloy, Si is added as the main alloying element. Adding Si as the main alloying element can considerably improve the strength of Al alloys. However, as discussed before, adding different alloying elements can contribute to a decrease in thermal conductivity [3]. The main chemical composition of the as-cast part is Al-Si12-Cu1, whereas, in the case of as-sintered aluminum 4000 series alloy, Si is regarded as the main alloying element. Using LFA measurement, the thermal conductivity was measured. All measurements were carried out in the temperature range between 20°C and 145°C. For each temperature, three shots were taken without any delay. In all cases, three samples of each kind were used for measurements.

As depicted in figure 4.27, when it comes to as-cast aluminum alloy, thermal diffusivity at room temperature (20°C) is 46.59 m^2/s. Thermal diffusivity for the as-cast aluminum alloy shows the highest, 46.71 m^2/s at 95°C, and again, it follows a declining trend after 95°C, stopping at 46.12 m^2/s at 145°C.
In the case of the as-sintered aluminum alloy, thermal diffusivity is highest at room temperature (20°C), which is 73.48 m^2/s and again, it follows a declining trend, stopping at 70.552 m^2/s at 145°C. In the case of the HIPed aluminum alloy, the thermal diffusivity at room temperature (20°C) is 79.25 m^2, which is the highest. Like as-sintered aluminum alloy, it follows a declining trend, stopping at 76.680 m^2/s at 145°C.

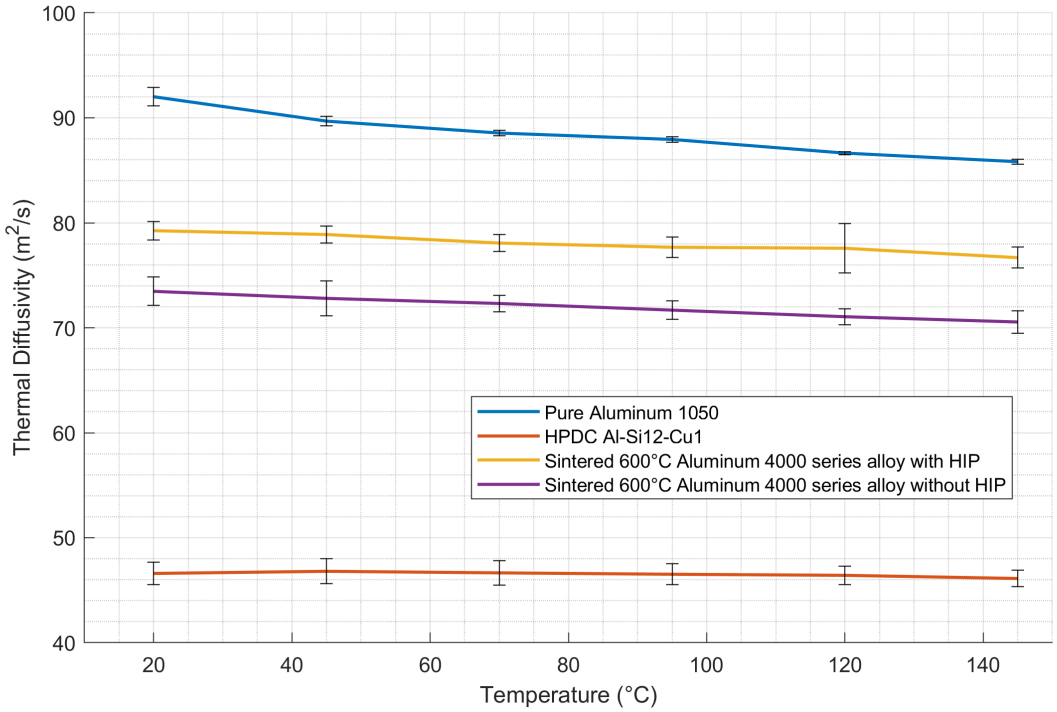

Figure 4.27: Comparison of thermal diffusivity between as-cast Al-Si12-Cu1, as-sintered aluminum 4000 series and HIPed aluminum 4000 series alloy

Regarding thermal conductivity, as depicted in figure 4.28, the average thermal conductivity of as-cast aluminum alloy at ambient temperature (20°C) is 97.94 W/mK. Thermal conductivity for the as-cast alloy shows the highest, 106.46 W/mK at 120°C, and again, it follows a declining trend after 120°C, stopping at 103.45 W/mK at 145°C.
In the case of the as-sintered aluminum alloy, the thermal conductivity at room temperature (20°C) is 154.41 W/mK. In contrast, it reaches its maximum, 163.96 W/mK, at 120°C, then decreases until it reaches 158.29 W/mK at 145°C. In the case of HIPed aluminum alloy, the thermal conductivity at room temperature (20°C) is 166.68 W/mK, reaching its maximal value at 120°C, which is 178.91 W/mK before decreasing to 172.041 W/mK at 145°C.
During the comparison between as-cast aluminum alloy and as-sintered aluminum alloy, in any case, the thermal conductivity is always higher for as-sintered aluminum alloy compared to as-cast aluminum alloy. Both show the highest thermal conductivity at 120°C, followed by a declining trend. The thermal conductivity of the as-sintered sample was improved up to 60% compared to the as-casted sample.

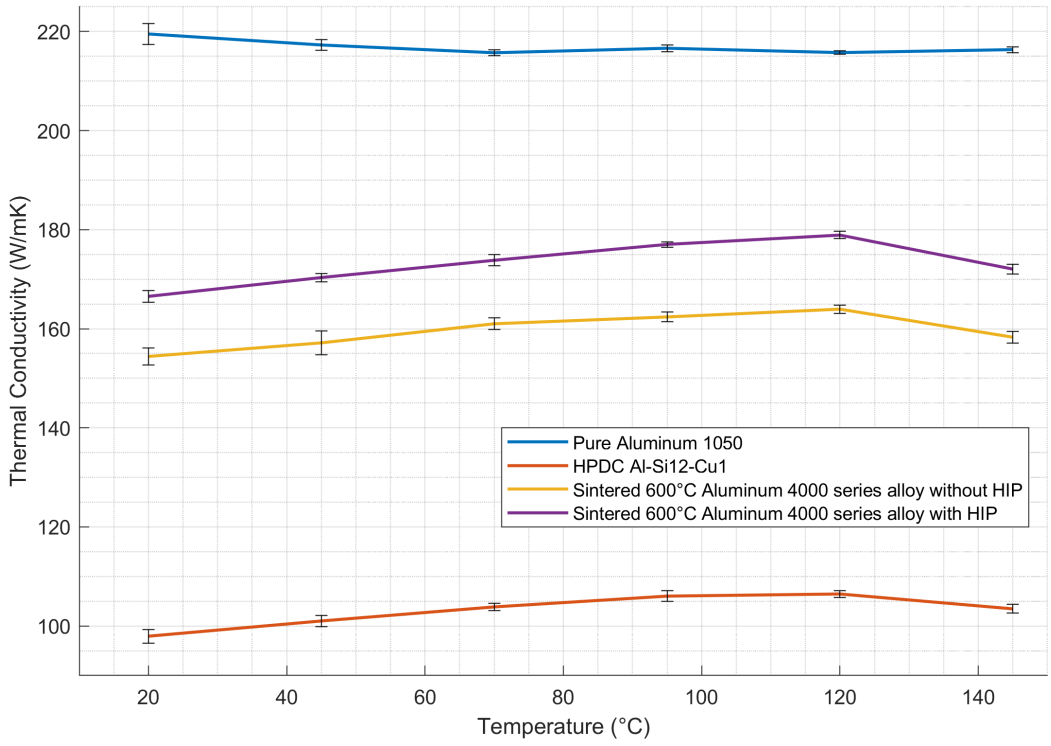

Figure 4.28: Comparison of thermal conductivity between as-cast Al-Si12-Cu1, as-sintered aluminum 4000 series and HIPed aluminum 4000 series alloy

However, while comparing the effect of HIPing with both as-cast and as-sintered aluminum alloy, it can be seen that HIP can, not only close out of pores but it can also increase the thermal conductivity up to 8% compared to as-sintered aluminum 4000 series alloy and up to 83% compared to as-cast Al-Si12-Cu1. The thermal conductivity is the highest at 120°C, which is 178.91 W/mK for HIPed sample. After 120°C, the thermal conductivity of the HIPed sample again decreased. Pure aluminum 1050 is used as a reference point for both thermal conductivity and thermal diffusivity.

The size and shape of alloying elements play an important role in determining the thermal conductivity [27]. As shown in figure 4.29, Si is mainly precipitated in plate form [3]. The main solubility of Si in Al-Si is nearly 1.65 wt% at eutectic temperature, and Al is nearly not soluble in Si [3] at room temperature. As discussed before, since Si precipitates act as an electron barrier and electron transportation is equivalent to thermal conductivity [27], the higher the percentage of Si precipitates present in α-Al matrix, the more barrier it would create for the electron to get transported. As a result, the thermal conductivity will get decreased. Due to this, when the Si coontent is higher in the case of HPDC aluminum alloy, the thermal conductivity gets reduced, but when it comes to as-sintered aluminum alloy which has a Si wt% lower than 10%, compared to HPDC aluminum alloy, the thermal conductivity gets increased upto 41%. By altering the morphology of Si precipitates, thermal conductivity can also be changed. By doing the HIPing, it can be seen that the plate-like morphology of aluminum alloy has been changed to a spherical shape as depicted in figure 4.29 due to the spherodization process. However, since the primary reason for doing the HIP is to close out the pores to densify the material fully, the spherodization needed to be globalized fully, which requires additional heat treatment to get a fully globalized spherodized microstructure to improve the thermal conductivity further.

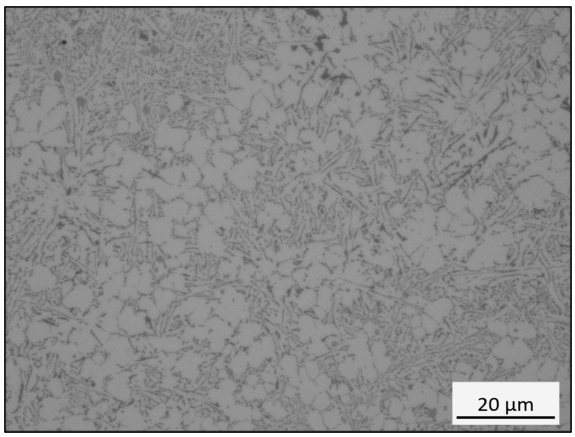

(a) As-cast Al-Si12-Cu1

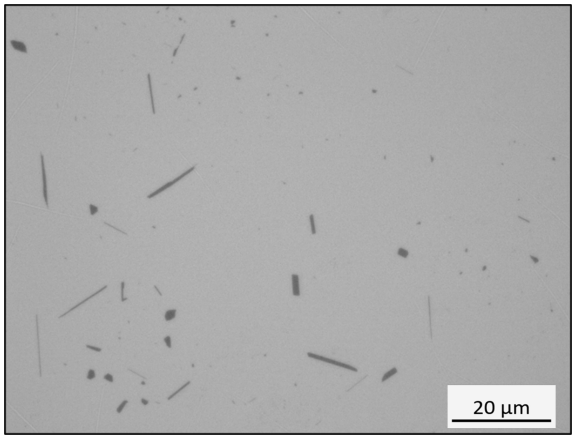

(b) As-sintered aluminum 4000 series alloy

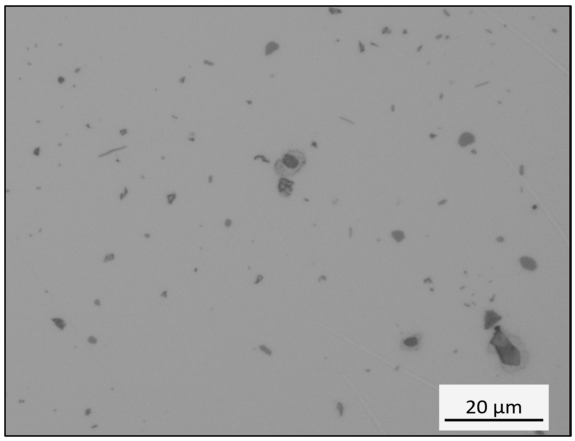

(c) HIPed aluminum 4000 series alloy

Figure 4.29: Optical micrographs between as-cast Al-Si12-Cu1, as-sintered aluminum 4000 series alloy and HIPed aluminum 4000 series alloy

4.7.3 Heat exchange performance test

The data obtained for the power loss for all artefacts in all three setups were analysed. Firstly the performance factor was derived to represent which test piece performs the best. The main objective of the project is to increase the heat dissipation capacity of the heat sink while reducing the weight of the final component. Hence, the performance factor(PF) of power(W) lost per unit mass (gm) was derived. For this purpose, the weight of each test piece was measured in CAD as well as cross-verified on the weighing scale. To visualise the performance at various temperature differences (ΔT) bar graph PF vs ΔT was plotted for all 3 setups. This can be seen in figure 4.30 and 4.31.

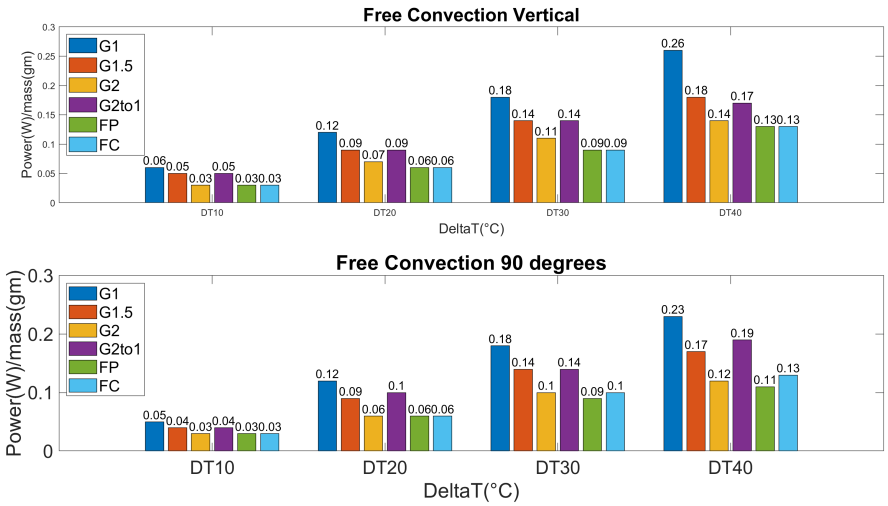

Figure 4.30: Performance(power/mass) graph for all Artefact in two self convection setups

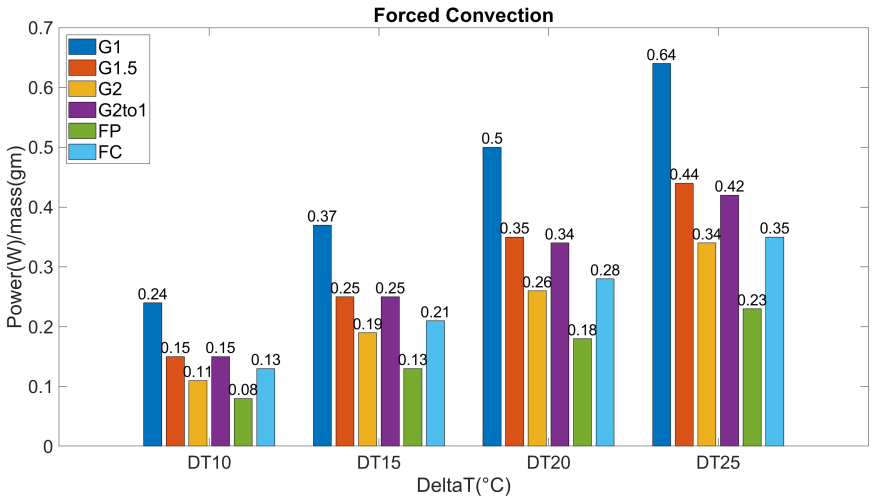

Figure 4.31: Performance(power/mass) graph for all artefact in forced convection setup

From the figure, it can be seen that gyroid 1mm (G1) performs the best in all the setups. In case of the free convection, performance increases significantly with the increase in temperature. These can be attributed to the greater flow of air upwards due to the higher buoyancy effect. In case of the forced convection as well G1 performed the best. While there was a significant in the performance of the casted fins at the same time. As a result of this relative increase in performance from free to forced convection was calculated and plotted onto the bar graph. The relative increase in the performance can be seen in the figure 4.32.

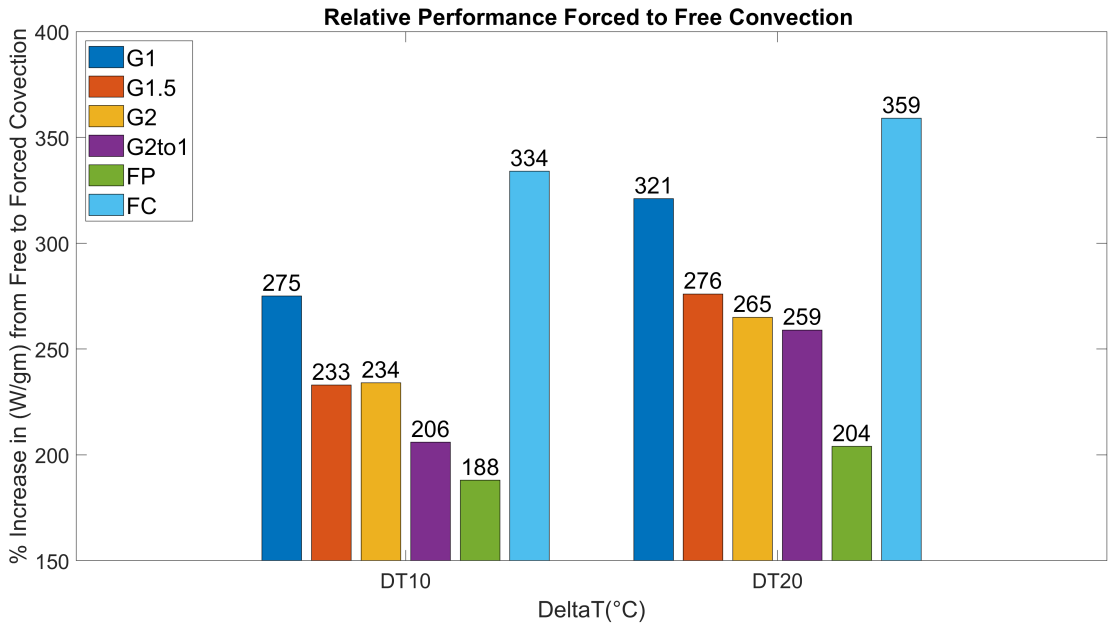

Figure 4.32: performance increase in percentage from free to forced convection

Since the same ΔT for both forced and free was only available at $\Delta T10\&20$ the comparative study was only done at these two temperature differences. The comparison was done between the free convection and forced convection for vertical setup only due to similarity in the setup and the free convection in horizontal was left out. From the evaluation, it can be seen that casted fins have the best improvement in forced setup compared to the free setup. While G1 also comes close second with a performance increase of 275% at $\Delta T = 10$ and 321% $\Delta T = 20$ in comparison to fins which was an increase of 334% and 359% respectively. More improvement at higher temperatures can be affiliated to the fact that the heat transfer coefficient increases with the increase in temperature difference [36].

4.8 Printing final design

The last stage in the project was to proceed with printing the final design. The idea behind the printing was to understand how this technology handles the printing of highly complex shapes of real-world application parts like Volvo Car Corporation's design for heatsink of XC90 as well as print the component that had better functionality than the existing one. The final design was driven by the knowledge gained from the various studies conducted previously in the project. The main change in the design was replacing the fins from the original design with the gyroid structures having the same enclosure volume as the fins. The gyroid thickness of 1mm was chosen this was based on the results from the heat exchange performance study in section 4.7.3. From the test print design for the gyroids, it was observed that these features when produced with sharp edges could be dangerous to handle, hence the boundary defining the shape of the gyroid in the final design was covered with a thin welt of 1mm, this help avoid the sharp edges in the final design. As per research conducted it was understood that the minimum thickness which can be cast using the HPDC is around 3mm. This was evident in the base section of the heat sink which houses the PCB and the rubber gasket seal. But with this technology, it is possible to print the lower thicknesses as already tested by most of the design artefacts produced previously. Since the other objective was to reduce the weight of the component therefore thickness of the base plate was reduced to 2mm while keeping the features on the baseplate housing the other components the same.

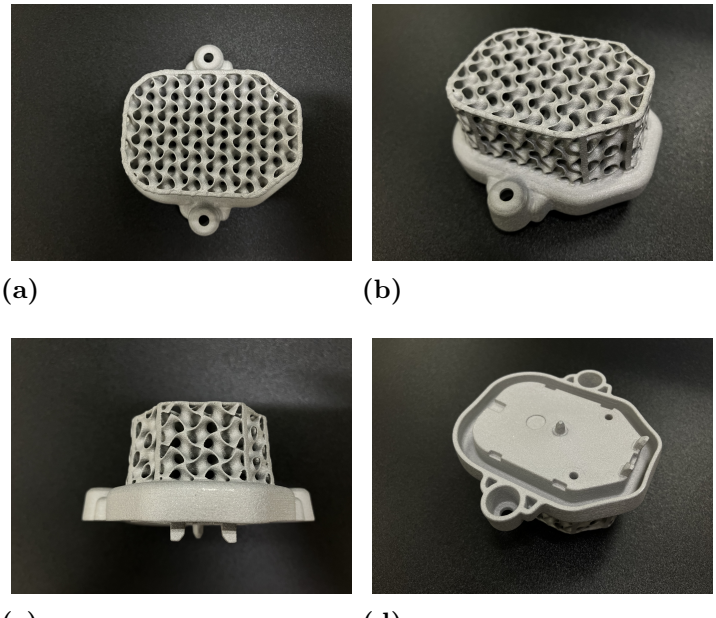

Figure 4.33: Shows the various views of the heatsink produced by BJT/M

Weight comparisons between the new and old heat sinks in the nTopology software showed a significant reduction in the weight from 167 gms to 97 gms which accounts for a 42% weight reduction. Considering there are two of these heatsinks in the

headlamp of XC 90. This meant that there was a total reduction in the weight by 140 gm per headlamp assembly. Furthermore based on the calculations developed during the previous studies it can be claimed that heat dissipated per unit mass increased 99% in free convection while 82% in forced convection.
It is also important to note that although there are several improvements compared to the existing design the produced component can't be still considered as optimised for the application based on predefined functional requirements. For this purpose, a detailed study needs to be done from this perspective.

4.8.1 Evaluating of the heatsink produced by BJT/M

In order to understand the geometrical deviations on the produced heatsink. The approach used for this was similar to that mentioned in the section3.4, wherein the printed part was scanned and then the mesh generated was superimposed on the nominal CAD data in the geometry inspection software and then deviations were compared using the heatmap data.
It was observed that the component was produced with relatively okay tolerances in most places, but in some of the areas, there were deviations as large as $+2mm$. This can be seen in the figure 4.34a. Maximum deviation was observed in the slot where the rubber gusset fit. Additionally, there was an angular deviation of around 2° in the gyroid cooling structure on the top, this was similar to the test pieces of gyroids produced previously, which emphasizes the point of proving angular compensations in these hollow features to prevent internal collapsing of such features. Detailed report for surface deviation can be found in Appendix B.

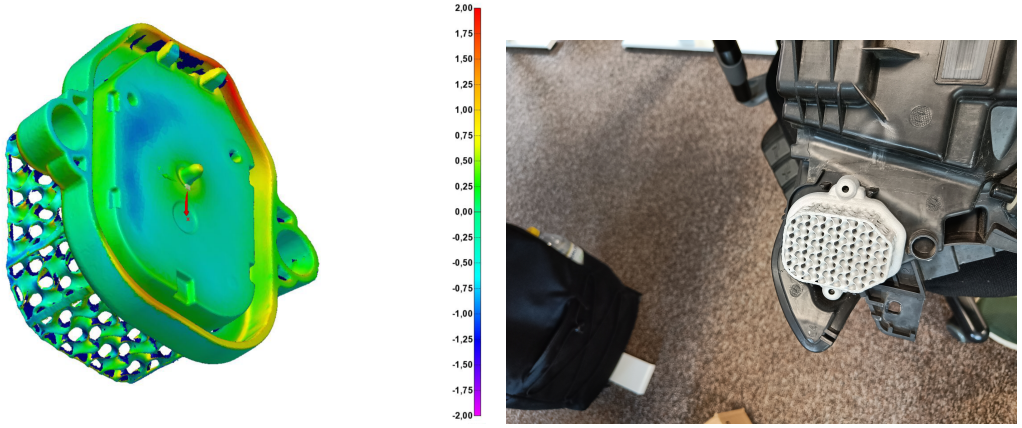

(a) **(b)**

Figure 4.34: Evaluation of the new heatsink.4.34a: Shows the surface deviations using the heatmap. 4.34b: Shows the heatsink assembled on headlamp

Furthermore, in a simple assembly, the produced part was located on the headlamp assembly to see if it could be located on the headlamp by locating the two de-bosses on it. produced heatsink assembled with ease onto the headlamp as can be seen in figure 4.34b.
More evaluations on these parts need to be conducted to understand various aspects of this produced outcome. Material characterization, material microstructure, and

mechanical performance tests can be a few of the evaluations, along with the complete assembly of other components like PCB, rubber gusset, and screws onto the heatsink.

5
Conclusions

In this chapter, we attempted to answer the research questions formulated in the above chapter 1.2. This was done based on the work done in this project and the knowledge gained from it. Furthermore, this chapter discusses all the delimitations encountered in this project.

5.1 Answering the research question

RQ1: How to design for selected application using the technology of BJT/M for aluminum alloys?

- The Design process varies depending upon the process chosen with ceramic or without ceramic support. When using the conventional sintering process designed guidelines mentioned in the Theory chapter can be used with adaptation based on the shape of the component. The design then needs to compensate for shrinkage and deformation. This can be done manually using the shrinkage values in X, Y and Z for the cubes and compensating in the opposite direction for deformation. For shapes like gyroids angular compensation of 2 degrees externally needs to be provided to prevent collapsing internally due to frictional deformation. While for features without the baseplate, higher compensation is required to prevent frictional deformation. Another way to compensate for all this would be by using the module for BJT of Al-alloys in Simufact software when it is commercially available. With the ceramic-supported sintering process, more studies need to be done. Both shrinkage and deformation differ in this process. Shrinkage was found to be lower than the normal process as well the effect of gravity on deformation was very less to neglected as ceramic media supported the hanging features and prevented them them sagging.

RQ2:What are the thermal and mechanical properties of Al-alloys produced by the BJT/M process?

- Material properties are understood from the application point of view. For this thesis, the primary targeted function was to improve the thermal conductivity which is directly connected to material performance. The effect of different alloying elements and the existence of porosity can have a detrimental effect on the thermal conductivity of the material. For this thesis, the used sintered alloy was aluminum alloy with Si as the main alloying element and the given high pressure die casted alloy from the production series model XC90 from VCC was aluminum with 12w% Si and 1wt% Cu as the secondary alloying

element. Due to the decreasing weight fraction of Si precipitates, the electron transportation increased which resulted in higher thermal conductivity up to 60% compared to the as-casted part. The thermal conductivity was further improved by doing post-processing known as Hot isostatic pressing. Due to partial spheroidization of the microstructure and the reduction of the pores and their size, the thermal conductivity was improved up to 83% compared to as-casted. The mechanical properties of the material can also be understood by looking through the microstructure. Since the weight fraction of Si is lower for the as-sintered part than the casted part, it resulted in a decrease in hardness. HV5 was found to be 51.91% less for as-sintered aluminum alloy compared to as-casted aluminum alloy and 48.98% less for as-sintered aluminum alloy when HK1 was considered. Hot isostatic pressing didn't change the hardness due to partial spheroidization.

RQ3:What does the design methodology look like in the different process steps compared to the existing technology in BJT/M?

- There are two major changes in the process steps when using ceramic filling as support material. The first change entailed is in the design process as design compensation needs to follow the rules that are applicable to this process i.e. different shrinkage and deformation. An additional step is added before sintering: manually preparing the metal box by placing the printed part and filling ceramic powder around the part. Hence, productivity also needs to be investigated. Sintering and debinding were performed in a vacuum environment instead of an inert gas such as Ar or N_2 for other alloys such as SS316L [1]. The vacuum environment can be replaced with inert gas such as N_2 and Ar which can result in increased or decreased densification and change in productivity. However, that, too, needs to be investigated by using different atmospheres.

RQ4:Does the produced application add any new features, improvements, performance, or other values to consider?

- This question can be better answered from the target application or component point of view. In this case that is a heat sink. The main function of the heatsink is to dissipate heat away from other components. Dissipation increased by 99% in free convection and 82% in forced convection compared to the existing heatsink. This is partly because of design freedom and partly because of improved material characteristics. Gyroid printing results in a significantly higher surface area for cooling while the material used in printing has higher thermal conductivity which was even increased further after post-processing which is due to the lower weight fraction of Si precipitates. Another improvement was with respect to weight saved for a component in the car, there was a 42% decrease in the weight of the new heatsink. This can indirectly lead to many added values in the Car such as less drag, higher mileage efficiency etc. These indirect benefits increased manyfold depending upon how many such heat sinks go in a car. This can be investigated in other studies to quantify them.

5.2 Limitations

It is very essential to understand the limitations of the project to access the quality of the work. In this project, a few limitations determined the final outcome of the project.
This project was strictly time-bound from the beginning. And needed to be finished in 8 months. This determined the scope of the work undertaken in the thesis. This technology of aluminum printing in BJT/M is quite novel. There are not any industrialized printers for aluminum while there are a few organizations and academia working with this technology. There are not many published works in this field. Since this was a master thesis project the budget was accordingly set both at VCC and Chalmers. This resulted in a limited number of printed as well as limited mechanical testing, material characterization, and design evaluation studies. Due to the confidentiality associated with the RICOH's business, some aspects were not disclosed in this project. These are key aspects for RICOH to develop its technology further and commercialize. Hence, it was mutually agreed to proceed without these things. While, at the same time, these could have helped in certain ways in this project. For example, the parameters used for sintering simulation as well as the final scaling factor determined by the Simufact software were not revealed, This would have helped in better evaluation of the simulation progress. Material composition was not revealed which could have resulted in understanding the microstructure in finer details for example, the use of Sr can result in finer precipitates of Si which can add more understanding of thermal conductivity at a deeper level. Developing debinding and sintering parameters using thermal analysis such as TGA, DSC, and DIL on the green body was not allowed as process parameters are not supposed to be disclosed publicly in a descriptive way. However, developing the process parameters adjusted for the main targeted function could have resulted in improved thermal conductivity.

5.3 Future work

Due to various delimitations, certain things were not explored during this project as well and the knowledge gained from the project called for more work on some aspects of the technology. Future work that needs to take place as a continuation of this project is presented in two sections. One is from the technology point of view another is from the application point of view.

Technology is currently under development as understood during various discussions during this project with RICOH. While we in this project could only carry out limited material characterization studies. Hence, further studies are recommended such as SEM as well as etching needs to be done in order to fully understand the microstructure. Heat treatment is also needed to be carried out which can be followed by HIP to understand the full spheroidization and how it will affect the mechanical performance. A lot more study needs to be conducted to better understand the design guidelines for both ceramic-supported sintering and conventional sintering

processes. This will require more produced artefacts in both processes and their further evaluation. Post-processing, such as heat treatment, also needs to be done in order to assess the change in thermal conductivity.

Application targeted in this project was heatsink. More focus was from a technology point of view and how it provided better results. In order to achieve the best results for this particular application, one needs to start by understanding the various requirements of the parts. These can come from various domains as well. One of them will be to understand the structural requirements of the component. As only hardness was done for this thesis, the tensile test also needed to be done in order to understand the tensile strength, ductility, and yield strength of the material. Furthermore, a CFD study is also recommended along with sensitivity analysis to understand which parameters affect the performance of heat dissipation the most. Then this can be optimized and applied to the new heatsink design. Life cycle analysis should also be conducted to understand the sustainable aspect of the material.

Bibliography

[1] A. C. Rios, "Experimental study and simulation of sintering of 316l components produced by binder jetting," Ph.D. dissertation, Chalmers University of Technology, 2023.

[2] R. M. German, P. Suri, and S. J. Park, "Review: liquid phase sintering," *Journal of materials science*, vol. 44, no. 1, p. 1–39, 2009. [Online]. Available: http://dx.doi.org/10.1007/s10853-008-3008-0

[3] J. K. Chen, H. Y. Hung, C. F. Wang, and N. K. Tang, "Thermal and electrical conductivity in al–si/cu/fe/mg binary and ternary al alloys," *Journal of materials science*, vol. 50, no. 16, p. 5630–5639, 2015. [Online]. Available: http://dx.doi.org/10.1007/s10853-015-9115-9

[4] Y. Bai and C. B. Williams, "An exploration of binder jetting of copper," *Rapid prototyping journal*, vol. 21, no. 2, p. 177–185, 2015. [Online]. Available: https://www.semanticscholar.org/paper/bdfcba6f67d74ee9081a3d19af07f83eccd4fc80

[5] R. Vasireddi and B. Basu, "Conceptual design of three-dimensional scaffolds of powder-based materials for bone tissue engineering applications," *Rapid prototyping journal*, vol. 21, no. 6, p. 716–724, 2015. [Online]. Available: https://eprints.iisc.ac.in/53384/

[6] 2021. [Online]. Available: https://www.iso.org/standard/69669.html

[7] A. Farzadi, M. Solati-Hashjin, M. Asadi-Eydivand, and N. A. Abu Osman, "Effect of layer thickness and printing orientation on mechanical properties and dimensional accuracy of 3d printed porous samples for bone tissue engineering," *PloS one*, vol. 9, no. 9, p. e108252, 2014. [Online]. Available: http://dx.doi.org/10.1371/journal.pone.0108252

[8] A. Mostafaei, A. M. Elliott, J. E. Barnes, F. Li, W. Tan, C. L. Cramer, P. Nandwana, and M. Chmielus, "Binder jet 3d printing—process parameters, materials, properties, modeling, and challenges," *Progress in materials science*, vol. 119, no. 100707, p. 100707, 2021. [Online]. Available: https://www.sciencedirect.com/science/article/pii/S0079642520300712

[9] "Center for additive and digital advanced production technologies." [Online]. Available: http://apt.mit.edu/am-process-comparisons

[10] G. M. L. and J. W. Halloran, *American Ceramic Society*, vol. 79, no. 10, p. 2601–2608, 10/1996. [Online]. Available: http://chrome-extension://efaidnbmnnnibpcajpcglclefindmkaj/https://www.researchgate.net/profile/John-Halloran-3/publication/279891733_Freeform_Fabrication_of_Ceramics_Via_Stereolithography/

[11] Y. Lee, P. Nandwana, and S. Simunovic, "Powder spreading, densification, and part deformation in binder jetting additive manufacturing," *Progress in additive manufacturing*, vol. 7, no. 1, p. 111–125, 2022. [Online]. Available: http://dx.doi.org/10.1007/s40964-021-00214-1

[12] S. Mirzababaei and S. Pasebani, "A review on binder jet additive manufacturing of 316l stainless steel," *Journal of manufacturing and materials processing*, vol. 3, no. 3, p. 82, 2019. [Online]. Available: https://www.mdpi.com/2504-4494/3/3/82

[13] A. Lores, N. Azurmendi, I. Agote, and E. Zuza, "A review on recent developments in binder jetting metal additive manufacturing: materials and process characteristics," *Powder metallurgy*, vol. 62, no. 5, p. 267–296, 2019. [Online]. Available: http://dx.doi.org/10.1080/00325899.2019.1669299

[14] N. D. Parab, J. E. Barnes, C. Zhao, R. W. Cunningham, K. Fezzaa, A. D. Rollett, and T. Sun, "Real time observation of binder jetting printing process using high-speed x-ray imaging," *Scientific reports*, vol. 9, no. 1, p. 2499, 2019. [Online]. Available: http://dx.doi.org/10.1038/s41598-019-38862-7

[15] T. Chartier, M. Ferrato, and J.-F. Baumard, "Influence of the debinding method on the mechanical properties of plastic formed ceramics," *Journal of the European Ceramic Society*, vol. 15, no. 9, p. 899–903, 1995. [Online]. Available: https://www.sciencedirect.com/science/article/pii/0955221995000594

[16] Y. Wu, R. M. German, D. Blaine, B. Marx, and C. Schlaefer, *Journal of materials science*, vol. 37, no. 17, p. 3573–3583, 2002. [Online]. Available: http://dx.doi.org/10.1023/a:1016532418920

[17] E. Hryha, L. Nyborg, A. Malas, S. Wiberg, and S. Berg, "Carbon control in pm sintering: industrial applications and experience," *Powder metallurgy*, vol. 56, no. 1, p. 5–10, 2013. [Online]. Available: http://dx.doi.org/10.1179/0032589912z.00000000085

[18] N. Lecis, M. Mariani, R. Beltrami, L. Emanuelli, R. Casati, M. Vedani, and A. Molinari, "Effects of process parameters, debinding and sintering on the microstructure of 316l stainless steel produced by binder jetting," *Materials science engineering. A, Structural materials: properties, microstructure and processing*, vol. 828, no. 142108, p. 142108, 2021. [Online]. Available: http://dx.doi.org/10.1016/j.msea.2021.142108

[19] R. M. German, *Sintering Theory and Practice*. Nashville, TN: John Wiley Sons, 1996.

[20] H. Ding, C. Zeng, J. Raush, K. Momeni, and S. Guo, "Developing fused deposition modeling additive manufacturing processing strategies for aluminum alloy 7075: Sample preparation and metallographic characterization," *Materials*, vol. 15, no. 4, p. 1340, 2022. [Online]. Available: http://dx.doi.org/10.3390/ma15041340

[21] S. H. Huo, M. Qian, G. B. Schaffer, and E. Crossin, *Aluminium powder metallurgy*. Elsevier, 2011, p. 655–701.

[22] M. Qian and G. B. Schaffer, *Sintering of aluminium and its alloys*. Elsevier, 2010, p. 291–323.

[23] A. Raza, T. Fiegl, I. Hanif, A. MarkstrÖm, M. Franke, C. Körner, and E. Hryha, "Degradation of alsi10mg powder during laser based powder bed fusion processing," *Materials design*, vol. 198, no. 109358, p. 109358, 2021. [Online]. Available: https://www.sciencedirect.com/science/article/pii/S0264127520308947

[24] R. N. Lumley, T. B. Sercombe, and G. M. Schaffer, "Surface oxide and the role of magnesium during the sintering of aluminum," *Metallurgical and Materials Transactions A*, vol. 30, no. 2, p. 457–463, 1999. [Online]. Available: http://dx.doi.org/10.1007/s11661-999-0335-y

[25] G. B. Schaffer and B. J. Hall, "The influence of the atmosphere on the sintering of aluminum," *Metallurgical and Materials Transactions A*, vol. 33, no. 10, p. 3279–3284, 2002. [Online]. Available: http://dx.doi.org/10.1007/s11661-002-0314-z

[26] F. Stadler, H. Antrekowitsch, W. Fragner, H. Kaufmann, E. R. Pinatel, and P. J. Uggowitzer, "The effect of main alloying elements on the physical properties of al–si foundry alloys," *Materials science engineering. A, Structural materials: properties, microstructure and processing*, vol. 560, p. 481–491, 2013. [Online]. Available: http://dx.doi.org/10.1016/j.msea.2012.09.093

[27] X. Zhang, Y. Zhou, G. Zhong, J. Zhang, Y. Chen, W. Jie, P. Schumacher, and J. Li, "Effects of si and sr elements on solidification microstructure and thermal conductivity of al-si-based alloys," *Journal of materials science*, vol. 57, no. 11, p. 6428–6444, 2022. [Online]. Available: http://dx.doi.org/10.1007/s10853-022-07045-7

[28] Z.-Y. Xiu, G.-Q. Chen, X.-F. Wang, G.-H. Wu, Y.-M. Liu, and W.-S. Yang, "Microstructure and performance of al-si alloy with high si content by high temperature diffusion treatment," *Transactions of the Nonferrous Metals Society of China*, vol. 20, no. 11, p. 2134–2138, 2010. [Online]. Available: http://dx.doi.org/10.1016/s1003-6326(09)60430-1

[29] "Aluminum and aluminum alloys, in asm specially handbook, asm international, metal park, ohio. - references - scientific research publishing." [Online]. Available: https://www.scirp.org/(S(i43dyn45teexjx455qlt3d2q))/reference/ReferencesPapers.aspx?ReferenceID=483115

[30] D. D. Pollock, *Physics of engineering materials*. Old Tappan, NJ: Prentice Hall, 1990.

[31] L. F. Mondolfo, *Aluminum–magnesium, aluminum–manganese alloys*. Elsevier, 1976, p. 806–841.

[32] C.-W. Kim, J.-I. Cho, S.-W. Choi, Y.-C. Kim, and C.-S. Kang, *The effect of alloying elements on thermal conductivity and casting characteristic in high pressure die casting of aluminum alloy*. Cham: Springer International Publishing, 2012, p. 237–242.

[33] K. Wang, W. Li, W. Xu, S. Hou, and S. Hu, "Simultaneous improvement of thermal conductivity and strength for commercial a356 alloy using strontium modification process," *Metals and materials international*, vol. 27, no. 11, p. 4742–4756, 2021. [Online]. Available: http://dx.doi.org/10.1007/s12540-020-00669-x

[34] C. Wen, J. Gan, C. Li, Y. Huang, and J. Du, "Comparative study on relationship between modification of si phase and thermal conductivity of al–7si alloy modified by sr/re/b/sb elements," *International journal of metalcasting*, vol. 15, no. 1, p. 194–205, 2021. [Online]. Available: http://dx.doi.org/10.1007/s40962-020-00436-z

[35] Q. Han, "The role of solutes in grain refinement of hypoeutectic magnesium and aluminum alloys," *Journal of magnesium and alloys*, vol. 10, no. 7, p. 1846–1856, 2022. [Online]. Available: http://dx.doi.org/10.1016/j.jma.2022.01.013

[36] W. contributors, "Heat sink," Feb 2023. [Online]. Available: https://en.wikipedia.org/w/index.php?title=Heat_sink&oldid=1139920127

[37] S. S. Haghighi, H. R. Goshayeshi, and M. R. Safaei, "Natural convection heat transfer enhancement in new designs of plate-fin based heat sinks," *International journal of heat and mass transfer*, vol. 125, p. 640–647, 2018. [Online]. Available: https://www.sciencedirect.com/science/article/pii/S0017931018309165

[38] M. Bahrami, "The basic requirement for heat transfer is the presence of a temperature difference. the temperature difference is the driving force for heat transfer, just as voltage difference for electrical current. the total amount of heat transfer q during a time interval can be determined from:." [Online]. Available: https://www.sfu.ca/~mbahrami/ENSC%20388/Notes/Staedy%20Conduction%20Heat%20Transfer.pdf

[39] M. Baharami, "Natural convection." [Online]. Available: https://www.sfu.ca/~mbahrami/ENSC%20388/Notes/Natural%20Convection.pdf

[40] W. Tang, H. Zhou, Y. Zeng, M. Yan, C. Jiang, P. Yang, Q. Li, Z. Li, J. Fu, Y. Huang, and Y. Zhao, "Analysis on the convective heat transfer process and performance evaluation of triply periodic minimal surface (tpms) based on diamond, gyroid and iwp," *International journal of heat and mass transfer*, vol. 201, no. 123642, p. 123642, 2023. [Online]. Available: https://www.sciencedirect.com/science/article/pii/S0017931022011115

[41] A. B. Varotsis, "What is design for additive manufacturing?" May 2022. [Online]. Available: https://ntopology.com/blog/what-is-design-for-additive-manufacturing/

[42] [Online]. Available: https://www.jabil.com/blog/design-for-additive-manufacturing.html

[43] O. Diegel, A. Nordin, and D. Motte, *A practical guide to design for additive manufacturing*. Singapore: Springer Singapore, 2019.

[44] M. Mani, P. Witherell, and H. Jee, "Design rules for additive manufacturing: A categorization," in *Volume 1: 37th Computers and Information in Engineering Conference*. American Society of Mechanical Engineers, 2017.

[45] E. Hryha, "Additive manufacturing: Overview of am technologies materials, material jetting," 2022.

[46] [Online]. Available: https://digitalmetal.tech/

[47] "design guideline for bjt by xometry," Oct 2020. [Online]. Available: https://www.xometry.com/resources/design-guides/design-guide-binder-jet-metal-3d-printing/

[48] [Online]. Available: https://www.hubs.com/knowledge-base/how-design-parts-binder-jetting-3d-printing/

[49] D. S. Nguyen and F. Vignat, "A method to generate lattice structure for additive manufacturing," in *2016 IEEE International Conference on Industrial Engineering and Engineering Management (IEEM)*. IEEE, 2016, p. 966–970.

[50] [Online]. Available: https://www.materialise.com/en/industrial/software/magics-data-build-preparation

[51] [Online]. Available: https://www.3ds.com/products-services/catia/

[52] [Online]. Available: https://www.ntop.com/

[53] [Online]. Available: https://www.ricoh.co.uk/business-services/all-services/additive-manufacturing-services/

[54] [Online]. Available: https://www.gom.com/en/products/zeiss-quality-suite/gom-inspect-pro?keyword=gom%20inspect&device=c&network=g&gclid=Cj0KCQjwiZqhBhCJARIsACHHEH_SO9bvV_hqKgujCQ7A_7NPg00H7LiDX_j5x5OkcHVdKwwPF01YPQoaAv30EALw_wcB

[55] Nov 2021. [Online]. Available: https://industry.nikon.com/en-us/products/3d-laser-scanners/manual-3d-scanning/modelmaker-h120/

[56] K. Lim, "Vickers hardness testing." [Online]. Available: https://www.struers.com/en/Knowledge/Hardness-testing/Vickers#findoutmore

[57] F. Neidhardt, "When and how must samples be coated during lfa measurements." [Online]. Available: https://analyzing-testing.netzsch.com/en/meta-nav/about-netzsch

[58] S. Feng, F. Li, F. Zhang, and T. J. Lu, "Natural convection in metal foam heat sinks with open slots," *Experimental thermal and fluid science*, vol. 91, p. 354–362, 2018. [Online]. Available: https://www.sciencedirect.com/science/article/pii/S0894177717302066

[59] [Online]. Available: https://www.omega.nl/pptst/KHRA-KHLVA-KHA-SERIES.html

[60] W. Villasmil, L. J. Fischer, and J. Worlitschek, "A review and evaluation of thermal insulation materials and methods for thermal energy storage systems," *Renewable and Sustainable Energy Reviews*, vol. 103, p. 71–84, 2019. [Online]. Available: http://dx.doi.org/10.1016/j.rser.2018.12.040

[61] [Online]. Available: https://www.aluflex.se/

[62] S. Hafenstein, L. Hitzler, E. Sert, A. Öchsner, M. Merkel, and E. Werner, "Hot isostatic pressing of aluminum–silicon alloys fabricated by laser powder-bed fusion," *Technologies*, vol. 8, no. 3, p. 48, 2020. [Online]. Available: https://www.mdpi.com/2227-7080/8/3/48

[63] M. Tocci, A. Pola, M. Gelfi, and G. M. La Vecchia, "Effect of a new high-pressure heat treatment on additively manufactured alsi10mg alloy," *Metallurgical and Materials Transactions A*, vol. 51, no. 9, p. 4799–4811, 2020. [Online]. Available: http://dx.doi.org/10.1007/s11661-020-05905-y

[64] Oct 2021. [Online]. Available: https://industry.nikon.com/en-aom/products/x-ray-ct/xt-h-225-xt-h-320/

[65] M. Zamani, "Al-si cast alloys - microstructure and mechanical properties at ambient and elevated temperature." [Online]. Available: https://www.uobabylon.edu.iq/eprints/publication_11_2133_6172.pdf

[66] C. H. Cáceres, M. B. Djurdjevic, T. J. Stockwell, and J. H. Sokolowski, "The effect of cu content on the level of microporosity in al-si-cu-mg casting alloys," *Scripta materialia*, vol. 40, no. 5, p. 631–637, 1999. [Online]. Available: https://www.sciencedirect.com/science/article/pii/S1359646298004928

[67] Q. Han, *Shrinkage porosity and gas porosity*. ASM International, 2008, p. 370–374.

[68] A. M. Samuel, E. Samuel, V. Songmene, and F. H. Samuel, "A review on porosity formation in aluminum-based alloys," *Materials*, vol. 16, no. 5, 2023. [Online]. Available: http://dx.doi.org/10.3390/ma16052047

[69] G. Hatti, V. H. Vishwanath, and K. R. Dinesh, "Effect of silicon content on

wear and hardness of al-si alloys," *IOP conference series. Materials science and engineering*, vol. 1065, no. 1, p. 012010, 2021. [Online]. Available: http://dx.doi.org/10.1088/1757-899x/1065/1/012010

A

Reports: Design Guideline Evaluations

A.1 Artefact 2A: Pins with conventional sintering Process

3 Prins_Only

Report Author: Anders Odham
Date: 2023-06-22

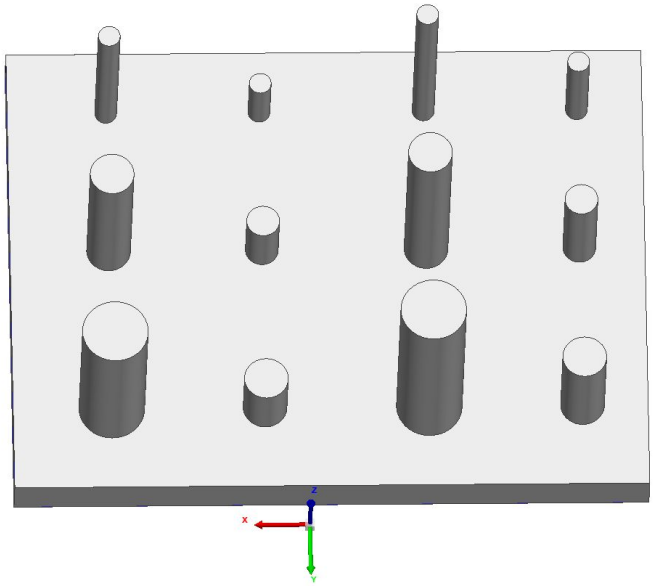

Organization:	Geometry verification center	**Part name:**	3 Prins_Only
Operator:	Anders Odham	**Part number:**	
E-mail:	anders.odhamii@volvocars.com	**Drawing #:**	
Workspace:	Workspace 2	**Serial #:**	
Project:	3_Pins_Only - piece 1	**Device:**	Modelmaker H120 on MCAx

Scanndata = Orang
Nufo = Gray

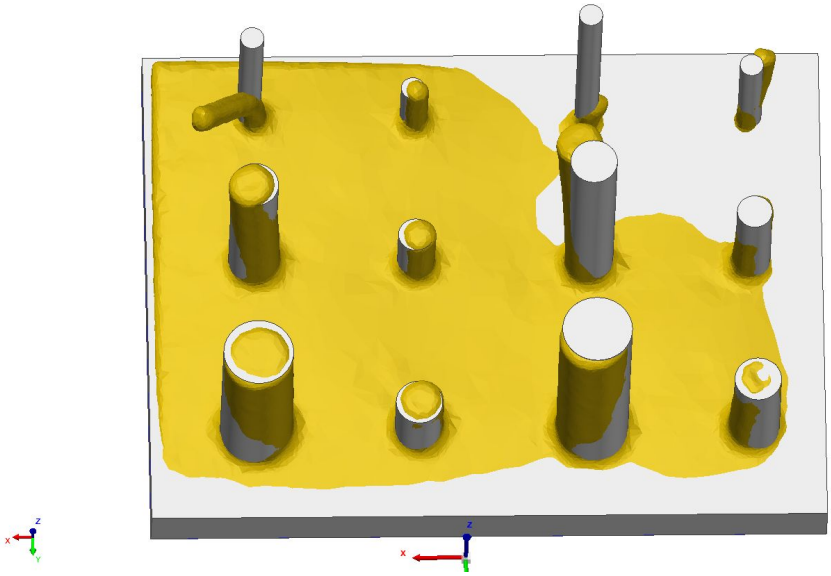

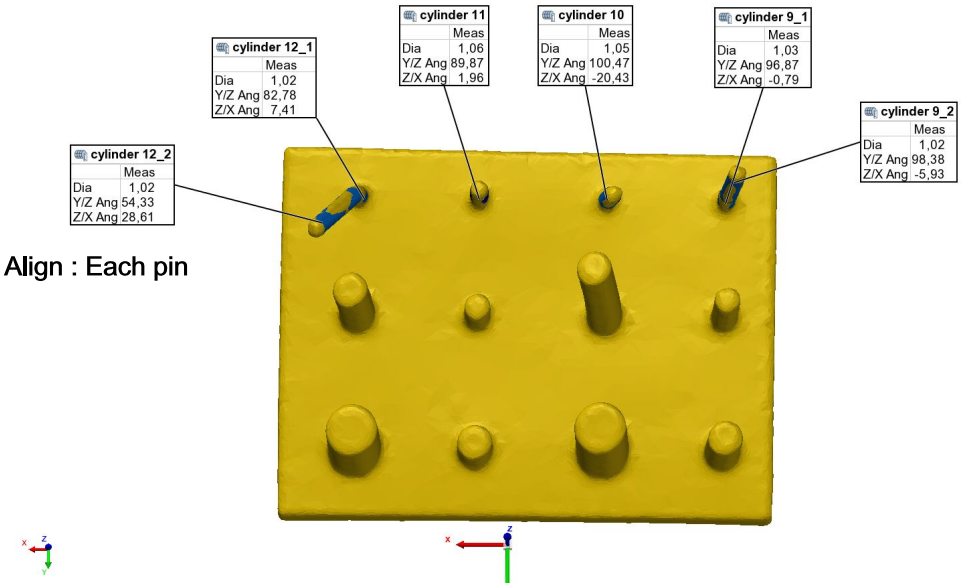

Align : Each pin

Organization:	Geometry verification center	Part name:	3 Prins_Only
Operator:	Anders Odham	Part number:	
E-mail:	anders.odhamii@volvocars.com	Piece:	piece 1

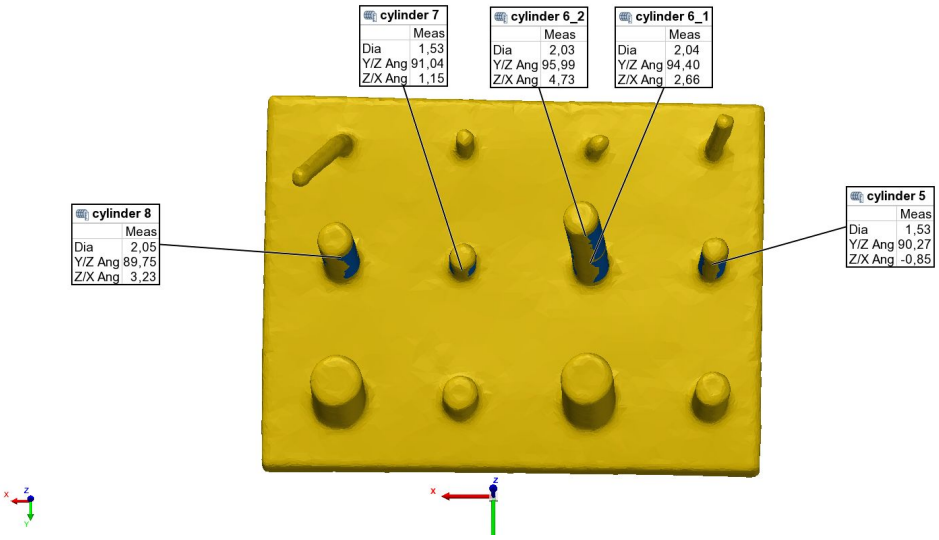

Align : Each pin

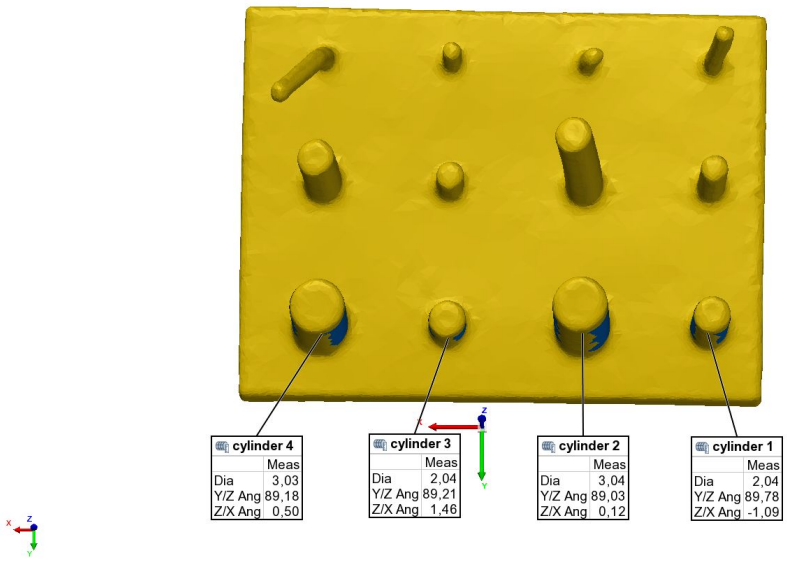

Organization:	Geometry verification center	**Part name:**	3 Prins_Only
Operator:	Anders Odham	**Part number:**	
E-mail:	anders.odhamii@volvocars.com	**Piece:**	piece 1

A.2 Artefact 2B: Pins with ceramic-supported sintering Process

Prins Only

Report Author: Anders Odham
Date: 2023-05-31

Scanndata = Orange
Nufo = Gray

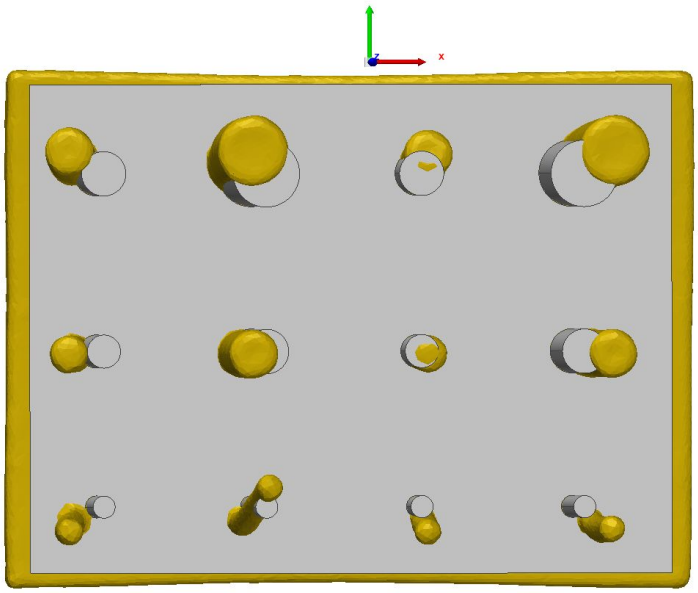

Organization:	Geometry verification center	Part name:	Prins Only
Operator:	Anders Odham	Part number:	
E-mail:	anders.odhamii@volvocars.com	Drawing #:	
Workspace:	Workspace 2	Serial #:	
Project:	NY_Pins_Only - piece 1	Device:	Modelmaker H120 on MCAx

Align: Reference Targets
3-2-1

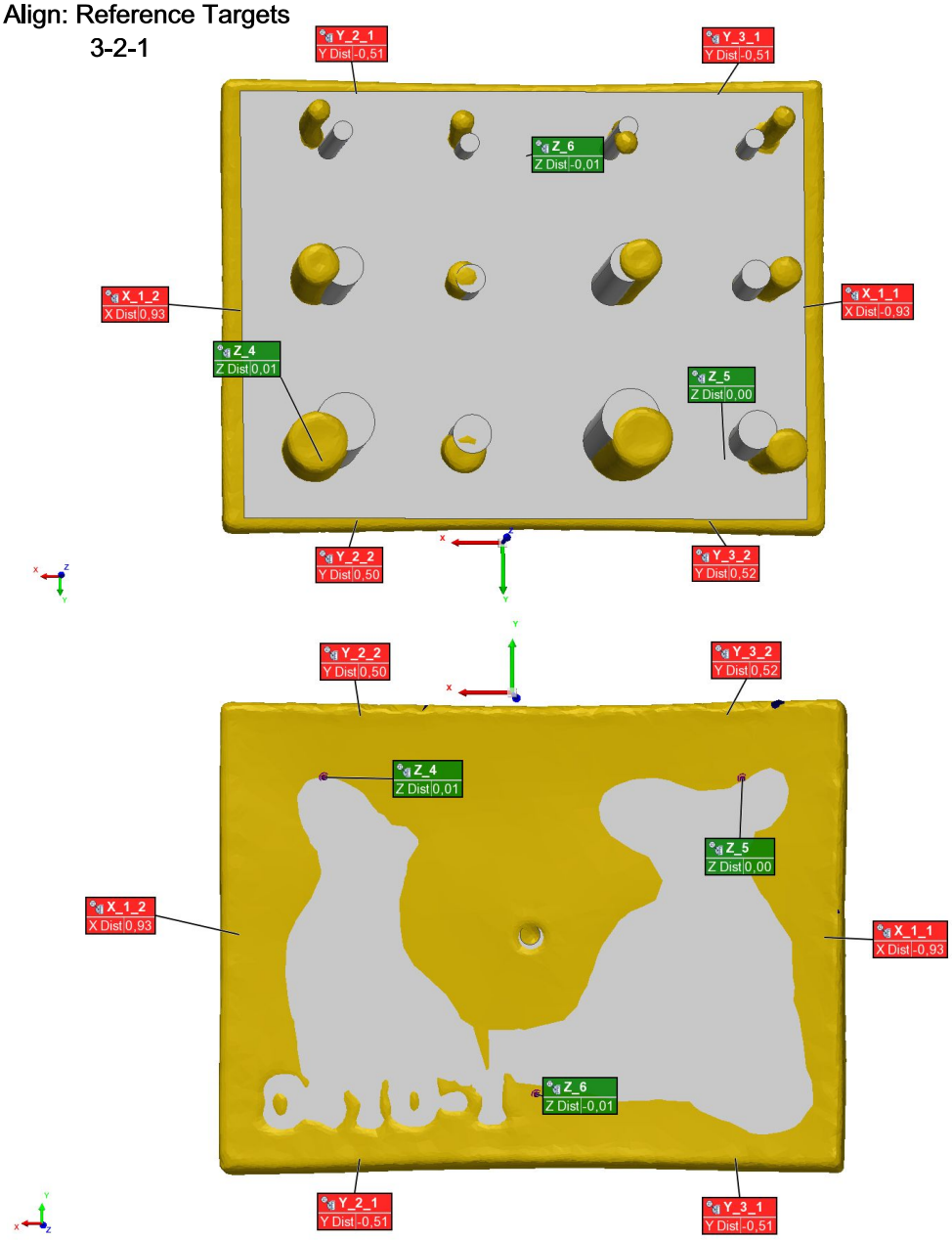

Organization:	Geometry verification center	**Part name:**	Prins Only
Operator:	Anders Odham	**Part number:**	
E-mail:	anders.odhamii@volvocars.com	**Piece:**	piece 1

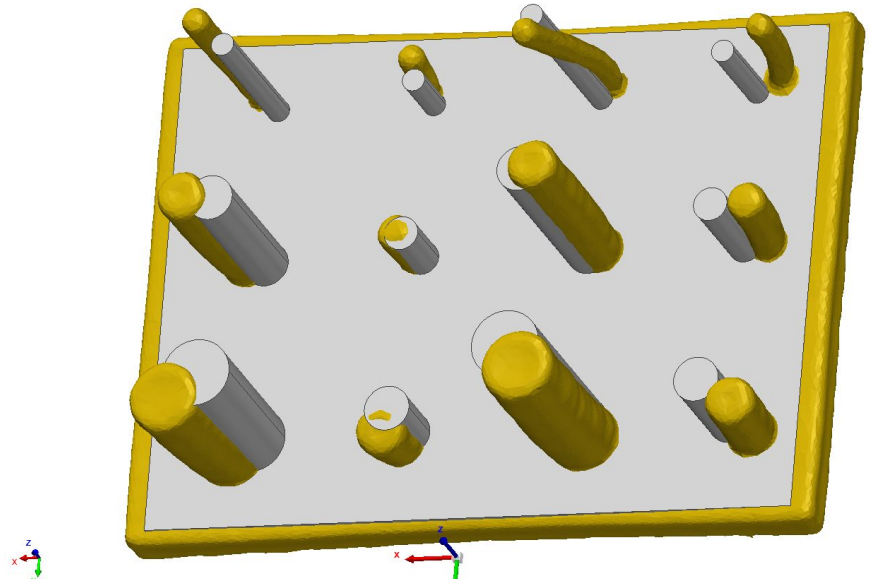

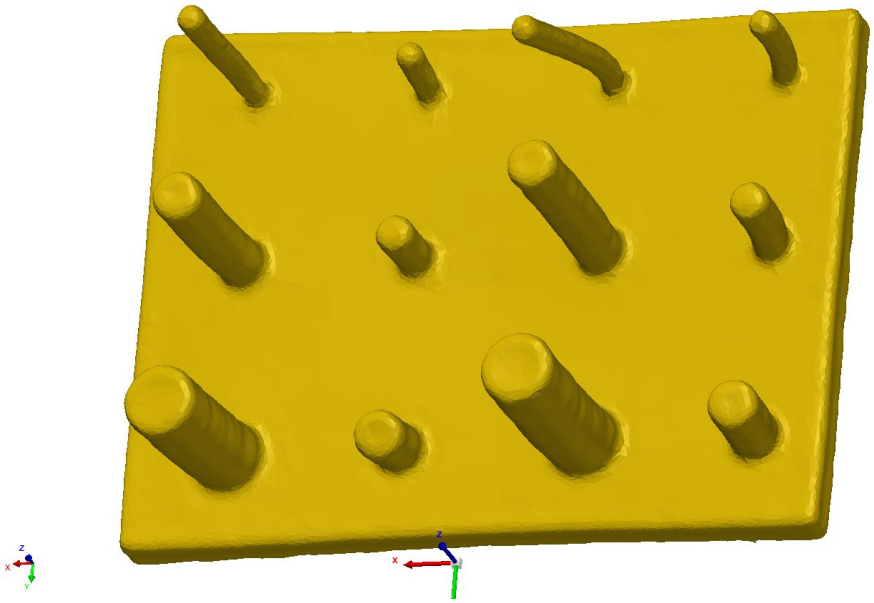

Organization:	Geometry verification center	**Part name:**	Prins Only
Operator:	Anders Odham	**Part number:**	
E-mail:	anders.odhamii@volvocars.com	**Piece:**	piece 1

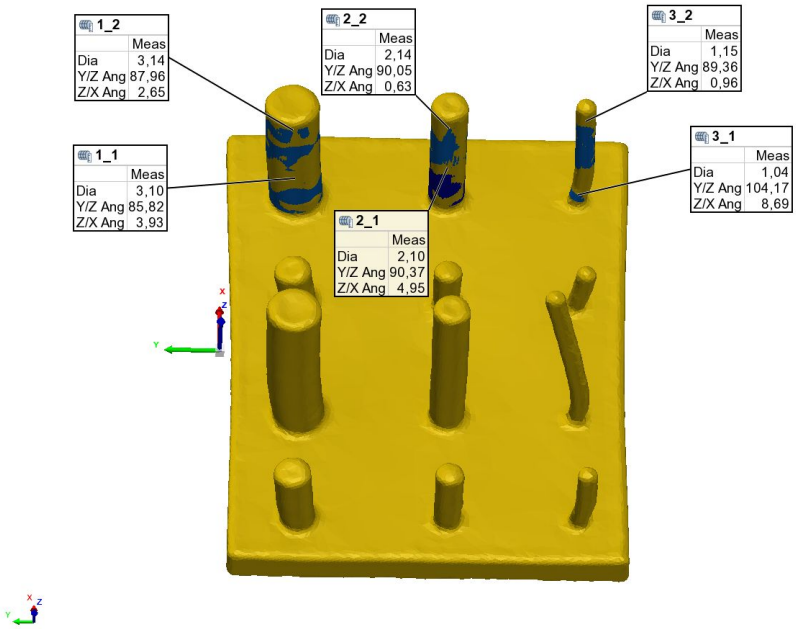

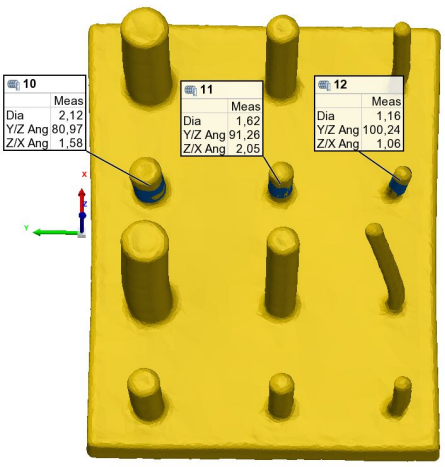

Organization:	Geometry verification center	**Part name:**	Prins Only
Operator:	Anders Odham	**Part number:**	
E-mail:	anders.odhamii@volvocars.com	**Piece:**	piece 1

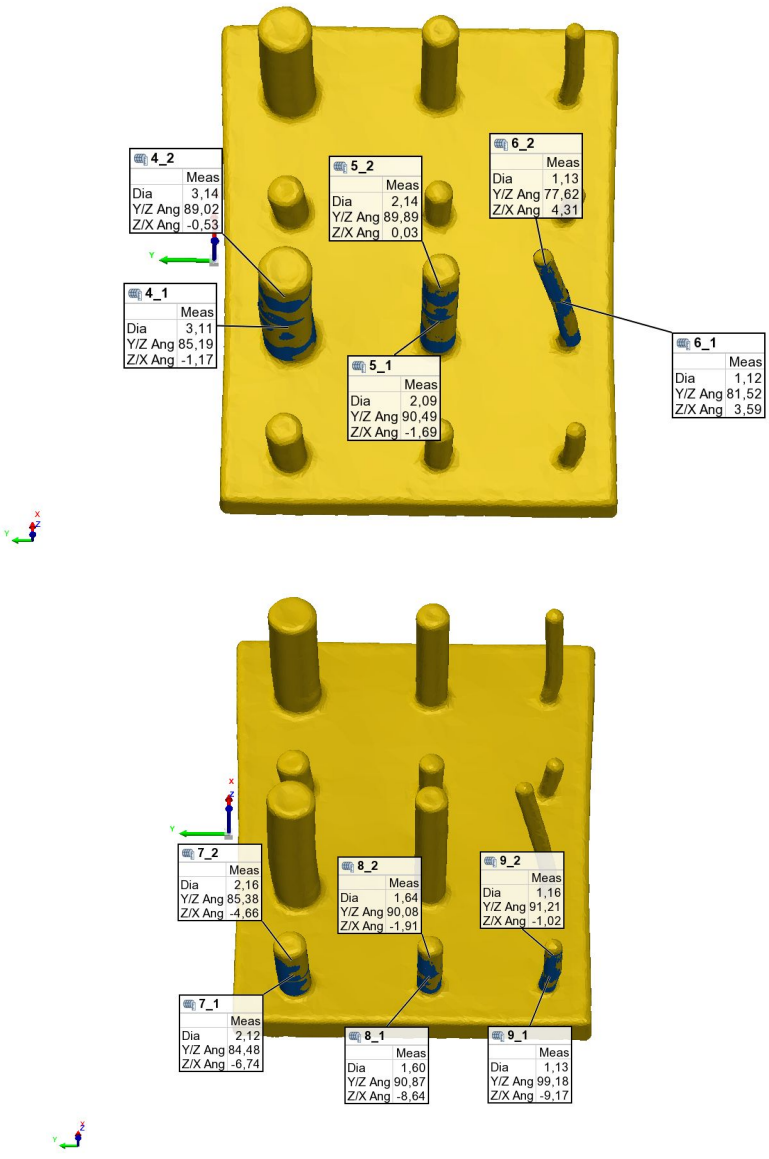

Organization:	Geometry verification center	**Part name:**	Prins Only
Operator:	Anders Odham	**Part number:**	
E-mail:	anders.odhamii@volvocars.com	**Piece:**	piece 1

A.3 Artefact 3A: Bridge with no compensation

PolyWorks by innovmetric

innovmetric

2 Bridge_Mock_Print_without_base

Report Author: Anders Odham
Date: 2023-06-13

Scanndata = Orange
Nufo = Gray

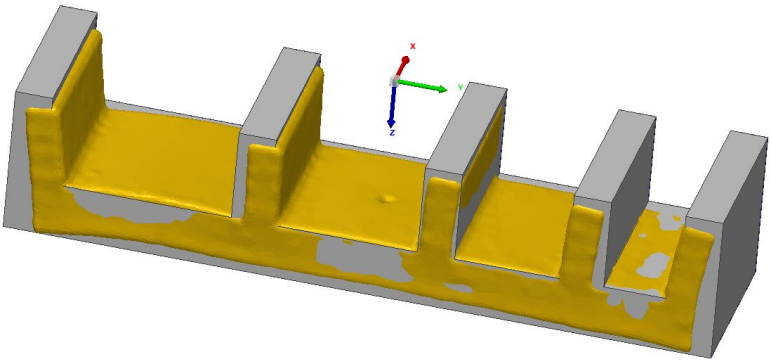

Organization:	Geometry verification center	Part name:	2 Bridge_Mock_Print_without_bas
Operator:	Anders Odham	Part number:	
E-mail:	anders.odhamii@volvocars.com	Drawing #:	
Workspace:	Workspace 2	Serial #:	
Project:	NY_ 2	Device:	Modelmaker H120 on MCAx

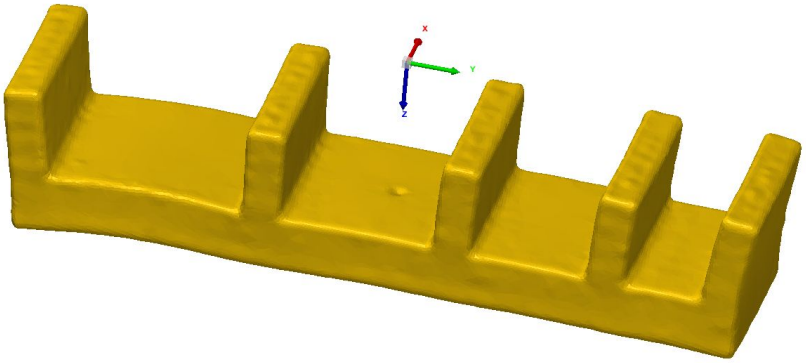

Align: Reference Target
3-2-1

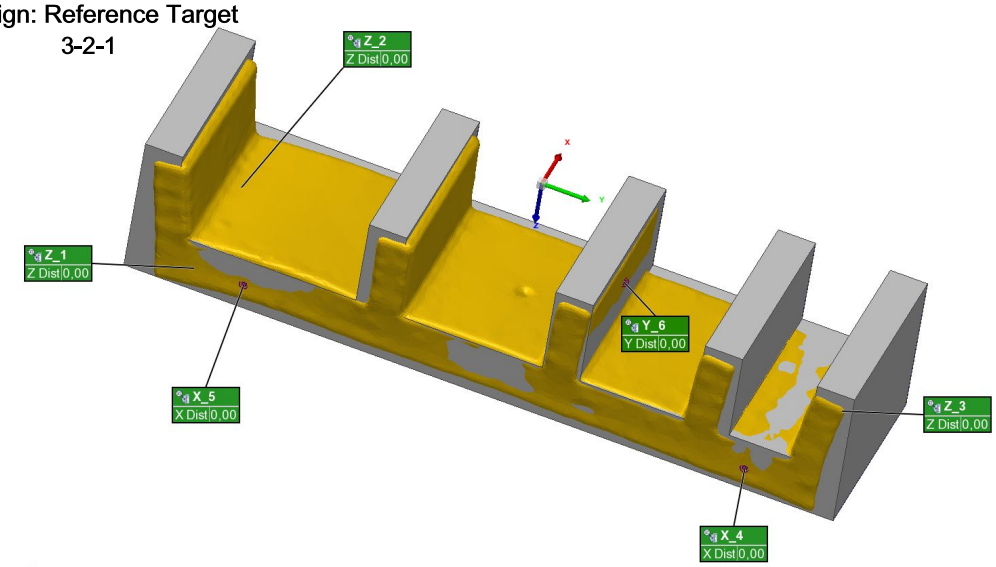

Organization:	Geometry verification center	Part name:	2 Bridge_Mock_Print_without_base
Operator:	Anders Odham	Part number:	
E-mail:	anders.odhamii@volvocars.com	Piece:	piece 1

Align: Reference Target
3-2-1

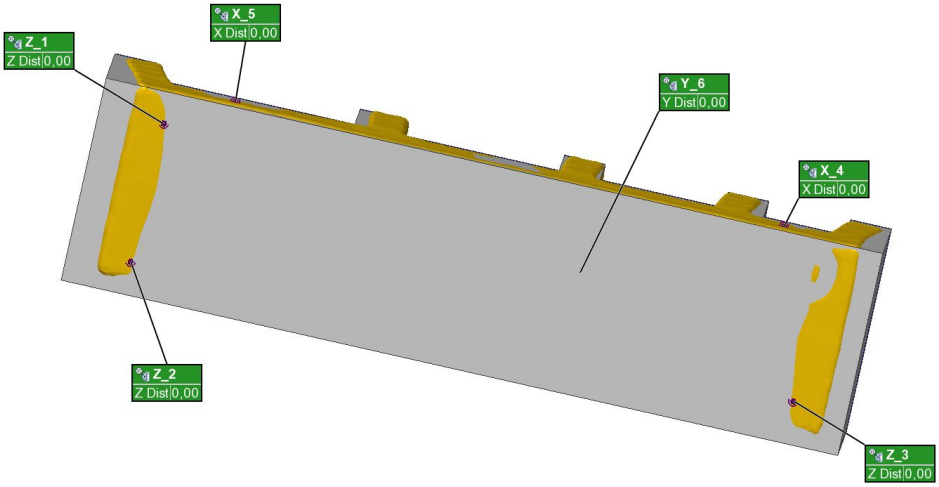

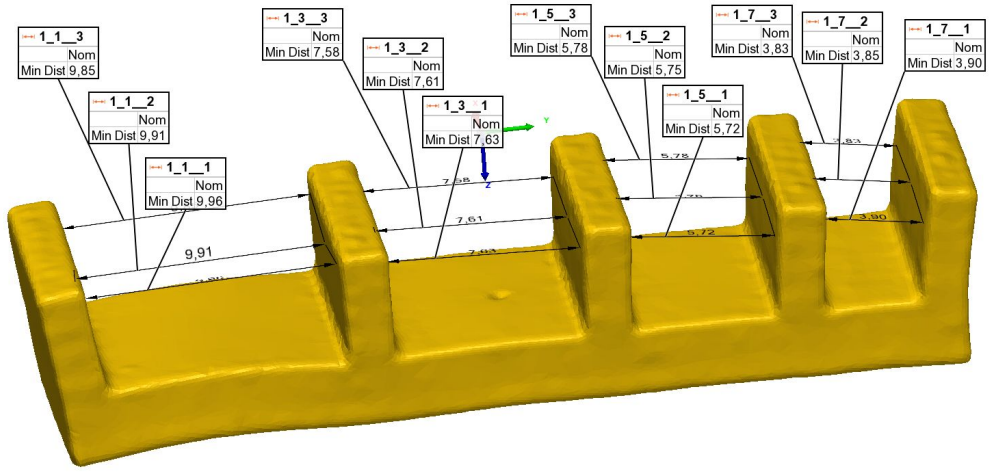

Organization:	Geometry verification center	**Part name:**	2 Bridge_Mock_Print_without_base
Operator:	Anders Odham	**Part number:**	
E-mail:	anders.odhamii@volvocars.com	**Piece:**	piece 1

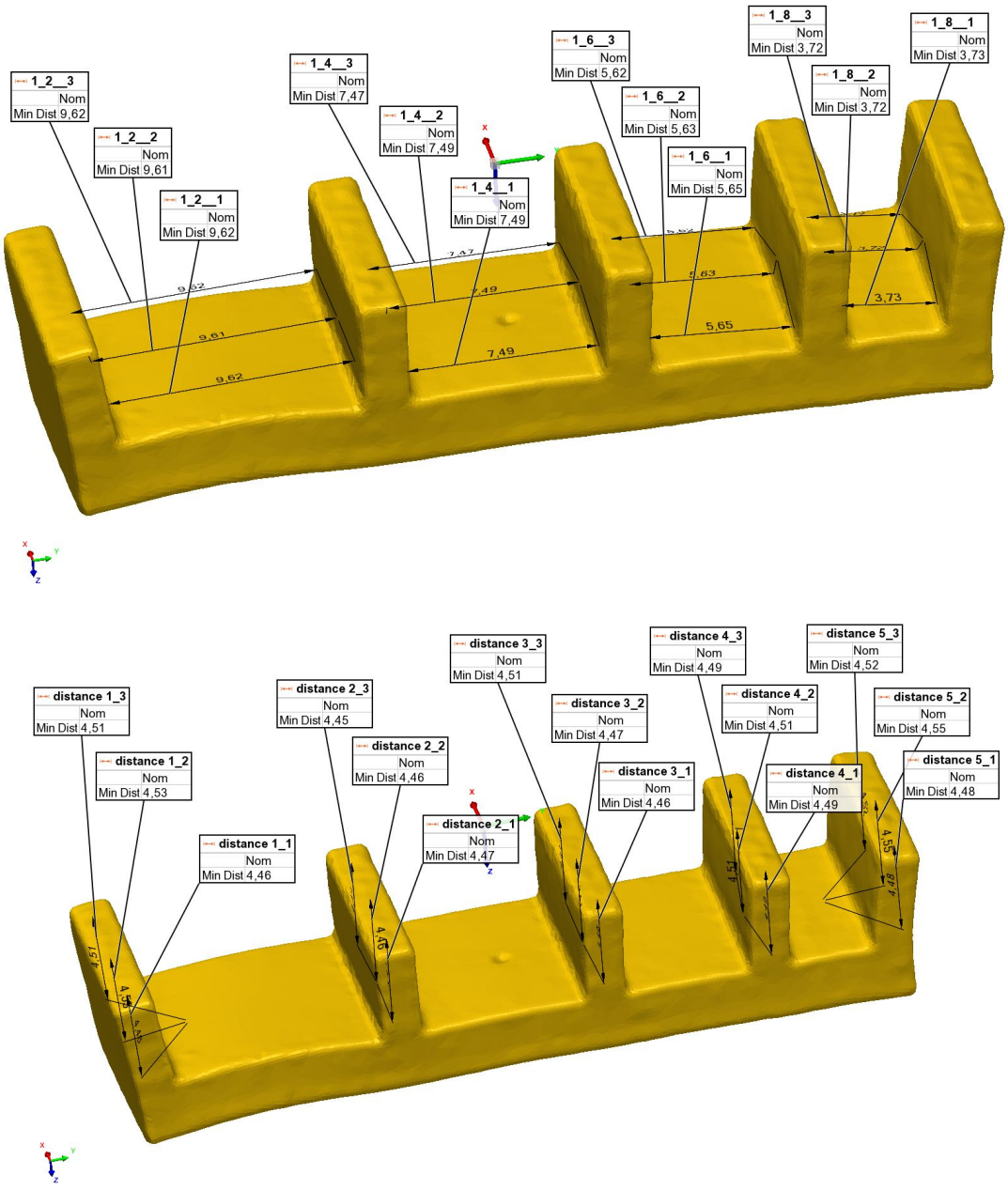

Organization:	Geometry verification center	**Part name:**	2 Bridge_Mock_Print_without_base
Operator:	Anders Odham	**Part number:**	
E-mail:	anders.odhamii@volvocars.com	**Piece:**	piece 1

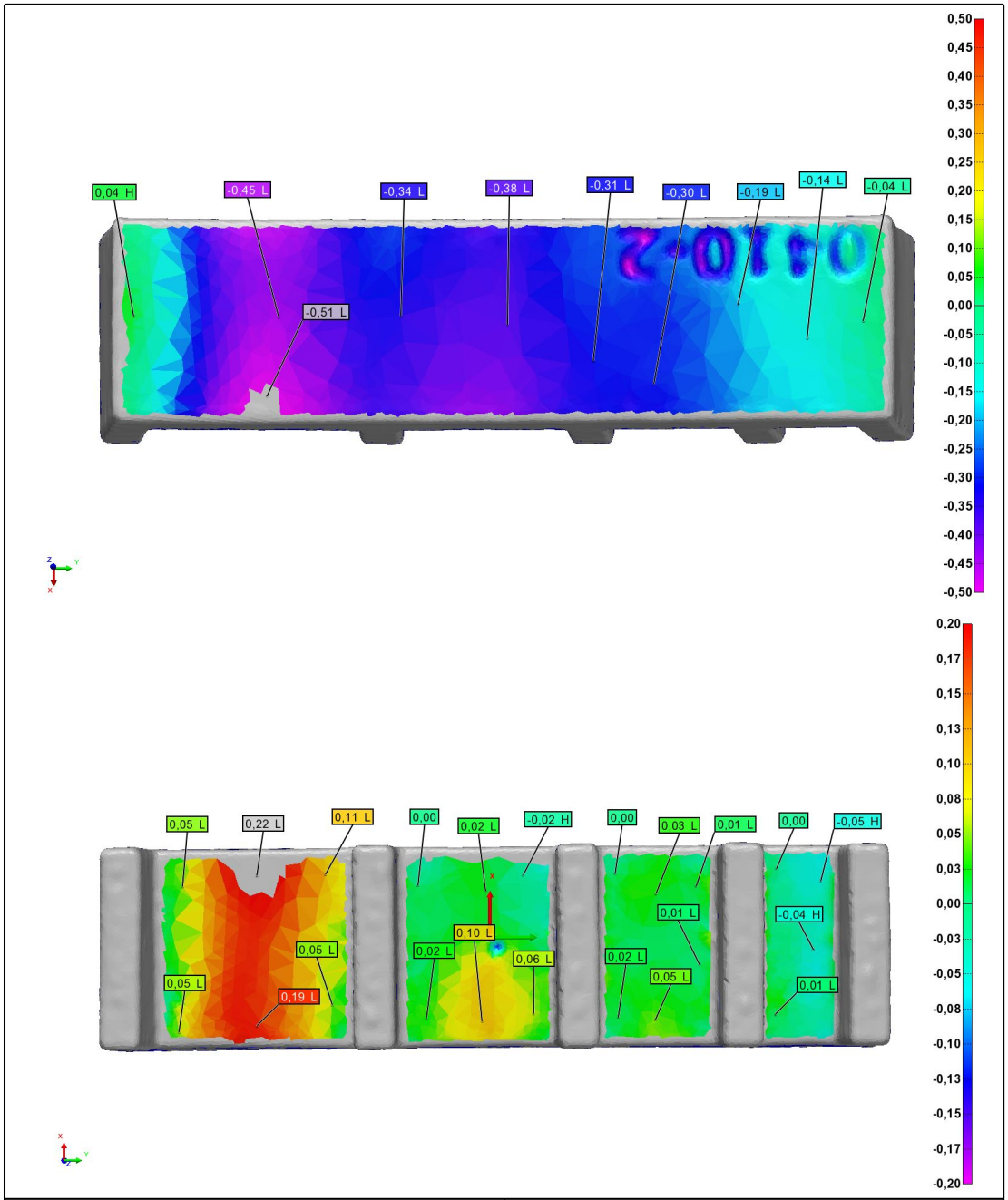

Organization:	Geometry verification center	**Part name:**	2 Bridge_Mock_Print_without_base
Operator:	Anders Odham	**Part number:**	
E-mail:	anders.odhamii@volvocars.com	**Piece:**	piece 1

A.4 Artefact 3B: Bridge with two spans compensated

PolyWorks by innovmetric

innovmetric

Bridge_Mock_Print_withou

Report Author: Anders Odham
Date: 2023-06-01

Scanndata = Orange
Nufo = Gray

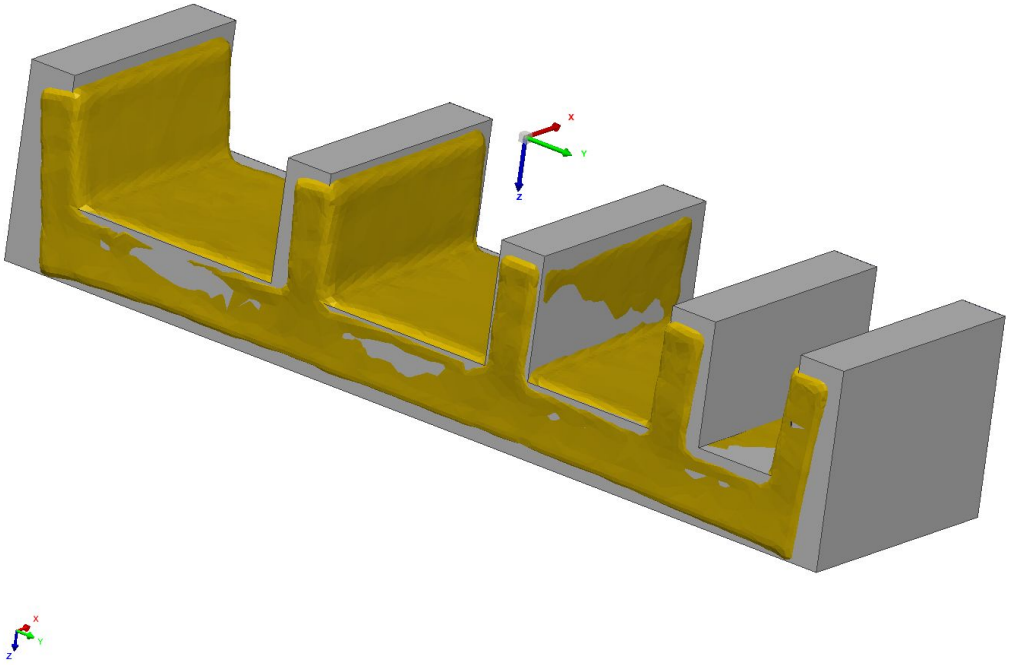

Organization:	Geometry verification center	Part name:	Bridge_Mock_Print_without_base
Operator:	Anders Odham	Part number:	
E-mail:	anders.odhamii@volvocars.com	Drawing #:	
Workspace:	Workspace 2	Serial #:	
Project:	NY_Bridge_Mock_Print_without_ba	Device:	Modelmaker H120 on MCAx

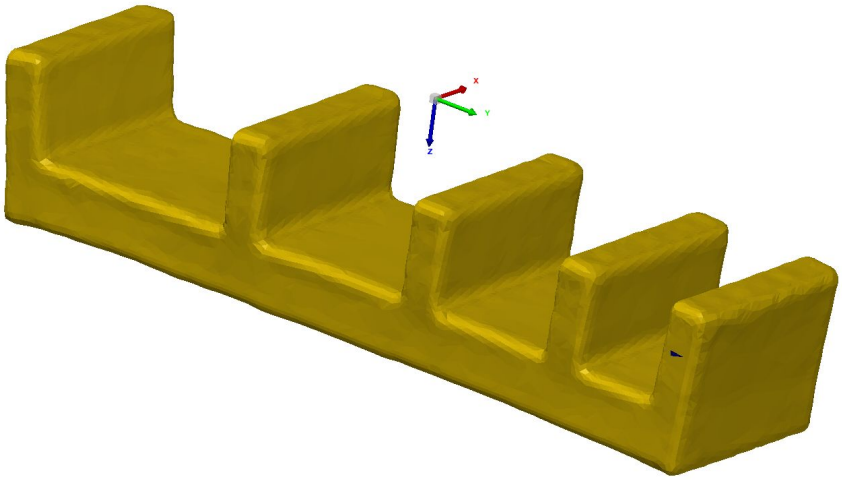

Align : Reference Target
3-2-1

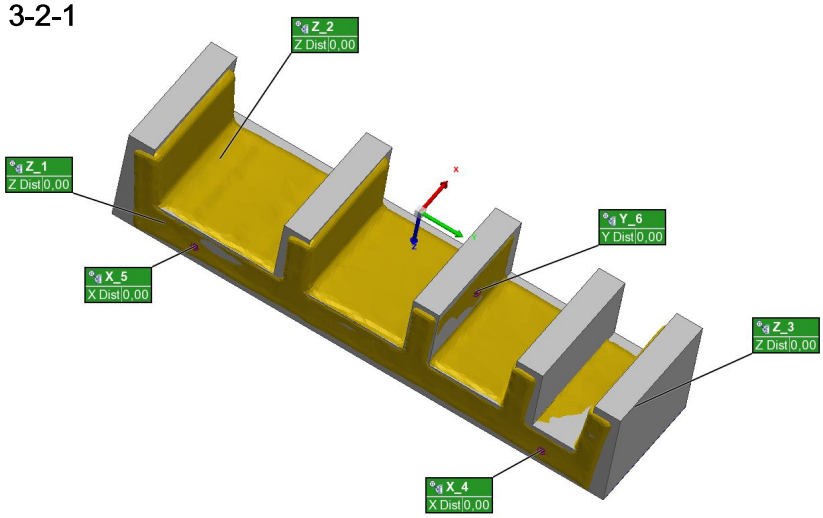

Organization:	Geometry verification center	Part name:	Bridge_Mock_Print_without_base
Operator:	Anders Odham	Part number:	
E-mail:	anders.odhamii@volvocars.com	Piece:	piece 1

Align : Reference Target
3-2-1

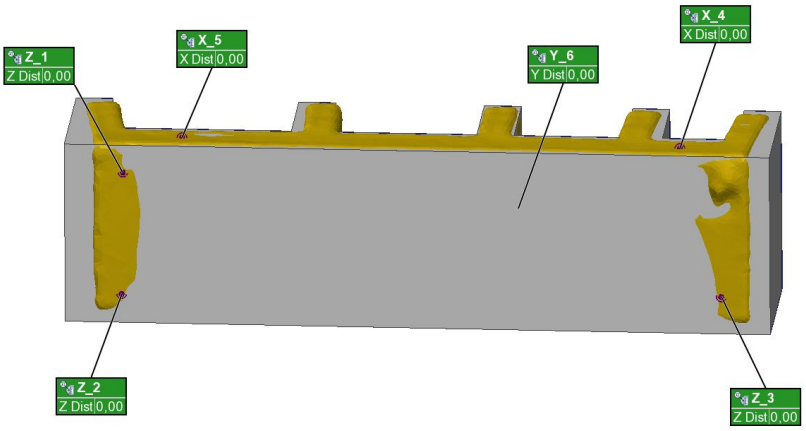

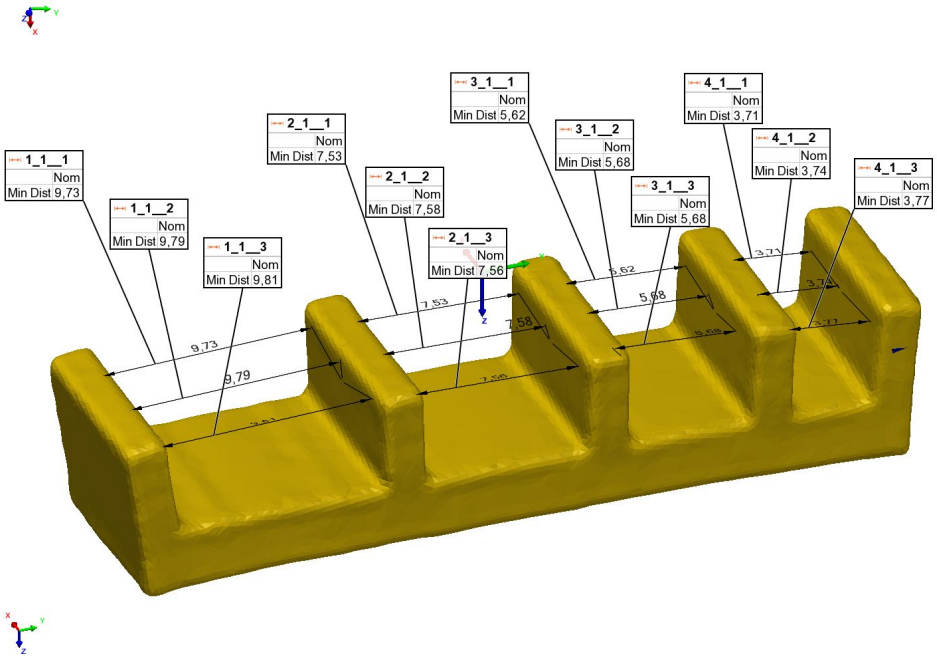

Organization:	Geometry verification center	**Part name:**	Bridge_Mock_Print_without_base
Operator:	Anders Odham	**Part number:**	
E-mail:	anders.odhamii@volvocars.com	**Piece:**	piece 1

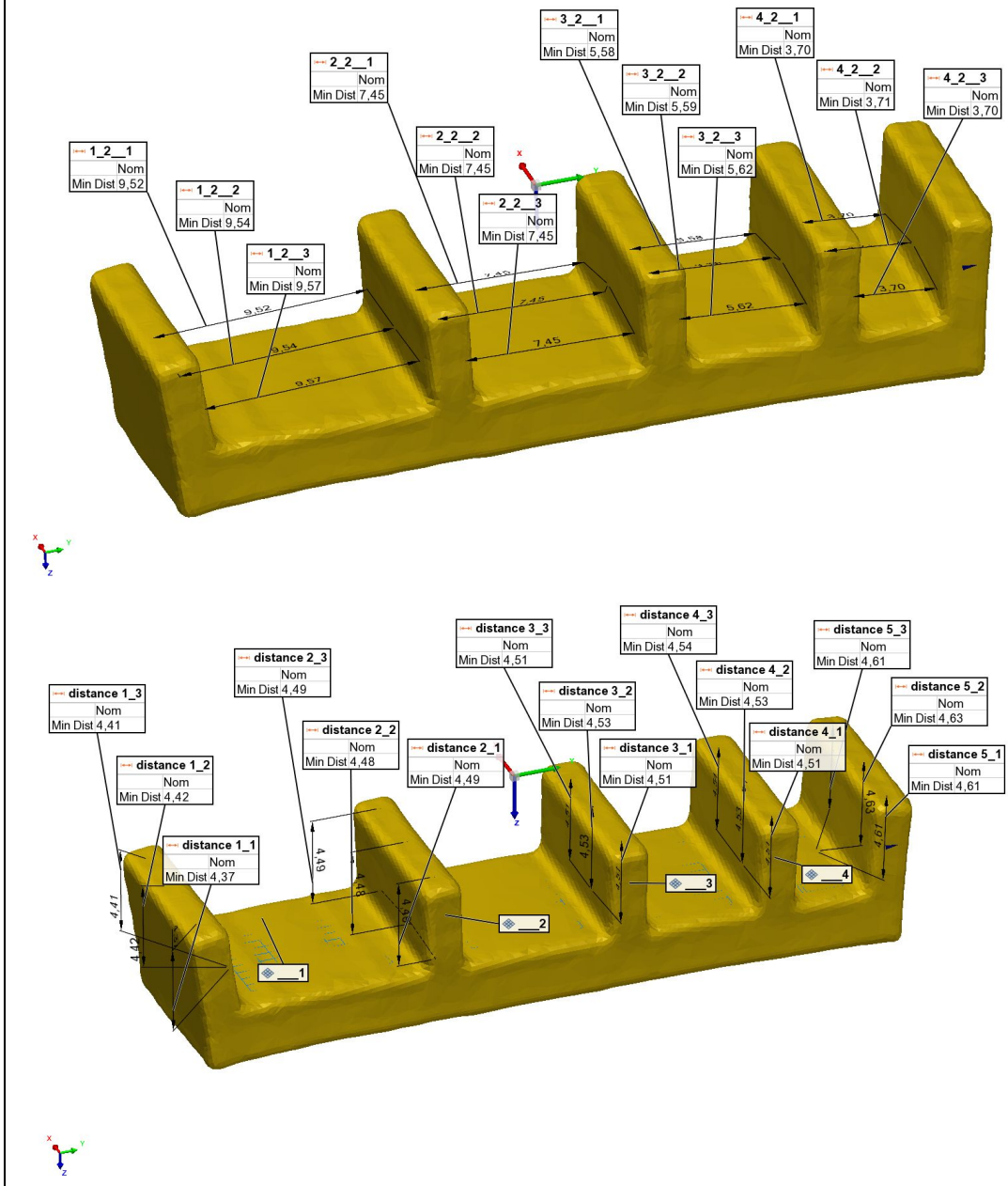

Organization:	Geometry verification center	**Part name:**	Bridge_Mock_Print_without_base
Operator:	Anders Odham	**Part number:**	
E-mail:	anders.odhamii@volvocars.com	**Piece:**	piece 1

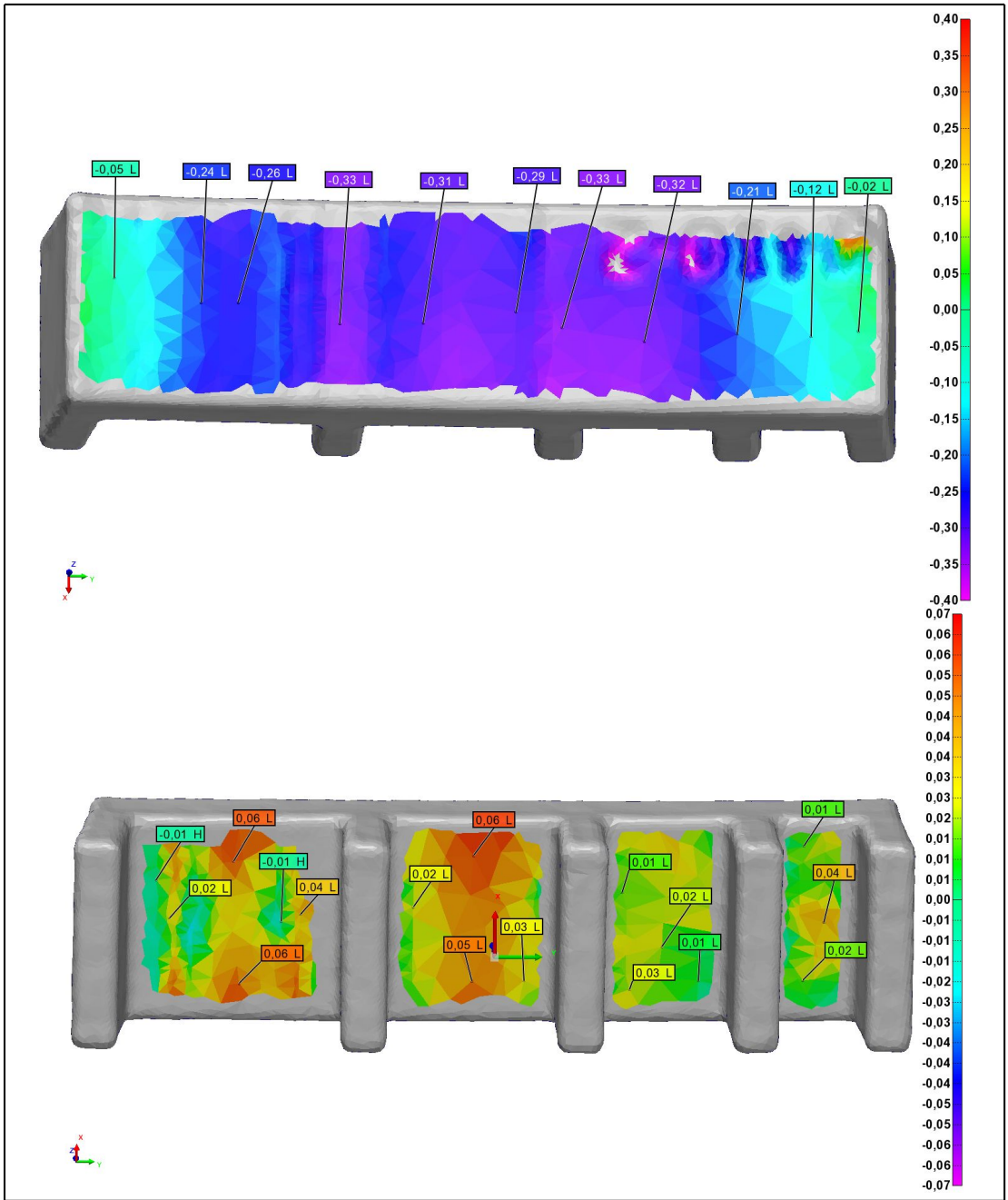

Organization:	Geometry verification center	**Part name:**	Bridge_Mock_Print_without_base
Operator:	Anders Odham	**Part number:**	
E-mail:	anders.odhamii@volvocars.com	**Piece:**	piece 1

A.5 Artefact 3C: Bridge compensated using Simufact

3DScan_SinteredBody_Simufact

Report Author: Anders Odham
Date: 2023-06-09

Scanndata = Orange
Nufo = Gray

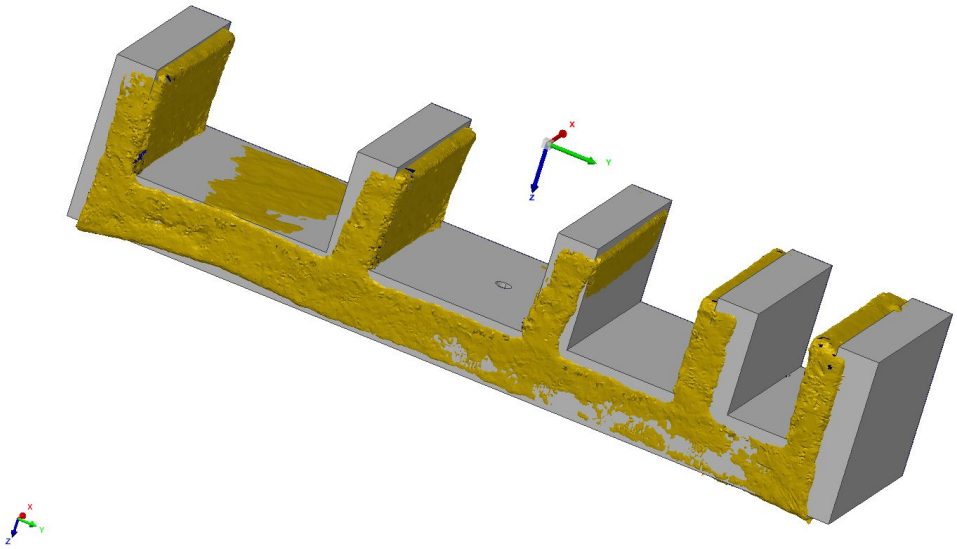

Organization:	Geometry verification center	Part name:	
Operator:	Anders Odham	Part number:	
E-mail:	anders.odhamii@volvocars.com	Drawing #:	
Workspace:	Workspace 2	Serial #:	
Project:	3DScan_SinteredBody_Simufact -	Device:	Modelmaker H120 on MCAx

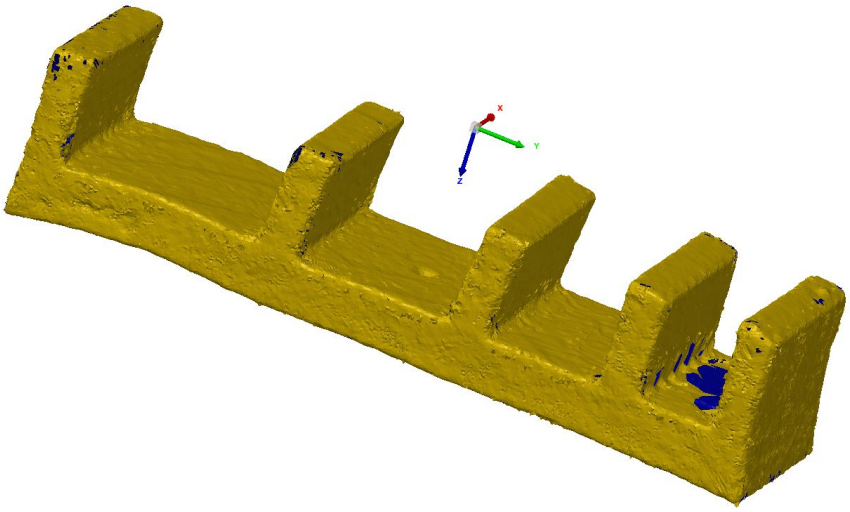

Align : Reference Target
3-2-1

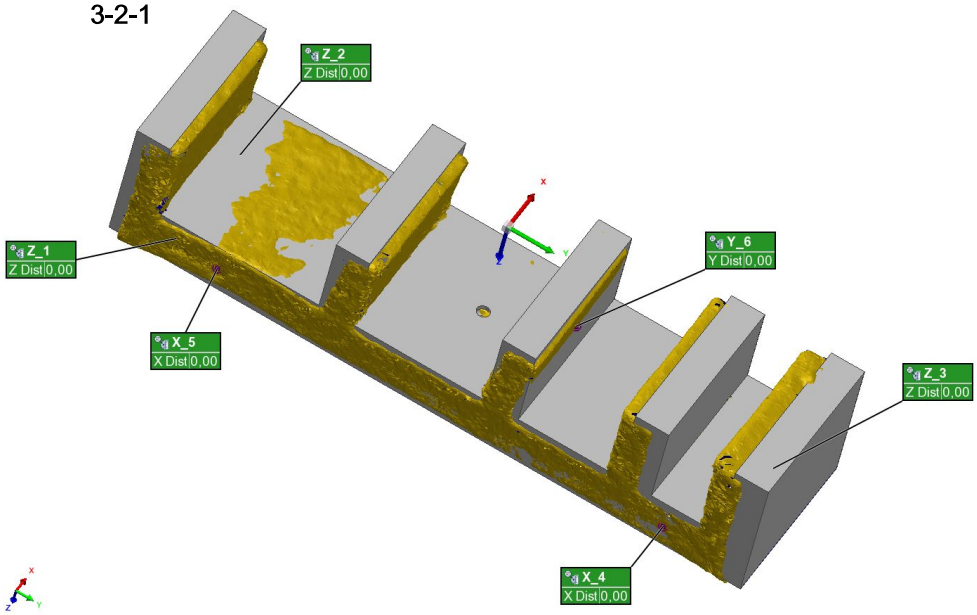

Organization:	Geometry verification center	Part name:	
Operator:	Anders Odham	Part number:	
E-mail:	anders.odhamii@volvocars.com	Piece:	piece 1

Align : Reference Target
3-2-1

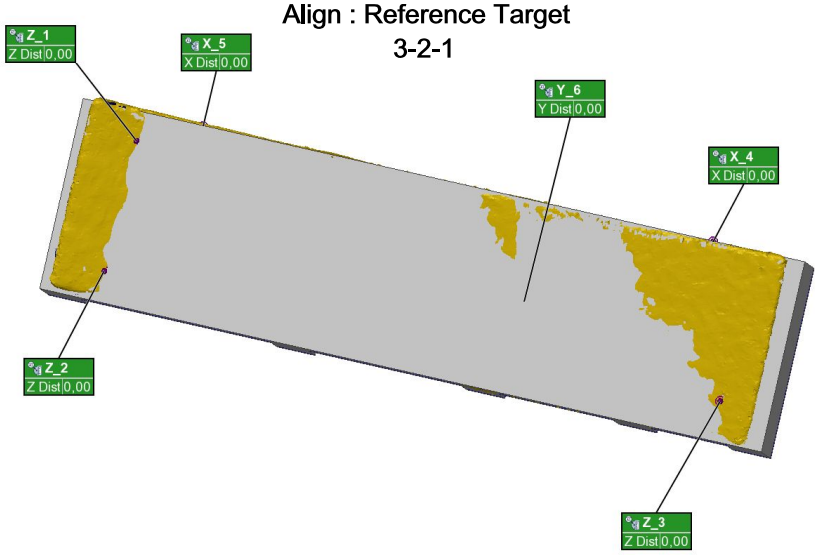

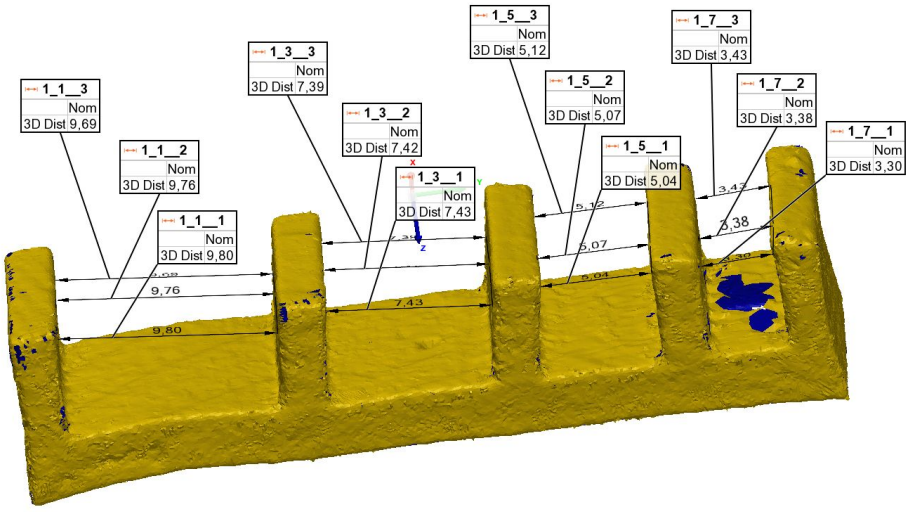

Organization:	Geometry verification center	Part name:	
Operator:	Anders Odham	Part number:	
E-mail:	anders.odhamii@volvocars.com	Piece:	piece 1

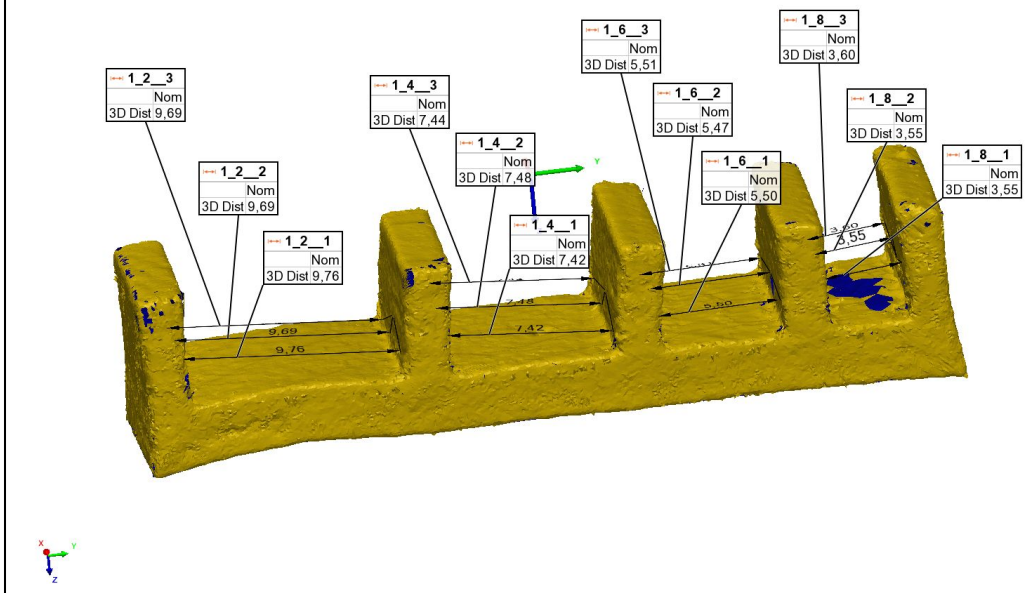

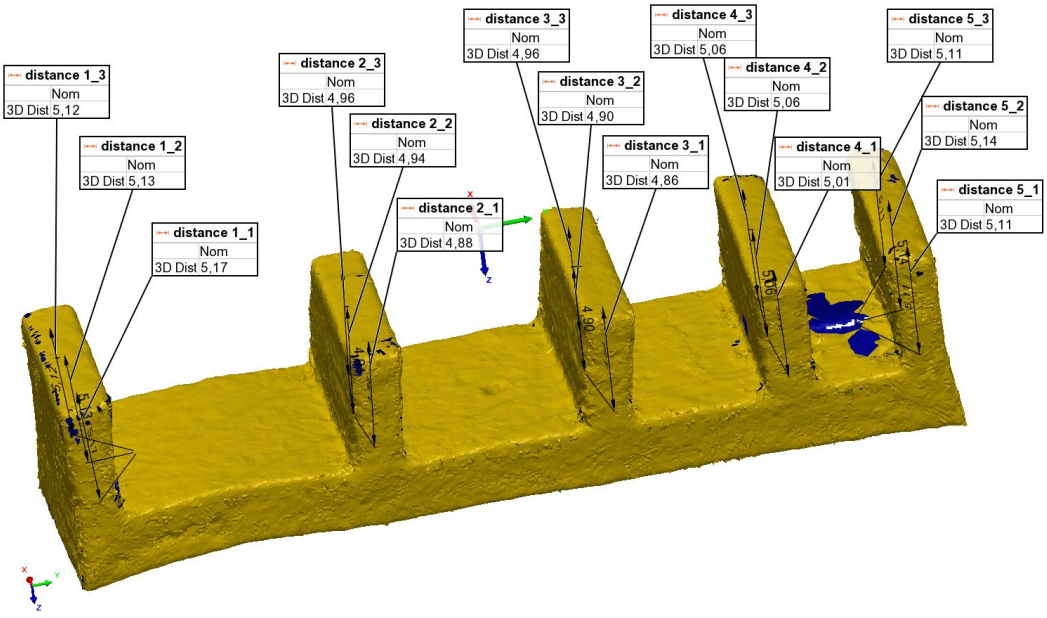

Organization:	Geometry verification center	**Part name:**	
Operator:	Anders Odham	**Part number:**	
E-mail:	anders.odhamii@volvocars.com	**Piece:**	piece 1

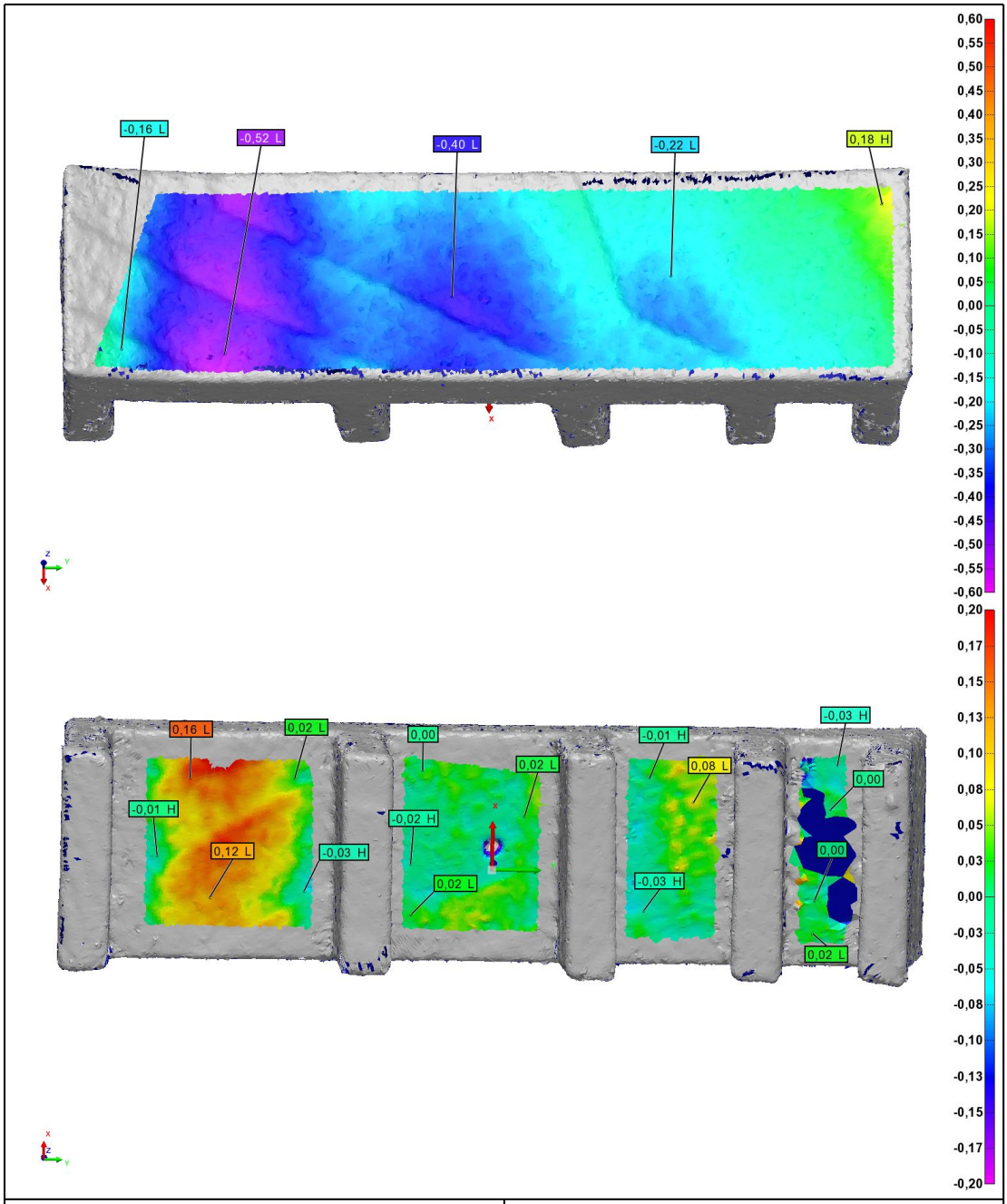

Organization:	Geometry verification center	**Part name:**	
Operator:	Anders Odham	**Part number:**	
E-mail:	anders.odhamii@volvocars.com	**Piece:**	piece 1

A.6 Artefact 4A: Bridge with base convectional sintering process

PolyWorks by innovmetric

innovmetric

01 Bridge_Mock_Print_With_Base.STEP

Report Author: Anders Odham
Date: 2023-06-15

Scanndata = Orange
Nufo = Gray

Align : Best-Fit

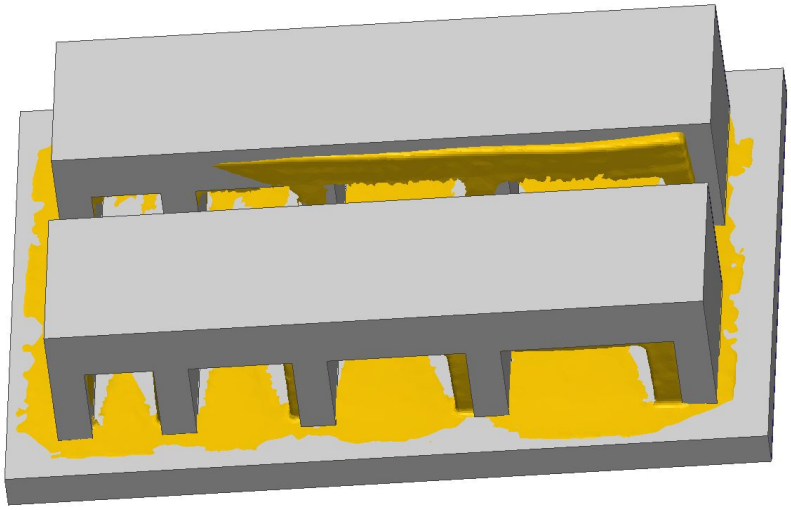

Organization:	Geometry verification center	Part name:	01_ Bridge_Mock_Print_with_base.STEP
Operator:	Anders Odham	Part number:	
E-mail:	anders.odhamii@volvocars.com	Drawing #:	
Workspace:	Workspace 2	Serial #:	
Project:	01 - piece 1	Device:	Modelmaker H120 on MCAx

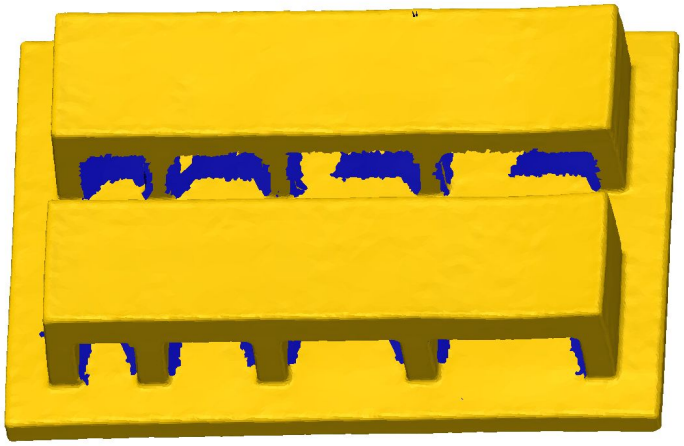

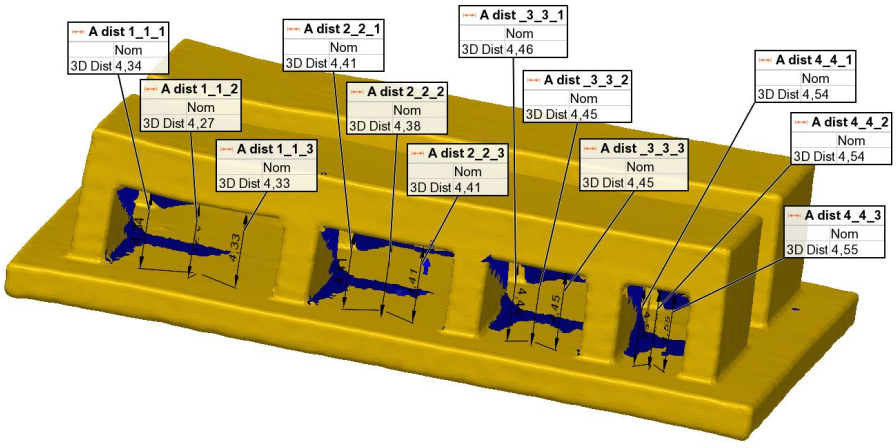

Organization:	Geometry verification center	**Part name:**	01_ Bridge_Mock_Print_with_base.STEP
Operator:	Anders Odham	**Part number:**	
E-mail:	anders.odhamii@volvocars.com	**Piece:**	piece 1

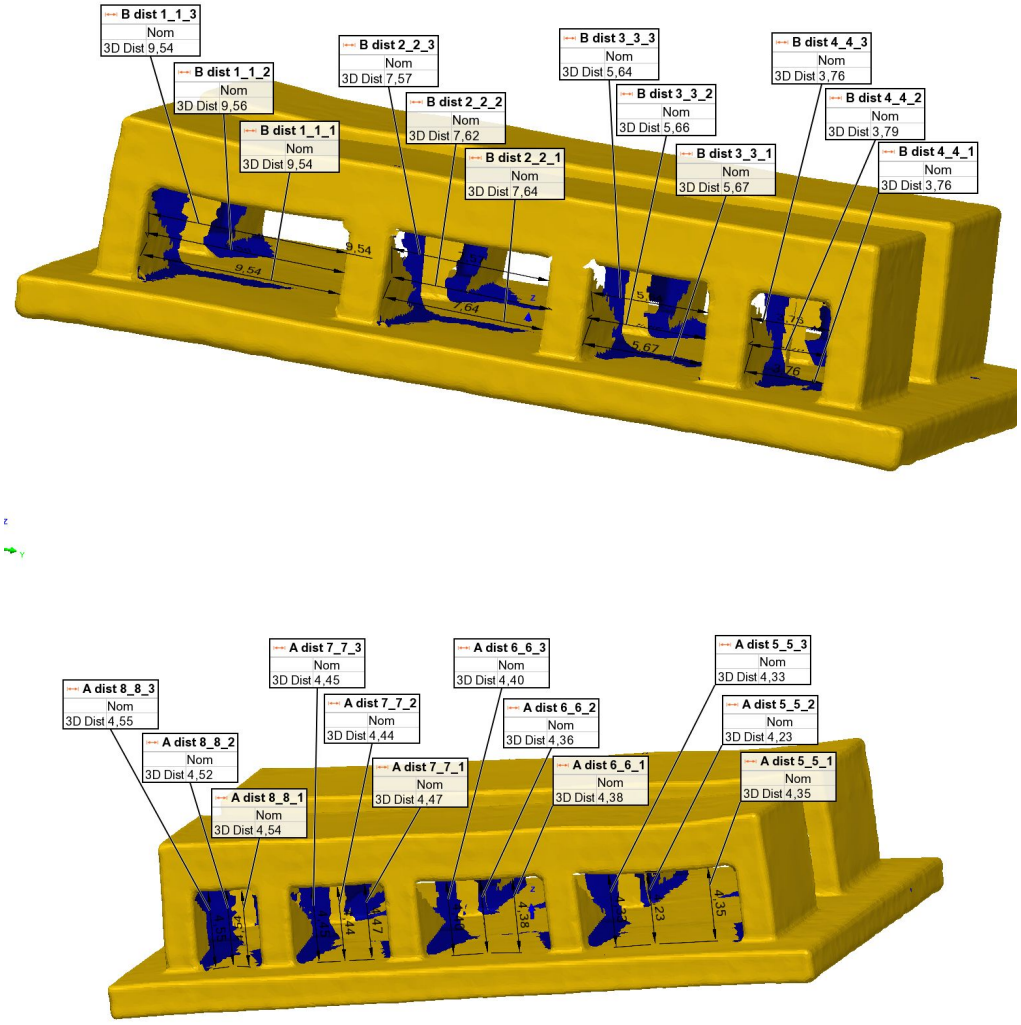

Organization:	Geometry verification center	**Part name:**	01_ Bridge_Mock_Print_with_base.STEP
Operator:	Anders Odham	**Part number:**	
E-mail:	anders.odhamii@volvocars.com	**Piece:**	piece 1

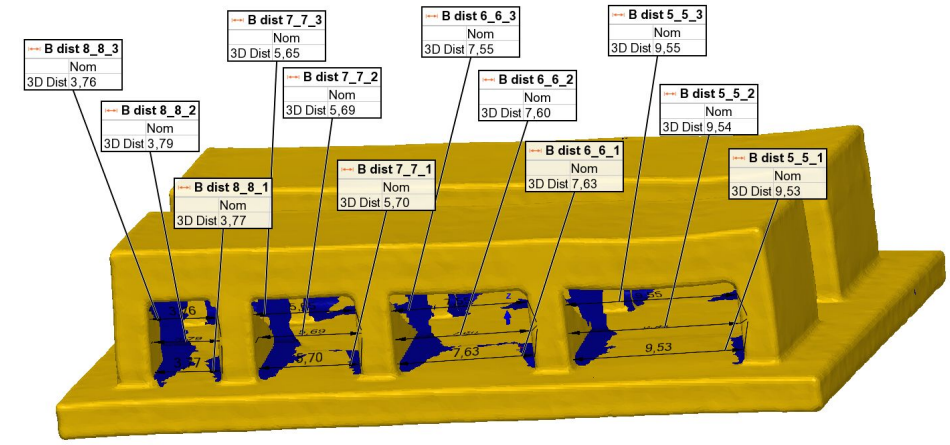

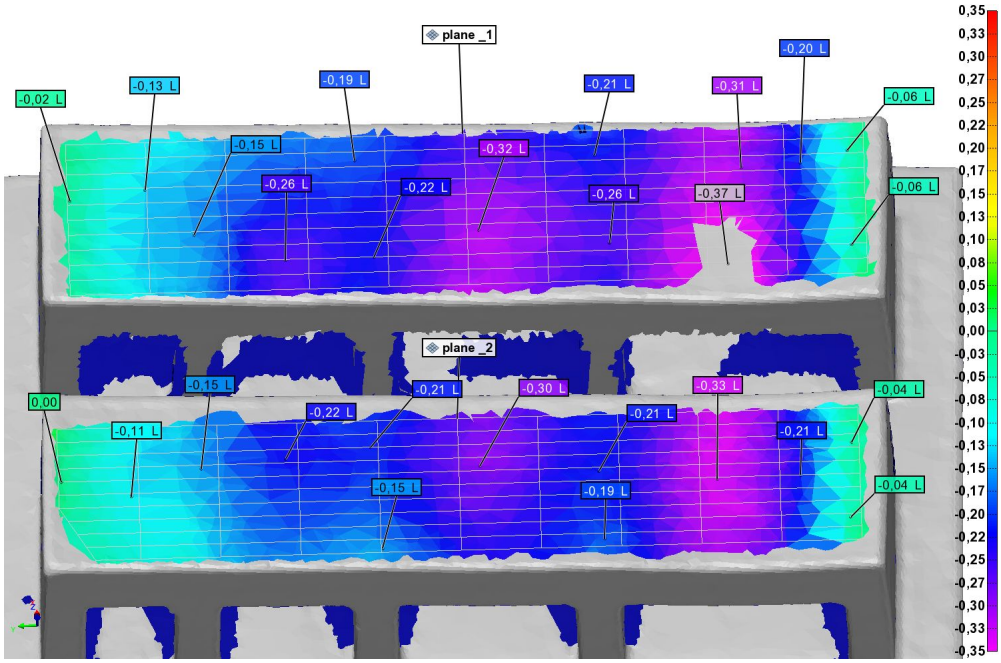

Organization:	Geometry verification center	**Part name:**	01_ Bridge_Mock_Print_with_base.STEP
Operator:	Anders Odham	**Part number:**	
E-mail:	anders.odhamii@volvocars.com	**Piece:**	piece 1

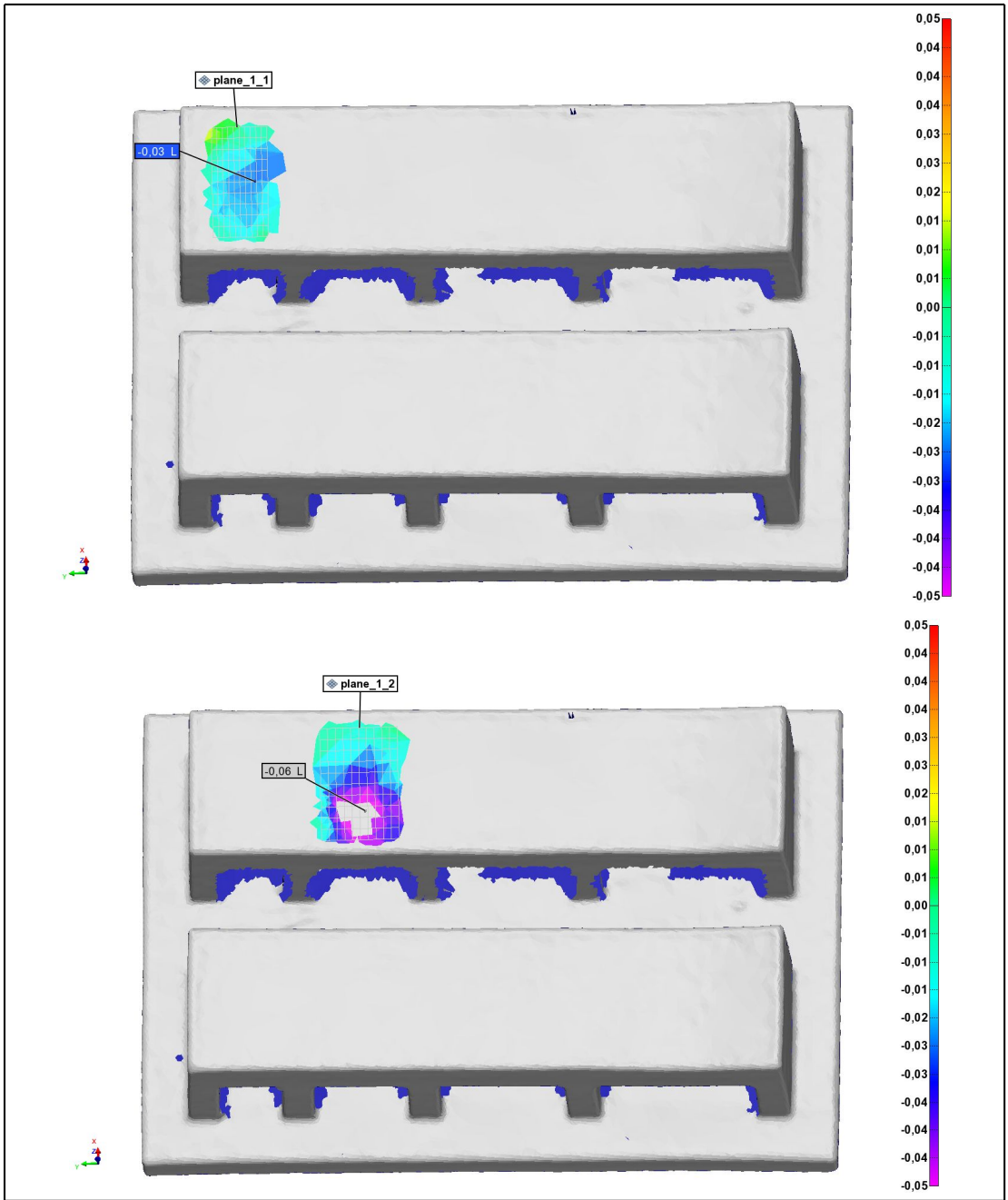

Organization:	Geometry verification center	**Part name:**	01_ Bridge_Mock_Print_with_base.STEP
Operator:	Anders Odham	**Part number:**	
E-mail:	anders.odhamii@volvocars.com	**Piece:**	piece 1

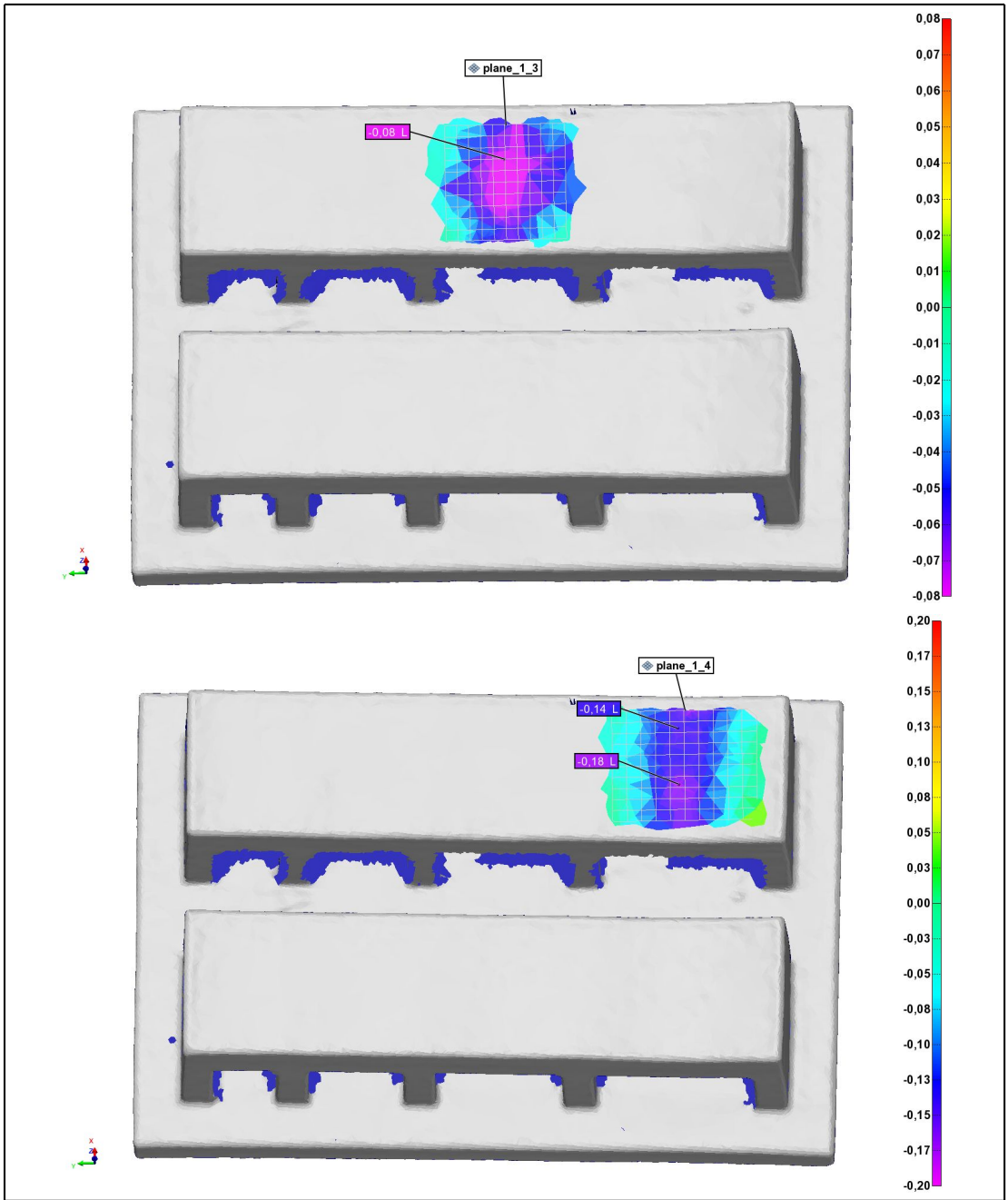

Organization:	Geometry verification center	**Part name:**	01_ Bridge_Mock_Print_with_base.STEP
Operator:	Anders Odham	**Part number:**	
E-mail:	anders.odhamii@volvocars.com	**Piece:**	piece 1

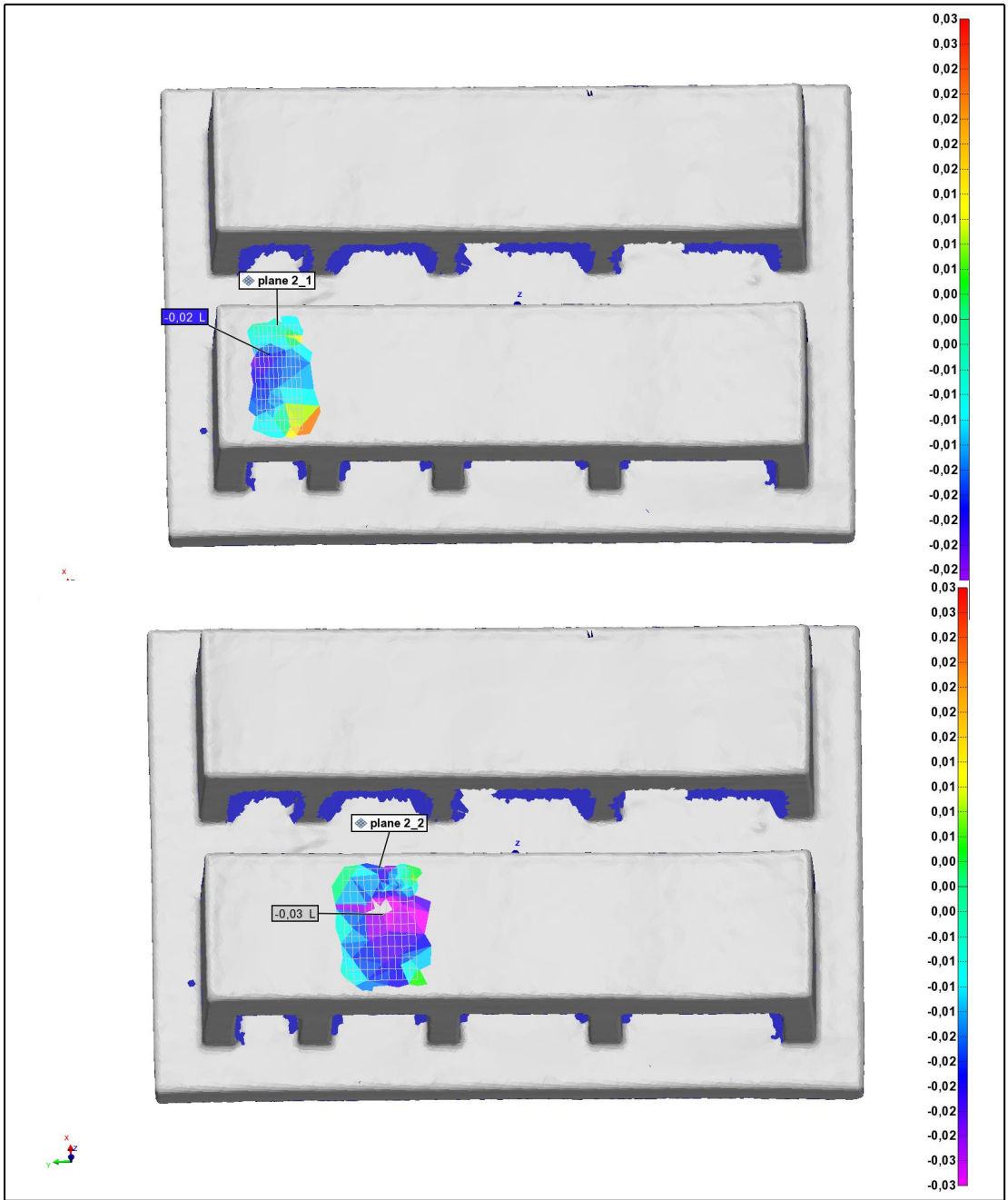

Organization:	Geometry verification center	**Part name:**	01_ Bridge_Mock_Print_with_base.STEP
Operator:	Anders Odham	**Part number:**	
E-mail:	anders.odhamii@volvocars.com	**Piece:**	piece 1

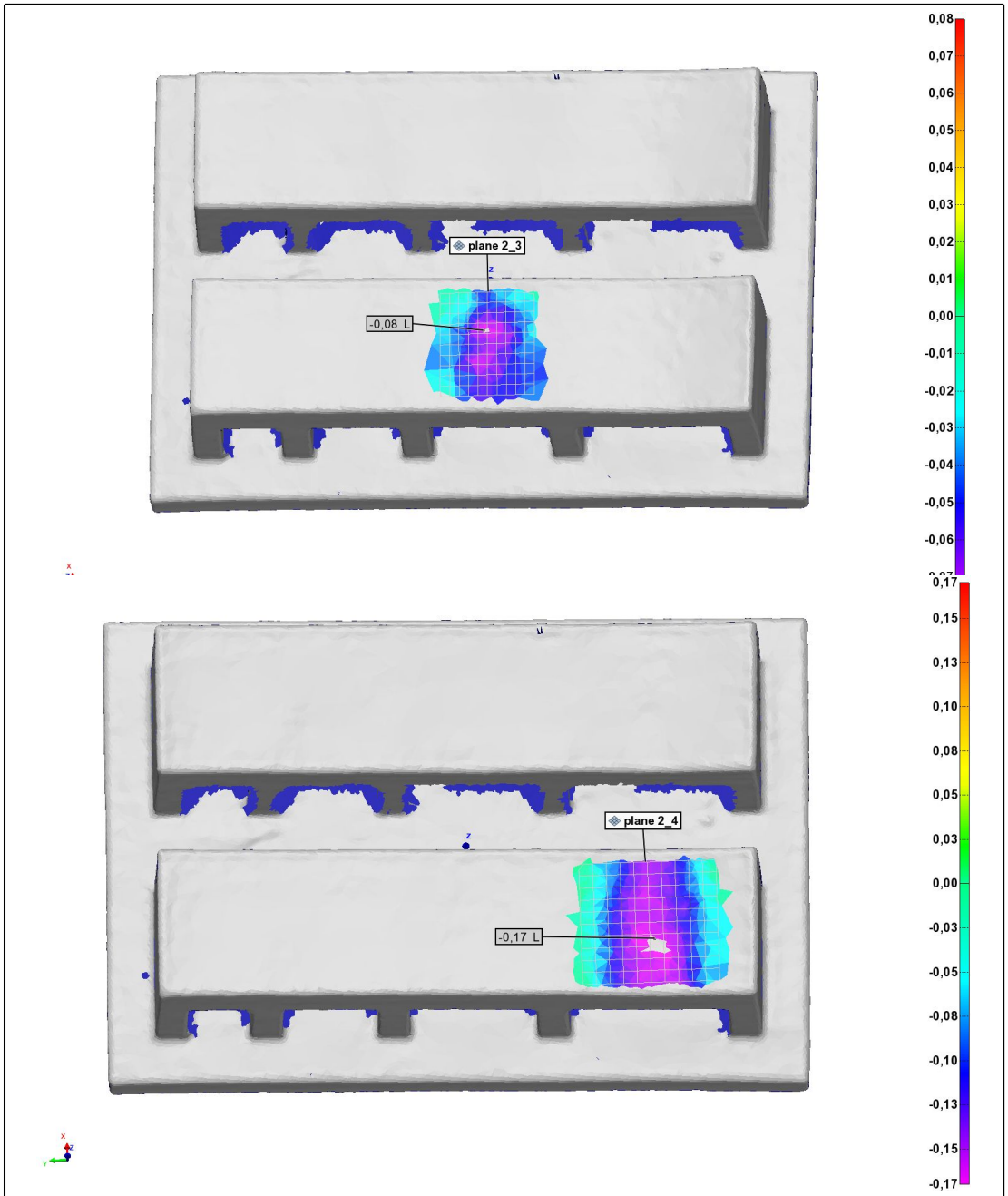

Organization:	Geometry verification center	**Part name:**	01_ Bridge_Mock_Print_with_base.STEP
Operator:	Anders Odham	**Part number:**	
E-mail:	anders.odhamii@volvocars.com	**Piece:**	piece 1

A.7 Artefact 4B: Bridge with base ceramic-supported sintering process

PolyWorks by innovmetric

innovmetric

02 Bridge_Mock_Print_With_Base.STEP

Report Author: Anders Odham
Date: 2023-06-19

Scanndata = Orange
Nufo = Gray

Align : Best-Fit

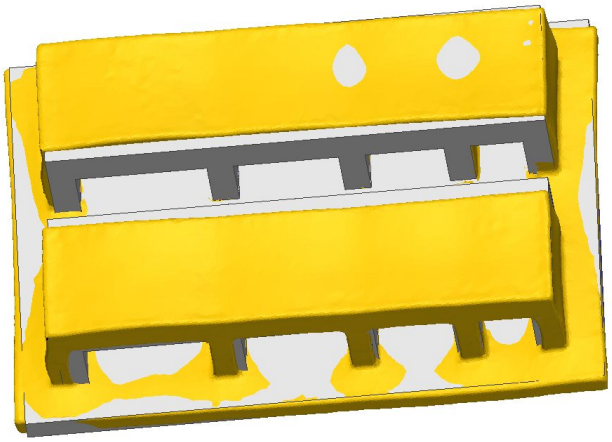

Organization:	Geometry verification center	Part name:	02_Bridg_Mock_Print_With_Base.STEP
Operator:	Anders Odham	Part number:	
E-mail:	anders.odhamii@volvocars.com	Drawing #:	
Workspace:	Workspace 2	Serial #:	
Project:	02 - piece 1	Device:	Modelmaker H120 on MCAx

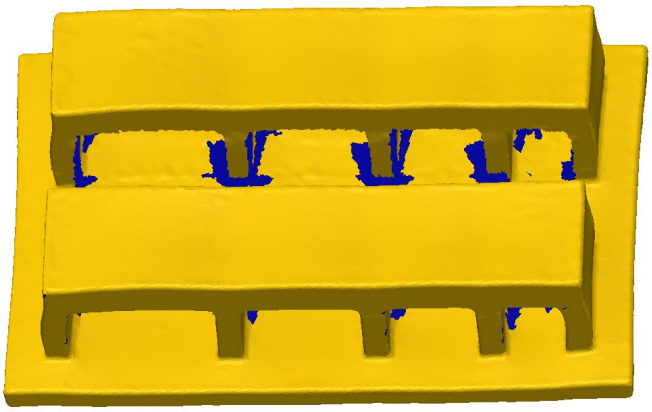

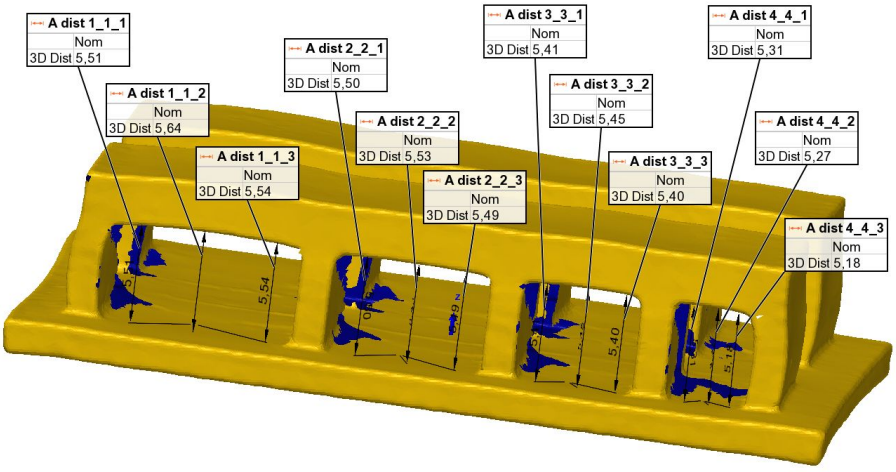

Organization:	Geometry verification center	**Part name:**	02_Bridg_Mock_Print_With_Base.STEP
Operator:	Anders Odham	**Part number:**	
E-mail:	anders.odhamii@volvocars.com	**Piece:**	piece 1

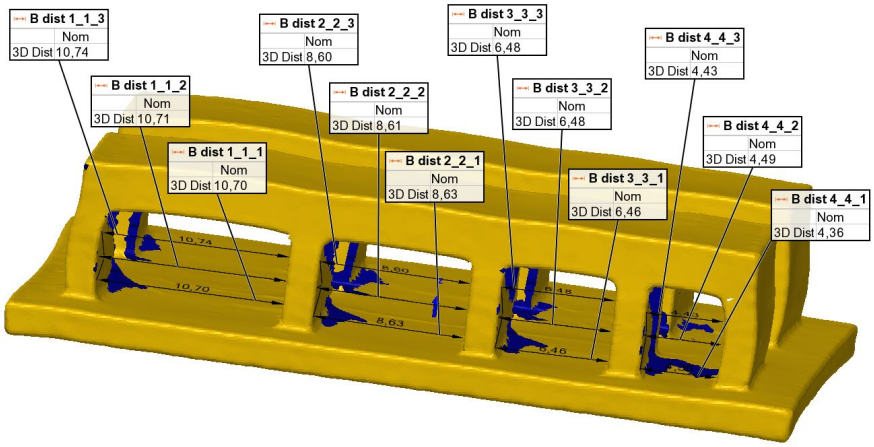

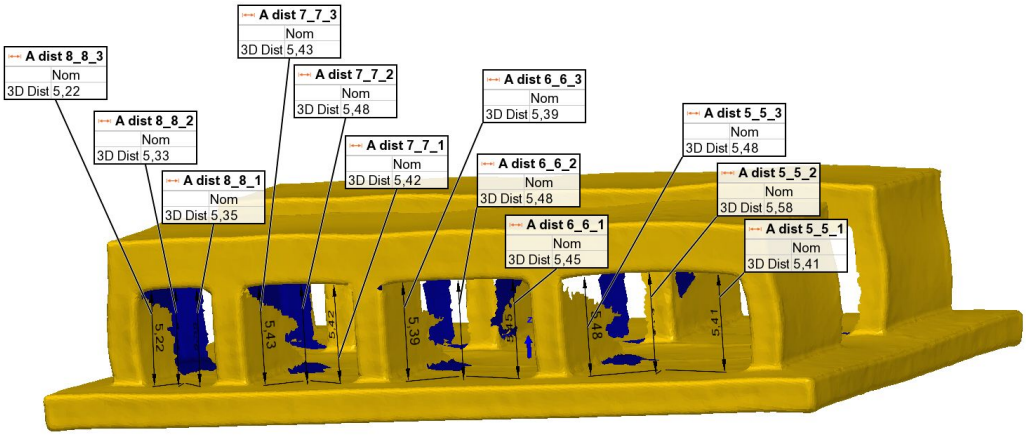

Organization:	Geometry verification center	**Part name:**	02_Bridg_Mock_Print_With_Base.STEP
Operator:	Anders Odham	**Part number:**	
E-mail:	anders.odhamii@volvocars.com	**Piece:**	piece 1

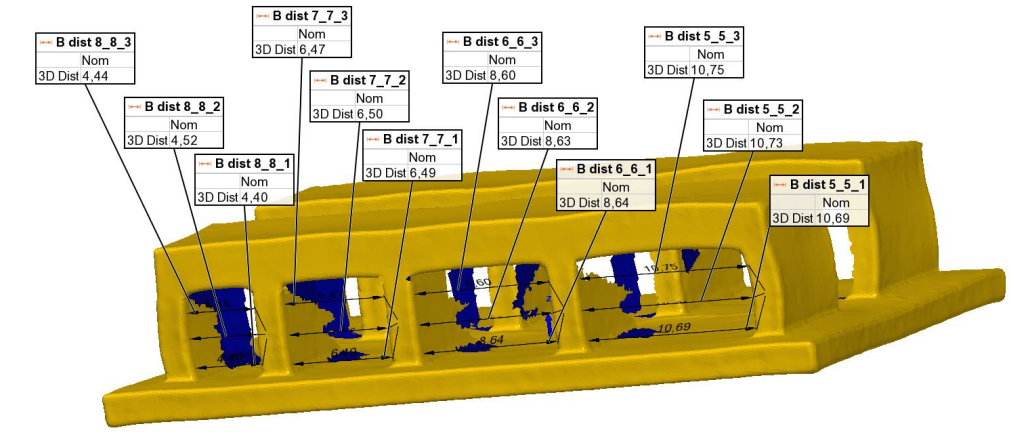

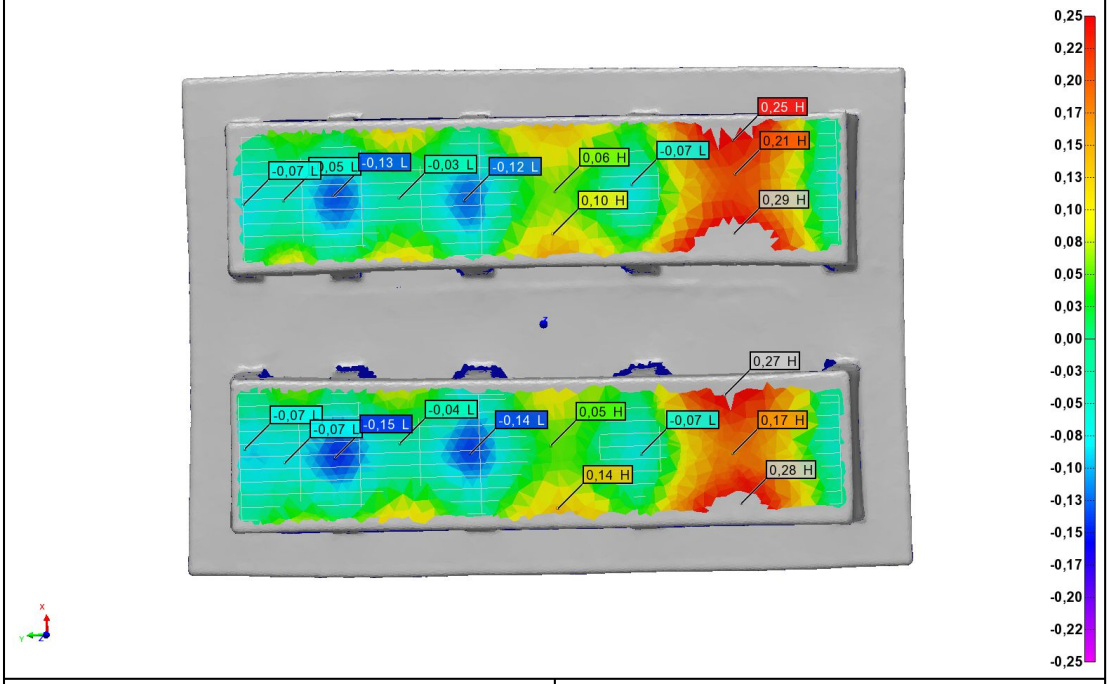

Organization:	Geometry verification center	**Part name:**	02_Bridg_Mock_Print_With_Base.STEP
Operator:	Anders Odham	**Part number:**	
E-mail:	anders.odhamii@volvocars.com	**Piece:**	piece 1

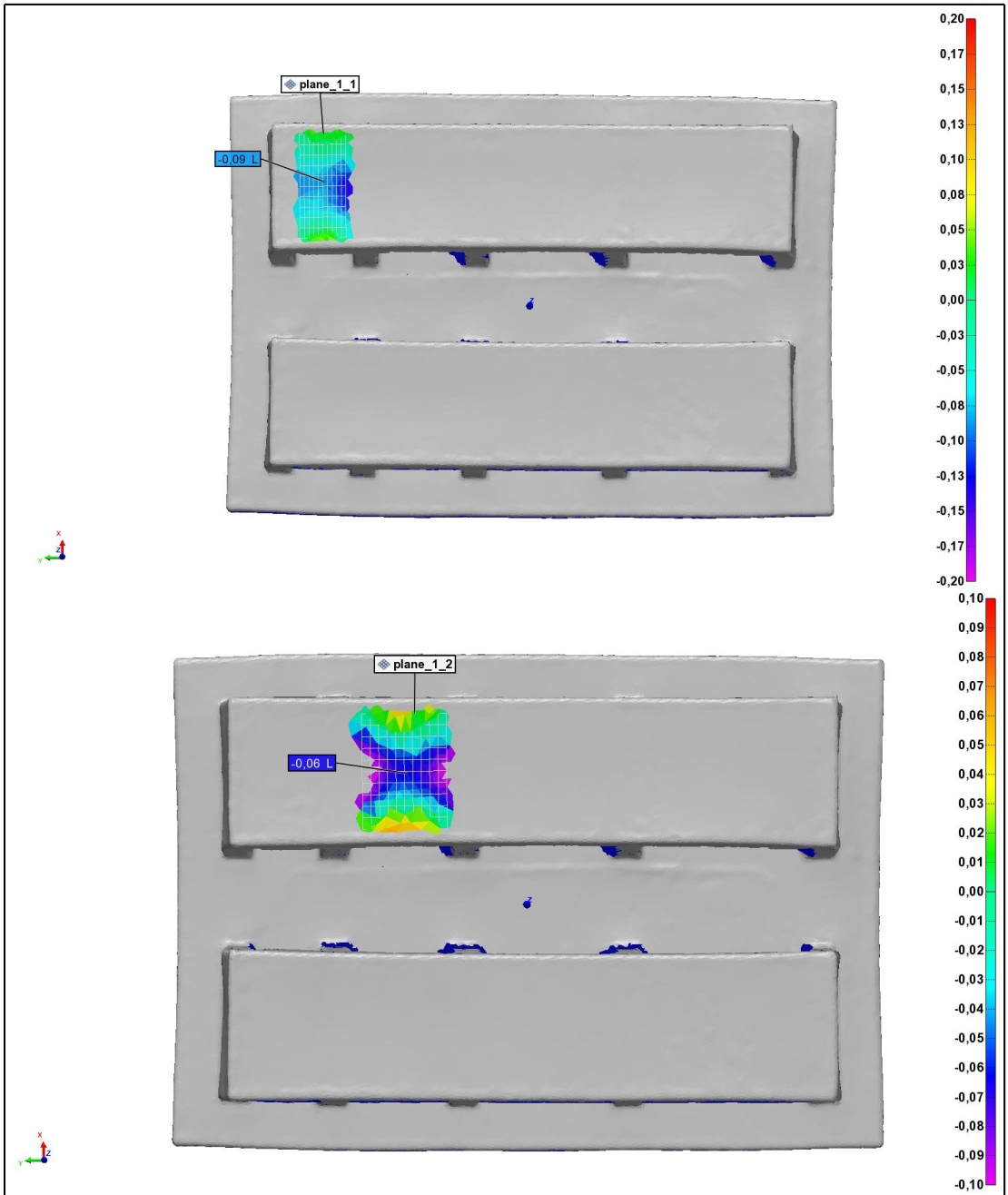

Organization:	Geometry verification center	**Part name:**	02_Bridg_Mock_Print_With_Base.STEP
Operator:	Anders Odham	**Part number:**	
E-mail:	anders.odhamii@volvocars.com	**Piece:**	piece 1

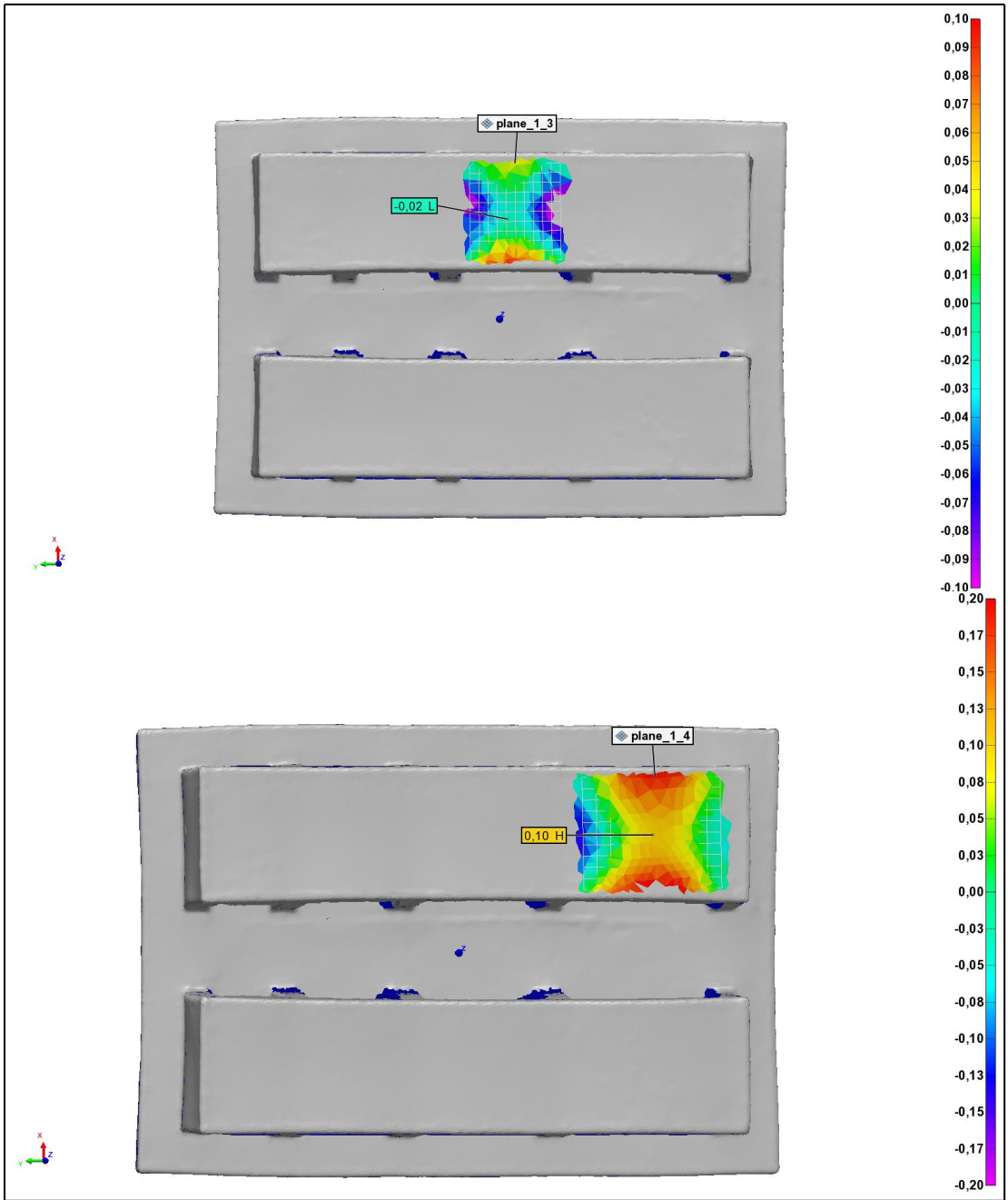

Organization:	Geometry verification center	**Part name:**	02_Bridg_Mock_Print_With_Base.STEP
Operator:	Anders Odham	**Part number:**	
E-mail:	anders.odhamii@volvocars.com	**Piece:**	piece 1

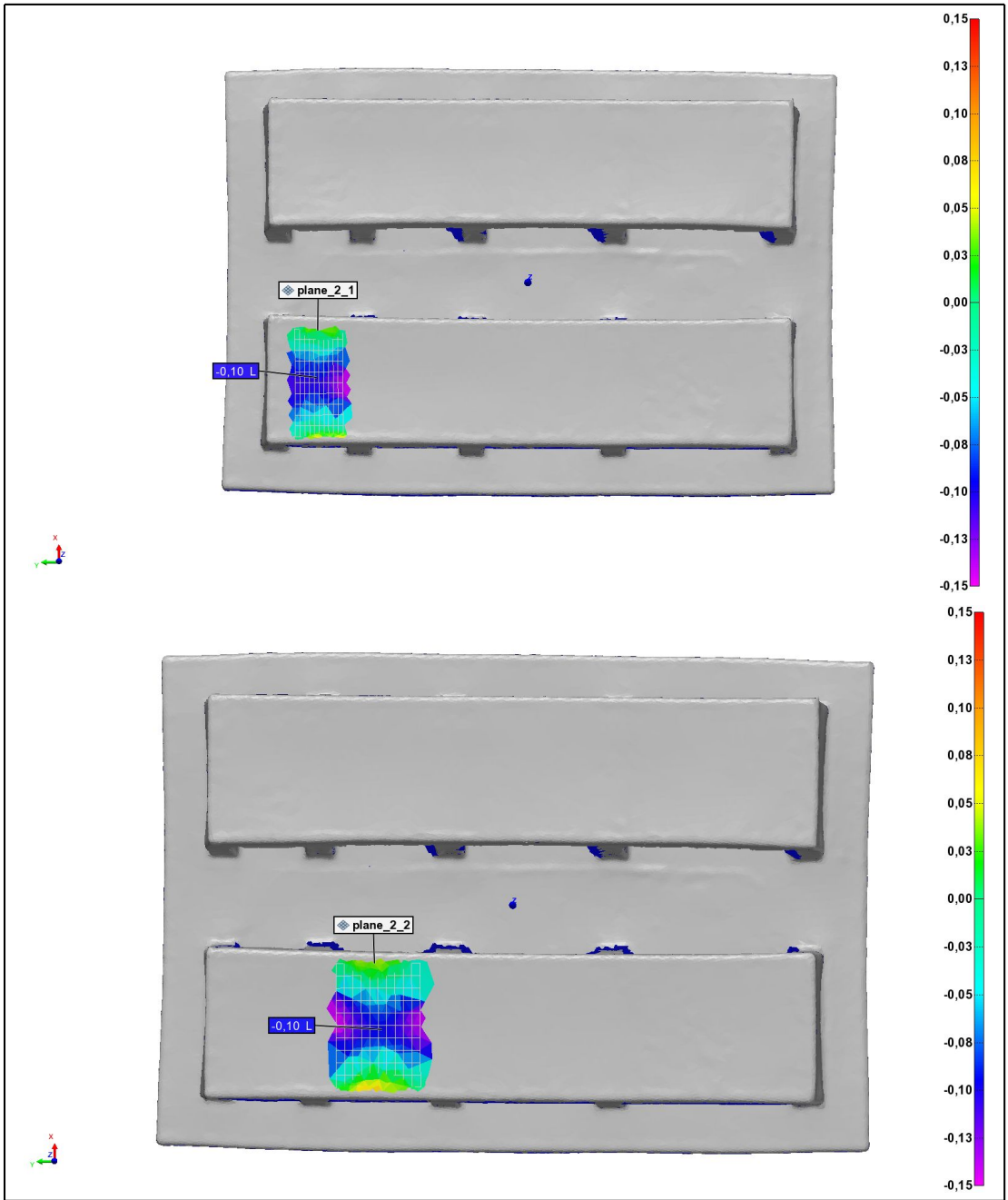

Organization:	Geometry verification center	**Part name:**	02_Bridg_Mock_Print_With_Base.STEP
Operator:	Anders Odham	**Part number:**	
E-mail:	anders.odhamii@volvocars.com	**Piece:**	piece 1

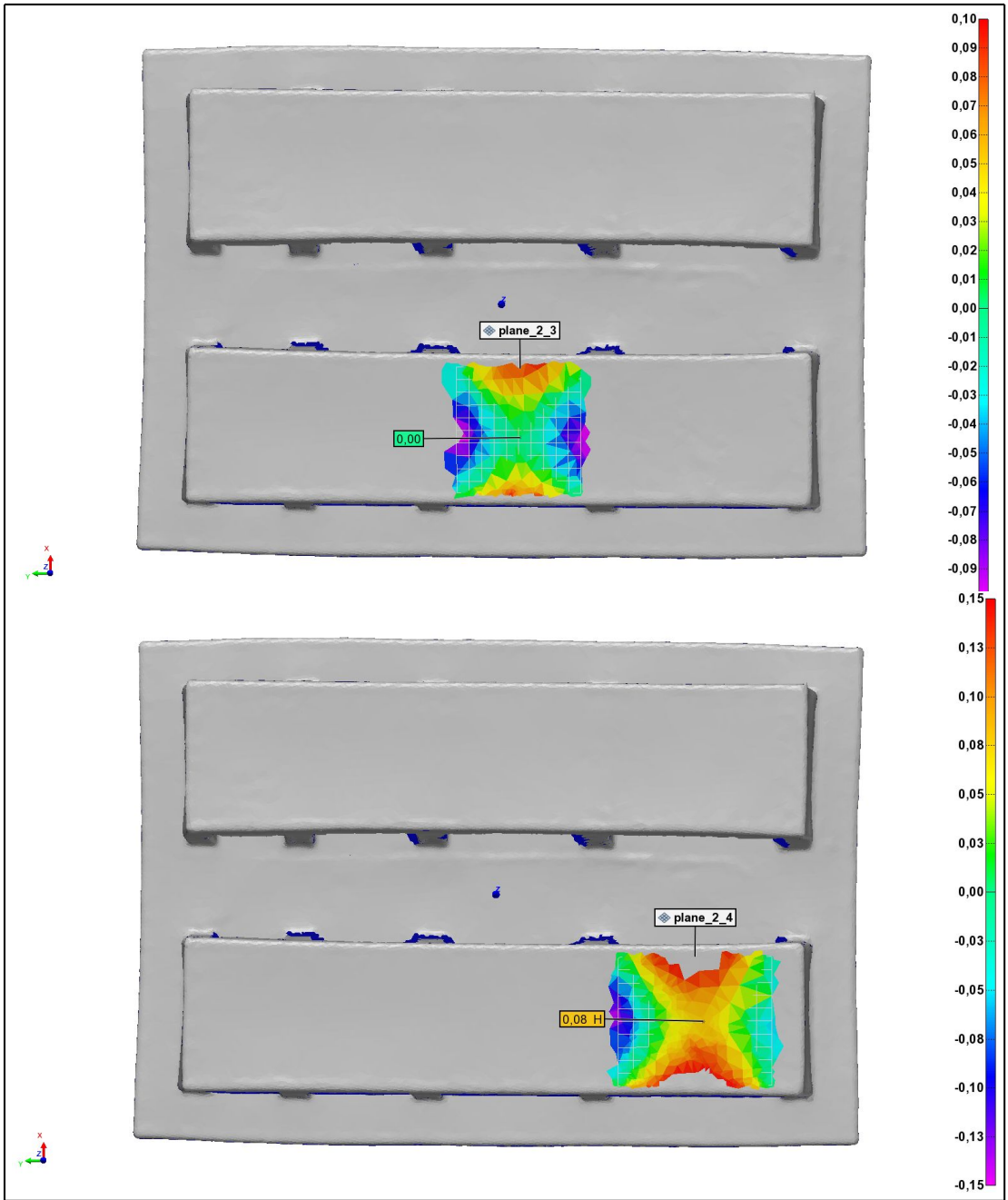

Organization:	Geometry verification center	**Part name:**	02_Bridg_Mock_Print_With_Base.STEP
Operator:	Anders Odham	**Part number:**	
E-mail:	anders.odhamii@volvocars.com	**Piece:**	piece 1

A.8 Artefact 5: Tree with ceramic-supported sintering

TREE_OHT_OHL_OHA

Report Author: Anders Odham
Date: 2023-06-27

Scanndata = Orange
Nufo = Gray

Align : Best-Fit

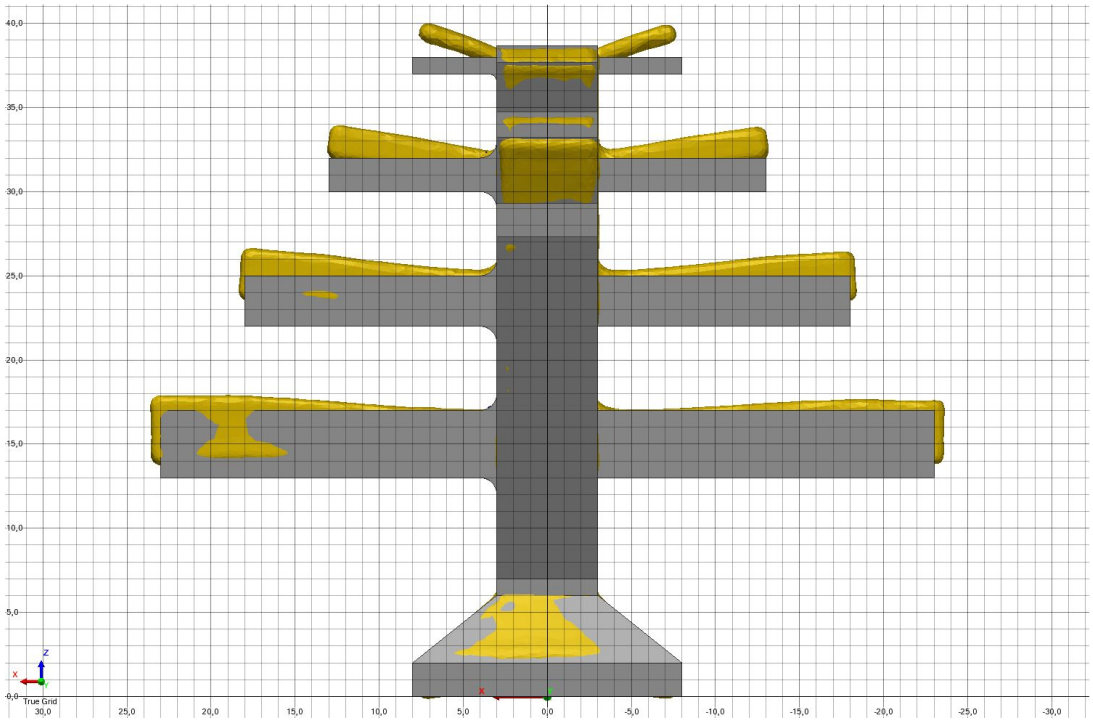

Organization:	Geometry verification center	Part name:	TREE_OHT_OHL_OHA
Operator:	Anders Odham	Part number:	
E-mail:	anders.odhamii@volvocars.com	Drawing #:	
Workspace:	Workspace 2	Serial #:	
Project:	NY_TREE_OHT_OHL_OHA -	Device:	Modelmaker H120 on MCAx

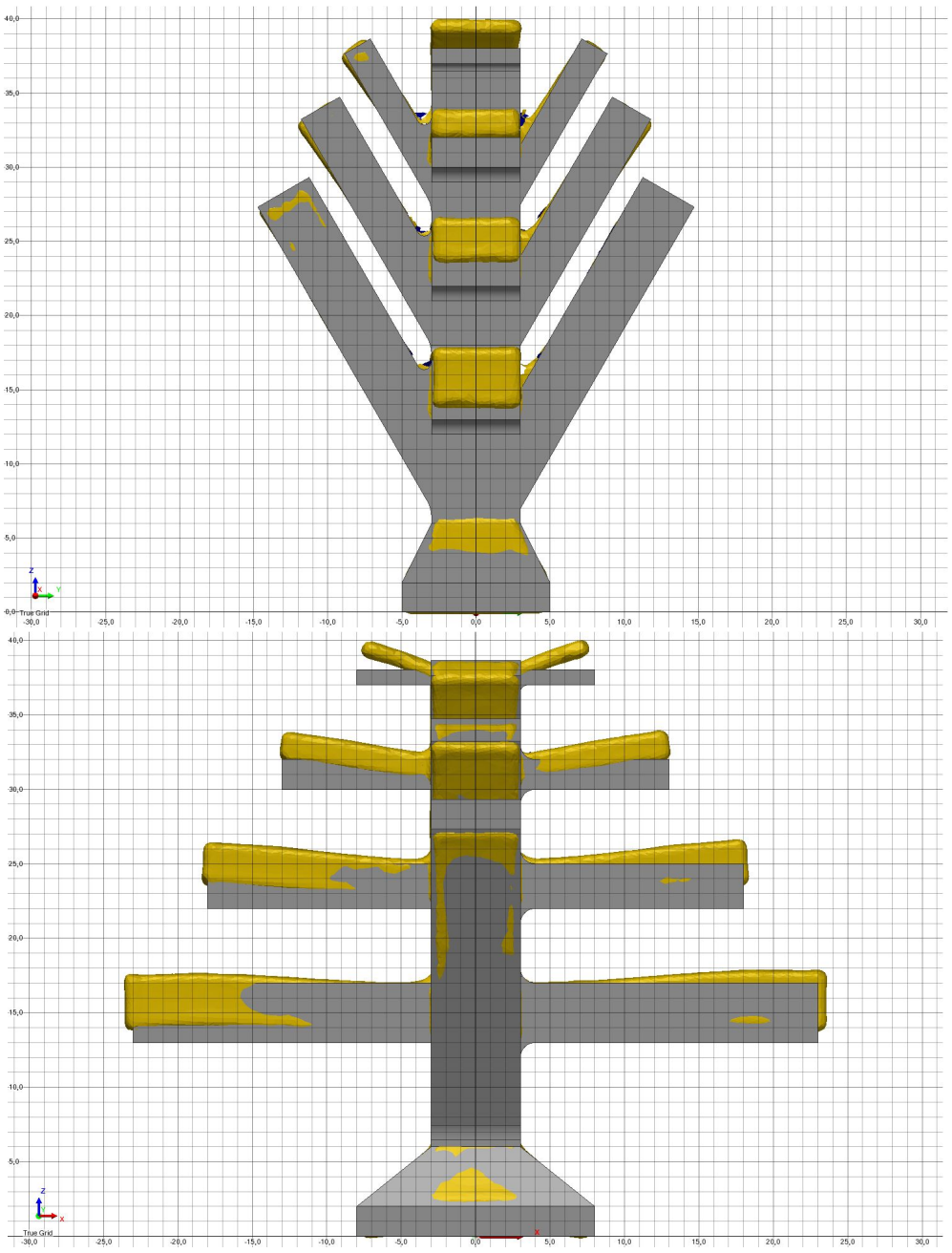

Organization:	Geometry verification center	**Part name:**	TREE_OHT_OHL_OHA
Operator:	Anders Odham	**Part number:**	
E-mail:	anders.odhamii@volvocars.com	**Piece:**	piece 1

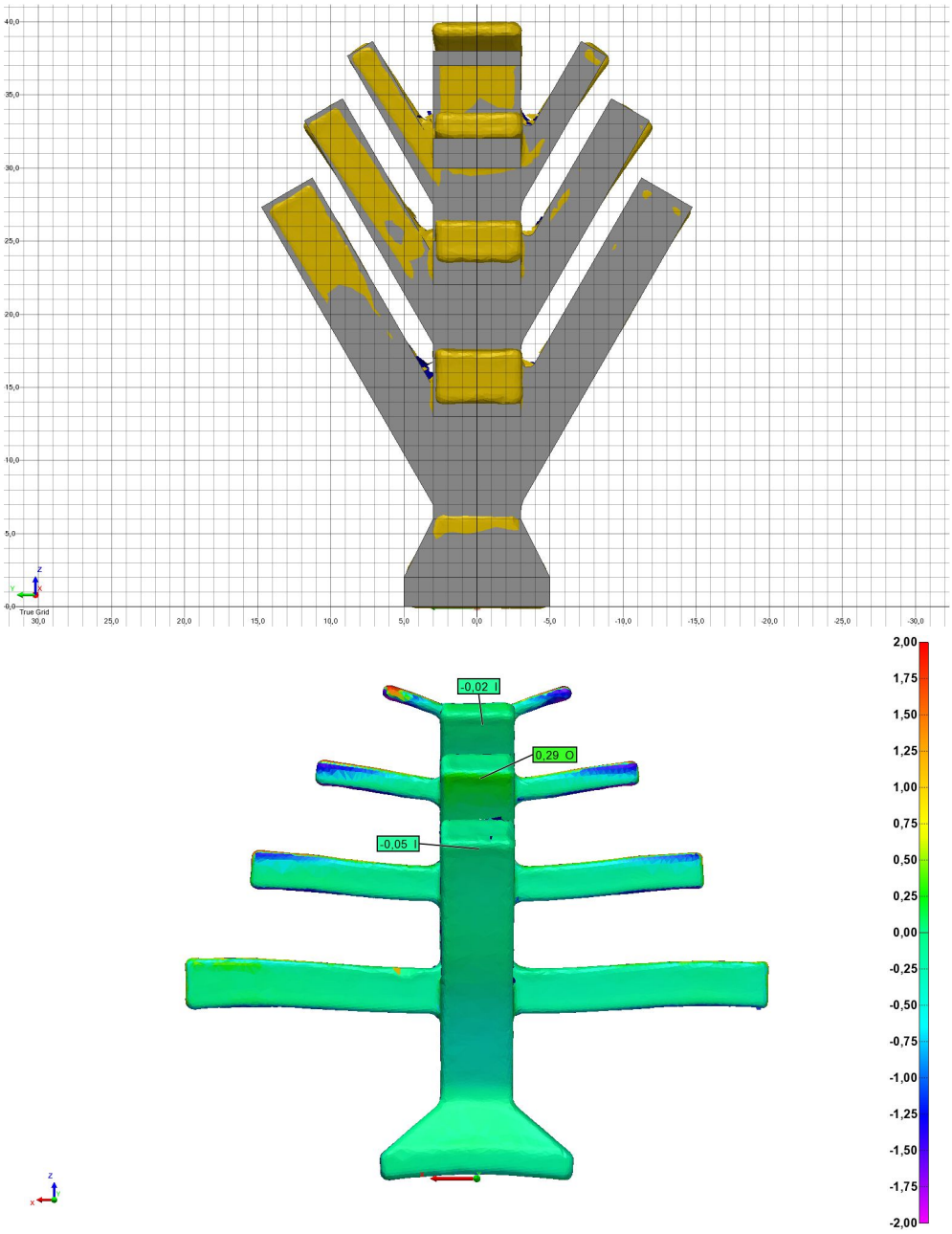

Organization:	Geometry verification center	**Part name:**	TREE_OHT_OHL_OHA
Operator:	Anders Odham	**Part number:**	
E-mail:	anders.odhamii@volvocars.com	**Piece:**	piece 1

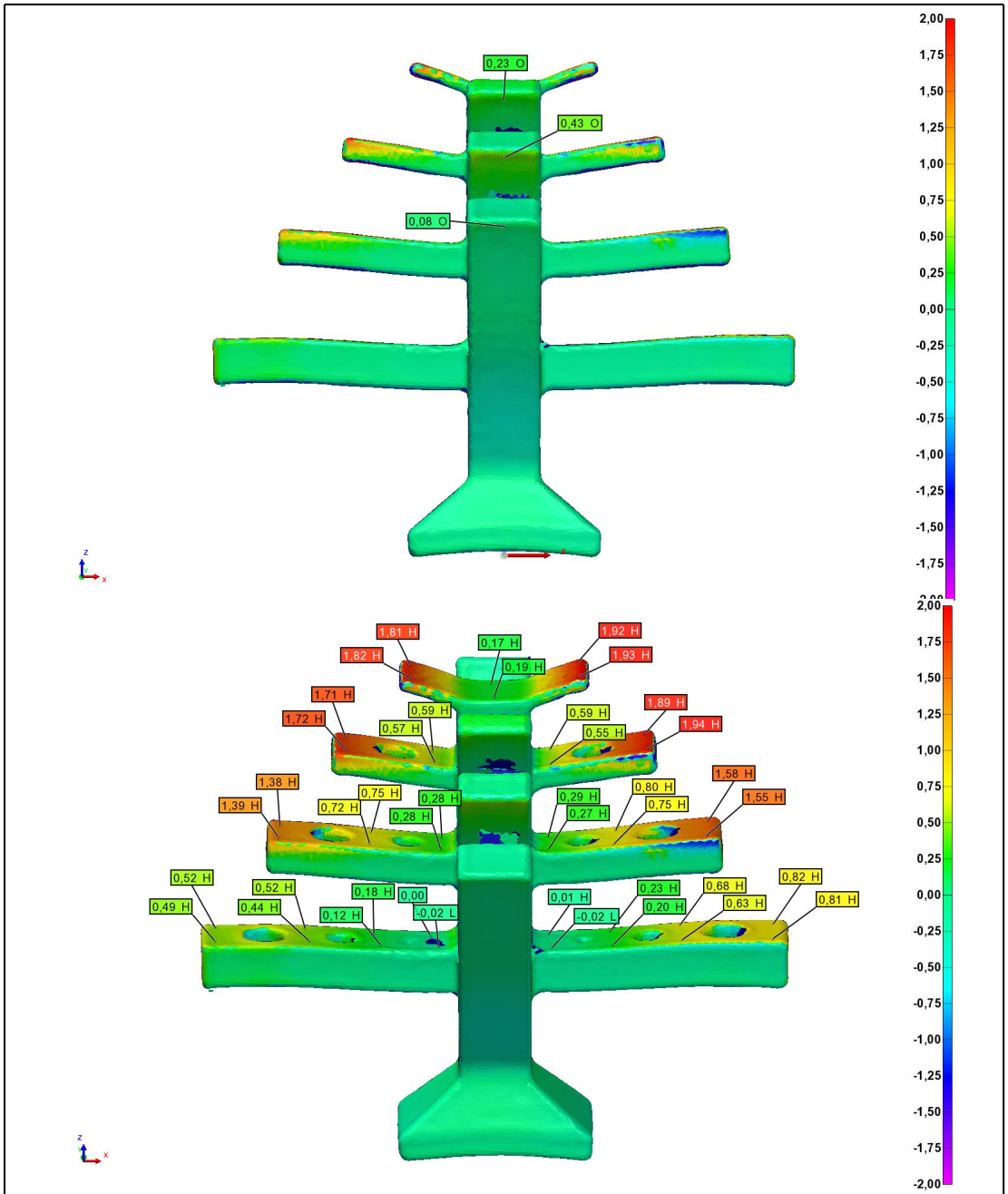

Organization:	Geometry verification center	**Part name:**	TREE_OHT_OHL_OHA
Operator:	Anders Odham	**Part number:**	
E-mail:	anders.odhamii@volvocars.com	**Piece:**	piece 1

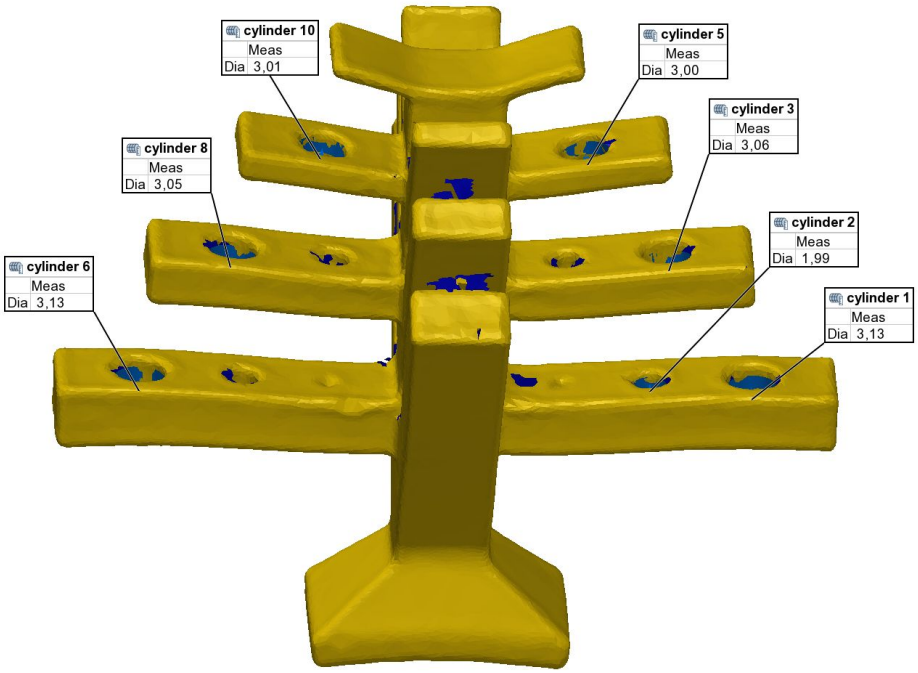

Organization:	Geometry verification center	**Part name:**	TREE_OHT_OHL_OHA
Operator:	Anders Odham	**Part number:**	
E-mail:	anders.odhamii@volvocars.com	**Piece:**	piece 1

A.9 Gyroid having 1mm thickness

PolyWorks by innovmetric

innovmetric

3D PRINT CUB 1

Report Author: Branko Markovic
Date: 2023-04-25

Gyroid 40X40X30_1mm

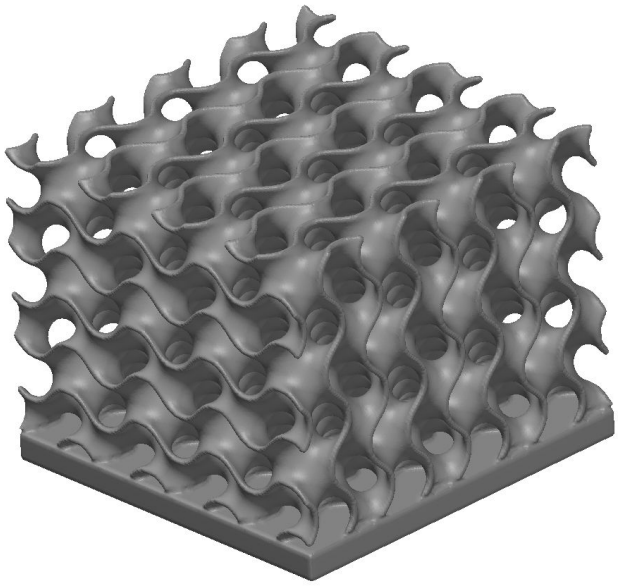

Organization:	Geometry Verification Center	**Part name:**	A02 1
Operator:	Branko Markovic	**Part number:**	Gyroid 40X40X30_1mm
E-mail:	bmarkovi@volvocars.com	**Drawing #:**	
Workspace:	3D PRINT CUB 1	**Serial #:**	
Project:	3D PRINT CUB 1 - piece 1	**Device:**	Modelmaker H 120

A02 1

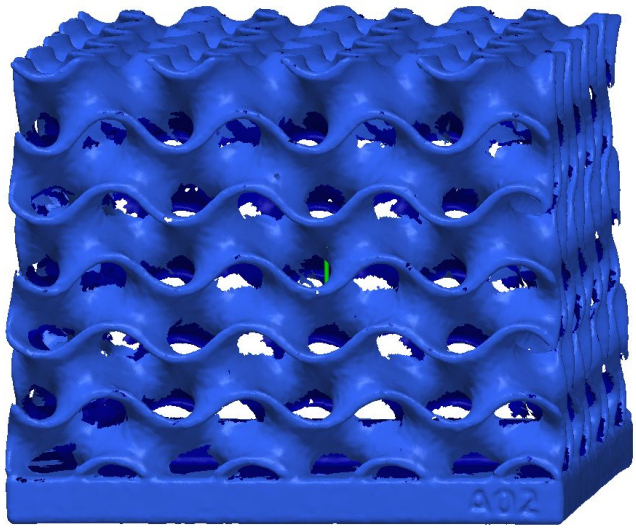

Organization:	Geometry Verification Center	**Part name:**	A02 1
Operator:	Branko Markovic	**Part number:**	Gyroid 40X40X30_1mm
E-mail:	bmarkovi@volvocars.com	**Piece:**	piece 1

RED PARTS USED FOR BESTFIT ALIGNMENT
OPPOSITE CORNER FROM NUMBERS

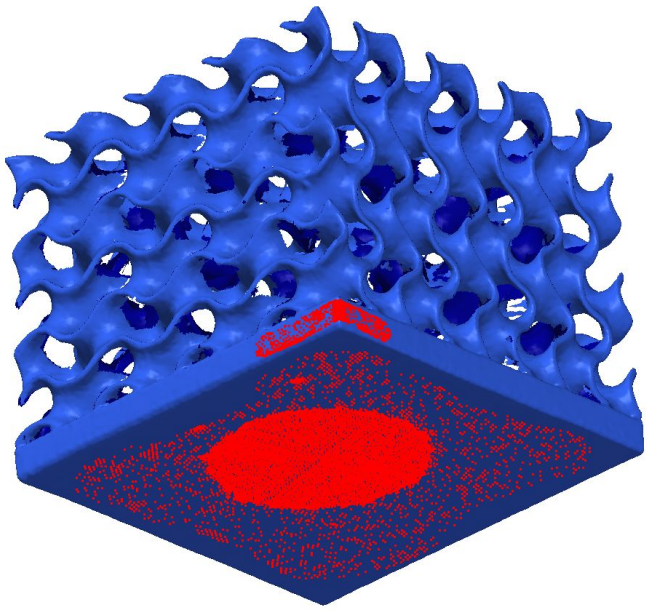

Organization:	Geometry Verification Center	**Part name:**	A02 1
Operator:	Branko Markovic	**Part number:**	Gyroid 40X40X30_1mm
E-mail:	bmarkovi@volvocars.com	**Piece:**	piece 1

TOLERANCE 3+/-3MM

Z X DIRECTION

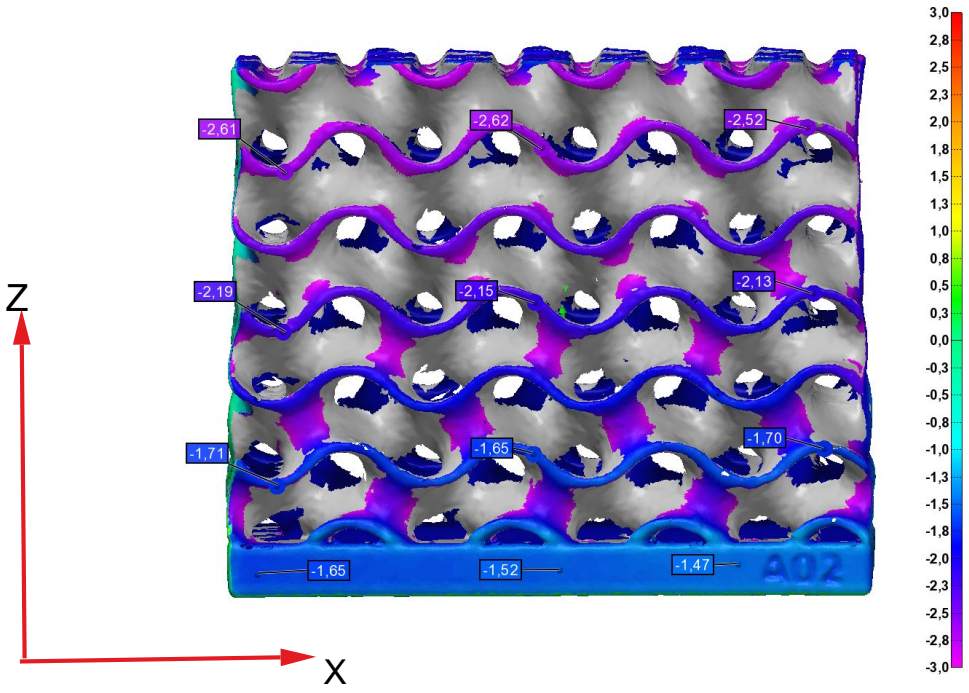

Organization:	Geometry Verification Center	**Part name:**	A02 1
Operator:	Branko Markovic	**Part number:**	Gyroid 40X40X30_1mm
E-mail:	bmarkovi@volvocars.com	**Piece:**	piece 1

TOLERANCE 3+/-3MM

Z Y DIRECTION

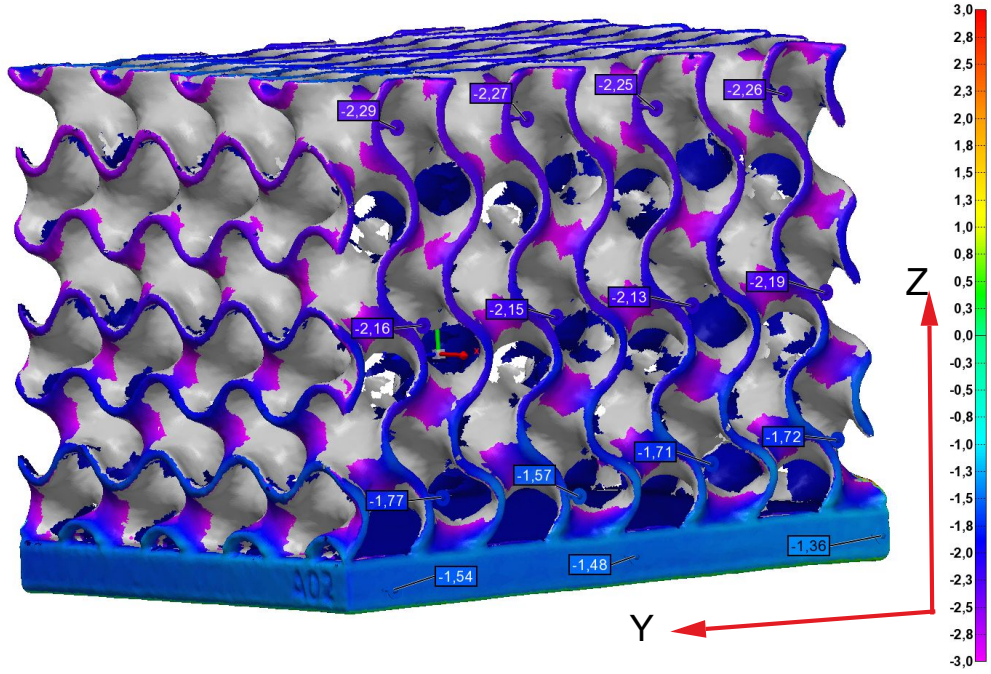

Organization:	Geometry Verification Center	**Part name:**	A02 1
Operator:	Branko Markovic	**Part number:**	Gyroid 40X40X30_1mm
E-mail:	bmarkovi@volvocars.com	**Piece:**	piece 1

TOLERANCE 3+/-3MM

Z X DIRECTION

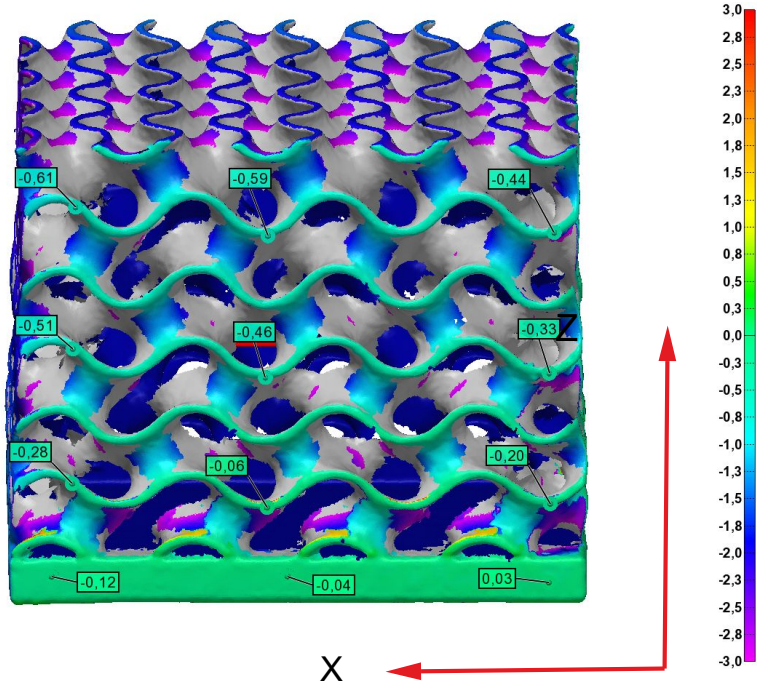

Organization:	Geometry Verification Center	**Part name:**	A02 1
Operator:	Branko Markovic	**Part number:**	Gyroid 40X40X30_1mm
E-mail:	bmarkovi@volvocars.com	**Piece:**	piece 1

TOLERANCE 3+/-3MM

Z Y DIRECTION

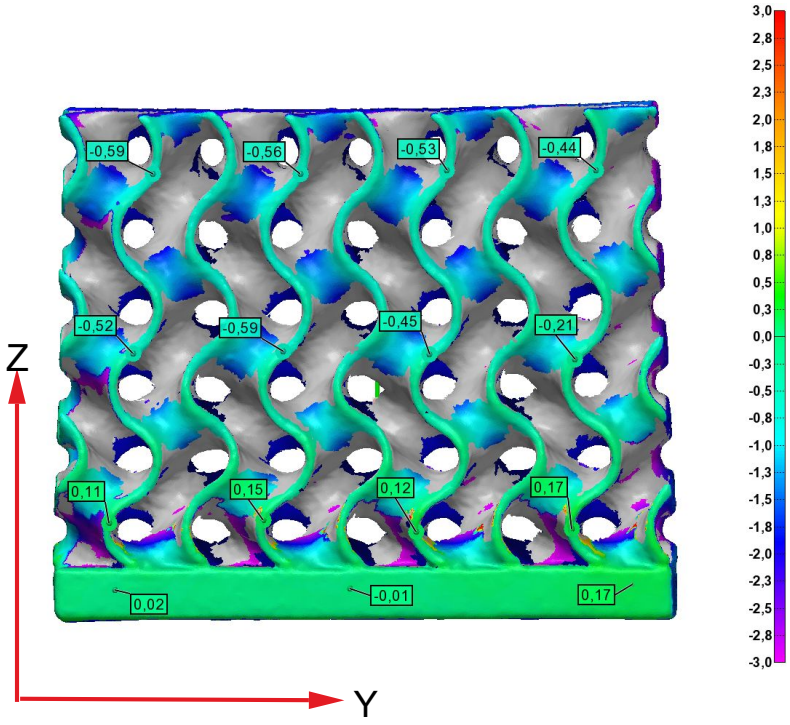

Organization:	Geometry Verification Center	**Part name:**	A02 1
Operator:	Branko Markovic	**Part number:**	Gyroid 40X40X30_1mm
E-mail:	bmarkovi@volvocars.com	**Piece:**	piece 1

TOLERANCE 3+/-3MM

TOP VIEW

X Y DIRECTION

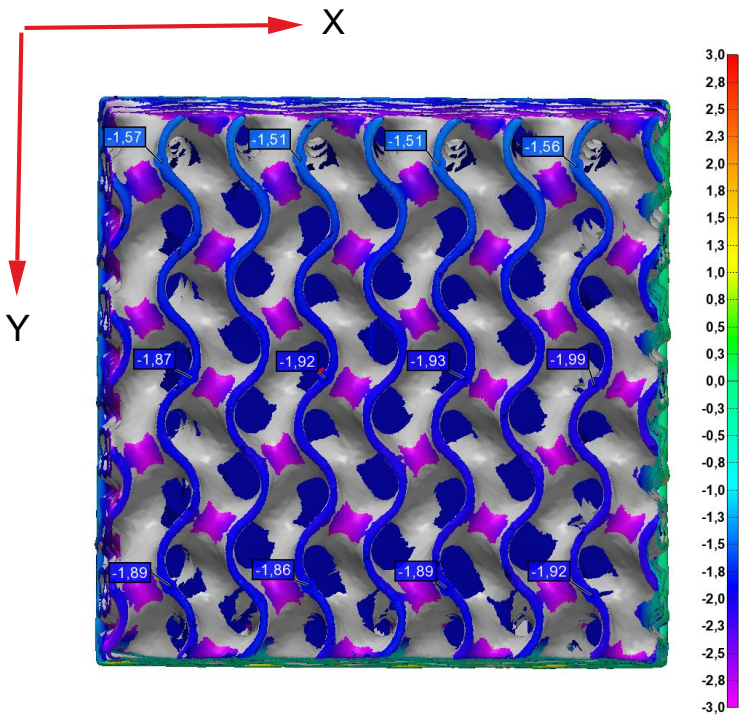

Organization:	Geometry Verification Center	**Part name:**	A02 1
Operator:	Branko Markovic	**Part number:**	Gyroid 40X40X30_1mm
E-mail:	bmarkovi@volvocars.com	**Piece:**	piece 1

A.10 Gyroid having 1.5mm thickness

PolyWorks by innovmetric

innovmetric

3D PRINT CUB 1,5

Report Author: Branko Markovic
Date: 2023-04-25

Gyroid 40X40X30_1,5mm

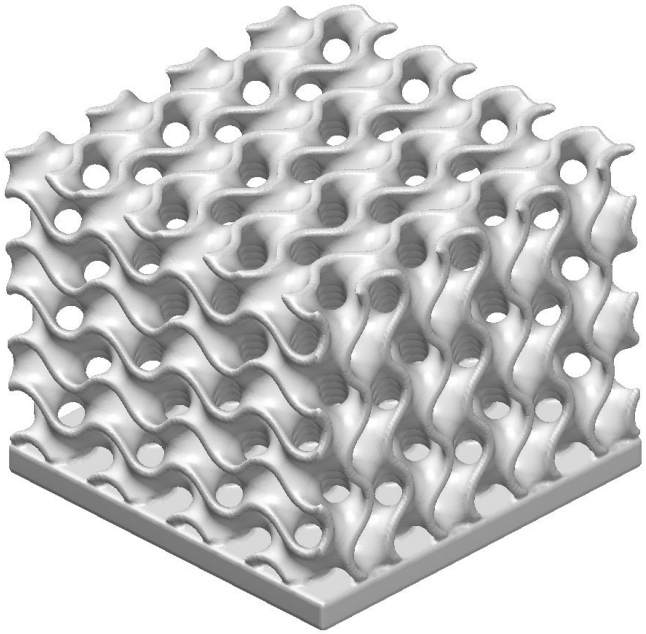

Organization:	Geometry Verification Center	**Part name:**	B02 1,5
Operator:	Branko Markovic	**Part number:**	Gyroid 40X40X30_1,5mm
E-mail:	bmarkovi@volvocars.com	**Drawing #:**	
Workspace:	3D PRINT CUB 1	**Serial #:**	
Project:	3D PRINT CUB 1,5 - piece 1	**Device:**	Modelmaker H 120

B02 1,5

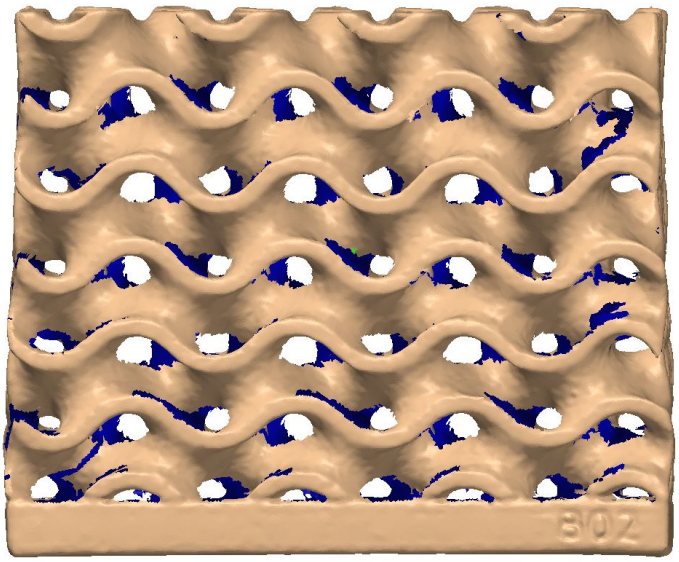

Organization:	Geometry Verification Center	**Part name:**	B02 1,5
Operator:	Branko Markovic	**Part number:**	Gyroid 40X40X30_1,5mm
E-mail:	bmarkovi@volvocars.com	**Piece:**	piece 1

RED PARTS USED FOR BESTFIT ALIGNMENT
OPPOSITE CORNER FROM NUMBERS

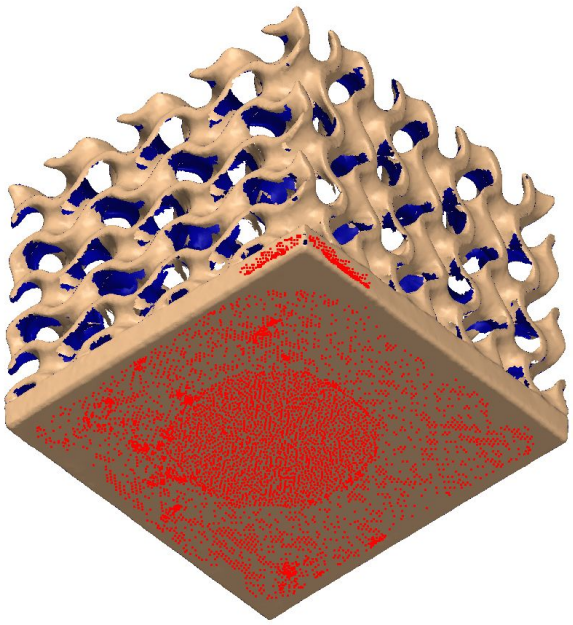

Organization:	Geometry Verification Center	**Part name:**	B02 1,5
Operator:	Branko Markovic	**Part number:**	Gyroid 40X40X30_1,5mm
E-mail:	bmarkovi@volvocars.com	**Piece:**	piece 1

TOLERANCE 3+/-3MM

Z X DIRECTION

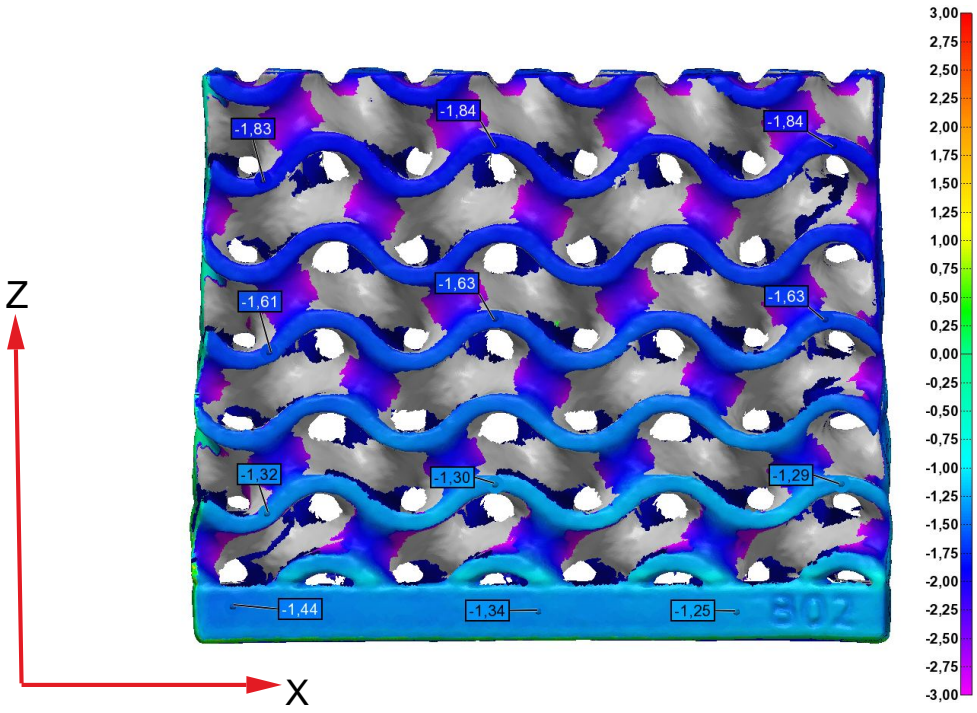

Organization:	Geometry Verification Center	**Part name:**	B02 1,5
Operator:	Branko Markovic	**Part number:**	Gyroid 40X40X30_1,5mm
E-mail:	bmarkovi@volvocars.com	**Piece:**	piece 1

TOLERANCE 3+/-3MM

Z Y DIRECTION

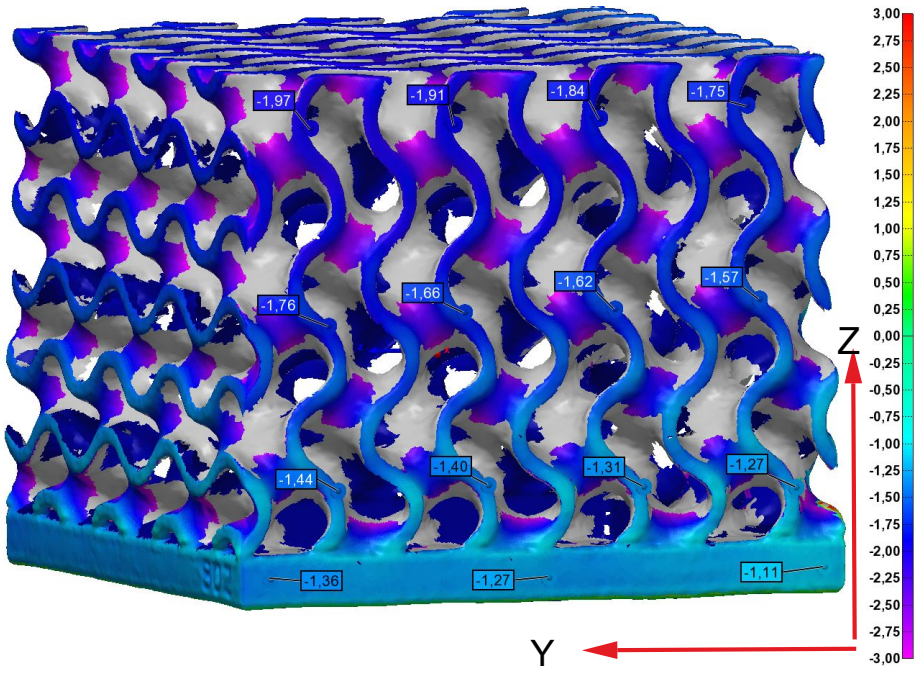

Organization:	Geometry Verification Center	**Part name:**	B02 1,5
Operator:	Branko Markovic	**Part number:**	Gyroid 40X40X30_1,5mm
E-mail:	bmarkovi@volvocars.com	**Piece:**	piece 1

TOLERANCE 3+/-3MM

Z X DIRECTION

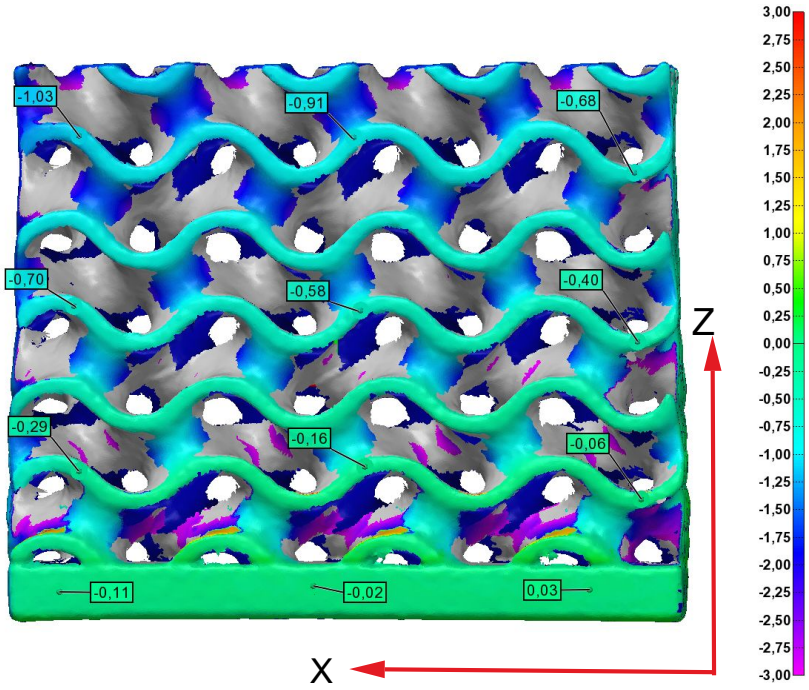

Organization:	Geometry Verification Center	**Part name:**	B02 1,5
Operator:	Branko Markovic	**Part number:**	Gyroid 40X40X30_1,5mm
E-mail:	bmarkovi@volvocars.com	**Piece:**	piece 1

TOLERANCE 3+/-3MM

Z Y DIRECTION

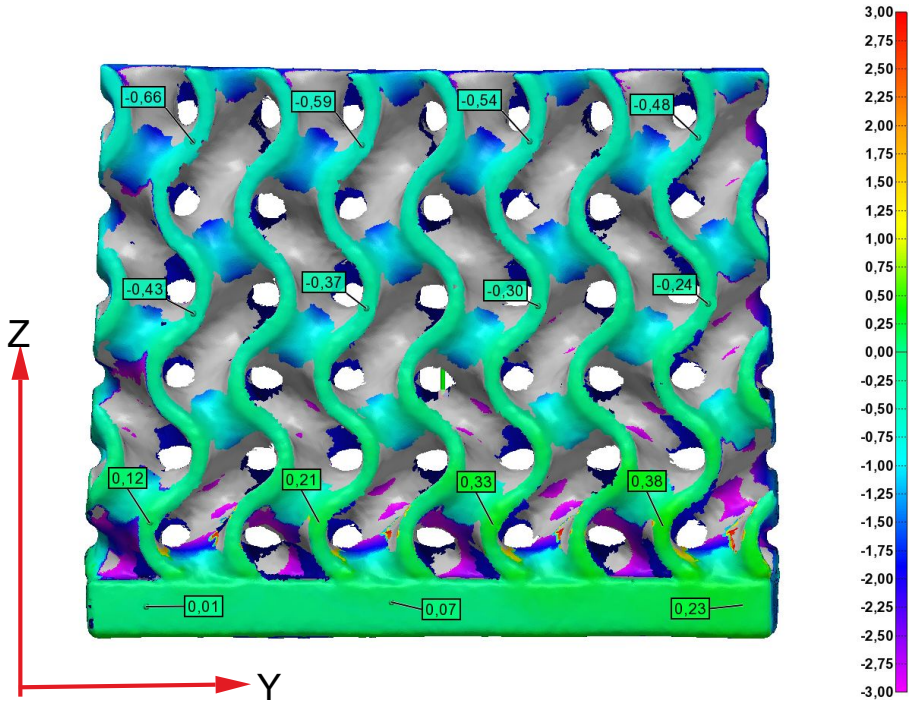

Organization:	Geometry Verification Center	**Part name:**	B02 1,5
Operator:	Branko Markovic	**Part number:**	Gyroid 40X40X30_1,5mm
E-mail:	bmarkovi@volvocars.com	**Piece:**	piece 1

TOLERANCE 3+/-3MM

TOP VIEW

X Y DIRECTION

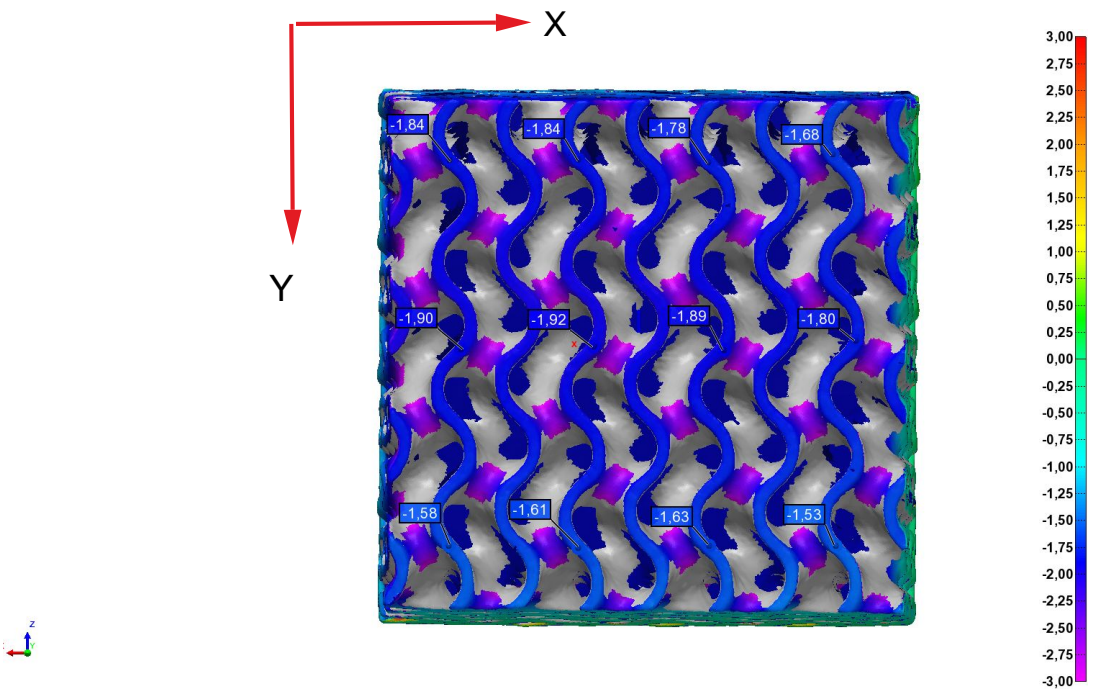

Organization:	Geometry Verification Center	**Part name:**	B02 1,5
Operator:	Branko Markovic	**Part number:**	Gyroid 40X40X30_1,5mm
E-mail:	bmarkovi@volvocars.com	**Piece:**	piece 1

A.11 Gyroid having 2mm thickness

PolyWorks by innovmetric

innovmetric

3D PRINT CUB 2

Report Author: Branko Markovic
Date: 2023-04-25

Gyroid 40X40X30_2mm

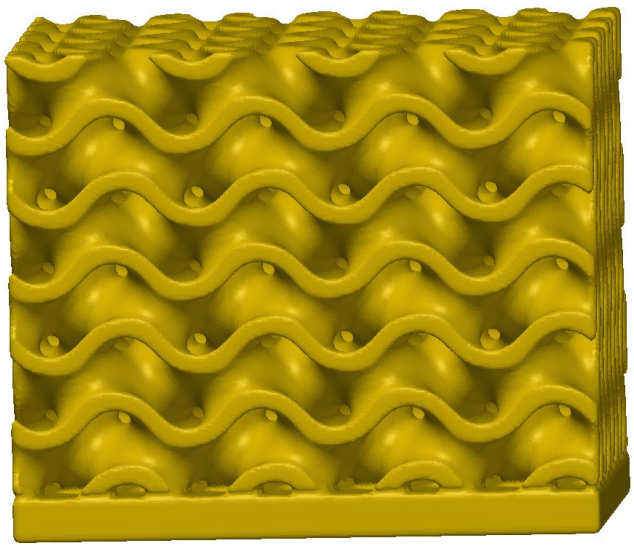

Organization:	Geometry Verification Center	**Part name:**	C02 2
Operator:	Branko Markovic	**Part number:**	Gyroid 40X40X30_2mm
E-mail:	bmarkovi@volvocars.com	**Drawing #:**	
Workspace:	3D PRINT CUB 1	**Serial #:**	
Project:	3D PRINT CUB 2 - piece 1	**Device:**	Modelmaker H 120

C02 2

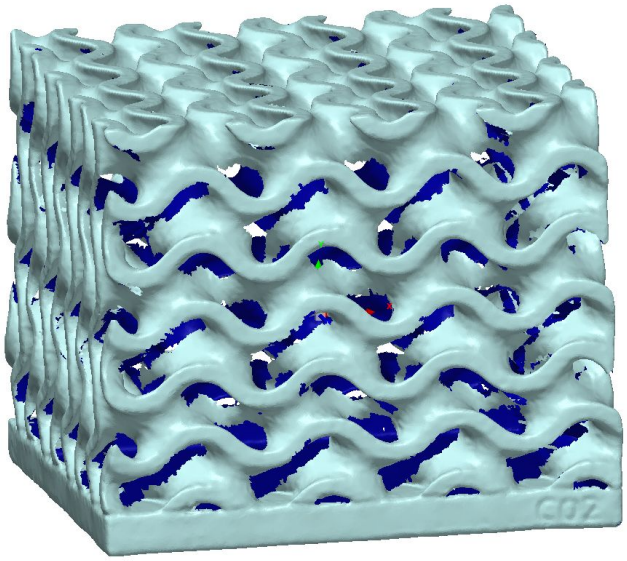

Organization:	Geometry Verification Center	**Part name:**	C02 2
Operator:	Branko Markovic	**Part number:**	Gyroid 40X40X30_2mm
E-mail:	bmarkovi@volvocars.com	**Piece:**	piece 1

RED PARTS USED FOR BESTFIT ALIGNMENT
OPPOSITE CORNER FROM NUMBERS

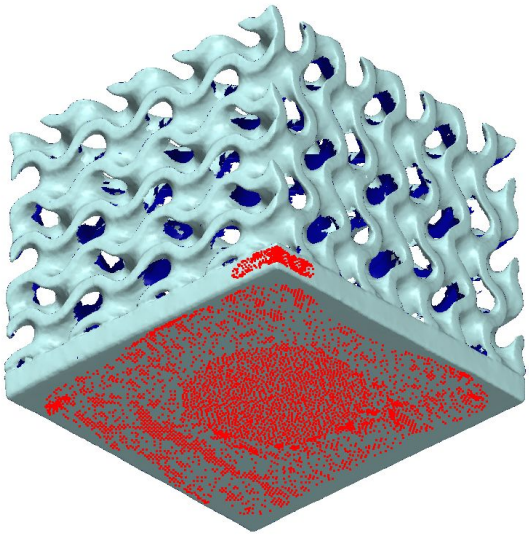

Organization:	Geometry Verification Center	**Part name:**	C02 2
Operator:	Branko Markovic	**Part number:**	Gyroid 40X40X30_2mm
E-mail:	bmarkovi@volvocars.com	**Piece:**	piece 1

TOLERANCE 3+/-3MM

Z X DIRECTION

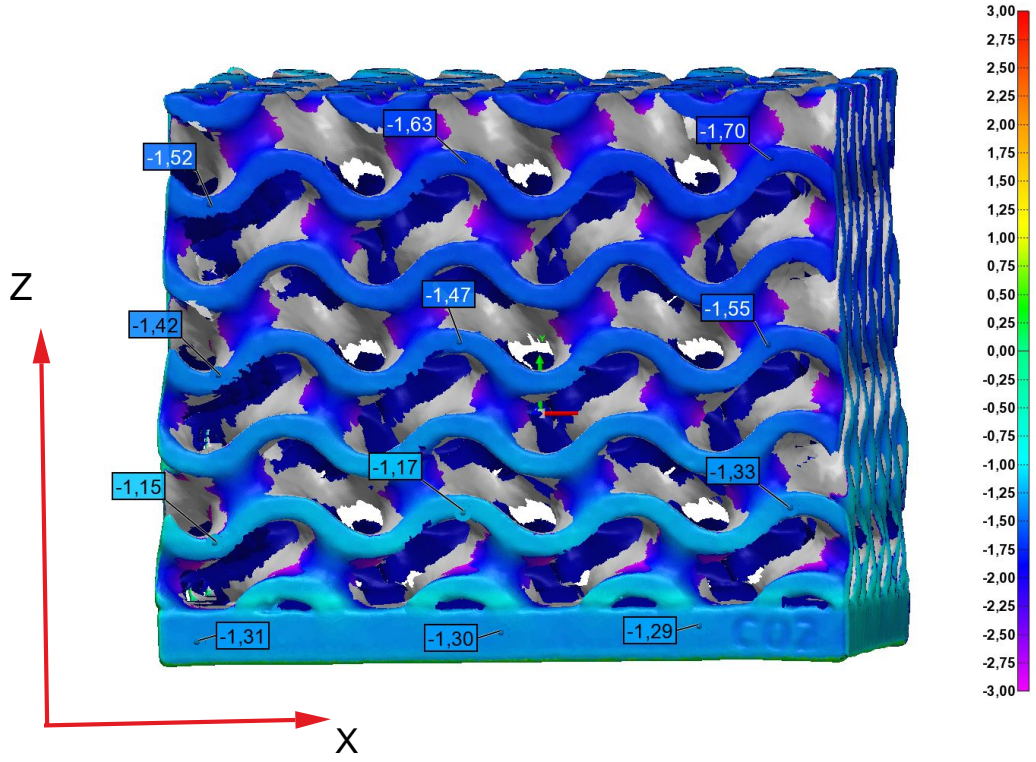

Organization:	Geometry Verification Center	**Part name:**	C02 2
Operator:	Branko Markovic	**Part number:**	Gyroid 40X40X30_2mm
E-mail:	bmarkovi@volvocars.com	**Piece:**	piece 1

TOLERANCE 3+/-3MM

Z Y DIRECTION

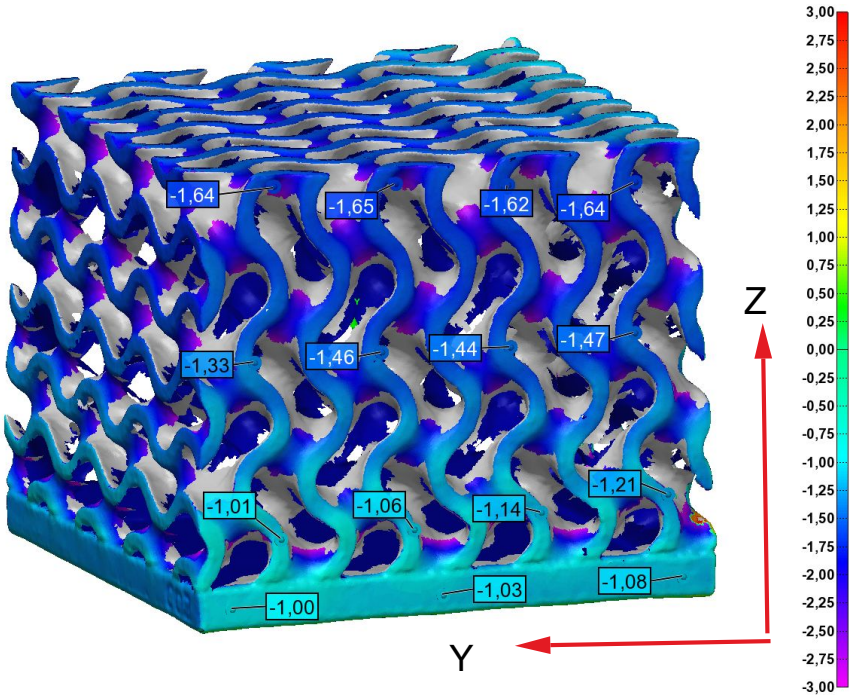

Organization:	Geometry Verification Center	**Part name:**	C02 2
Operator:	Branko Markovic	**Part number:**	Gyroid 40X40X30_2mm
E-mail:	bmarkovi@volvocars.com	**Piece:**	piece 1

TOLERANCE 3+/-3MM

Z X DIRECTION

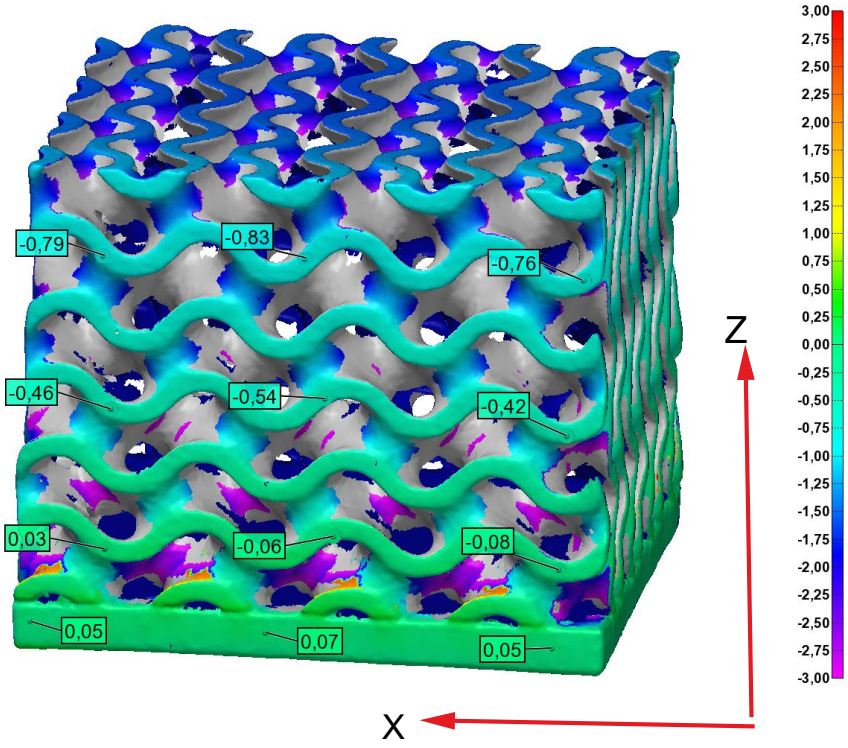

Organization:	Geometry Verification Center	**Part name:**	C02 2
Operator:	Branko Markovic	**Part number:**	Gyroid 40X40X30_2mm
E-mail:	bmarkovi@volvocars.com	**Piece:**	piece 1

TOLERANCE 3+/-3MM

Z Y DIRECTION

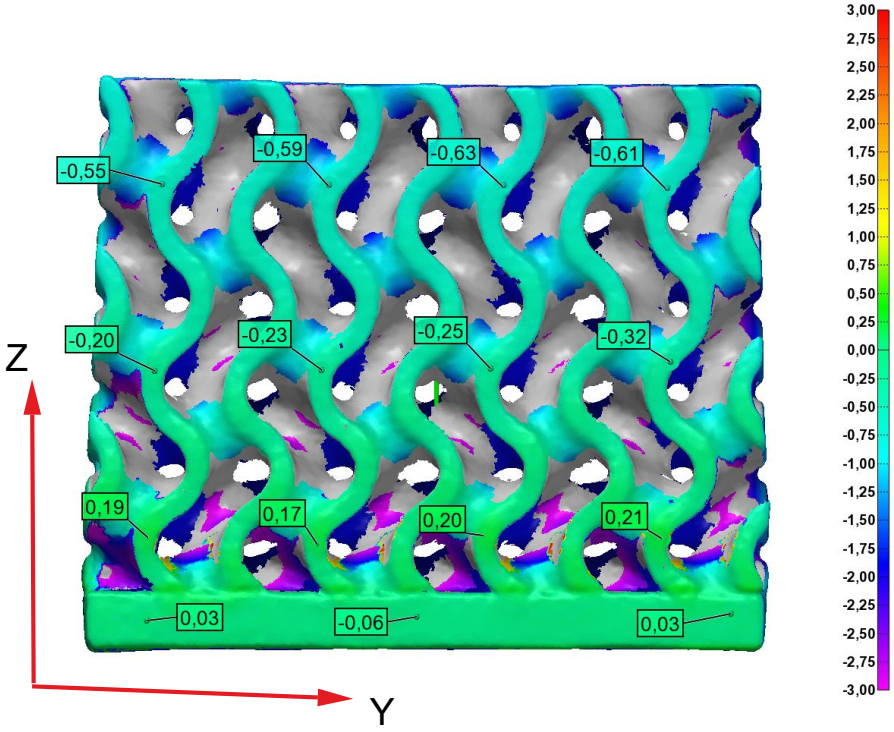

Organization:	Geometry Verification Center	**Part name:**	C02 2
Operator:	Branko Markovic	**Part number:**	Gyroid 40X40X30_2mm
E-mail:	bmarkovi@volvocars.com	**Piece:**	piece 1

TOLERANCE 3+/-3MM

X Y DIRECTION

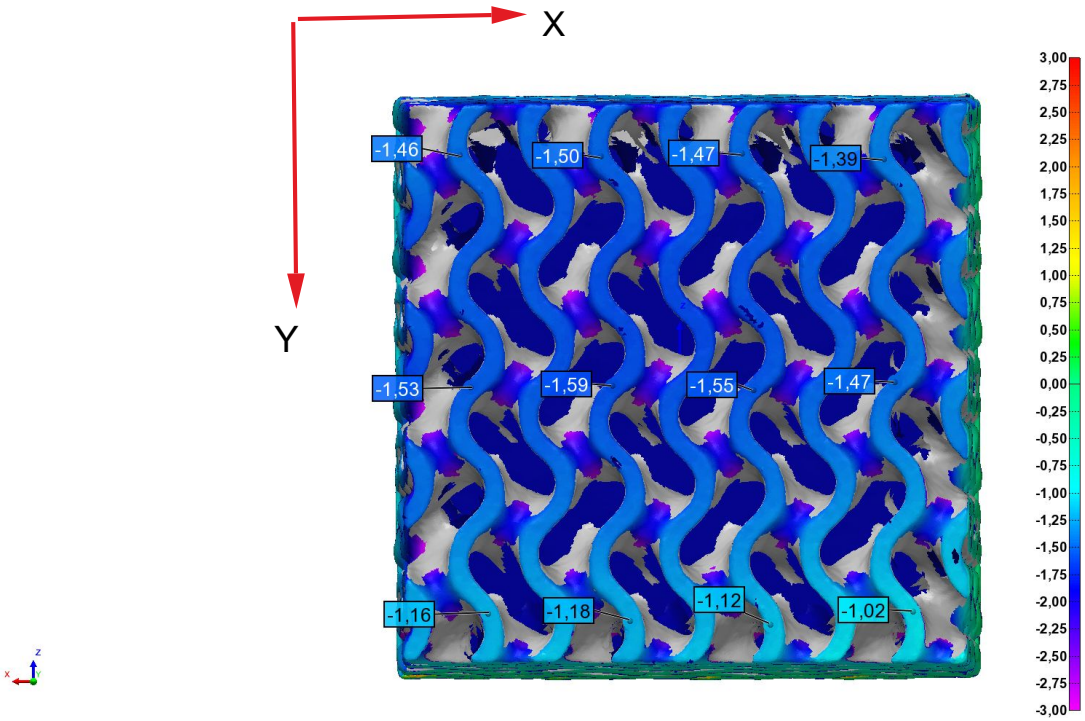

Organization:	Geometry Verification Center	**Part name:**	C02 2
Operator:	Branko Markovic	**Part number:**	Gyroid 40X40X30_2mm
E-mail:	bmarkovi@volvocars.com	**Piece:**	piece 1

A.12 Gyroid having 2 to 1mm thickness

PolyWorks by innovmetric

innovmetric

3D PRINT CUB 2 TO 1

Report Author: Branko Markovic
Date: 2023-04-24

Gyroid 40X40X30_2to1mm

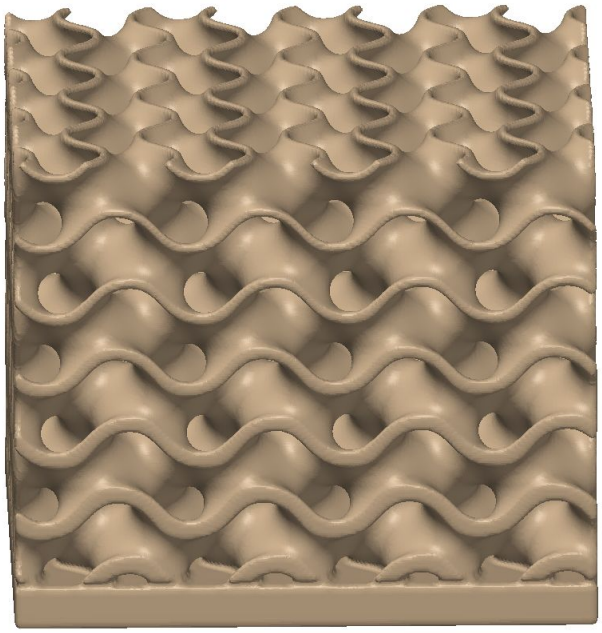

Organization:	Geometry Verification Center	**Part name:**	D02 2 TO 1
Operator:	Branko Markovic	**Part number:**	Gyroid 40X40X30_2to1mm
E-mail:	bmarkovi@volvocars.com	**Drawing #:**	
Workspace:	3D PRINT CUB 1	**Serial #:**	
Project:	3D PRINT CUB 2 TO 1 - piece 1	**Device:**	Modelmaker H 120

D02 2 TO 1

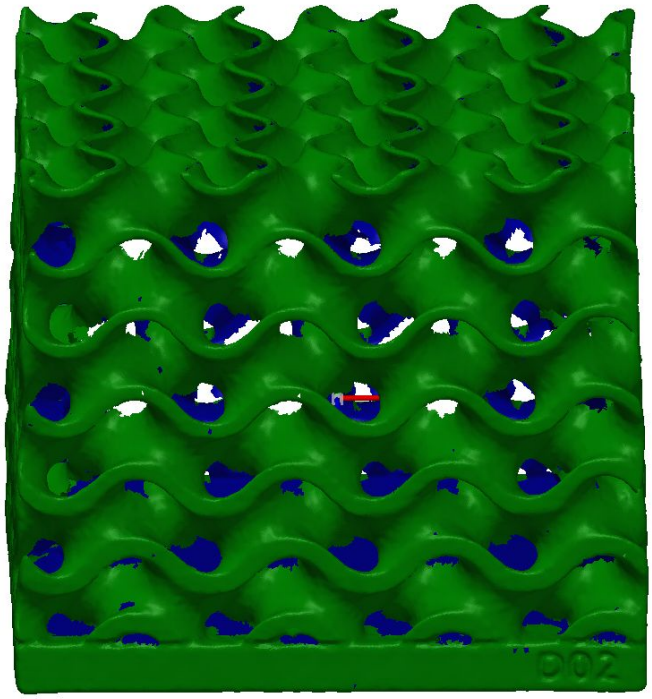

Organization:	Geometry Verification Center	**Part name:**	D02 2 TO 1
Operator:	Branko Markovic	**Part number:**	Gyroid 40X40X30_2to1mm
E-mail:	bmarkovi@volvocars.com	**Piece:**	piece 1

RED PARTS USED FOR BESTFIT ALIGNMENT
OPPOSITE CORNER FROM NUMBERS

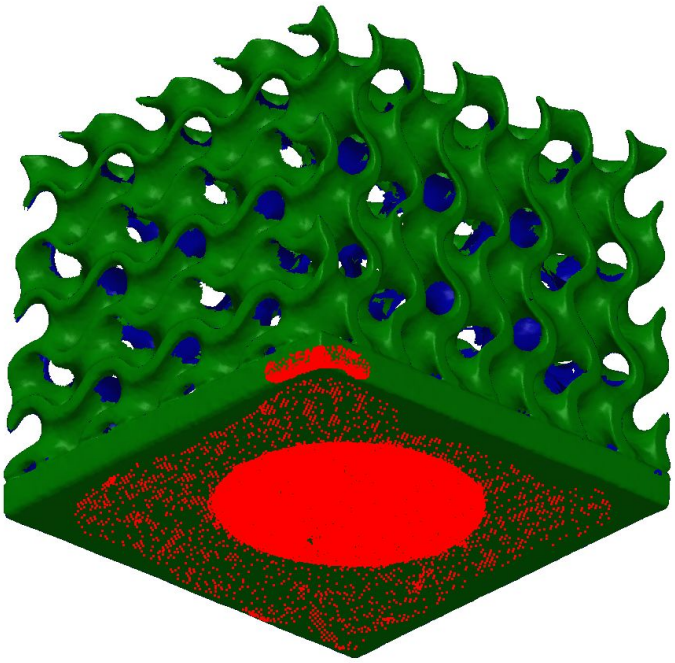

Organization:	Geometry Verification Center	**Part name:**	D02 2 TO 1
Operator:	Branko Markovic	**Part number:**	Gyroid 40X40X30_2to1mm
E-mail:	bmarkovi@volvocars.com	**Piece:**	piece 1

TOLERANCE 3+/-3MM

Z X DIRECTION

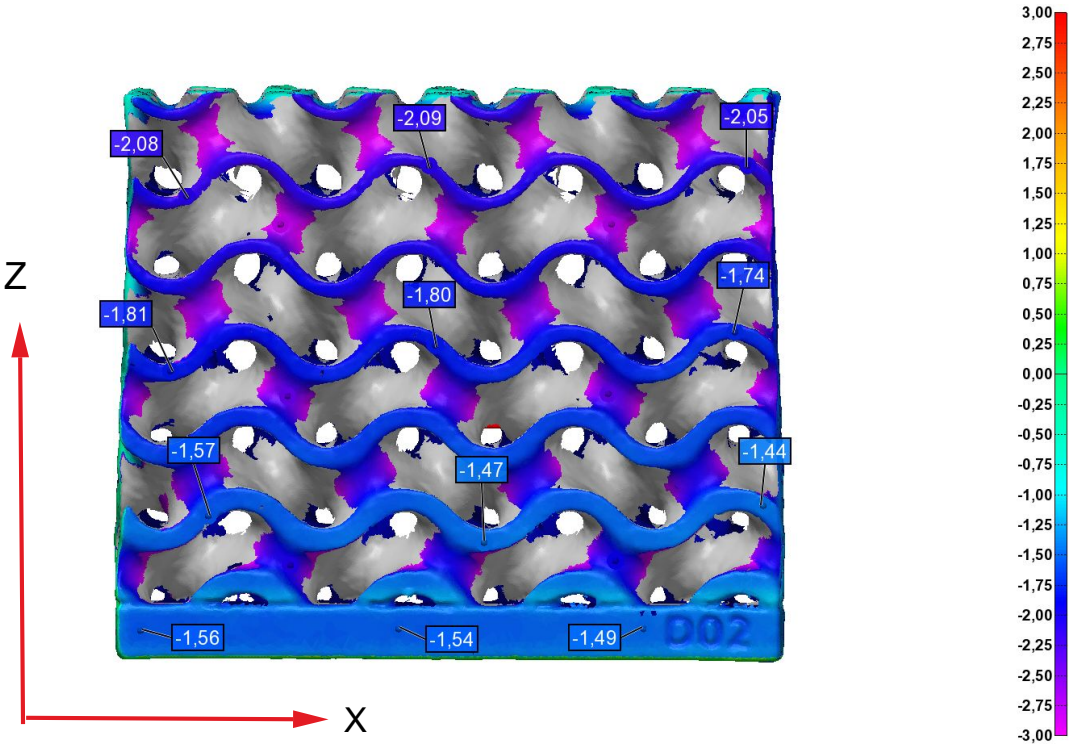

Organization:	Geometry Verification Center	**Part name:**	D02 2 TO 1
Operator:	Branko Markovic	**Part number:**	Gyroid 40X40X30_2to1mm
E-mail:	bmarkovi@volvocars.com	**Piece:**	piece 1

TOLERANCE 3+/-3MM

Z Y DIRECTION

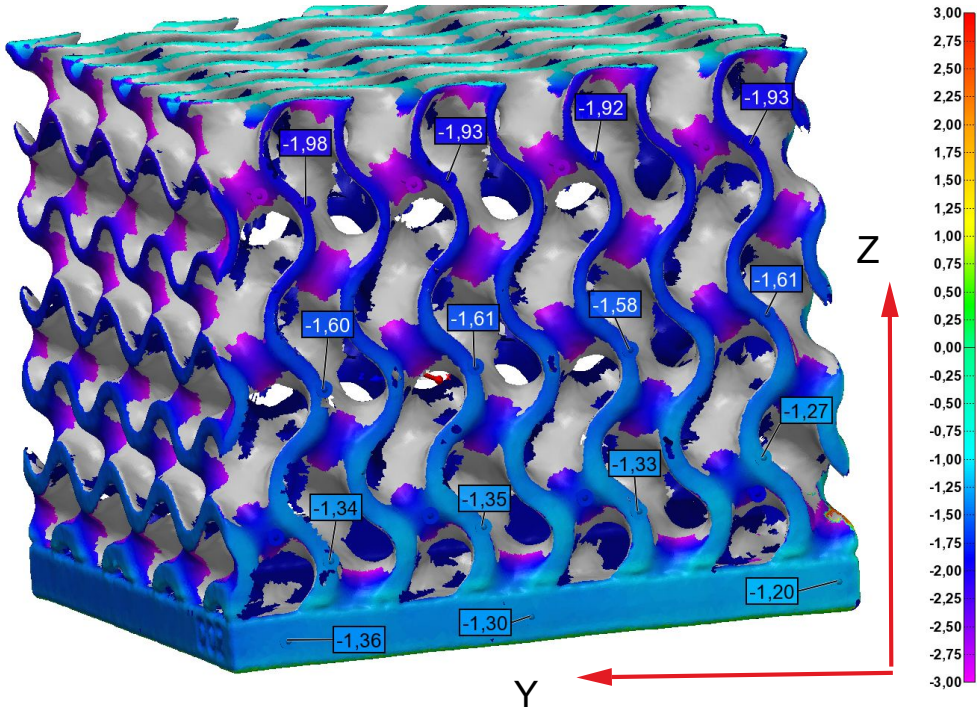

Organization:	Geometry Verification Center	**Part name:**	D02 2 TO 1
Operator:	Branko Markovic	**Part number:**	Gyroid 40X40X30_2to1mm
E-mail:	bmarkovi@volvocars.com	**Piece:**	piece 1

TOLERANCE 3+/-3MM

Z X DIRECTION

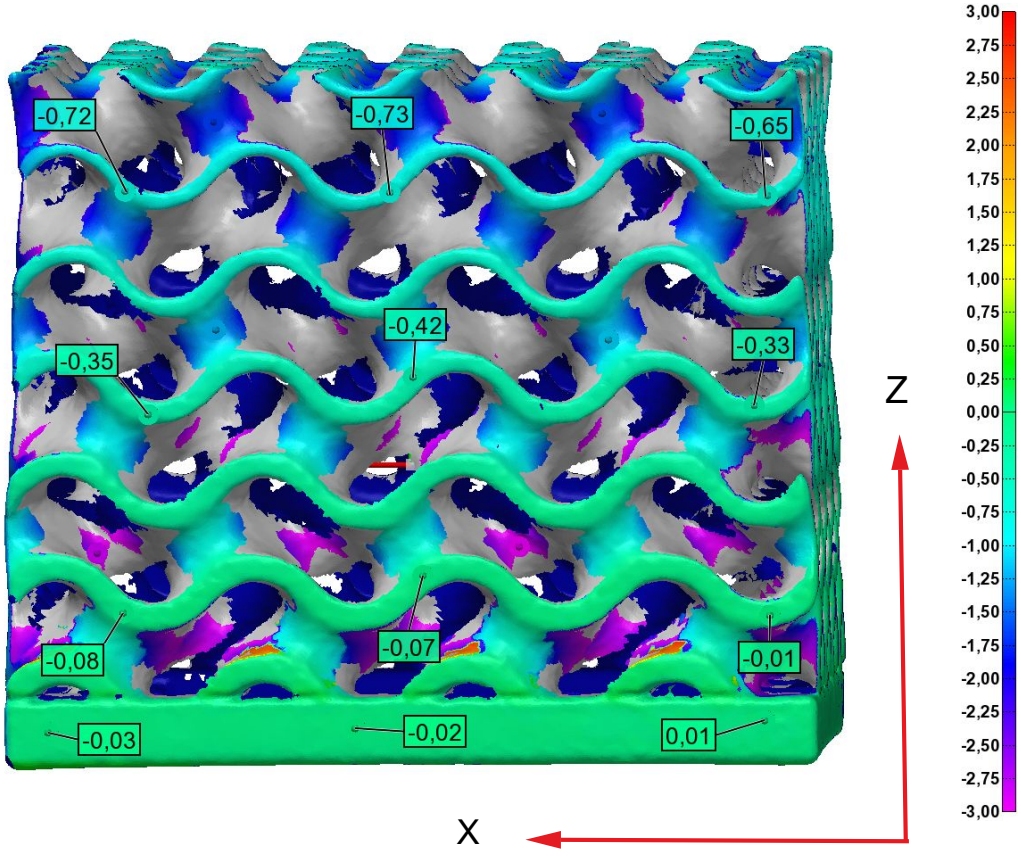

Organization:	Geometry Verification Center	**Part name:**	D02 2 TO 1
Operator:	Branko Markovic	**Part number:**	Gyroid 40X40X30_2to1mm
E-mail:	bmarkovi@volvocars.com	**Piece:**	piece 1

TOLERANCE 3+/-3MM

Z Y DIRECTION

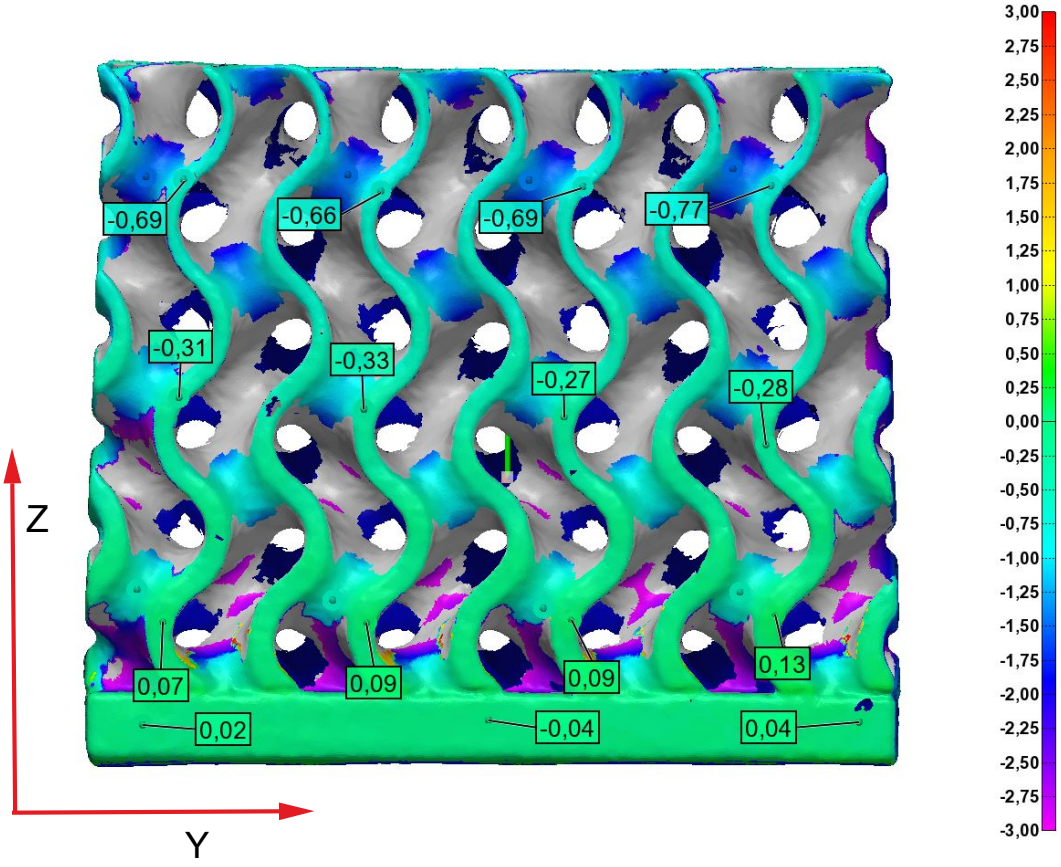

Organization:	Geometry Verification Center	**Part name:**	D02 2 TO 1
Operator:	Branko Markovic	**Part number:**	Gyroid 40X40X30_2to1mm
E-mail:	bmarkovi@volvocars.com	**Piece:**	piece 1

TOLERANCE 3+/-3MM

TOP VIEW

X Y DIRECTION

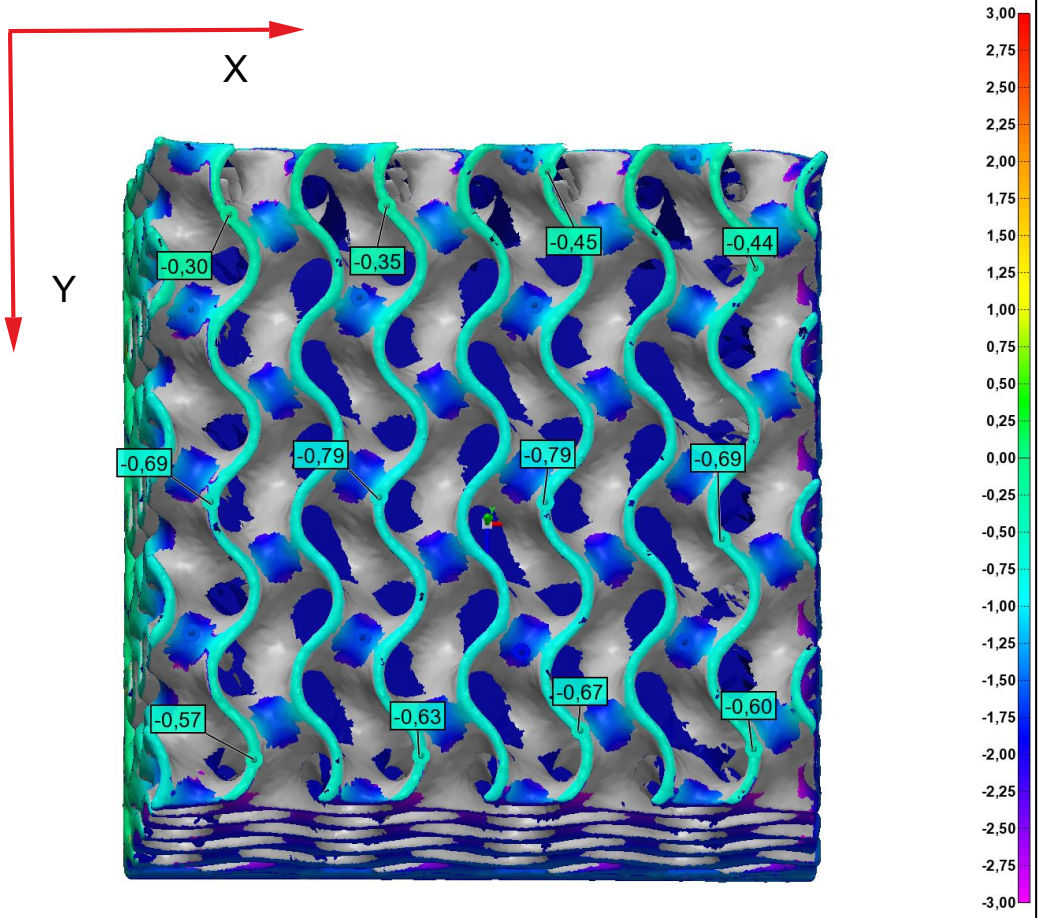

Organization:	Geometry Verification Center	**Part name:**	D02 2 TO 1
Operator:	Branko Markovic	**Part number:**	Gyroid 40X40X30_2to1mm
E-mail:	bmarkovi@volvocars.com	**Piece:**	piece 1

B

Reports: Final Heat Sink evaluation

Final Heat Sink_REV06

Report Author: Anders Odham
Date: 2023-06-27

Scanndata = Orange
Nufo = Gray

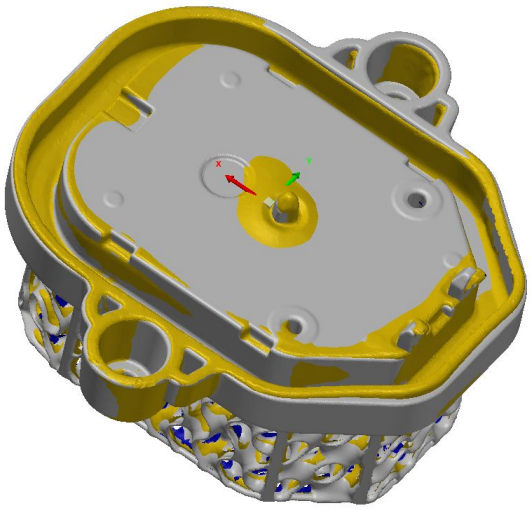

Organization:	Geometry verification center	Part name:	Final Heat Sink_REV06
Operator:	Anders Odham	Part number:	
E-mail:	anders.odhamii@volvocars.com	Drawing #:	
Workspace:	Workspace 2	Serial #:	
Project:	Sista - piece 1	Device:	Modelmaker H120 on MCAx

Align: 3-2-1

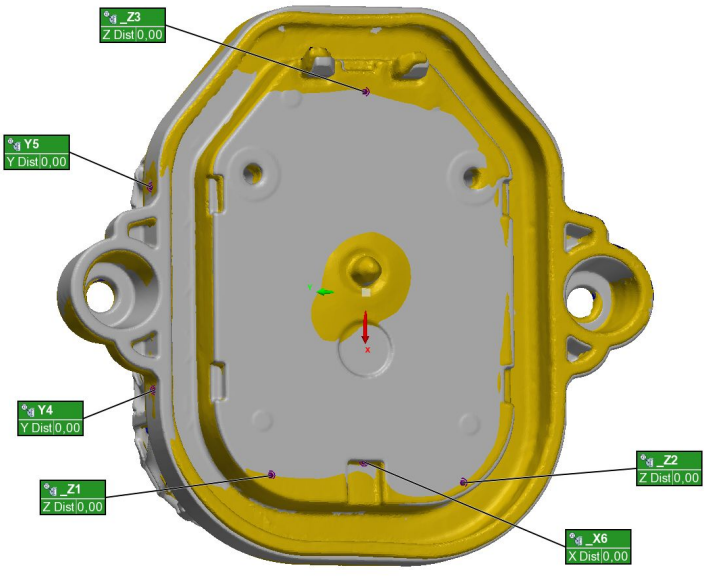

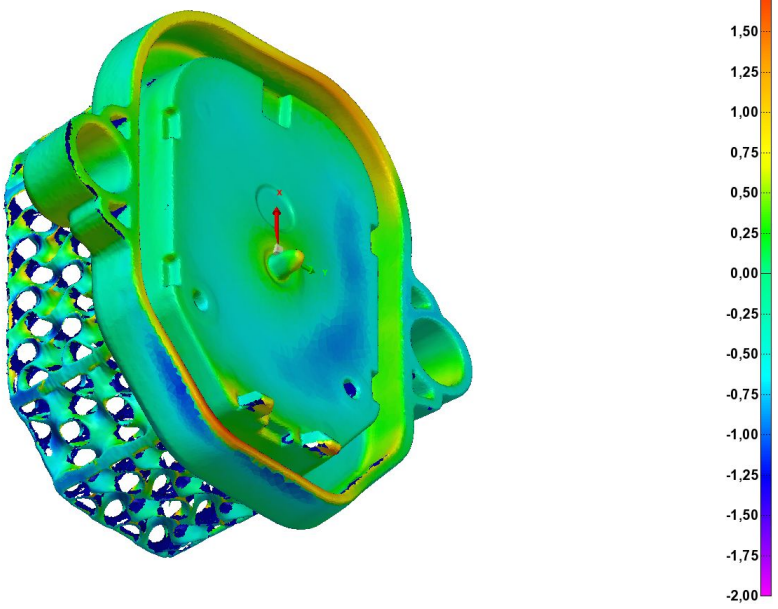

Organization:	Geometry verification center	**Part name:**	Final Heat Sink_REV06
Operator:	Anders Odham	**Part number:**	
E-mail:	anders.odhamii@volvocars.com	**Piece:**	piece 1

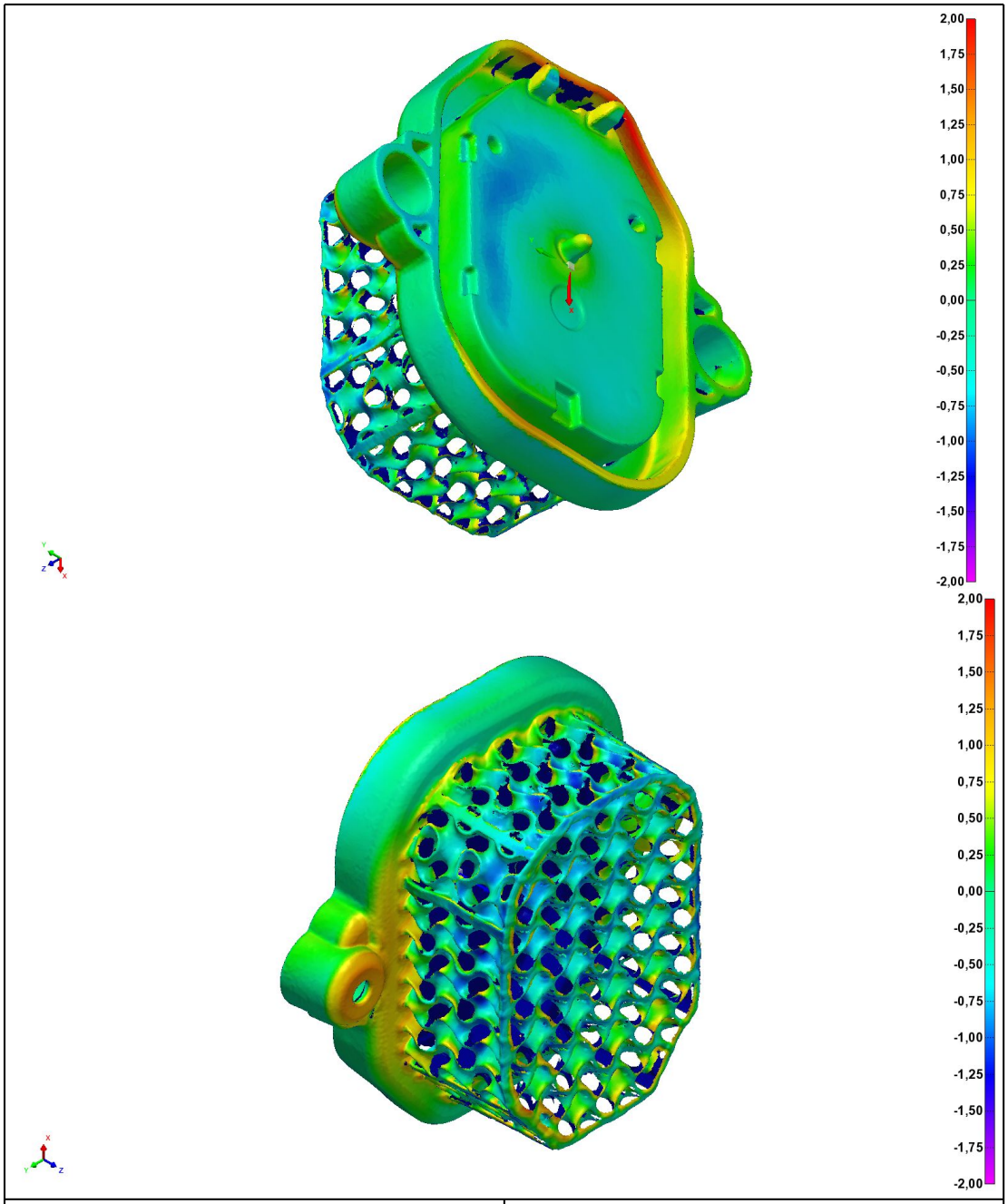

Organization:	Geometry verification center	**Part name:**	Final Heat Sink_REV06
Operator:	Anders Odham	**Part number:**	
E-mail:	anders.odhamii@volvocars.com	**Piece:**	piece 1

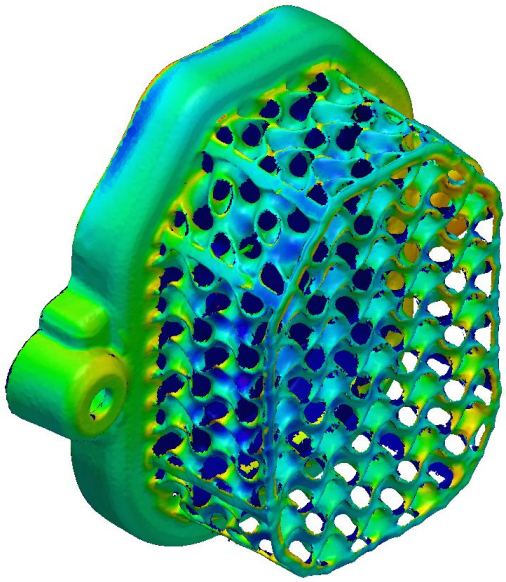

Organization:	Geometry verification center	**Part name:**	Final Heat Sink_REV06
Operator:	Anders Odham	**Part number:**	
E-mail:	anders.odhamii@volvocars.com	**Piece:**	piece 1

DEPARTMENT OF SOME SUBJECT OR TECHNOLOGY
CHALMERS UNIVERSITY OF TECHNOLOGY
Gothenburg, Sweden
www.chalmers.se

CHALMERS
UNIVERSITY OF TECHNOLOGY